EQUILIBRIUM CONTRAST IMAGING

FOR EXTRACELLULAR VOLUME QUANTITATION

Thesis submitted for the degree of Doctor of Philosophy

University College London, June 2016

Dr Steven Bandula MA MB BChir MRCS FRCR
Centre for Medical Imaging
University College London

Declaration

I, STEVEN BANDULA, CONFIRM THAT THE WORK PRESENTED IN THIS THESIS IS MY OWN. WHERE INFORMATION HAS BEEN DERIVED FROM OTHER SOURCES, I CONFIRM THAT THIS HAS BEEN INDICATED IN THE THESIS.

ABSTRACT

In disease and senescence, the balance between cells and the surrounding interstitium is altered. Cell injury and inflammation induce fibrosis, with collagen deposition leading to expansion of the interstitium. When diffuse, this expansion can affect the structure and function of the whole organ. Examples of diffuse fibrosis include liver cirrhosis and myocardial fibrosis, which are becoming more prevalent as the population ages. Traditional assessment of such diseases involves invasive biopsy, but for many tissues, biopsy is poorly tolerated and carries a significant complication risk.

Recently our group has developed a new technique (equilibrium imaging) that utilises the extracellular contrast agents employed widely in MRI and CT to quantify tissue fractional extracellular volume (ECV). Early work demonstrated a significant elevation in myocardial ECV in hypertrophic cardiomyopathy and aortic stenosis. Equilibrium contrast imaging potentially offers a powerful new non-invasive tissue biomarker for 'extracellular disease', and promises new insights into the biology of these conditions.

In this thesis I develop the equilibrium imaging technique, beginning with an evaluation of the basic principles of extracellular volume estimation by EQ-MRI - using a 3-dimensional engineered tissue model. I show an association between ECV quantified during construction of six engineered models with ECV measured using EQ-MRI (R^2=0.77, p=0.02). I then explore the use of equilibrium imaging in quantifying two disease processes that alter the extracellular volume – diffuse fibrosis and amyloidosis. EQ-MRI is used in systemic amyloidosis to demonstrate significant elevation in ECV within the liver (0.32) and spleen (0.39) compared with healthy volunteers (p<0.01). I then translate the basic EQ method to a new modality – computed tomography, a potentially simpler

and more widely available imaging platform. EQ-CT is used to show an association between ECV and a histological comparator in cardiac valve disease (r=0.71); and in liver cirrhosis (r=0.64). EQ-MRI is also used as a reference test to investigate diffuse 99mTc-DPD skeletal muscle uptake in systemic ATTR amyloidosis. Using a novel scoring system to quantify uptake, I show that skeletal muscle ECV increases with 99mTc-DPD soft tissue score (R^2=0.34) - suggesting that skeletal muscle is a significant target organ for amyloid deposition.

Technical development of the CT technique required the optimisation of image acquisition and processing for quantitative attenuation measurement within tissues, and advancement of the contrast protocol to allow rapid ECV estimation using a bolus only dynamic equilibrium technique.

In summary, this research thesis presents methological development and validation of EQ imaging for tissue extracellular volume fraction quantification.

CONTENTS

Chapter **Page**

Tables and Figures

Abbreviations

3D ..... Three dimension
99mTc-DPD ..... Technetium-DPD
AIDR ..... adaptive iterative dose reduction
AIF ..... arterial input function
AL ..... Light chain amyloidosis
ALT ..... alanine aminotransferase
APRI ..... aspartate aminotransferase/platelet ratio index
ARFI ..... acoustic radiation force impulse elastography
AUROC ..... Area Under the Receiver Operator Curve
CBC ..... Complete Blood count
CCl4 ..... Carbon tetrachloride
CE ..... Conformité Européenne
CMR ..... Cardiac Magnetic Resonance imaging
CNR ..... Contrast to Noise Ratio
CPA ..... Collagen Proportionate Area
CT ..... Computed Tomography
CT ..... Computed Tomography
DCE-MRI ..... Dynamic Contrast Enhanced – MRI
DIA ..... digital image analysis
DICOM ..... Digital Imaging and Communications in Medicine
DLP ..... Dose length product
DMEM ..... Dulbecco's modified Eagle's medium
DOTA ..... tetracarboxylic acid
DPD 3,3-diphosphono-1,2-propanodicarboxylicacid
Dyn ..... Dynamic
ECG ..... Electrocardiogram
ECM ..... Extracellular Matrix
ECV ..... Extracellular volume fraction
ECVdyn ..... ECV using dynamic equilibrium
ECVss ..... ECV using steady state equilibrium
EF ..... ejection fraction
eGFR ..... Estimated Glomerular Filtration Rate
ELF ..... Enhance Liver Fibrosis
EQ ..... Equilibrium Contrast Imaging
FDG-PET ..... Fludeoxyglucose – Positron Emission Tomography
FLASH ..... fast low angle shot
FOV ..... Field Of View
GAG ..... Glycosaminoglycan
Gd ..... Gadolinium contrast

GFR.....Glomerular Filtration Rate
HA .....Hyaluronic Acid
HBV .....Hepatitis B Virus
HCV .....Hepatitis C Virus
HPLC.....High Performance Liquid Chromatography
HPLC.....High performance liquid chromatography
HRCT .....High Resolution Computed Tomography
HSCs .....Hepatic Stellate Cells
HU .....Hounsfield units
HVPG.....hepatic venous pressure gradient
IQR .....Interquartile Range
IR .....Inversion Recovery
kDa .....Kilo Dalton
kPa .....kilopascals
kV .....KiloVolts
LGE .....late gadolinium enhancement technique
LOX .....lysyl oxidase
LVEDP.....left ventricular end diastolic pressure
MEG .....motion-encoding gradient
MMP2 .....metalloprotease
MOLLI.....Modified Look Locker Inversion recovery
MRE.....Magnetic Resonance Elastography
MRI.....Magnetic Resonance Imaging
NAC .....National Amyloidosis Centre
NAFLD .....non-alcoholic fatty liver disease
NaOH.....Sodium hydroxide
NASH .....non-alcoholic steatohepatitis
PACS.....picture archiving and communication system
PG.....Proteoglycans
PPH.....Protocollagen Proline Hydroxylase
R1 .....Relaxivity (1/T1)
ROI .....Region of Interest
SAFIRE .....Sinogram AFfirmed Iterative Reconstruction
SAP .....Serum Amyloid P
SD.....Standard Deviation
ShMOLLI.....Shortened Modified Look Locker Inversion recovery
SI .....Signal intensity
SLRPs.....Small Leucine-Rich Proteoglycans
SNR.....Signal to Noise Ratio
SPECT .....Single-photon Emission Computed Tomography
ST .....Soft Tissue

T1 ..... T1 relaxation time
TE ..... Transient Elastography
TGF-β..... transforming factor beta
TGFβ..... transforming growth factor beta
TI ..... Time to Inversion
TIMP1..... tissue inhibitor of matrix metalloprotease 1
TNF..... Tumour necrosis factor
TR ..... Repetition Time
TTR ..... Transthyretin
UCL..... University College London
UCLH..... University College London Hospitals NHS Trust
WIP..... Work In Progress

Funding

CRDC Pre doctoral fellowship

This competitive local entry-level fellowship funded by the UCLH Charities and awarded by the UCL Clinical Research and Development Committee (CRDC ref E006) provided salary (£67,875) and expenses (£7,125) to complete 15 months full time research. The project title: Equilibrium contract imaging using computerised tomography 'EQ-CT' as a measurement of tissue interstitial volume; development and validation in the liver and heart. The fellowship allowed me to complete initial experiments toward development of the equilibrium CT technique, including contrast administration protocol and gather pilot data for a more substantial fellowship application. The fellowship began on 1/07/2010 and ended on 30/09/2011.

NIHR doctoral fellowship

This fellowship scheme is aimed at allowing pre-CCT level doctors to complete patient-based clinical or applied health research. I submitted an application in January 2011 entitled 'Equilibrium Contrast Imaging – development and validation in the heart and liver' and was interviewed on 28/06/2011. I was subsequently awarded a 36-month fellowship, with

£450k funding to complete this work. The fellowship began on 01/10/2011 and ended on 30/09/2014.

National Amyloidosis Centre bursary

The National Amyloidosis centre is the sole UK centre specialising in amyloidosis and acute phase protein related diseases. The centre runs a programme of research dedicated to improving management of these conditions, lead by Prof Philip Hawkins. After completing initial technical development and early proof of concept studies showing that EQ-CT was able to identify and quantify amyloid within specific tissues, the centre award me with funding of up to £50k to validate the technique against clinical outcomes in a larger cohort of patients.

ACKNOWLEDGEMENTS

Completion of this thesis would not have been possible without the kind support and encouragement of my supervisors, colleagues, friends and family.

I am tremendously fortunate to have three outstanding supervisors who have given generously of their time, supported completion of this work and inspired me to pursue an academic career. I'd like to thank Shonit Punwani for the introduction to research, encouraging me to undertake this endeavour and for supporting me throughout. Thank you to James Moon for his enthusiasm, guidance and for allowing me to join the Equilibrium Imaging group. Stuart Taylor has been a model primary supervisor. I'd like to thank Stuart for being supportive and patient, and for always providing insightful and sapient advice.

Thank you to the research fellows with whom I toiled - Thomas Treibel, Steve White, Marianna Fontana, Sanjay Banypersad, Jason Yeung, and Tarig Magdeldin. Thank you also to my colleagues at UCLH, the Royal Free and UCL; in particular the Radiographers Elaine Atkins, Preeya Patel, Gareth Askey, Gemma Lewis and Angrea Bangay.

Lastly I'd like to thank my wonderful wife and daughter – for their wily distraction, that kept me going; and for allowing this selfish indulgence.

PREFACE

This thesis represents original work by the author and has not been submitted in any form to another institution. Where use has been made of the work of others it has been duly acknowledged in the declaration at the beginning of each chapter.

The work described was performed at the Centre for Medical Imaging, University College London under the supervision of Professor Stuart Taylor and Dr. Shonit Punwani (UCL Centre for Medical Imaging) and Professor James Moon (UCL Institute of Cardiovascular Science). Experiments and imaging studies were conducted at University College London Hospital, the Royal Free London, The Heart Hospital, and UCL Institute of Orthopaedics and Musculoskeletal Science (IOMS).

1 INTRODUCTION

1.1 Thesis Overview

As complex multicellular organisms, humans are composed of a host of metabolically active cells, supported within a protein framework. In health, this structure provides the medium through which cells exchange components necessary for intra cellular metabolism, allowing them to contribute physically and metabolically to the function of their constituent tissue.

In disease and senescence, the delicate relationship between cells and their surrounding framework can be disrupted. Cell injury and inflammation leads to fibrosis with expansion of the interstitium and reduction in cellularity. This fibrosis can occur focally leading to 'scar' or diffusely affecting whole organs. Familiar examples of diffuse fibrosis that ultimately lead to organ failure include pulmonary fibrosis and liver cirrhosis.

As we better understand the role the interstitium plays in disease, it is clear that diffuse interstitial dysfunction frequently plays a more significant and previously unrecognised role in disease. In the heart, pathologists already identify disease states such as 'idiopathic myocardial fibrosis' that are virtually unrecognised clinically. Yet in the heart, diffuse fibrosis is very likely to play as significant a role as in other organs such as the liver, and may be associated with adverse outcomes including heart failure, arrhythmia and death.

One of the principle reasons for our limited understanding of the importance of interstitial disease has been an inability to reliably and accurately interrogate the interstitium. The current reference standard of invasive tissue biopsy is limited by its technical difficulty, complication rate, and sampling error. This has led to the development of a number of non-

invasive tests, including serum biomarkers and tissue elastography, although these are frequently organ specific or suffer from similar sampling error.

Recently, **equilibrium contrast imaging** has been developed to non-invasively quantify diffuse interstitial expansion in a range of organs. This technique potentially offers a new tissue biomarker for 'extracellular disease', and promises new insights into the biology of these conditions.

This thesis broadly aims to develop the equilibrium imaging technique into a robust and validated clinical test that can be used to quantify extracellular volume (ECV) in a range of tissues and diseases.

The manuscript comprises 13 chapters, with experimental chapters summarised below. Unless otherwise stated, all work is that of the author. Peer-reviewed publications related to each chapter are summarised in Appendix 1.

Chapter 1 provides a background to the thesis and starts by exploring current understanding of the structure and function of the interstitial space, and the specific proteins and other elements that occupy its volume. Pathological process which lead to expansion of the extracellular volume are then described with specific reference to diffuse fibrosis within the heart and liver; and systemic amyloidosis. Section (ii) describes existing techniques used to assess the extracellular volume and extracellular expansion in disease – laying out the justification for development of new methods. Section (iii) then gives a background of the contrast techniques that led to the first use of equilibrium contrast imaging to quantify the extracellular volume, followed by a more detailed description of the underlying theory.

In **chapter 2** the overall research hypothesis is set out, with the specific aims and objectives to be addressed with the subsequent chapters.

Chapter 3 provides a technical description of methods utilised in the development of EQ imaging, including comparative biomarkers, imaging technologies, data processing and statistical methods.

In **Chapter 4** the basic principle of extracellular volume measurement by equilibrium imaging are tested using EQ-MRI and an engineered 3 dimensional tissue model.

In **Chapter 5** the equilibrium cardiac MRI methodology developed by colleagues at UCLH and the Institute of Cardiovascular Science is applied to the liver and spleen of patients with systemic Amyloidosis to assess disease burden. Measurements are validated by comparison with the current reference standard of Serum Amyloid P component scintigraphy.

Chapter 6 describes the translation of the equilibrium imaging technique from MRI to a computed tomography imaging platform, with development of an iodinated contrast equilibrium protocol. The contrast protocol is verified by CT in a group of healthy volunteers and CT based myocardial ECV measurement validated by comparison with MRI in a group of patients with aortic stenosis.

In **chapter 7** use of the technique is extended by application to measurement of diffuse fibrosis within the liver. Patients with viral hepatitis and a range of parenchymal disease severity - from no fibrosis to cirrhosis - are evaluated with equilibrium CT and comparison is made with the reference histological standard and an existing plasma biomarker panel.

Development of equilibrium contrast CT is extended further in **chapters 8 and 9** with evaluation of the artefacts behind error in tissue attenuation measurement, and optimisation of the iodinated contrast protocol to refine the technique into a practical and clinically applicable test.

Finally, in **chapter 10** equilibrium MRI is used to investigate skeletal muscle amyloid deposition in systemic Amyloidosis, and to corroborate soft tissue uptake seen on DPD scintigraphy.

1.2 Ethical Approval

At the outset of this project I made an application to the London Queens Square Research Ethics Committee and was granted approval (Ref: 09/H0716/75) for the experiments described. Major amendments were made to allow recruitment of additional patients with aortic stenosis undergoing surgery; to perform scans at a second centre and thirdly to recruit an additional cohort of patients with systemic amyloidosis. I made a final forth major amendment in May 2015 to allow a reduction in the renal function threshold for recruitment exclusion – mirroring clinical departmental and Royal College of Radiologist' policy.

Ethical approval for equilibrium MRI (EQ-MRI) in aortic stenosis and amyloidosis was obtained from the UCL/UCLH research ethics committee by Dr. Andrew Flett (Ref: 07/H0715/101) with a substantial amendment by Dr. Daniel Sado to allow collection of EQ-MRI data in a group of healthy volunteers (n=100).

1.3 Background

1.3.1 Composition, structure and function of the interstitium

The vertebrate extracellular space is filled with an intricate network of macromolecules. This extracellular matrix (ECM) was once considered an inert structural scaffold, simply providing mechanical support for the cells within a tissue. Many decades later we appreciate the ECM as a complex dynamic structure, playing a central role in modulating biochemical and biomechanical cues that are a crucial part of tissue morphogenesis, differentiation and homeostasis. This importance is highlighted by the range of conditions arising from monogenic disorders of ECM components, which include osteogenesis imperfect, Ehlers-Danlos and Marfan's syndrome (1).

Although essentially composed of water, polysaccharides and proteins, the extracellular matrix within each tissue has a unique composition and topology, adapted to the functional requirements of the particular tissue. The matrix can become calcified, forming the rock like structure of bone and teeth, can have large amounts of linearly arranged fibrous elements with enormous tensile strength as seen in tendons, and can form the transparent matrix of the cornea. However this phenotype is not static. A constant interplay between the matrix and cells allows dynamic remodelling of the ECM, and alteration of tissue properties and function in response to physiological and pathological cues. This is mediated by a number of mechanism including chemical signalling, transmembrane mechanical coupling and cell surface receptors (2).

The ECM is generally composed of two main classes of macromolecules. The insoluble fibrous proteins, which provide the structural elements are the collagens, elastins, fibronectins and laminins. The second group, soluble proteoglycans (PG) make up the ground substance; a hydrated gel, which occupies the majority of the extracellular volume.

I will consider some of these major components in detail before discussing their role in extracellular expansion and resultant tissue dysfunction.

1.3.2 Structural interstitial proteins

Collagens are the most abundant protein within the ECM, comprising up to 30% of the total protein mass of a multicellular animal and are chiefly responsible for maintaining its structural integrity. Collagens provide tensile strength; regulate cell adhesion and support chemotaxis and migration.

The collagens typically comprise of long, stiff, triple-stranded helical molecules of three collagen chains (α chains) wound into a rope like superhelix (Figure 1.1). These α chains are rich in proline and glycine - proline stabilises the helical conformation and being the smallest amino

acid, allows tight packing of the α chains. Approximately 25 distinct α chains have so far been identified, with expression of various combinations producing the 20 or so collagen molecules that have been found so far. The most abundant collagen within the body is Type I, which forms the principle collagen in skin, fascia, tendons and scar. Type III co-polymerises with type I within the wall of blood vessels and bowel. Type II collagen occurs within the cornea and vitreous body of the eye and within cartilage. Types V and XI are minor components found co-polymerised with Types I and II (3). Once synthesized by fibroblasts or related cells specific to the tissue type e.g. chondroblasts, myofibroblasts or osteoblasts – α chains assemble in the extracellular space to form procollagen. Cleavage of terminal procollagen peptides by specific procollagen metalloproteinases produces collagen molecules that are able to assembly into higher-order collagen fibrils, stabilised by covalent cross-linking between residues that dramatically increases the tensile strength of the fibril. The alignment and organisation of fibres is dependent on tissue function, for example in tendons, fibres are aligned along the long axis or rotate into this axis on loading, thus providing the greatest resistance to strain.

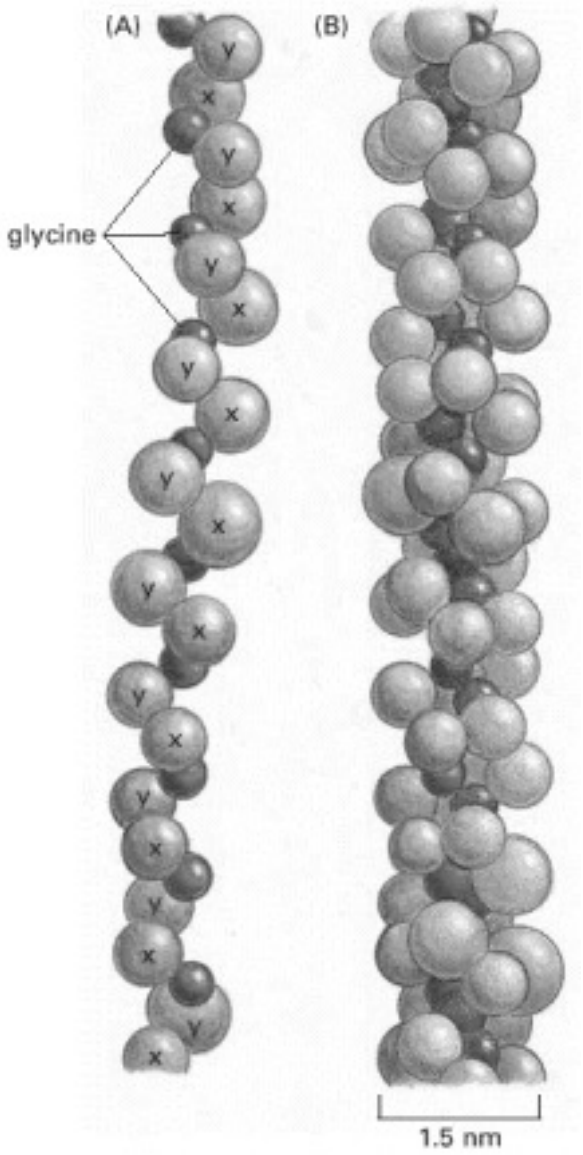

Figure 1.1 Collagen α chain and molecule

From 'Molecular Biology of the Cell. 4th edition. Alberts B, Johnson A, Lewis J, et al. New York: Garland Science; 2002. (A) A single collagen αchain arranged as a left-handed helix, with three amino acids per turn and glycine as every third amino acid. (B) Part of a collagen molecule in which three αchains are wrapped around each other forming a triple-stranded helical rod.

Elastin is a highly hydrophobic protein, rich in proline and glycine, which forms the main component of the elastic fibres that give tissues their elasticity. This property is crucial for tissues such as the lungs and artery walls – allowing them to stretch and recoil. By intertwining elastin fibres with collagen fibrils, tissues acquire resilience and can limit the amount of stretching. Soluble tropoelastin is secreted into the extracellular space and

assembles into elastic fibres, which becoming extensively cross-linked. There is controversy over the structural conformation that accounts for the elasticity, however the leading view is one of a loose random coil, rich in hydrophobic residues and cross linked with covalent bonds that can stretch and contract (2). The elastin core is covered with a sheath of microfibrils, composed of a number of distinct glycoproteins, including fibrillin, which bind elastin and are essential for integrity of the fibre. Mutations in fibrillin result in Marfan's syndrome, a relatively common condition with affected individuals being prone to aortic dilatation and rupture.

Fibronectin is a member of a group of molecules that typically have multiple domains with specific binding sites for other matrix macromolecules and for cell surface receptors. This group is intimately involved in the organisation of the extracellular matrix and attachment of cells to it, and is essential for cell migration and cellular differentiation. The fibronectin molecule can be stretched, exposing cryptic binding sites within the molecule, which mediate pleiotrophic change in cellular behaviour (adhesion, migration etc).

1.3.3 Proteoglycans

Proteoglycan (PG) molecules within the extracellular space form a highly hydrated, gel-like ground substance into which the fibrous structural proteins are embedded. The volume of this gel allows the matrix to resist compressive forces while permitting the diffusion of a range of substances – including metabolites, nutrients and hormones – between cells and the blood. PGs are composed of glycosaminoglycan (GAG) chains, covalently joined to a specific protein core (with the exception of hyaluronic acid) and are classified by core protein, localisation and GAG composition. There are three main families, small leucine-rich proteoglycans (SLRPs), modular proteoglycans and cell-surface proteoglycans (3,4). By definition, at least one sugar side chain of a proteoglycan must be a GAG, but unlike

other glycoproteins, proteoglycans can be huge, containing as much as 95% carbohydrate by weight, in the form of long unbranched GAG chains.

Glycosaminoglycans are unbranched polysaccharide chains of repeating disaccharide units, with one of the two sugars always being an amino sugar (N-acetylglucosamine or N-acetylgalactosamine) and the second usually a uronic acid (glucuronic or iduronic). Sulfate or carboxyl groups on most of these sugars make GAGs highly negatively charged – a key property making GAGs the most anionic molecules produced by animal cells. This makes the molecules extremely hydrophilic. Negative charges attract a cloud of cations, notably Na+ that are osmotically active, causing large amounts of water to be drawn in. The polysaccharide chains are also stiff and resistant to folding into the globular structure typically adopted by polypeptide chains. GAGs therefore form highly extended conformations, occupying a huge volume relative to their mass, and will form a hydrated gel even at very low concentrations. The osmotic swelling pressure, or turgor thus produced provides mechanical support and allows the matrix to withstand large compressive forces.

Hyaluronan, or Hyaluronic acid (HA) is the simplest of the glycosaminoglycans, consisting only of a repeating sequence of disaccharide units. Unlike the other GAGs, HA contains no sulphated sugars, and has an enormous chain length of thousands of monomers that are not generally linked to any core protein. HA is at the extreme end of the GAG spectrum, but its structure and chemical properties are illustrative of the group and have been extensively studied. In the early 1950s, Ogston and Stainer (5) described how the polyanion behaved hydrodynamically like a large solvated sphere containing a thousand times more water than organic material. Further investigation demonstrated a stiff random coil conformation to the molecule (6). HA acting as a network forming and space-filling component fulfils a wide range of roles, acting to create space for cell migration during embryonic development, in wound healing and within articular cartilage and synovial fluid.

Aggrecan, the major proteoglycan in cartilage, assembles with HA to form aggregates with over 100 GAG chains creating a large osmotic swelling pressure, occupying a volume of approximately 2 × 10-12 cm3 – i.e. as large as a bacterium (Figure 1.2). The water swollen Aggrecan matrix is critical to the biomechanical properties of cartilage. Combining with collagen also makes the cartilage matrix network stiff and resistant to deformation, and fluid flow. Cartilage is then viscoelastic – both stiff and elastic – and can resist sudden impact loading and show inelastic deformation with sustained loads (7).

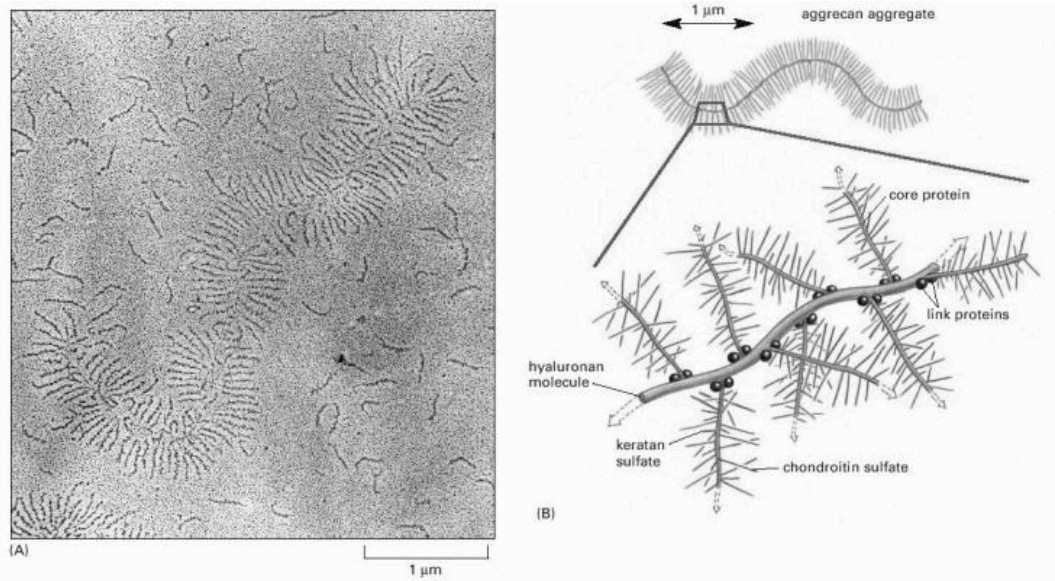

Figure 1.2 Electron micrograph of an aggrecan aggregate

From 'Molecular Biology of the Cell. 4th edition. Alberts B, Johnson A, Lewis J, et al. New York: Garland Science; 2002. (A) A single collagen αchain arranged as a left-handed helix, with three amino acids per turn and glycine as every third amino acid. (B) Part of a collagen molecule in which three αchains are wrapped around each other forming a triple-stranded helical rod.

The extracellular space is then composed of a number of different contributing matrix elements – the main elements being collagen,

proteoglycans and water. In this thesis I will consider various indirect methods to quantify this extracellular volume. These techniques focus only on one or two of the main elements (usually collagen or water), with quantity or volume acting as a surrogate for the EQ volume as a whole. A true measure of the extracellular volume should encompass all of the extracellular space elements, although a reliable method to quantify this space has yet to be devised. The seemingly obvious solution would be direct visualisation and measurement of the fractional cellular or extracellular volume within a tissue, using microscopy. However, the majority of microscopy preparation techniques result in some physical disruption of tissue, cellular hypoxia and swelling. Water-soluble molecules are also washed out of the extracellular matrix when tissue sections are exposed to aqueous fixations solutions, and changes in pH, ionic, or osmotic conditions can drastically matrix protein conformation. Thus, indirect methods must be used.

1.3.4 Interstitial expansion in disease

The basic constituents of the interstitium are essentially the same in all tissues, although their relative quantities vary enormously. Rather than a static structure, the interstitium is in a constant state of turnover - growing, repairing and remodelling. This dynamic process is controlled by a host of cytokines, growth factors, enzymes, hormones and cell-to-cell signalling which allows tissues to adapt to changes in their physical and chemical environment.

However certain diseases will exhaust cellular adaptation and interstitial homeostasis - leading to an accumulation of disorganised proteins with consequent effects on tissue functions. The main disease processes in which this occurs are (i) diffuse fibrosis and (ii) amyloidosis.

1.3.5 Diffuse fibrosis in the heart

Focal fibrosis within the heart resulting from myocardial infarction remains a leading worldwide cause of cause of heart failure – and considerable emphasis has been placed over the past 4 decades on understanding its pathophysiology, treatment and prevention. Diffuse myocardial fibrosis has also been recognised for some time (8) but its importance in diseases such as myocarditis, cardiomyopathy (9) and valve disease has only recently been appreciated. The pathological remodeling of the myocardium associated with diffuse fibrosis leads to ventricular systolic and diastolic dysfunction, and eventual heart failure, but this pathway is potentially reversible (10).

Myocardial remodelling is a complex process involving genome expression, molecular, cellular, as well as interstitial changes. Early work examining interstitial changes showed that increasing skeletal (11) or myocardial (12) workload results in an increase in protocollagen proline hydroxylase (PPH) production, an enzyme participating in collagen biosynthesis. The increase in PPH is followed by an increase in extracellular collagen components, with an increase in larger diameter type I collagen fibres relative to other subtypes, and higher degree of fibre cross linking by lysyl oxidase (LOX). These changes are required to support the accompanying increase in myocyte mass, thus facilitating muscle growth and augmented muscular force. Weber et al. described a second ‘physiologic’ phase of this work-induced hypertrophy (12) wherein remodelling of these new elements occurs. Removal of the increased loading during this phase however causes the myocardium to remodel and revert back to normal. Progressive loading beyond this point leads to a maladaptive ‘pathologic’ phase, where alterations in collagen subtype proportions occurs; fibril arrangement and binding become disordered and matrix remodelling may become irreversible. Here the balance between structural and maintenance proteins is lost and there is accumulation of disordered ineffective matrix – Figure 1.3. These changes, coupled with

myocyte degeneration results in a drop in contractility indices, leading clinically to myocardial failure (10).

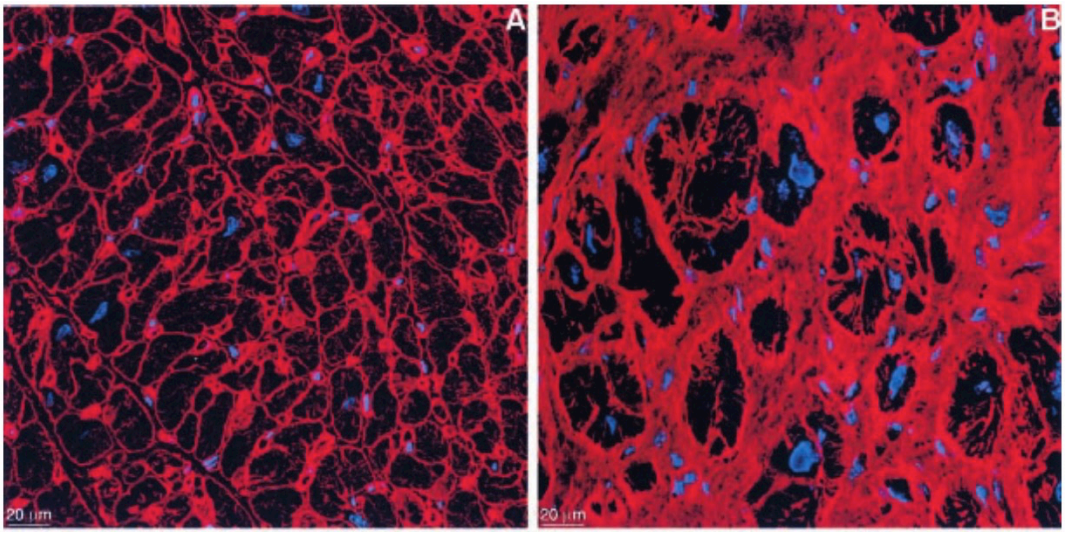

Figure 1.3 Stained electron microscopy image

Electron microscopy image with Fibronectin stained red and myocyte nuclei blue. (A) normal myocardium with fine septa between unstained myocytes. (B) severe fibrosis with few myocytes. From Hein et al. Circulation 2003

A disproportionate accumulation of interstitial collagen is a characteristic feature of sustained arterial hypertension and is responsible for progressive abnormalities of diastolic relaxation, filling and ultimately systolic dysfunction. Associated left ventricular hypertrophy is an adaptation to these changes and is known to be a risk factor for arrhythmias, cardiac failure and sudden death. Hein et al. investigated the relationship between cardiac function and myocardial morphology in patients with aortic stenosis – demonstrating worsening fibrosis and myocyte degeneration with increasing left ventricular end diastolic pressure (LVEDP) and later falling ejection fraction (EF). A low grade inflammation was present with leukocytes and macrophages - the likely mediators of cytokine production such as ACE and TFG-β_1 leading to reactive fibrosis (13). TFG-β_1 regulates the turnover of collagen by myocardial fibroblasts, and abnormal persistence of myofibroblasts is seen

as a hallmark of fibrotic disease. TFG-$\beta_1$in turn is controlled by angiotensin II synthesised locally by ACE. Increased expression and activity of ACE leading to upregulation of collagen mRNA is seen in aortic stenosis, cardiomyopathy, and also near an infarct scar. Proteins such as transforming growth factor (TGF), endothelin-1, angiotensin II (Ang II), connective tissue growth factor (CCN2/CTGF), and platelet-derived growth factor (PDGF) act in a network that contributes to myofibroblast differentiation and persistence.

Invasive tissue sampling has shown that myocardial fibrosis is likely to play a crucial role in adverse myocardial remodelling, but the scarcity of human data has prevented assessment of the clinical importance of this process in terms of morbidity and mortality. Wider evaluation of the population significance will require development of non-invasive methods of assessment. These techniques could enable appropriate patient risk stratification, and allow evaluation of drugs and interventions targeting myocardial fibrosis.

1.3.6 Diffuse fibrosis in the liver

Diffuse fibrosis and derangement of the extracellular environment leading to organ dysfunction is the hallmark of chronic liver disease, and is a major cause of worldwide morbidity and mortality. In 2004, the direct cost of chronic liver diseases in the United States was estimated at $2.5bn; with indirect costs adding an additional $10.6 billion to this value (14,15).

Diffuse liver fibrosis can occur as a rapidly progressive process over weeks or months as a result of drug injury or hepatitis C infection after transplantation, but it is the sustained activation that accompanies chronic liver diseases which allows for significant accumulation of fibrosis. This chronicity compared with diffuse fibrosis in other organs such as the kidneys or lungs is likely a reflection of the liver's unique regenerative

capacity. In the normal liver, fibrous interstitial elements are quantitative small compared with other organs; however small changes in the EC matrix can affect liver function.

In the healthy liver, collagen types I, III, and V, the major constituents of fibrillar collagen, are confined mainly to the portal tract and central vein wall, while type IV collagen, in association with laminin and entactin-nidogen, form a low-density basement membrane-like material along the sinusoid wall (a true basement membrane is usually absent). The low density of this basement membrane-like structure is critical for allowing easy diffusion between blood and liver cells.

Despite the diversity of agents that are noxious toward the liver (viruses, drugs, alcohol, autoantibodies, iron, etc.), the liver responds via a standardized pathway. The most prevalent diseases, including - viral hepatitis, alcoholic steatohepatitis (ASH), and non-alcoholic steatohepatitis (NASH) are characterised by an inflammatory response with leukocyte infiltration that produces high levels of profibrinogenic cytokines such as transforming factor beta (TGF-β), metalloprotease (MMP2), and tissue inhibitor of matrix metalloprotease 1 (TIMP1), which can be detected in the blood plasma. Metabolic diseases such as haemochromatosis however also induce diffuse fibrosis and lead to cirrhosis, but lack an inflammatory cell infiltrate, demonstrating multiple routes for activation of this standard pathway. One potential set of common mediators are the reactive oxygen species. These unstable compounds, which include superoxide and hydroxyl radicals and hydrogen peroxide are generated through lipid peroxidation in hepatocytes, macrophages and Hepatic Stellate Cells (HSCs) (16). Production is enhanced by ethanol and fatty acids, leading to cell injury.

The mechanism of liver fibrogenesis is complex and incompletely understood, however human and animal studies suggest that hepatocellular damage is followed by a signaling response which leads to

activation of the innate immune system, hepatic stellate cell activation and EC matrix deposition. Some authors have suggested that in the case of viral hepatitis, an immune response to antigens normally sequestered within the EC matrix is the cause of the necroinflammation and subsequent fibrosis. Tumour necrosis factor (TNF) appears to be key a cytokine, responsible in health for normal hepatocyte proliferation during liver regeneration, HSC activation and for apoptosis of damaged cells though the TNF receptor 1. Tarrats et al. showed that specific knock out of the TNF receptor 1 in bile duct ligated mice led to a significant reduction in HSC proliferation and fibrogenesis (17).

The pattern of accumulation of extracellular matrix components leading to cirrhosis varies with disease. Fibrosis due to viral hepatitis begins in the portal triads and manifests initially as fibrous expansion of the portal triads. Stellate fibrous septa then extend from the portal triads into the surrounding hepatic parenchyma, lengthening and thickening to eventually form fibrous bridges (bridging fibrosis) that link adjacent portal triads and central veins. As the injury continues, the bridges enlarge and coalesce, dividing the liver into cellular islands of dense hepatocytes – regenerative nodules – surrounded by bands of highly disorganised and loosely arranged fibrosis tissue which expand the extracellular space. These fibrotic bands carve through the liver parenchyma. Architectural distortion also follows as liver cell regeneration occurs around these fibrous septa – these regenerative nodules are the hallmark or cirrhosis. Advanced disease is also associated with an angiogenic reaction that leads vascularisation of the fibrotic tissue and redistribution of the normal vascularisation within the liver lobule.

In contrast, fibrosis due to non-alcoholic fatty liver disease (NAFLD) and in alcohol liver disease begins adjacent to the central veins. Fibrotic matrix is deposited in a peri-sinusoidal pattern (chicken-wire fibrosis) with elements surrounding individual hepatocytes (18). With disease progression the fibrosis extends to the portal tracts, producing fibrotic tracts which when

extensive becoming indistinguishable from cirrhosis secondary to viral hepatitis.

The traditional view of diffuse liver fibrosis as an irreversible process has been dispelled, with studies now showing that once identified, even advanced fibrosis can be reversed. Removal of the causative agent is the most effective treatment and spontaneous resolution of liver injury can occur following successful treatment of an underlying disease process e.g. alcohol induced liver injury, viral hepatitis, haemachromatosis and autoimmune hepatitis. Treatment of chronic hepatitis C viral infection has been studied extensively, with viral clearance using IFN-alpha plus Ribavirin resulting in nearly half of patients with cirrhosis demonstrating significant improvement of fibrosis. For patients with end stage cirrhosis with complications resulting from organ failure and portal hypertension, transplantation is currently the only shown to improve survival and quality of life.

Various strategies for blocking or reversing progression of liver fibrosis have been evaluated in experimental animal models and small clinical trials with some success. These include the use of anti-inflammatory agents, modulators of HSC activation; antioxidants and disruptors of TGF-beta synthesis. Inhibition of the renin-angiotensin system has also been evaluated. There however remains no standard therapy for liver fibrosis, with translation and evaluation in humans slowed by the need for serial biopsy and long-term follow-up.

1.3.7 Systemic amyloidosis

The amyloidoses are a group of disorders in which a misfolded pathogenic protein aggregates into insoluble fibrils that accumulate in the extracellular space, leading to disruption of tissue structure and function. Biochemical and environmental factors allow the normally soluble protein to adopt partially folded states leading to self-association and formation of a cross-β structure and protofilaments measuring 2-5 nm in diameter which either

coil together or adhere to form fibrils. Amyloid fibrils differ from other protein aggregates as they show apple green birefringence when stained by Congo red and viewed by microscope under polarized light. This method of Amyloid identification, although technically challenging and requiring a long staining process has been the reference standard since the 1950s.

The amyloidoses form a heterogeneous group of clinical conditions, involving one or more organs – including the heart, kidneys, liver, and nervous system. In its localised form the disease largely affects the organ of the precursor protein synthesis, and can cause intra and extracellular protein synthesis - examples include neurodegenerative disorders such as Parkinson's, Alzheimer's, and Huntington's disease. In contrast all the systemic amyloidoses are extracellular, with precursor protein secreted at a site distinct from the major sites of deposition.

Systemic amyloidosis is the quintessential extracellular disease; it is a relatively rare multisystem condition in which amyloid protein deposition occurs in various tissues and organs, causing organ dysfunction through interstitial expansion. It may present to almost any specialty with non-specific symptoms including fatigue, weakness, loss of appetite, and weight loss, frequently leading to delayed diagnosis. There are several different types of systemic amyloidosis.

Key indicators to the diagnosis of possible systemic amyloidosis include: nephrotic syndrome, autonomic neuropathy (postural hypotension, diarrhoea), soft tissue infiltration (macroglossia, carpal tunnel syndrome), cutaneous bleeding (periorbital, gastrointestinal), malnutrition/cachexia and genetic predisposition (family history/ethnicity). Other organ involvement, particularly in AL amyloidosis, may cloud the cardiac presentation (nephrotic syndrome, autonomic neuropathy, pulmonary or bronchial involvement). Table 1.4 gives an outline of the clinical phenotype of the common amyloid subtypes.

Transthyretin (TTR) is a homotetrameric protein that transports thyroxine and binds retinol. Extracellular amyloid deposition of TTR is associated with two types of amyloidosis, familial amyloidotic polyneuropathy (FAP; or ATTR amyloidosis, an autosomal dominant disease) with deposits formed by TTR point mutants, and systemic senile amyloidosis (SSA) with wild-type (wt) TTR deposits (19). Wild type transthyretin (TTR) amyloid deposits, which predominantly accumulate in the heart, are very common at autopsy in the elderly. Whilst the associated clinical syndrome known as senile systemic amyloidosis is diagnosed rarely in life, there is increasing evidence that this disorder is much under-diagnosed. With increasing longevity and improved diagnostic methods, it may be identified as a substantial public health problem.

Light chain amyloidosis (AL) is the most commonly diagnosed systemic amyloidosis in the Western world, with an incidence of 10 patients per million per year (19). It is a fatal progressive disease characterized by extracellular deposition of light chains into insoluble fibrillar aggregates. Most AL amyloidosis patients are more than 45 years old with an average age of 67 years old. AL amyloidosis patients have a median survival of 12–40 months after diagnosis (19). AL amyloidosis is caused by an abnormal proliferation of monoclonal plasma cells that secrete a high amount of free light chains into the bloodstream. These light chains self-assemble and deposit as insoluble amyloid fibrils in various organs, ultimately causing organ failure and death. Current treatments target the plasma cell population and are not curative. Although this deposition can occur almost anywhere in the body, the most frequent sites of AL amyloidosis deposition are the kidneys, heart, peripheral nerves, gastrointestinal tract, and liver. Patients with clinical cardiac involvement have the worst prognosis with a median survival of less than a year. The variation in pattern of tissue deposition is poorly understood.

All amyloid deposits contain the non-fibrillar glycoprotein amyloid P component, which is derived from and identical to serum amyloid P component (SAP). SAP labelled with radioactive iodine can be used as a specific tracer to determine the distribution and extent of AL amyloid deposition. Tissue retention of SAP scintigraphy may be related to survival in patients with systemic disease. Jager et al. showed that patients with greater than 60% extravascular retention of labelled SAP corresponded to a mean survival of just 4 month, compared with 23 month for those with <60%.

Therapeutic options are limited in systemic AL amyloidosis, but cytotoxic chemotherapy has been employed to suppress the underlying pathogenic B-cell or plasma cell clone. This is however often limited by dysfunction of amyloid infiltrated organs. Recent work by Richards et al. has demonstrated impressive clearance of amyloid from the liver and other tissues by targeting with a therapeutic IgG anti-SAP antibody. SAP scintigraphy was used to qualitatively demonstrate marked reduction in hepatic amyloid load.

Amyloid type	Precursor protein	Typical onset	Other organ involvement	Treatment	Prognosis (median survival)
Primary (AL) Amyloidosis	Monoclonal light chain	6th to 7th decade (but can be any)	Heart, kidney, liver, soft tissue, neuropathy	Chemotherapy or ASCT	48 months (8m advanced stage disease.
Transthyretin Amyloidosis ATTR (V30M)	Variant TTR	3rd or 4th decade	Peripheral and autonomic neuropathy	Liver transplantation	Good with liver transplant for V30M
ATTR (T60A)	Variant TTR	6th decade	Heart, Peripheral and autonomic neuropathy	Liver transplant possible in selected	Variable with liver transplant
Wild Type ATTR	Wild-type TTR	70 years	Heart, carpal tunnel syndrome	Supportive	7-8 years
ATTR Ile 122	Variant TTR	6th – 7th decade	Heart, carpal tunnel syndrome	Supportive	7-8 years
Apolipoprotein A1 (ApoA1)	Variant apolipoprotein	6th– 7th decade	Predominantly renal	Renal (+/- liver) transplant	Usually slowly progressive (yrs)
Secondary (AA) amyloidosis	Serum amyloid A (SAA)	Any	Renal, liver	Treat underlying condition	Good
Atrial natriuretic peptide (ANP)	ANP	70 years or older	Heart	Not needed	

Table 1.4 Summary of clinical phenotype by amyloidosis type

1.4 Evaluating interstitial expansion

Current methods to evaluate diseases that cause alteration in the extracellular environment focus on quantifying secondary extracellular disease specific processes (e.g. collagen deposition in fibrosis); resultant tissue property changes (e.g. tissue shear wave propagation) or systemic overspill of disease related components (e.g. plasma biomarkers). These methods provide useful surrogate markers of disease and are used as comparators in this thesis.

The volume of the extracellular space and its relationship with disease has yet to systematically explored. Methods that interrogate ECV already exist, but are not widely used - largely as a result of their complexity. Global ECV measures have been studied in relation to sodium disturbances, diabetes and hypertension; and simpler schemes for measurement proposed (20). More recently extracellular tracers have allowed focussed assessment of tissue ECV, but these techniques are again complex.

The main existing techniques for evaluating extracellular disease and measuring extracellular volume will be discussed further.

1.4.1 Histological analysis

Tissue sampling and histological analysis is currently the ‘reference standard’ technique for evaluation of the interstitium and diffuse fibrosis. Although it plays an important role in the current management of a host of diseases, it is far from an idea test, suffering a number of technical and methodological limitations.

Collecting tissue for histological analysis frequently involves technically difficult and invasive procedures with an associated complication risk. In the liver, percutaneous biopsy carries a significant risk of haemorrhage. An audit of liver biopsies performed in district general hospitals in the UK found a mortality rate from haemorrhage of between 0.13 and 0.33% (21).

The use of image guidance, and centralisation of liver services to high volume specialist centres may help reduce these risks.

Depending on aetiology, diffuse fibrosis is also commonly a non-homogenous process. Biopsy of organs such as the liver where only 1/50000th of the organ is sampled, suffers significant sampling error. Bedossa et al. illustrated this by comparing fibrosis staging in large surgical specimens with 25mm long virtual biopsy samples and found a 25% rate of discordance (22) between the two.

Although fibrosis within the liver is a continuous process – following the patterns previously described, a variety of semiquantitative histopathological scoring systems have been used to classify or stage the progression of disease to cirrhosis. The first systematic scoring system was described by Knodell et al (23) in 1981 and used numerical categorical labels as shorthand for subjective description of specific histological features observed within liver biopsy specimens. More recent histological scoring systems include the Ishak (23) and METAVIR (24) systems, which incorporate a mixture of histological features, but no individual score is related specifically to the amount of fibrosis. Ishak score (Table 1.5) for example places greater emphasis on the subjective degree of nodularity and architectural change – and is therefore prone to intra and inter observer variability. The numerical categorical labels have been widely misunderstood as continuous measurement quantities, and the lack of an arithmetic relationship between stages (ie stage 4 is not twice that of stage 2) causes confusion - particularly amongst clinicians. The categorical system has also lead to inappropriate use of statistical method (other than those appropriate for order categorical assignments) in numerous scientific publications. A further issue is that these semi-descriptive assessments are relatively aetiology specific because of the differing histological patterns of disease. This adds additional complexity to interpretation of fibrosis score and does not allow non-disease specific

evaluation – for example in the assessment of surrogate markers and non-invasive methods.

Change	Score
No fibrosis	0
Fibrous expansion of some portal areas, with or without short fibrous septa	1
Fibrous expansion of most portal areas, with or without short fibrous septa	2
Fibrous expansion of most portal areas, with occasional portal to portal bridging	3
Fibrous expansion of portal areas with marked bridging as well as portal-central	4
Marked bridging (portal to portal and/or portal-central) with occasional nodules (incomplete cirrhosis)	5
Cirrhosis, probable or definite	6
Maximum score	**6**

Table 1.5 Summary of modified Ishak Soring

Histopathological characteristics with corresponding modified Ishak Score.

The limitations of these scoring systems have led to the development of objective, systematic numerical methods. Routine histological evaluation of fibrosis is usually performed with trichrome or reticulin stains, each of which identify collagen to some extent but are not specific and the amount of staining dose not necessarily correspond quantitatively with the amount of hepatic collagen. PicroSirius red has an affinity for most hepatic collagens including types I and III, with reliable and reproducible correlation between bound stain and collagen determined biochemically (25). Computer assisted/ digital image analysis (DIA) of Picrosirius red stained sections allows for accurate morphometric assessment of collagen, while staining of structures which do not contribute to the disease process can be expressly excluded. Segmentation of collagen compared with the area of tissue examined produces a fibrosis area ratio or ‘Collagen Proportionate Area’. DIA studies have looked at fibrosis in many liver conditions, producing overall similar results ranging from 1–4% fibrous tissue in normal liver to 15–35% fibrous tissue in cirrhosis. By weight comparison: normal human liver is estimated to contain approximately 5.5 mg/g of collagen, and cirrhotic liver contains of the order

of 30 mg/g (26). CPA has been assessed against both hepatic venous pressure gradient (HVPG) (27) and clinical outcomes in recurrent hepatitis C (28). Manousou showed CPA to be more predictive of clinical outcome than both Ishak stage and HVPG.

Similar schemes have been applied to diffuse fibrosis within other organs – e.g. the heart. In severe aortic stenosis, myocardial fibrosis quantified by collagen volume fraction (CVF) after section staining with Picro Sirius Red is associated with the degree of ventricular functional improvement and mortality after valve replacement (29). CVF is also used widely used in drug research, allowing direct assessment of the effect of cardiac anti-fibrotic therapies (30).

1.4.2 Pharmacokinetic modelling

Pharmacokinetic analysis has been used to evaluate the distribution of hydrophilic solutes (such as beta-lactam antibiotics), which are limited to the extracellular space. Measurement has also helped understand fluid changes in the critically ill where for example after surgery, burns or major trauma, interstitial oedema can expand the body weight by over 10%.

Reference methods for measuring whole body ECV are based on dilution of indicators such as radiosodium, and bromide that distribute throughout the EC space and are slowly excreted by the kidneys as a result of tubular reabsorption. ECV (and GFR) can also be measured from mean transit time of a marker through its distribution volume (31), but each of these methods are technically challenging.

1.4.3 Plasma biomarkers

The past decade has seen fibrosis marker research focus on serological tests. Direct markers reflect the shedding of peptides involved in the accumulation of fibrillar extracellular matrix, its degradation or in tissue inflammation into the circulation. These are generally more specific than

indirect markers, which are a mixture of biochemical and clinical parameters. The predictive ability of these markers can be enhanced by their combination into a panel by a mathematical algorithm.

In the liver, serological markers such as the aspartate aminotransferase/platelet ratio index (APRI), FibroTest and the ELF test (discussed further in chapter 3) have been shown to provide accurate estimate of fibrosis (34). The strength of APRI is that it can be calculated using routine laboratory assays at the bedside/clinic:

APRI = (AST/upper limit of normal) x 100/platelet count].

Serological markers have been used to provide information on prognosis in patients with symptomatic heart failure, idiopathic or ischaemic dilated cardiomyopathies, and after acute MI. Natriuretic neuropeptides (ANP; BNP) are synthesised by muscle cells primarily in the atria in response to high blood volumes. Ventricular NT-proBNP is upregulated in cardiac failure and has use for diagnosis and prognosis. NT proBNP has also a strong prognostic value of death in acute and chronic heart failure and also predicts short and long term mortality in patient with suspected or confirmed unstable CVD.

1.4.4 Positron Electron Tomography

FDG-PET has been used to probe fibrotic disease. The degree of cellular FDG uptake is related to the cellular metabolic rate and the number of glucose transporters. FDG is transported into cells by glucose transporters and is phosphorylated by hexokinase enzyme to 18F-2-FDG-6 phosphate but is not metabolized. Increased numbers of glucose transporters are seen in activated inflammatory cells, and there is also increased affinity of these glucose transporters for deoxyglucose caused by various cytokines and growth factors.

In 2009 Groves et al. described FDG-PET/CT finding in patients with diffuse parenchymal lung disease (35). This is a spectrum of diseases,

which includes idiopathic pulmonary fibrosis, with unknown causation. Environmental exposure is thought to produce to repetitive injury to the alveolar epithelium producing accumulation of transforming growth factor beta (TGF β), fibroblast and myofibroblasts, which mediate a cascade that leads to lung tissue scarring. Increased FDG uptake was seen in areas of lung fibrosis – identified on HRCT by ground glass, reticulation and honeycombing. This finding suggested that the morphological changes on HRCT did not simply represent burnt out inert disease, but that the inflammatory process causing fibrosis was active. FDG-PET may then provide useful information on the background inflammatory process driving fibrosis in other organs and which could potentially be a target for pharmacological manipulation.

1.4.5 Ultrasound Elastography

The effect of disease on the mechanical properties of tissues has long been appreciated and forms the basis for subjective clinical palpation. Diffuse fibrosis, for example in cirrhosis, results in an increase in tissue stiffness, causing the liver to feel hard on palpation. Measurement of tissue elasticity is called elastography, and assessment techniques include transient elastography (FibroScan®), ARFI, Real Time Elastography, Shear Wave mode elastography and elasto-MR.

Uni-dimensional transient ultrasound elastography, as implemented by FibroScan uses a mechanical transducer to produce a shear wave, whose velocity is measured using a one dimensional ultrasound probe – figure 5. The propagation velocity is directly related to the stiffness of the medium, defined by the Young modulus. Elasticity is expressed in kPa (kilopascals) and is measured at depth ranging from 25 to 65 mm in a 1 × 4 cm area: allowing a sample volume many hundreds of times larger than that evaluated by biopsy. The obtained values range from 2.5 kPa to 75 kPa – a normal value being around 5 kPa. Mean liver elasticity in healthy individuals is 5.81 ± 1.54 and 5.23 ± 1.59 kPa respectively for men and

women (36). Assessment can be performed at the bedside or clinic using a dedicated portable device and approximately 10 measurements are taken to achieve a sample success rate of >60%. TE however may also suffer sampling error, and of limited valve in patients who are obese, with narrow intercostal spaces or ascites.

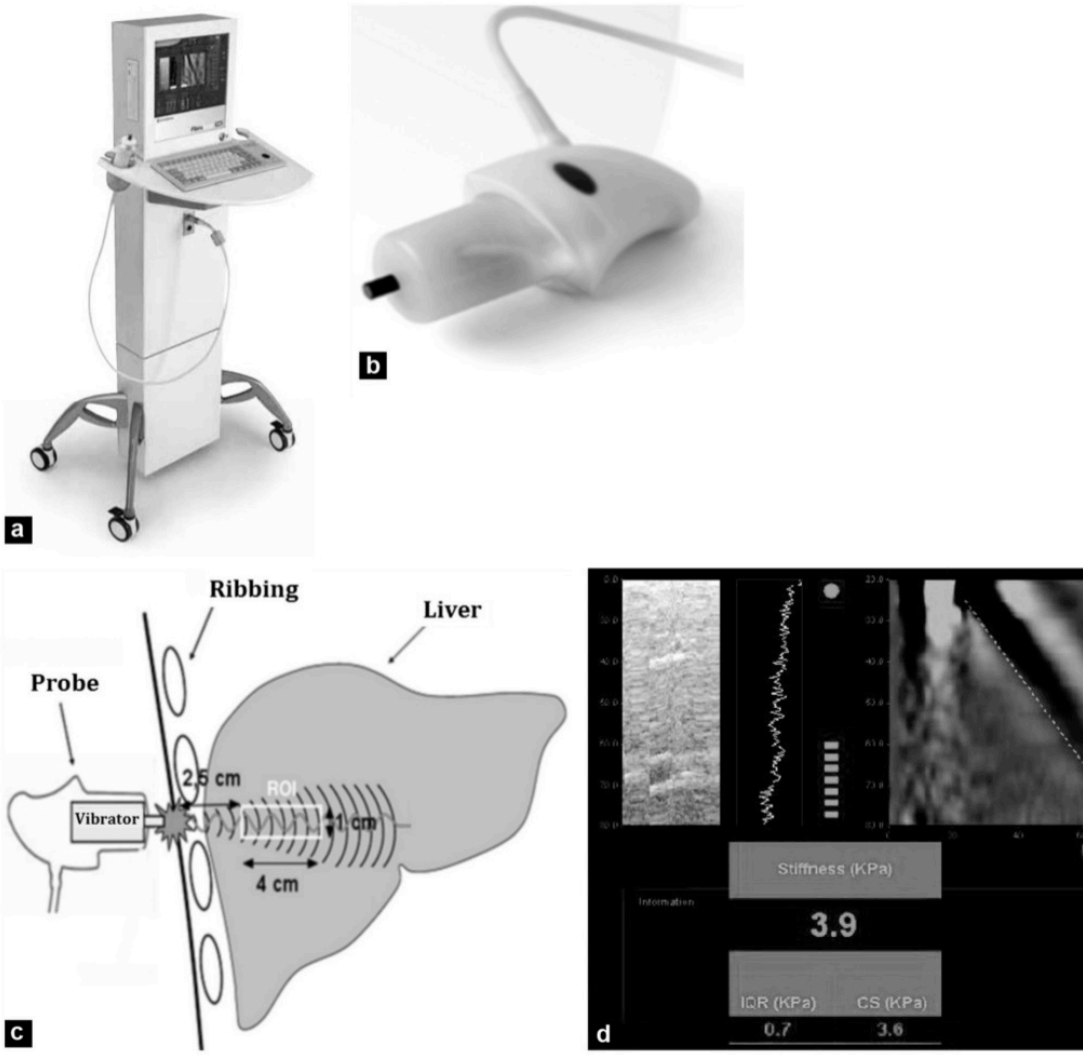

Figure 1.6 Transient Elastography

Taken from Frulio et al. Fibroscan equipment, probe, diagram illustrating measurement principle and results.

FibroScan offers many of the characteristics of an ideal test; it is quick, painless; reproducible (37) and accurate (Figure 1.6). The technique is simple and can be learned quickly. The equipment is also portable and

results available immediately, which allows clinicians to use in a clinic setting. Limitations include thin intercostal spaces, ascites, obesity and need for dedicated expensive equipment. The evaluated liver parenchyma is also not visualised. Foucher et al in 2006 showed a significant association between TE and clinical and biological parameters of liver disease – Figure 1.7 (32).

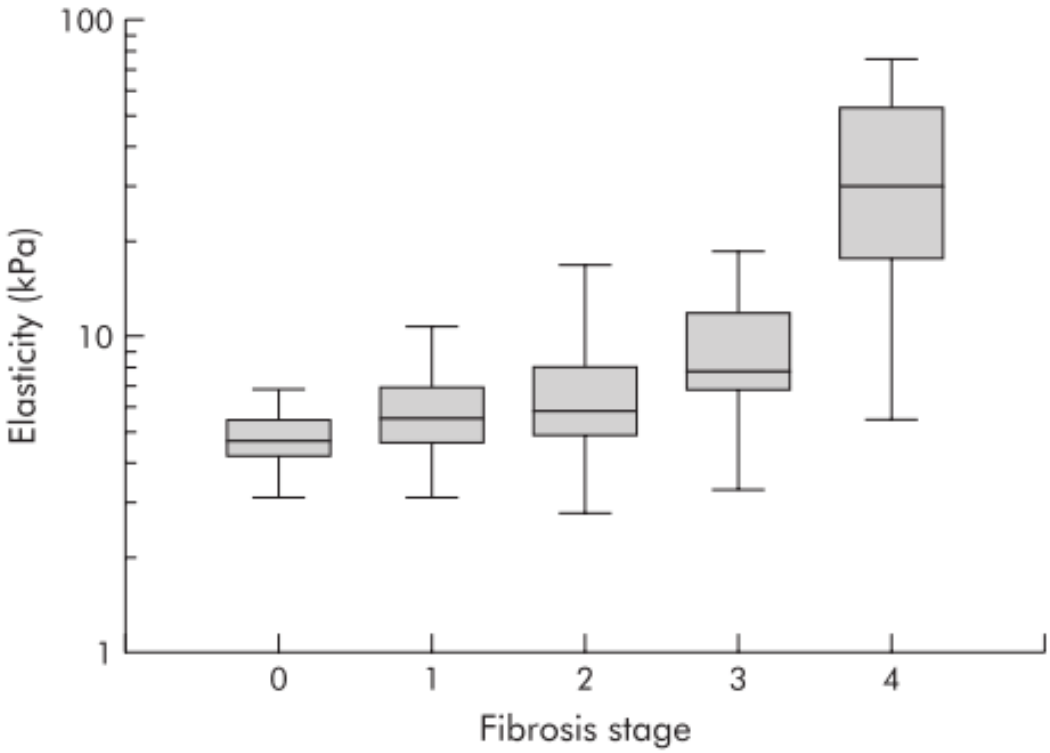

Figure 1.7 Box-and-whisker plot of elasticity vs fibrosis stage

Taken from Foucher et al Gut 2006 (16020491) - Liver stiffness values by TE for each fibrosis stage (0–4). The vertical axis is a logarithmic scale. The top and bottom of the boxes are the first and third quartiles. The length of the box represents interquartile ranges, within which are located 50% of the values. The lines through the middle of the boxes represent median values.

Gomez-Dominguez et al. evaluated this technology in 103 patients undergoing liver biopsy and compared stiffness values with pathological

METAVIR score. The AUROC result to detect F>2 fibrosis was 0.76 with a sensitivity of 90% but a specificity of only 34%. In 18.4%, the method failed to yield diagnostic data (due to obesity and/or ascites) (38)

The diagnostic performance of the FibroScan® has been examined in four meta-analyses (39, 40, 41, 42, 40). Mean AUROC for diagnosis of significant fibrosis and cirrhosis in the meta analysis which included the largest number of studies (n = 50) were 0.84 and 0.94, respectively, and performance varies little with underlying disease (42). As with other methods, testing is again against liver biopsy – with limitations discussed in section 1.4.1.

More recently, 2 dimensional acoustic radiation force impulse elastography (ARFI) has been developed which uses mechanical excitation of tissue with short duration acoustic pulses that produce shear waves within tissues. The shear wave velocity (in m/s) is then measured in a small (6x10mm) area of tissue – with a normal range of 0.5-4.4 m/s. ARFI is enabled within a flexible ROI at variable depths and can be incorporated into a routine ultrasonographic examination of the abdomen. Results are also much less affected by obesity and ascites. Necroinflammatory activity – reflected in a raised alanine aminotransferase (ALT) level affects the accuracy of both transient elastography, and ARFI (33).

1.4.6 Magnetic resonance elastography

MR elastography is new technology that also characterises the biomechanical properties (43) of in vivo tissues. Shear waves are generated continuously (50-500Hz) by an external mechanical driver (figure 1.6), which are imaged using modified phase-contrast MR sequences. A motion-encoding gradient (MEG) oscillating at the same frequency as the driver is applied and conventional MR imaging is performed. The phase of harmonically vibrating tissue is directly proportional to its displacement and an MR image containing information about the propagating wave in its phase is called a wave image. Typically

two such wave images are collected with opposite polarity of the MEG, and a phase-difference image calculated to remove non-motion-related phase information. From the wave images showing the propagation of shear waves in the tissue, mathematical inversion algorithms based on equations of motion, with simplifying assumptions like isotropy, homogeneity, and incompressibility, allow for the calculation of mechanical properties like the shear modulus and production of tissue stiffness maps (elastogram) for clinical interpretation - (Figure 1.9. Fibrotic livers produce longer wavelengths and higher stiffness valves compared with normal tissues.

Figure 1.8 MRI Elastography – mechanical driver

External mechanical driver used to apply sheer waves to the abdomen for MR Elastography. The driver is located away from the magnetic field of the MRI unit and usually transmitted via flexible tube to a passive driver placed over the anterior abdominal wall (for liver imaging). Example mechanical active driver (Resoundant, Rochester, MN).

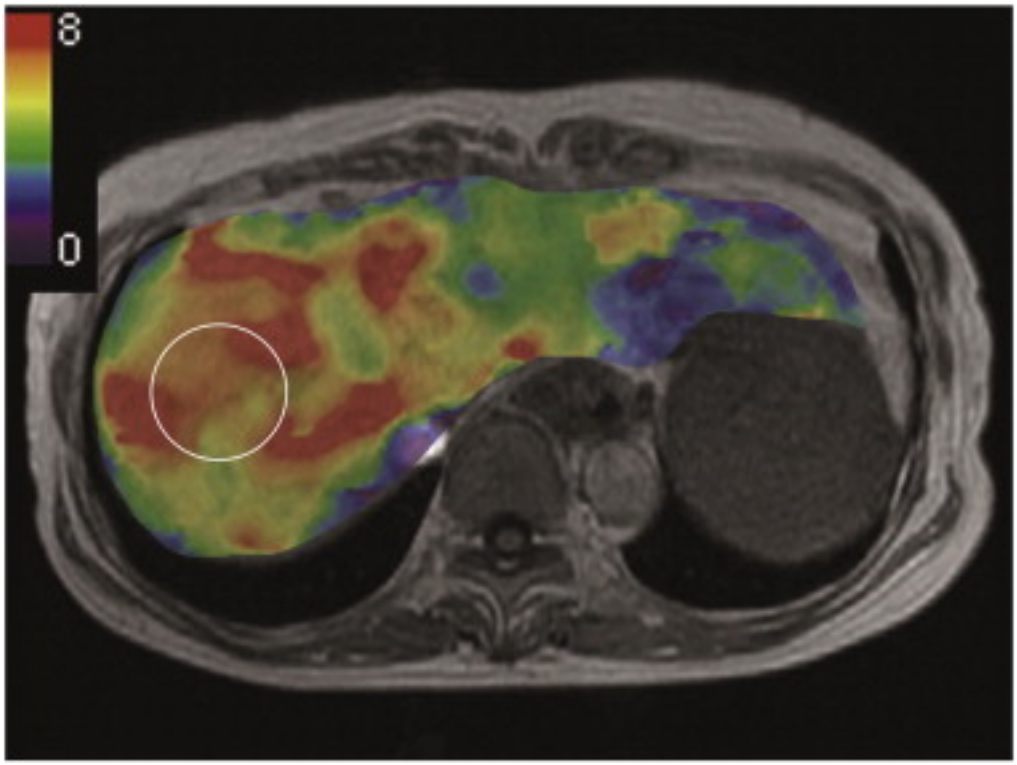

(Figure 1.9 Example MRI Elastogram

Elastogram in a patient with cirrhosis (F4) (Taken from Ichikawa et al. Magn Reson Imaging. 2015 Jan;33(1):26-30)

Compared with TE, MRE has demonstrated superior discriminative ability for hepatic fibrosis stage (44). Shintaro et al. found that even at the histopathological METAVIR F1 cutoff, mean (95% confidence interval) area under the receiver operating characteristic curve values were significantly higher or MRE than TE (0.97 [0.92– 0.99] vs. 0.87 [0.76–0.93]; P = 0.0126).

MRE allows capture of a two dimensional section of tissue ((Figure 1.9) rather than the one dimensional sample on TE. MRE also does not suffer limitations of ascites and narrow intercostal spaces but claustrophobia and other typical contraindications to MRI apply. Low liver signal return resulting from parenchymal iron deposition can also present a challenge.

1.4.7 Dynamic contrast enhanced (DCE-MRI) and diffusion weighted MRI (DWI-MRI)

By analysing the temporal enhancement pattern of a tissue following intravenous administration of a paramagnetic contrast agent, dynamic contrast enhanced MRI (DCI-MRI) allows a number of physiological tissue properties to be derived related to microvascular blood flow – such as vessel permeability, surface area and tissue volume fractions. Semi-quantitative analysis provides a description of the tissue enhancement curve characteristics, but values are dependent on signal intensity (SI), which in turn are dependent on scanning conditions. These values also lack intrinsic physiological meaning and are difficult to interpret.

Absolute parameters can be deduced by converting SI into gadolinium (Gd) concentration using T1 maps; and using appropriate mathematical modelling reflecting the two-compartment pharmacokinetics exhibited by extracellular contrast agents (intra and extravascular extracellular spaces). The most widely used model by Tofts et al. (45) calculates the parameters K_{trans} (bulk transfer coefficient which governs the leakage of contrast from the vascular to the extravascular compartment) and V_e (fractional volume of the extravascular extracellular distribution space). Evaluation of these parameters within tumours with DCE-MRI has been widely evaluated to aid tumour diagnosis (46), staging and assess response to treatment (47).

Early evaluation of the ability of DCE-MRI to distinguish extracellular volume changes secondary to diffuse fibrosis used semi-quantitative perfusion parameters and a single compartment model. Zhou et al found that the maximum slope of increase (MSI) – reflecting a reduced rate of blood flow – could predict mild and moderate stages of fibrosis (S1-3); and time to peak (TTP) enhancement, reflecting transit time could predict high stage fibrosis (S4) (48) – a result of increased vascular resistance and liver capillarization. However, the single compartment model and semi-quantitative approach did not allow specific consideration of the alteration

in compartment permeability and extracellular volume that is known to occur in liver fibrosis.

Li et al. used a dual input extended Tofts model to assess CCl4-induced fibrosis in rabbits. Ktrans best predicted fibrosis stage through the range from normal, non-advanced to advanced fibrosis ($p < 0.001$ for all). Ve decreased with fibrotic stage, with significant differences between control, overall and advanced fibrosis groups ($p = 0.009$). This negative association contradicts previous similar work using DCE-MRI, which the authors suggest may be the result of fibrosis related cellular proliferation, loss of endothelial fenestration or regenerative architectural distortion.

Benjaminsen et al. showed that the partition coefficient obtained using Kety analysis (1 tissue compartment model) within human melanoma xenografts increased with histological extracellular space fraction and with radial heterogeneity. No correlation was found with measures of microvascular density or perfusion.

DCE-MRI therefore offers potential as a tool to explore extracellular changes related to disease. However, use of this technique presents a number of challenges. There is currently no consensus on DCE protocol, and practice varies immensely. Depending on the scan timing, T1 measurement method, pharmacokinetic model, and curve fitting technique there can be large variation in measured parameters, limiting reproducibility. Movement of tissues over the prolonged acquisition time can introduce error and even with use of the high temporal resolution imaging sequences, data registration and movement correction is often required. Sampling of the tissue arterial input function (AIF) required for pharmacokinetic model also demands high spatial, temporal resolution and scan coverage to encompass feeding vessels. (49).

1.5 Equilibrium contrast imaging – background

Soon after Roentgen discovered the X-ray, scientists appreciated the need for extraneous agents to improve radiographic soft tissue contrast. In 1896 Sehrwald compared the properties of in-vitro halogens (e.g. iodine and bromide) with other metal salts and organic compounds – Figure 1.10, before Haschek and Lindenthal administered a paste of mercury sulphide and lime into the blood vessels of an amputated hand to produce the first contrast angiogram - Figure 1.11. Todays contrast agents are stable, inert, water (but not fat) soluble molecules, with negligible protein binding; Iohexol contains organically bound iodine and has been used widely in medical imaging for the past 30 years. Both iodinated and gadolinium based agents are extracellular tracers which when administered into the blood, circulate in the plasma and move passively into the tissue interstitium without crossing intact cell membranes, before being excreted by the kidneys. Their various vascular and interstitial phases provide exquisite soft tissue contrast and markedly enhance diagnostic performance when used.

Fig. 1 Search for X-ray absorbing materials. *1*, iodine; *2*, bromine; *3*, chlorinated water 0,5%; *4*, potassium iodide; *5*, potassium bromide; *6*, potassium chloride; *7*, iodoform; *8*, bromoform; *9*, chloroform; *10*, airol; *11*, sponge; *12*, thyroiodine 3% + 97% lactose; *13*, fluorcalcium; *14*, potassium cyanide; *15*, silver nitrate; *16*, adhesive tape; *17*, lead plaster; *18*, empty glass; *19*, muscle of 1-year-old pig; *20*, thyroid gland of 1-year-old pig; *21*, muscle of 4-year-old ox; *22*, thyroid gland of 4-year-old ox. (from Sehrwald 1896)

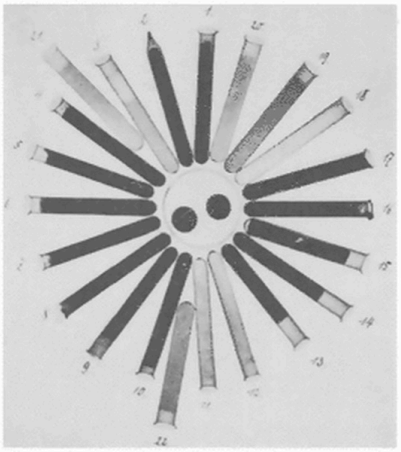

[1] Clinical Development, Schering AG, Müllerstr. 178, 13342 Berlin, Germany.
[2] Research Laboratories, Schering AG, Müllerstr. 178, 13342 Berlin, Germany.

Figure 1.10 A selection of X-ray absorbing materials

From Wilhelm Conrad Röntgen and the Early History of the Roentgen Rays by Otto Glasser 1993.

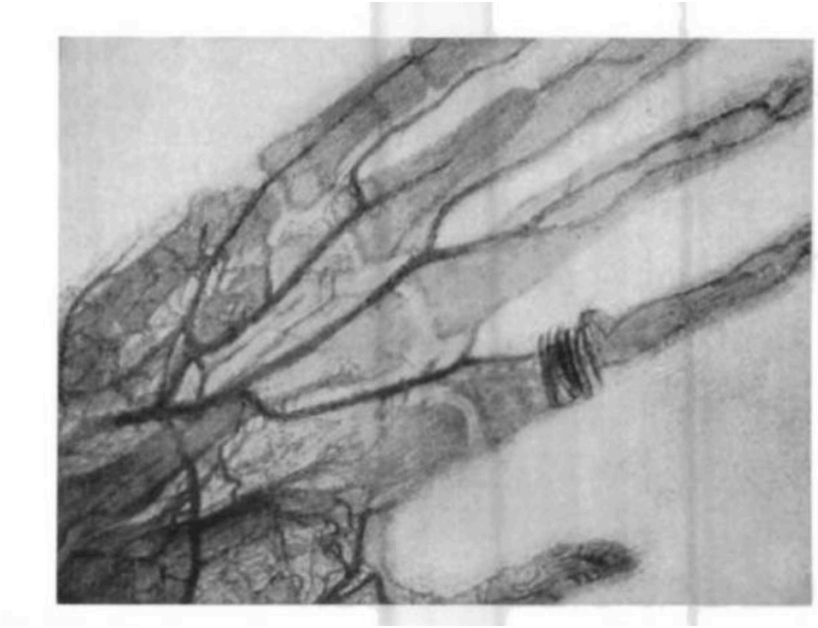

Figure 1.11 An early angiogram

From Wilhelm Conrad Röntgen and the Early History of the Roentgen Rays by Otto Glasser 1993. An early angiogram showing opacified blood vessels in an amputated hand (Vienna Jan 1806).

Contract agents have for some time been used to assess myocardial diseases which cause alteration in the extracellular space. Following acute ischaemic injury, loss of cell membrane integrity and interstitial oedema leads to a local increase in extracellular contrast agent volume of distribution (50). Following infarction, myocyte death leads to replacement by hydrated collagen matrix into which contrast agent molecules can accumulate. Contrast accumulated within this expanded extracellular space can be resolved on T1 weighted MRI, forming the basis for the late gadolinium enhancement technique (LGE) on cardiac MRI (CMR). Using an inversion recovery sequence with an inversion time (TI) set to null (blacken) remote normal myocardium, LGE allows direct subjective appreciation of the spatial extent of focal scarring and has become the reference standard for clinical assessment of focal myocardial fibrosis (51, 52).

The LGE method is however less useful in the case of diffuse fibrosis where there is no normal adjacent tissue to act a reference and where

extracellular volume changes are less marked. Assessment of diffuse fibrosis therefore requires more sensitive, absolute extracellular volume estimation. However, quantifying EC contrast accumulation is complicated by the wash-in and wash-out effects as plasma concentration rises following intravenous injection and falls as the contrast agent is redistributed and renally cleared.

Arheden et al. (53) described a method to quantify the myocardial partition coefficient (that is the ratio of the myocardial to blood extracellular distribution volume) of Gadopentetate Dimeglumine in rats by measuring the change in T1 relaxation time within the myocardium compared with the left ventricular blood pool after contrast administration. In order to compensate for clearance processes causing a constant change (reduction) in blood and tissue Gd concentration, imaging was performed between 5 and 29 minutes after contrast administration. At this delayed time point the rate of change of contrast concentration is reduced; and where contrast kinetics are rapid compared with T1 measurement time, good estimation of the partition co-efficient can be achieved.

Tong et al. (54) then showed that a bolus plus infusion method (in a ratio of 50:1) could be used to achieve a constant concentration of contrast within the plasma. Movement across the capillary wall allows equalisation of contrast concentrations between the plasma and interstitium, during which time there is no concentration gradient and no net movement between the two compartments – a steady state equilibrium. In 2001 Flacke et al. (50) combined the methods described by Arheden and Tong in humans, establishing a technique for measurement of the myocardial partition coefficient in vivo using a bolus followed by a 30 to 40 minute infusion of Gadopentetate dimeglumine. In this study, the myocardial partition coefficient (λ) was measured in healthy volunteers (n=12) and compared with a group of patients with acute (n=5) and chronic (n=5) myocardial infarction. Although the sample size was small, λ in both the

acute and chronically infarcted myocardium was significantly elevated compared with healthy tissue ($p<0.001$).

1.6 Equilibrium Imaging - theory

As described in section 1.5, contrast agents commonly used in modern CT and MR imaging (Iohexol and Gadolinium) are extracellular tracers that passively diffuse between blood and tissue, partitioning in the extracellular space (the interstitium) and the equivalent space in blood (the plasma volume), without crossing the cell membrane – and can thus be described using a two compartment model – Figure 1.12.

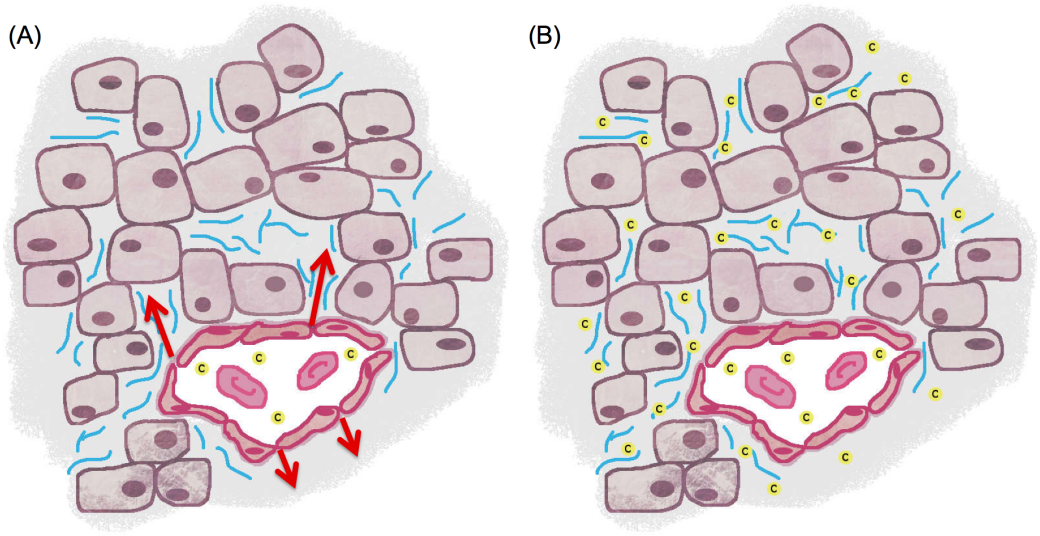

Figure 1.12 Schematic 2 compartment model

Schematic diagram showing passage of contrast agent molecules from the intravascular to the extravascular extracellular compartments.

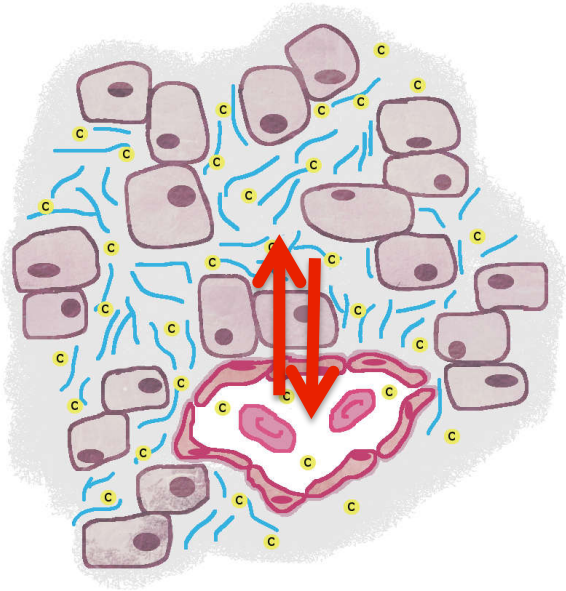

Figure 1.13 Schematic contrast equilibrium

Schematic diagram showing equal net movement of contrast agent molecules between the tissue interstitium and blood plasma – a state of equilibrium

By administering these agents as a primed infusion (bolus followed by an infusion to replace renal losses) it is possible to engineer a state where the concentration of contrast within the plasma and interstitium are constant

and equal, and where there is no net motion of contrast across the capillary wall (contrast steady state equilibrium) – Figure 1.13. During this state, the relative quantities of contrast within a unit volume of tissue and blood are dependent only on the respective fractional extracellular volume (ECV) within each. Therefore:

$$\mathbf{ECV_{tissue} / ECV_{blood} = (\Delta tissue / \Delta blood)}$$

and

$$\mathbf{ECV_{tissue} = (\Delta tissue / \Delta blood) \times ECV_{blood}}$$

where Δtissue = tissue signal post contrast – tissue signal pre contrast

The ECV within the tissue can then be estimated by measuring the attenuation or signal before and after contrast equilibrium, and by measuring the ECV of blood as 1-haematocrit – Figure 1.14.

$ECV_{tissue} = (\Delta tissue / \Delta blood) \times (1\text{-haematocrit})$

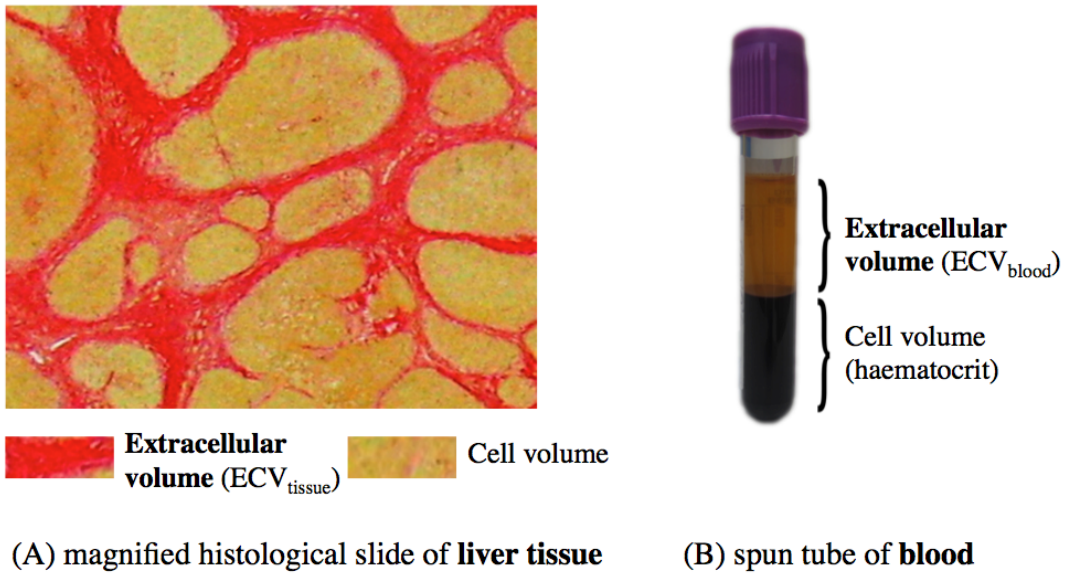

Figure 1.14 Tissue and blood extracellular volume

A magnified histological slide of liver tissue with matrix components in the extracellular space stained red, illustrating the extracellular volume; (B) a blood tube after centrifugation; with separation of the cellular (blood cell) and extracellular (plasma) components.

Measurement of contrast change is simple using X-ray based techniques such as computed tomography, where iodinated contrast agent concentration is linearly related to attenuation of the incident X-ray beam. The scenario with MRI and Gadolinium chelates is however more complex. Gadolinium is a paramagnetic metal whose unpaired electrons (55) cause effective shortening of T1 relaxation time of adjacent hydrogen protons (resulting in higher signal return on T1 weighted imaging). T1 relaxation time is then inversely related to contrast concentration – a relationship that is however only linear over a certain range of contrast concentrations (56).

In 2010 Flett et al (57) showed that contrast static steady state could be achieved within blood and myocardium using a primed infusion (bolus plus slow infusion) of Gadolinium-DTPA – Figure 1.15. Repeat measurement of T1 signal using an inversion recovery T1 mapping technique during the infusion showed variation of < 5% in T1; confirming static equilibrium.

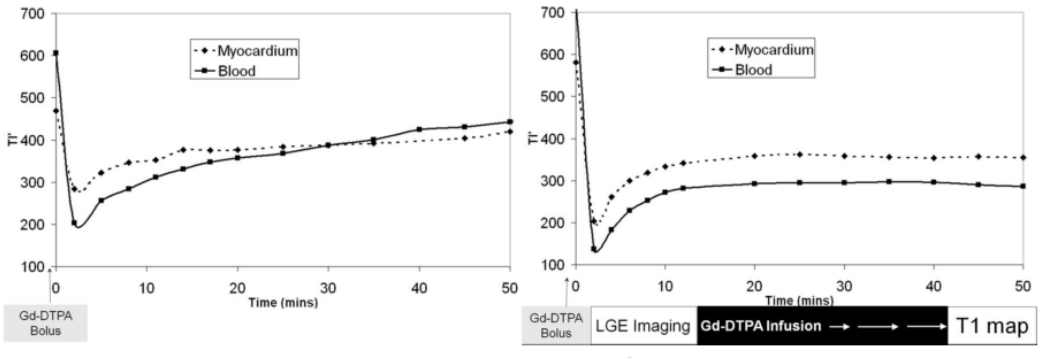

Figure 1.15 T1 related signal change after primed infusion

From Flett et al. T1' is directly related to T1 relaxation time. After contrast bolus, TI' drops rapidly as contrast concentration rises, but then falls as contrast is redistributed and renally cleared. Adding a slow infusion counteracts renal clearance and results in a steady state static equilibrium – i.e. constant contrast concentration

This contrast equilibrium cardiac MRI technique (EQ-CMR) was then applied in a group of patients with severe aortic stenosis – a disease process leading to diffuse myocardial fibrosis. ECV was calculated:

$$ECV_{myocardium} = (1 - haematocrit) \times \frac{\Delta R1_{myocardium}}{\Delta R1_{blood}}$$

where: $\Delta R1 = (1/T1)_{post\ contrast} - (1/T1)_{pre\ contrast}$

Myocardial ECV was compared with a collagen quantified from biopsy specimens collected at the time of surgical valve replacement (collagen volume fraction), with results demonstrating a close association between the two ($r^2 = 0.796$ $p = 0.001$) - Figure 1.16. This work has then introduced the possibility of clinical non-invasive evaluation of myocardial fibrosis.

The importance of the myocardial fibrosis, as measured by EQ-CMR has since been demonstrated by its relationship with mortality. Wong et al. measured myocardial ECV in 793 patients without amyloidosis or hypertrophic cardiomyopathy using EQ-CMR and found a significant relationship between ECV and mortality – even after adjusting for characteristics such as age and ejection fraction.

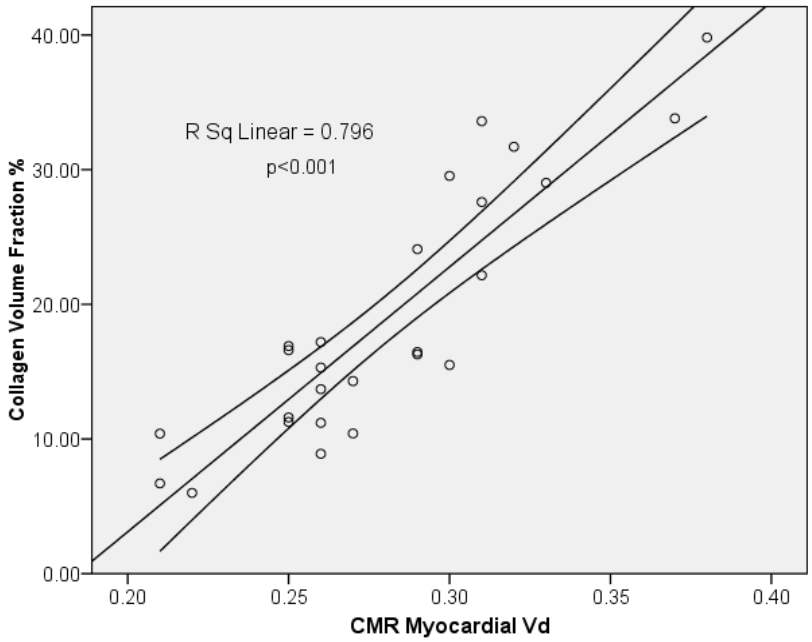

Figure 1.16 Myocardial ECV vs CVF

From Flett et al. Association between myocardial contrast volume of distribution (ECV) and histological collagen volume fraction (CVF).

It should be noted that equilibrium contrast imaging does not strictly evaluate the whole extracellular volume, but rather the volume of extracellular water in which the contrast agent distributes. However, the majority of extracellular volume is occupied by the intrafibrillary aqueous domains of proteoglycans, into which the relatively small soluble contrast agent molecules are free to pass. Expansion of the interstitium occurs with concurrent increases in both extracellular protein and water, thus offering potential for changes in EC water to closely track the extent of EC disease. In order for equilibrium contrast imaging to provide useful assessment of extracellular disease we must then assume that:

- the volume of the collagen is small compared with its associated aqueous domain
- extracellular expansion occurs with concurrent increases in protein content and aqueous volume

1.7 EQ imaging technique summary

The Equilibrium Contrast MRI (EQ-CMI) protocol then consists of 3 basic elements:

- administration of a purely extracellular contrast agent such as Gadolinium (Gd-DTPA) to achieve equilibrium between blood and tissue concentrations, thus eliminating the effect of contrast kinetics;
- imaging before and after contrast equilibrium to measure the produced change in signal;
- and a blood test to measure the extracellular volume fraction within blood. Tissue ECV can then be simply calculated using the formula:

$$ECV = (1\text{-haematocrit}) \times (\Delta R1_{tissue} \div \Delta R1_{blood})$$

where $\Delta R1 = (1 \div T1)_{post\ contrast} - (1 \div T1)_{pre\ contrast}$

1.8 Development of a new clinical biomarker test

Quantitative biomarkers which allow objective measurement of a biological, pathological or therapeutic process can provide powerful prediction of relevant clinical outcomes and end-points. In order to become a valid clinical and research tool, diagnostic biomarkers must successfully negotiate developmental, validation and implementation phases before clinical acceptance.

Early technical development requires measurement validation with demonstration of test performance (accuracy, precision, specificity, and sensitivity). This is then followed by clinical validation, where the association between the biomarker result and a clinical outcome, is assessed. Both analytical and clinical validations precede demonstration of clinical utility, which requires evidence of improved, measurable clinical outcomes directly related to the use of the test.

A example of this development pipeline is summarised below:

1. Technical development
2. Comparison against histology
3. Comparison in disease vs health
4. Correlation with imaging markers
5. Correlation with blood biomarkers
6. Assessment in multiple clinical scenarios
7. Assessment in early disease or with aging
8. Ability to track change over time, and after Rx
9. Predictive/prognostic value
10. Test standardisation
11. Define normal reference ranges
12. Test as Surrogate trial endpoint
13. Clinical use and regulatory approval
14. Test improves clinical outcome

Non invasive evaluation of tissue ECV has undergone initial technical development, with comparison against histology and demonstrated early potential as a biomarker of interstitial disease. In the following chapters the ECV biomarker will be developed further.

2 AIMS, OBJECTIVES AND HYPOTHESES

2.1 Thesis Hypothesis

Tissues in which the interstitium is expanded by diffuse fibrosis or amyloidosis will demonstrate an elevated extracellular volume fraction (ECV) that can be measured using equilibrium contrast imaging (EQ)

2.2 Aims and Objectives

2.2.1 Basic Principles

Rationale: Extracellular volume estimation by equilibrium contrast imaging necessitates a tissue 2-compartment model assumption. Contrast agents are assumed to be exclusively extracellular tracers, which do not cross the cell membrane. There is no direct experimental evidence proving a relationship between changing tissue extracellular volume fraction and ECV measured by EQ imaging, as the extracellular volume cannot be easily measured directly.

Hypothesis: Increasing extracellular volume within a 2-compartment engineered tissue model will lead to increases in ECV measured using EQ-MRI

Aim: Test the basic assumptions of EQ imaging estimation of ECV using a 3 dimensional engineered tissue model (tumouroid)

Objectives:

i. Multiple engineered tissue models will be constructed with known extracellular volume fractions.

ii. EQ-MRI will be used to measure the ECV within tumouroids and compared with that measured directly during their construction.

2.2.2 EQ-MRI ECV in extra cardiac tissues

Rationale: EQ-MRI has been successfully developed and applied in the heart in systemic amyloidosis (1) – providing potentially useful non-invasive estimation of cardiac amyloid burden. Although cardiac involvement is the major cause of mortality and morbidity in both AL and ATTR type, extra cardiac amyloidosis is also important. Hepatic amyloidosis for example can cause derangement of liver function and rarely hepatic failure (2) and evaluation of extra cardiac involvement could aid diagnosis and prognostication.

Hypothesis: ECV measured within the liver, spleen and skeletal muscle of patients with systemic amyloidosis will be higher than that of healthy volunteers and that ECV will track disease burden measured by current reference techniques

Aim: develop EQ-MRI for evaluation of ECV within tissues outside of the heart

Objectives:

i. EQ-MRI will be used to measure ECV within extracardiac organs in patients with systemic amyloidosis
ii. Comparison will be made with a group of healthy volunteers
iii. ECV will be compared with amyloid organ involvement as measured with current reference standard of SAP serum amyloid P scintigraphy

2.2.3 Translation of EQ imaging to Computed Tomography

Rationale: MRI based estimation of extracellular volume fraction has been established. Although MRI allows for high soft tissue and post contrast agent contrast to noise ratio (CNR), computed tomography (CT) is a faster, cheaper and more widely available imaging technology. Additionally, there are concerns over the effect on signal of water exchange between compartments; whereas the relationship between iodinated contrast agent concentration and attenuation is linear. Translation of the equilibrium contrast technique to a CT platform would add further validity, widen the availability of this test and provide an alternative modality when MRI is contraindicated.

Hypothesis: ECV quantified using equilibrium contrast computed tomography is equivalent to that measured using EQ-MRI

Aim: Translate the EQ technique to a computed tomography platform using iodinated contrast agents

Objectives:

i. An equilibrium iodinated contrast protocol will be devised
ii. ECV measurements will be made using EQ-CT in patients with diffuse tissue fibrosis and amyloidosis involving the heart and liver

2.2.4 EQ-CT in liver fibrosis

Rationale: Chronic liver disease causing fibrosis and cirrhosis is a growing worldwide problem. Non-invasive assessment of liver fibrosis could potentially reduce the need for invasive liver biopsy and allow early intervention. Several non-invasive methods already exist but these have limitations. Equilibrium contrast imaging may allow simple accurate whole organ ECV assessment as a surrogate measure of fibrosis.

Hypothesis: Increasing diffuse fibrosis within the liver will be associated with increasing ECV measured using equilibrium contrast CT

Aims: Evaluate the ability of EQ-CT to detect and quantify diffuse liver fibrosis

Objectives:

i. Recruit a group of patients with viral hepatitis and evaluate the liver using EQ-CT
ii. Compare ECV with existing measures of liver fibrosis (serum biomarkers and histology)

2.2.5 Quantitative CT for ECV measurement

Rationale: Quantitative tissue assessment using computed tomography is limited by accuracy and precision of attenuation measurement using clinical CT systems. In developing EQ-CT I noted specific instances of image artefact induced variation in measured attenuation.

Hypothesis: Unexpected variations in measured CT Hounsfield number are due to system artefacts; and application of corrective methods will reduce in this variation.

Aim: Investigate artefacts leading to error in CT attenuation measurement, and evaluate methods to mitigate their effect

Objectives:

i. Evaluate attenuation variation within equilibrium phase CT image data acquired as part of work within previous chapters
ii. Quantitative variation within and between scans; and investigate the effect of applying different reconstruction methods
iii. Perform a subjective assessment of the artefact type underlying the attenuation variation

2.2.6 Optimisation of EQ-CT

Wider use of CT based ECV estimation requires development of accurate, rapid and convenient test.

Hypothesis: ECV can be measured using CT and rapid dynamic contrast equilibrium – with values comparable to that measured using the reference standard bolus and infusion steady state equilibrium

Aim: Optimise the EQ-CT contrast and scan acquisition protocol

Objectives:

- **i.** determine the feasibility of Dynamic-Equilibrium Computed Tomography (DynEQ-CT) to quantify cardiac amyloidosis
- **ii.** compare DynEQ-CT to clinical parameters and steady state equilibrium cardiovascular magnetic resonance (CMR) as standards of reference

2.2.7 Estimation of musculoskeletal amyloid using EQ imaging

Rationale: The use of ^{99m}Tc-DPD scintigraphy has highlighted skeletal muscle as a significant target organ in systemic transthyretin (ATTR) amyloidosis. The clinical significance of this deposition is unclear, but non-specific symptoms of weakness and malaise are common in the systemic disease.

Aim: to quantify skeletal muscle tracer uptake on ^{99m}Tc-DPD, and evaluate this as a measure of amyloid disease burden by comparison with muscle extracellular volume fraction, quantified using equilibrium contrast MRI (EQ-MRI).

Objectives:

iii. devise a grading system for skeletal muscle ^{99m}Tc-DPD uptake and grade uptake in a group of patients undergoing clinical imaging

iv. measure skeletal muscle ECV within this group using EQ-MRI and compare ECV with DPD grade

3 METHODS

3.1 ELF serum biomarker

Serum biomarkers have been broadly discussed in a chapter 1, however the Enhanced Liver Fibrosis (ELF) panel is used in chapter 7 as a surrogate measure of liver fibrosis and will be specifically described here. The test comprises an algorithm combining quantities of three specific ECM matrix components and metabolites. Quantitative serum measurements of tissue inhibitor of metallo-proteinases-1 (TIMP-1), amino-terminal propeptide of type III procollagen (PIIINP) and hyaluronic acid (HA) made using specific immune assays are combined into a single valve using the equation:

$$\text{ELF score} = 2.494 + 0.846 \ln(C_{HA}) + 0.735 \ln(C_{PIIINP}) + 0.391 \ln(C_{TIMP\text{-}1})$$

The ELF assay was evaluated in a large multicentre study carried out by the European Liver Fibrosis Group (1). This study included over 1000 patients and showed high sensitivity and negative predictive value, particularly in liver diseases characterised by initial peri-sinusoidal fibrosis such as non-alcoholic steatohepatitis (NASH), post-transplant HCV hepatitis and haemochromatosis. Subsequent studies have demonstrated a close association between ELF and HVPG (widely considered one of the strongest independent predictor of clinical outcome (2) in HCV; and the ability of the ELF predict liver-related outcomes in primary biliary cirrhosis (3). Parkes et al in Gut 2010 (4) found ELF to be at least as accurate as liver biopsy in predicting liver-related outcomes, supporting its use as a prognostic marker.

The ELF assay therefore offers a less invasive, and potentially more cost effective alternative to liver biopsy and has since been implemented as a CE marked quality-controlled test, making it suitable for patient use.

However, ELF, as with other serological fibrosis markers is not disease or organ specific (5), and may overestimate disease by reflecting extrahepatic abnormal extracellular matrix turnover. Evidence also suggests an association with inflammatory activity (6).

3.2 High performance liquid chromatography (HPLC)

Development of an iohexol steady state equilibrium protocol required measurement of the concentration of iodine (carried by iohexol) within the plasma, without exposing test volunteers to ionising radiation. Liquid chromatography is a technique that allows the separation and quantification of components within a liquid sample. High performance liquid chromatography (HPLC) can accurately measure plasma iodine concentration and has been widely used to estimate Iohexol clearance and glomerular filtration rate (7).

Liquid, or the more recent 'flash' chromatography involves placement of a small volume of a liquid sample into a tube packed with porous particles of 3-5µm in diameter. The sample is then forced along the packed tube high pressure delivered by a pump, and separation occurs by chemical or physical interaction between components of the sample and the packing particles. Separated components can then be detected at the exit of the column and their amounts measured – Figure 3.1. Thus HPLC offers significantly faster, more efficient and sensitive separation compared with traditional liquid chromatography.

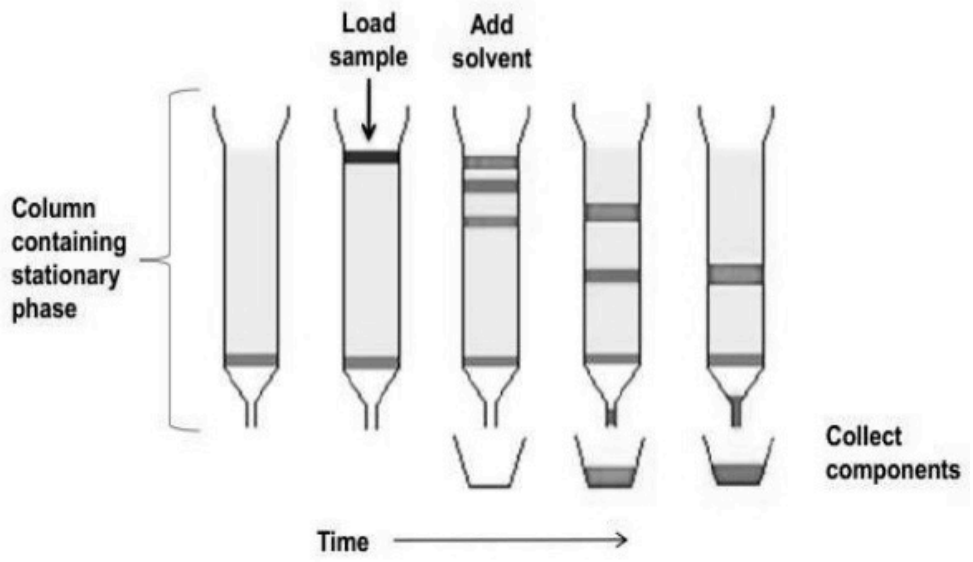

Figure 3.1 Principles of liquid chromatography

A sample is loaded into top of column of porous particles and forced along using pressure or solvent flow. Separation occurs by differential interaction between the sample and column material.

Experimental samples were prepared at the UCLH Clinical Research Facility main laboratory within 1 hour of venesection. Whole blood samples were centrifuged at 2000rpm for 8 minutes and the plasma separated and frozen at -80°C pending transportation to the processing laboratory.

The Iohexol assay was provided by Dr. Helen Aitkenhead, Principal Clinical Scientist, Dept of Chemical Pathology, Great Ormond Street Hospital, London, WC1N 3JH.

3.3 Computed tomography

CT is a form of photon absorptiometry, where linear attenuation is measured in multiple projections and reconstructed into an image map of normalised (Hounsfield) units. Values within the reconstructed attenuation map reflect the imaged material (density and atomic number). System manufacturers have invested heavily in technology to produce consistent, reliable and diagnostic images.

CT scan data was acquired using 2 scanner platforms:

Somatom sensation, 64, 2004 model release date (3rd generation); 64 slice, 40 detector rows, filtered back projection reconstruction

Toshiba Aquilion one, 2010 model release date (3rd generation); 640 slice; 320 x 0.5 mm detector rows; Beam hardening correction software; Adaptive Iterative Dose Reduction reconstruction

Patient preparation and scan acquisition were performed by myself, with assistance from a collaborating research fellow (T. Treibel) and CT radiographers (E. Atkins; P. Patel).

3.4 Magnetic resonance imaging (MRI) – T1 mapping

T1 is a parameter that describes the speed with which protons recover Z-axis (longitudinal) magnetisation after being excited by a radiofrequency pulse. This relaxation process is summarised by an exponential time constant, T1, which describes the non-linear rate of recovery. Reconstructing the longitudinal recovery curve using a magnetic resonance experiment with mathematical curve fitting of the data points can derive the T1 valve. Several techniques have been proposed using different acquisition schemes to sample the T1 recovery signal. Generally multiple images with different T1-weighting are acquired and a model used to estimate T1.

The reference method for T1 relaxometry is an inversion recovery (IR) experiment (8) where signal intensity is measured at variable time points after an inversion pulse. Full recovery of the longitudinal (Z) magnetisation is allowed between sequential inversion pulses ensuring that the recovery curve is accurately sampled. This method is used in chapters 4, 5 and 10, with curve fitting performed using a sum of least squares method (see appendix 2 for T1 recovery function derivation).

The IR method is however time consuming and not practical for clinical use. Acquisition across multiple breath-holds is also prone to motion error. The Look-Locker sequence was introduced to measure the relaxation time at multiple time points after an initial excitation (8). Further rapid relaxometry sequences have been implemented that use sequential inversion recovery measurements within a single breath-hold - including the modified Look-Locker inversion recovery (MOLLI) Figure 3.2, and shortened MOLLI (ShMOLLI). The MOLLI sequence uses multiple single-shot images, acquired along the recovery curve after an inversion pulse at the same phase of the cardiac cycle. Data from 3 inversion-recovery experiments over a single breath hold and 17 heart beat acquisition are then merged into one. This scheme has the potential for reduced heart rate dependence compared with the standard Lock-Locker approach, but it requires long breath holds – an issue in the elderly or those with cardiopulmonary disease. The shMOLLI sequence also uses sequential inversion recovery measurements but in a single shorter breath hold – typically 9 seconds. Here the longitudinal magnetisation is not allowed to fully recover between inversion pulses, but a conditional data analysis algorithm is used to prevent the Z magnetisation being significantly affected by the preceding inversion pulse (9). Data from both methods can be displayed as a colour pixel-wise T1 map, where each pixel reflects the relaxation time with the imaged tissue.

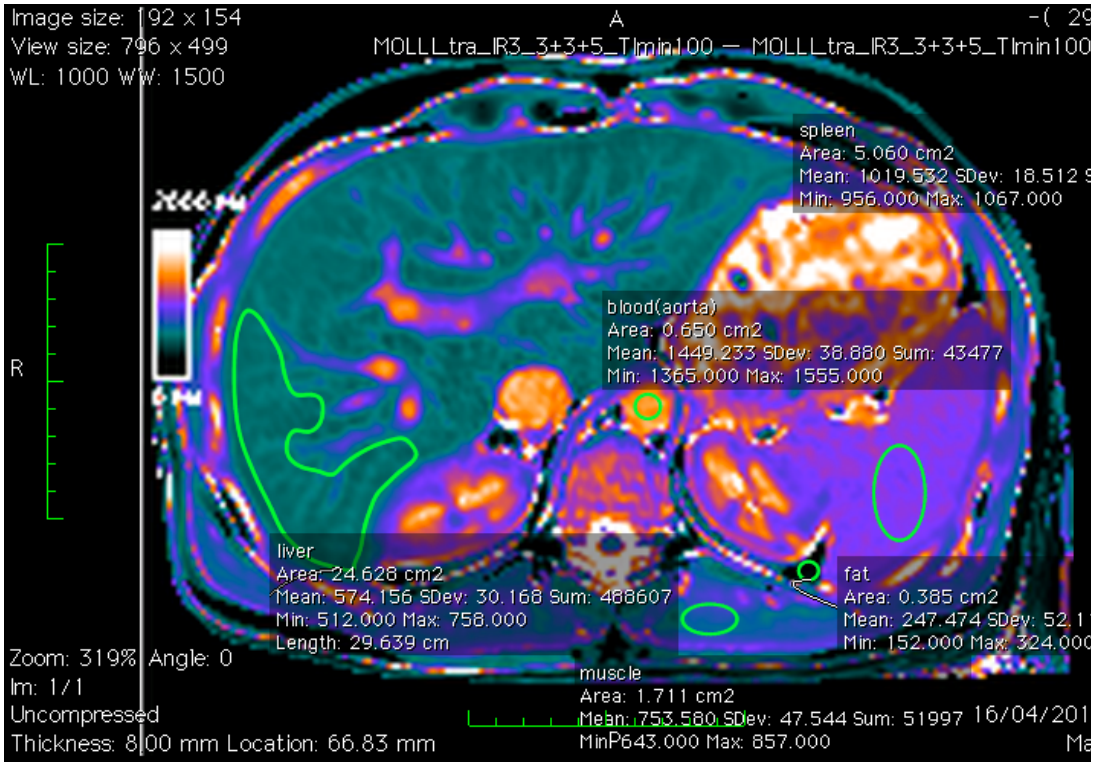

Figure 3.2 Example MOLLI T1 map image

Example axial T1 map acquired through the upper abdomen using a MOLLI acquisition (Siemens WIP). T1 relaxation times are measured within regions of interest drawn within the liver, spleen, paravertebral skeletal muscle, fat and aortic blood.

Other techniques include the saturation recovery single-shot acquisition (SASHA), and saturation pulse prepared heart rate independent inversion recovery (SAPPHIRE) sequences, with each implemented differently by the various scanner manufacturers.

T1 measurements are influenced by several factors, such as the acquisition protocol, magnetization transfer, blood flow, T2 effect, and motion. The T1 relaxation time of a given tissue is dependent on its composition with each exhibiting a characteristic range of normal values at a certain magnetic field strength. Changes in tissue T1 relaxation time in disease have been reported in the heart, with myocardial infarction, heart failure valvular heart disease and systemic disease such as amyloidosis (10) leading to T1 prolongation (9) Figure 3.3.

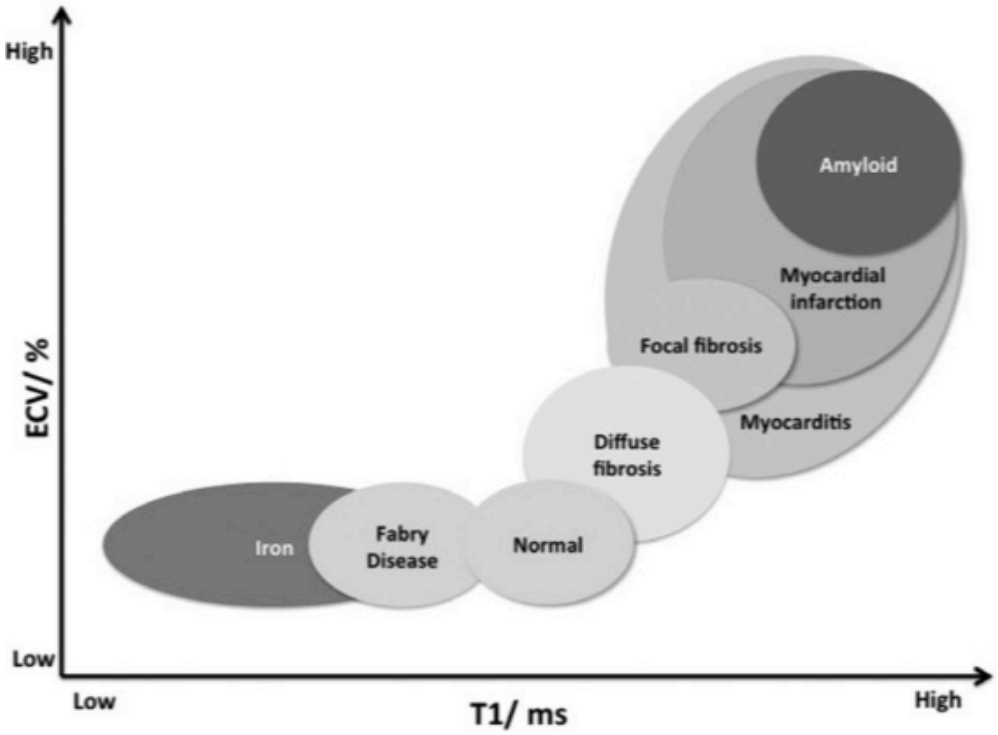

Figure 3.3 Native T1 vs ECV in disease

1346-9843 Native T1 value vs extracellular volume in various myocardial processes (concept slide from Martin Ugander SCMR 2014). Note the large overlap in T1 relation times between the various disease states and healthy tissue.

3.5 Image data processing

CT and MRI image data acquired at University College London Hospital was stored on the hospital Picture Archiving and Communication System (PACS) before being exported to a secure research server. All image datasets were reviewed by myself for incidental findings and any serious, or potential serious findings were reported to the identifying clinical team and GP; and a report documented on the hospital Radiology Information System (RIS).

DICOM data were then fully anonymised in accordance with UCL Centre for Medical Imaging policy using an open source application (DICOMCleaner, PixelMed Publishing Bangor, PA).

Region of interest (ROI) analysis was performed using an open source image software (OsiriX v4.1.2; OsiriX Foundation, Geneva, Switzerland).

3.6 DPD scintigraphy

Bisphosphonate bone scintigraphy agents have long been reported to localize to cardiac amyloidosis. Recent evaluation of this approach suggests that two such tracers, 99mTc-labelled 3,3-diphosphono-1,2-propanodicarboxylic acid (DPD)10–12 and 99mTc-labelled pyrophosphate (PYP) may have use for imaging cardiac amyloidosis – with high sensitivity for cardiac uptake in ATTR amyloidosis. The low cost and availability of bone scintigraphy make use of DPD and PYP imaging of cardiac amyloid an attract possibility, although the basis for its localization in the heart and its limitations in clinical practice have not been fully determined. DPD scans as part of this thesis work were performed at the National Amyloidosis Centre, under lead technologist David Hutt. Patients were scanned using a GE® Medical Systems hybrid SPECT-CT gamma camera (Infinia Hawkeye 4) following administration of 700MBq of intravenously injected 99mTc-DPD. Three hour (delayed) whole body planar images were acquired followed by a single photon emission computed tomography (SPECT) of the heart with a low-dose, non-contrast CT scan. Gated/non-gated cardiac SPECT reconstruction and SPECT-CT image fusion was performed on the GE Xeleris workstation. Cardiac retention of 99mTc-DPD was visually scored according to the classification described by Perugini et al. as follows: Grade 0 - no visible myocardial uptake in both the delayed planar or cardiac SPECT-CT scan;

Grade 1 - cardiac uptake on SPECT-CT only or cardiac uptake of less intensity than the accompanying normal bone distribution;

Grade 2 – moderate cardiac uptake with some attenuation of bone signal;

Grade 3 – strong cardiac uptake with little or no bone uptake;

3.7 SAP scintigraphy

^{123}I-SAP scintigraphy is the only modality in routine clinical use for the assessment of the extent and distribution of visceral amyloid deposition in all types of amyloidosis. Serum amyloid P (SAP) is a non-fibrillar glycoprotein found in all types of amyloid deposits as well as circulating blood plasma. Hawkins et al developed a method using radiolabelled SAP as a tracer for a deposits, and ^{123}I-SAP is used routinely at the National Amyloidosis centre for in vivo amyloid imaging. Method as follows:

A weight adjusted dose of purified human SAP component, radiolabelled with 200MBq of ^{123}I is injected into the patient. Anterior and posterior whole body, planar images are captured on a General Electric (GE)® Infinia gamma camera no less than 6 hours after the injection. Total amyloid load in the liver and spleen are graded visually (by Prof. Philip Hawkins, with over 15 years experience in reporting SAP scans in the UK, having co-invented the scan with Prof. Sir Mark Pepys in 1988). Grading criteria were as follows:

None – No tracer uptake into organs. Normal blood pool signal.

Small – tracer uptake into organs with blood still clearly visible

Moderate – Tracer uptake into organs with blood pool only just visible

Large – Tracer uptake into organs with no blood pool visible

SAP is a very effective method for identifying and measuring amyloid in large solid organs, especially the liver and spleen which have a fenestrated epithelium that allows efficient localisation of this large molecule. However, this radionucleotide is costly and not commercially available, and only two centres in the world, in London, UK, and Groningen, the Netherlands currently use this technique routinely.

3.8 Collagen Proportionate Area

Collagen proportionate area has been mentioned in section 1.8.1. This histological analysis method employed digital image analysis to quantify specific stained elements within a slide image. CPA analysis is used within this thesis to quantify fibrosis histologically. Analysis was performed by Mr. Andrew Hall, Department of Histopathology, Royal Free Hospital using the following method. Tissue is mounted within a paraffin block of at least 1cm^2. Sections cut at 3 μ m and stained with picro-Sirius red. Image capture uses a Canon Powershot A640 digital camera and Zeiss KS3000 software for digital image analysis. Using image analysis software, a greyscale slider is used to select the tissue area that is then calculated as a total tissue area in pixels. A red, green, blue (RGB) threshold is used to detect areas of stained collagen and the collagen mask area calculated. The ratio between the total tissue are and collagen mask (CPA) is expressed as a decimal fraction.

3.9 Statistics

All statistical analyses were performed by myself using Prism statistical package; version 5 (Graphpad Software Inc., San Diego, CA). Normal distribution was assessed using the Kolmogorov-Smirnov test, and Gaussian variables presented as a mean and standard deviation. Non Gaussian variables are presented as median and interquartile range.

Non Gaussian variables were compared between 2 groups using a Mann-Whitney U test. Variation between more than 2 groups was assessed using a Kruskal-Wallis test, where the dependent variable was continuous or ordinal.

Association between variables was assessed using Pearson correlation and linear regression used to evaluate model prediction of a dependent

variable. Bland-Altman analysis was used to assess agreement between two different measurement techniques.

A P valve of <0.05 was considered significant.

4 INITIAL VALIDATION OF EQUILIBRIUM CONTRAST IMAGING FOR EXTRACELLULAR VOLUME QUANTIFICATION USING A 3D ENGINEERED TISSUE MODEL

4.1 Author Declaration

The experiments presented in this chapter were performed, and the data analysed and written by the author under the supervision of Dr. Shonit Punwani and Dr. Umber Cheema. Cell cultures and building of tissue models was completed with the assistance of Tarig Magdeldin. This work was published in the journal article: Bandula, S., Magdeldin, T., Stevens, N., Yeung, J., Moon, J. C., Taylor, S. A., … Punwani, S. (2016). Initial validation of equilibrium contrast imaging for extracellular volume quantification using a three-dimensional engineered tissue model. Journal of Magnetic Resonance Imaging: JMRI, 43(5), 1224–9. doi:10.1002/jmri.25066

4.2 Introduction

As discussed in chapter 1, diseases in which an altered tissue environment precipitates expansion of the extracellular volume are common and include myocardial fibrosis and hepatic cirrhosis. Equilibrium contrast (EQ) imaging is an emerging technique that allows non-invasive interrogation of the tissue extracellular volume fraction (ECV) using already widely used contrast agents and has potential as a useful biomarker for extracellular disease (1).

Contrast agents are purely exclusively extracellular tracers, allowing their behaviour to be modelled by assuming a 2-compartment approximation. Estimation of ECV is performed by administering contrast agents in such a way as to create a state of equilibrium between the intravascular extracellular and extravascular extracellular compartments – whereby there is no net movement of contrast molecules between the two compartments. The tissue partition coefficient can then be calculated by using imaging techniques, notably CT and MRI, to measure the relative contrast enhancement in the tissue compared with the blood. Correcting for the fractional extracellular volume within blood, which is easily measured with a complete blood count (1-haematocrit), yields the tissue ECV (2,3).

This thesis seeks to validate the EQ method in disease processes that cause expansion of the extracellular space i.e. diffuse fibrosis and amyloidosis by comparing ECV with various clinical parameters and surrogate markers of the extracellular volume e.g. histological collagen fraction and extracellular protein component scintigraphy. However, the two-compartment model has limitations as MRI images water rather than the tracer (gadolinium) directly, and a number of assumptions are present, for example concerning water exchange (5). Confirmation of the underlying principles of the EQ technique requires comparison with a direct measure of the extracellular space. Several groups have attempted to quantify the extracellular volume using microscopy (light, confocal and electron) (6–8) but in all methods, sample preparation leads to variable distortion of tissue structure and measurement error. An alternative method, proposed in this chapter, is to artificially engineer a tissue of a specific volume, containing a known quantity of extracellular collagen matrix and known volume of cells – thus allowing the true extracellular volume to be calculated. Establishing a state of contrast equilibrium within this engineered tissue would allow comparative estimation of ECV by EQ imaging.

Recently three-dimensional engineered tissue constructs have been described which more closely model sophisticated cell orientation and matrix interactions than existing 2D models. Nyga et al. described construction of a three-dimensional in vitro colorectal cancer model or 'tumouroid' with good structural and biomimetic properties (9).

The experiments presented in this chapter aim to test the underlying principles of equilibrium MRI using a 3D engineered tissue model. Models are constructed with known cellular and extracellular volumes and ECV measured using EQ-MRI.

4.3 Materials and methods

4.3.1 Tumouroid construction

3D tissue models were constructed using HT29 human colon adenocarcinoma cells - from the European Collection of Cell Cultures, Sigma Aldrich, Dorset, UK - seeded into a collagen hydrogel. Cells were cultured in 2D monolayers in Dulbecco's modified Eagle's medium (DMEM) supplemented with 10% FBS, 100 units/ml penicillin and 100μg/ml streptomycin (from Invitrogen, Paisley, UK) at 37°C in standard cell culture conditions (5% CO2/air and 95% humidity). Total cell volume within a culture was quantified by centrifugation of the culture at 1500rpm for 5 minutes and measuring the dimensions of the formed cylinder of cells. Total cell number within each culture was counted using a haemocytometer.

Collagen hydrogels containing HT29 cells were prepared as described by Nyga et al (9) with a slightly modified protocol. In brief, 3.2ml of type I collagen (rat tail collagen type I, 2.04 mg/ml in 0.6% acetic acid, First Link UK) was mixed with 0.4ml of 10x concentrated minimum essential Eagle's medium (MEM) (Invitrogen). The solution was neutralized in a drop-wise manner, first with 5M and then 1M NaOH, and assessed by a visible

colour change from yellow to bright pink, indicating a pH change to 7.3. The cell suspension, in 0.4ml medium, was added and mixed gently to avoid bubbles. Acellular gels were set using DMEM instead of a cell suspension. The volume ratios of collagen type I:MEM:cell suspension were: 8:1:1. This cellular collagen solution was thoroughly mixed and transferred to a mould, then left to incubate for 30 minutes at room temperature, allowing the gel to set. Typically 4ml of HT29 cell–gel solution was used. Once set, the volume of the HT29-containing cellular collagen gel was reduced by partial plastic compression (10). The mould containing the gel was placed on a 165 μ m steel mesh and a nylon mesh on absorbent paper. The gel was compressed under a 175 g load for 30 seconds. The gel was turned over and the process repeated for a further 30 seconds. The final dimensions of the collagen gel containing the cells was 22mm x 10mm x 8mm. Cellular tumouroids were constructed with cultures containing 5, 6, 10, 15 and 31 million cells respectively, and an acellular tumouroid was used as a control. Each of the tumouroids were then placed into 6 separate specimen pots each containing 20ml DMEM. Cell number selection was guided by previous experience (9), and although the produced cell density was not representative of biological tissue, increasing the density further was not possible. Once constructed, tumouroids containing a higher number of cells lacked sufficient integrity to allow handling, and would disintegrate before imaging could be completed. In this model the tumouroid represented tissue parenchyma and surrounding DMEM solution represented the vascular compartment. Gadolinium contrast agent added to the DMEM would diffuse passively along a concentration gradient into the tumouroids until a state of static equilibrium is reached where the extracellular concentration within the collagen gel is equal to that within the DMEM. A schematic illustration and photograph of the experimental setup for a single tumouroid is given in Figure 4.1; Figure 4.2; note the similar hue of the tumouroid and surrounding medium made photographic visualization difficult.

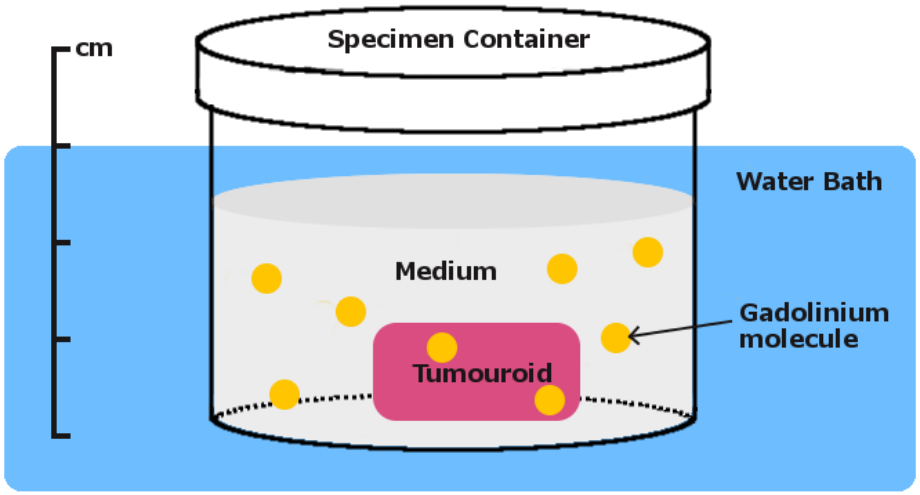

Figure 4.1 Schematic showing single tumouroid

Experimental schematic showing a single tumouroid with surrounding medium (DMEM) after addition of Gadolinium contrast. The specimen container is held within a water bath for thermal stability and to minimise susceptibility artefact arising from an air-fluid interface.

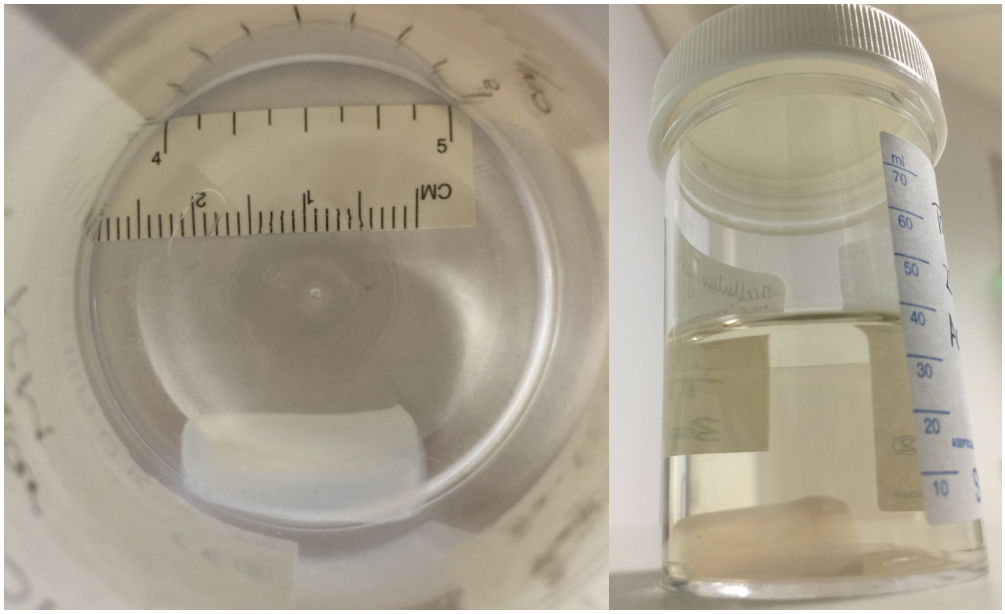

Figure 4.2 Photograph of Sample tumouroid

Sample tumouroid within specimen pot containing normal saline – semi-opaque culture medium would obscure view of the sample.

4.3.2 Tumouroid model EQ-MRI

Due to a practical limitation on the number of cells that could be simultaneously cultured, tumouroids were manufactured and imaged in 2 groups of 3. Once manufactured, tumouroids were stored at room temperature and imaged within 24 hours. Specimen pots containing the tumouroids were placed into a temperature monitored water bath within the MRI scanner room. After a 2-hour interval to allow temperature stabilisation, the water bath was moved onto the scanner table with the pots aligned in a line running across the scanner table from right to left. The T1 relaxation time within the gels was measured using a 3T clinical MRI scanner (Achieva 3T, Philips Healthcare, Best, The Netherlands) as follows:

A single transverse slice was planned through the pots allowing all of the tumouroids to be visualised on a single image. T1 relaxometry was performed using a reference standard inversion recovery technique (table 4.1). A turbo spin echo inversion recovery sequence was used to acquire a single slice with an inversion time (TI) of 50ms (Table 4.3), and repeated with TI of 100, 300, 500, 800, 1000 and 1500ms. Data acquisition for each T1 measurement took approximately 20 minutes. Image data was loaded into analysis software (OsiriX v4.1.2; OsiriX Foundation, Geneva, Switzerland) and regions of interest drawn within the DMEM fluid, and centre of the tumouroid. In order to reconstruct the T1 recovery curve (Figure 4.4), signal intensity (SI) was plotted against relaxation time and points to the left of intersection with the X-axis changed from positive to negative. Data was fitted to the recovery function:

$$M(t) = M(0)*[1-2\exp(-t/T1)]$$

using a least squares method to solve for T1 relaxation time.

Parameter	Value
Imaging sequence	Turbo spin echo
TSE factor	16
TE	7.9
TR	5000
TI	50 – 1500
Slice thickness	2mm
FOV (RL x AP)mm	140 x 72
Voxel size (RL x AP)mm	1 x 0.926

Table 4.3 EQ-MRI imaging parameters

Table of EQ-MRI imaging sequence parameters

Contrast equilibrium was then modelled by replacing a volume of DMEM within each specimen pot with gadopentetate dimeglumine (Dotarem; Guerbet, Paris, France) to achieve a concentration of 1.4mmol/L Gd (approximate blood concentration following clinical intravenous bolus administration) whilst giving a final volume of 20ml.

The T1 relaxation time measurement was then repeated at 45, 170, 260, 350 and 375 minutes after contrast addition (Figure 4.5). In a preliminary experiment, steady state contrast equilibrium (<5% change in T1 over 30 minutes) was found to occur within the tumouroid and surrounding medium between 240 and 300 minutes following contrast addition.

The ECV within each tumouroid was the calculated using the formula:

$$ECV_{tumouroid} = (\Delta R1_{tumouroid} / \Delta R1_{DMEM})$$

where $\Delta R1 = (1/T1)$ at steady state equilibrium - $(1/T1)$ pre- Gd

4.3.3 Statistical Analysis

A statistical package (Prism, version 5; GraphPad Software, San Diego, Calif.) was used for all data analysis. Linear regression analysis was performed to assess model prediction of directly measured ECV (ECVm) by EQ-MRI measured ECV (ECVeq). A P valve of <0.05 was considered significant. Bland-Altman comparison assessed agreement between ECVm and ECVeq.

4.4 Results

Steady state contrast equilibrium between tumouroids and medium was confirmed between 350 and 375 minutes after contrast addition, with a less than 5% change in T1 (Figure 4.6).

The fractional extracellular volume by direct volume measurement (ECVm) ranged between 0 and 11%. ECVm and corresponding values of ECV measured by EQ-MRI (ECVeq) within each collagen gel are given in table 4.7. ECVeq was shown to be a good predictor of ECVm (R2=0.77, P=0.02). The regression line Y-axis intercept (when X=0) was 0.045 ± 0.019 with a slope of 1.28 ± 0.35 (Figure 4.8). Bland-Altman comparison of ECVm and ECVeq (Figure 4.9) demonstrated 95% limits of agreement between -0.002 and 0.114 with a bias (SD) of 0.056 (0.03).

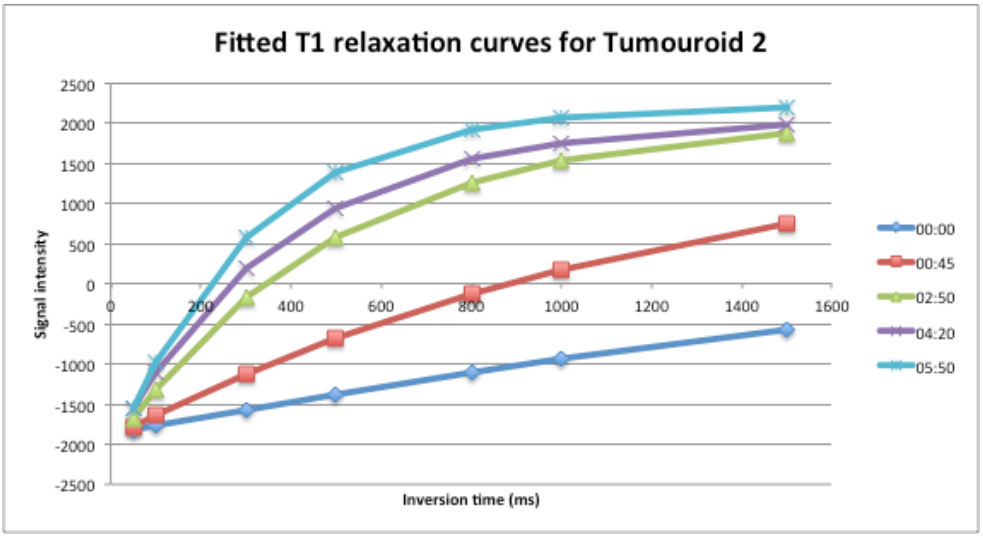

Figure 4.4 Fitted T1 relaxation curves

T1 relaxation curves within a tumouroid before (t=0) and at 4 time points following addition of Gadolinium to the surrounding medium. T1 relaxation becomes more rapid as gadolinium diffuses into the hydrogel.

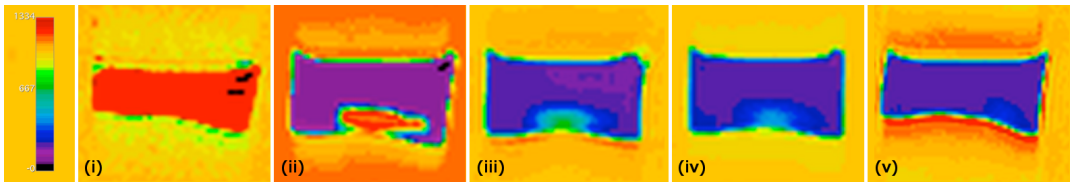

Figure 4.5 Single tumouroid colour scale T1 maps

Colour scale T1 maps (generated using Jim, version4; Xinapse Systems Ltd, West Bergholt, UK) showing tumouroid No.5 containing 15 Million cells held with a medium containing specimen pot at: (a) pre contrast, and (b) 45mins, (c) 2hr 50mins, (d) 4hr 20mins and (e) 5hr 50mins post contrast (WL667; WW1335). Note that following the addition of contrast agent there is centripetal reduction in T1 relaxation time as gadolinium diffuses into the tumouroid. At equilibrium the concentration of gadolinium within the tumouroid is less than that of the surrounding media because of the volume occupied by cells.

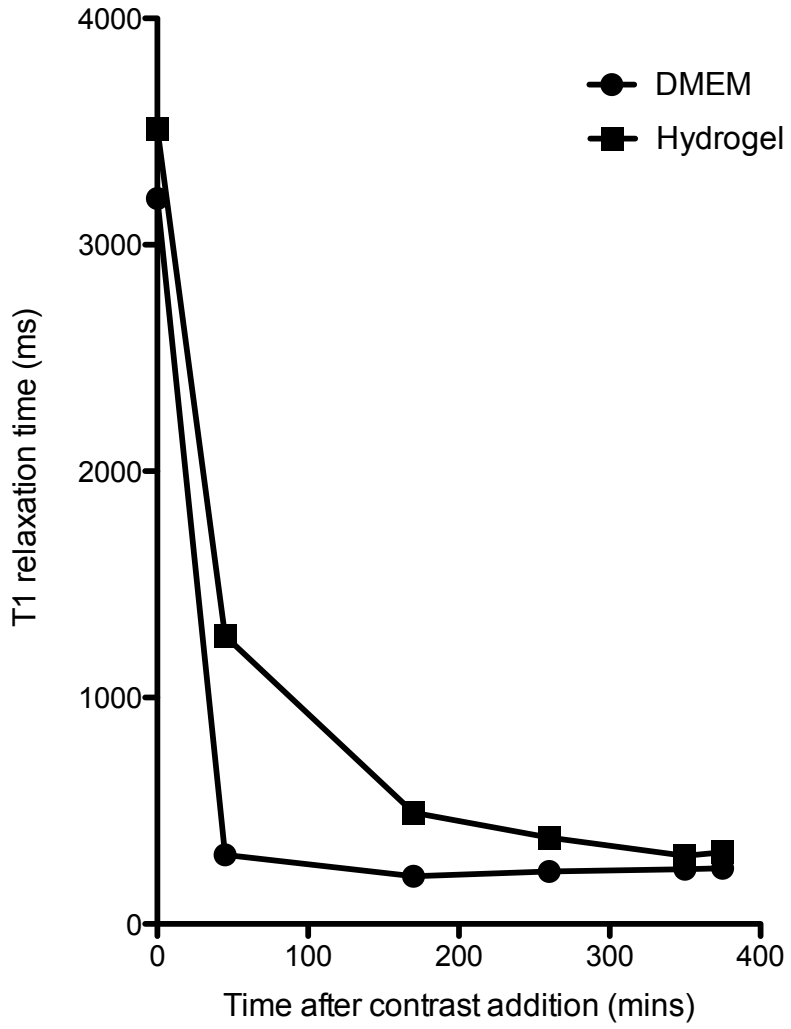

Figure 4.6 T1 relaxation over time in single experiment

Change in T1 relaxation time with time after administration of Gd within tumouroid No.5 and its surrounding medium. There is immediate shortening of T1 measured within the DMEM after addition of Gadolinium. T1 within the tumouroid however falls more gradually as gadolinium diffuses into the collagen gel, eventually reaching a steady state where there is no concentration gradient between DMEM and the extracellular compartment of the tumouroid

Tumouroid No.	Cell no. x10^6	ECV_m	ECV_{eq}
1	0	1	0.963
2	5	0.982	0.894
3	6	0.979	0.963
4	10	0.965	0.926
5	15	0.95	0.864
6	31	0.89	0.821

Table 4.7 Tumouroid results summary

Number of cells contained within each tumouroid with fractional extracellular volume quantified by direct volume and equilibrium imaging measurement

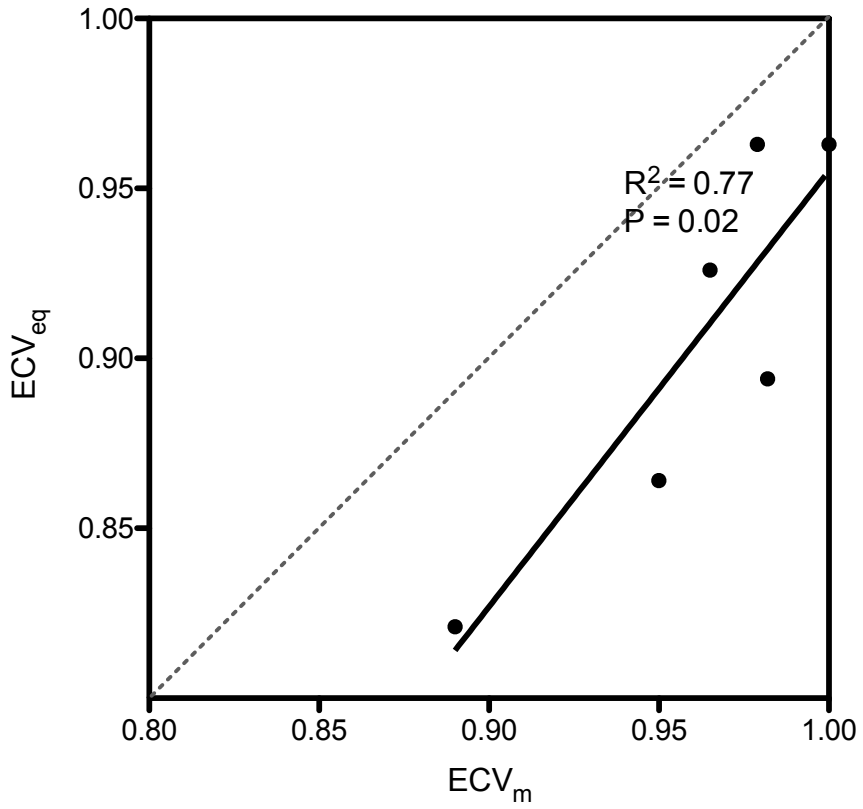

Figure 4.8 Comparison of extracellular volume measurements

Plot showing fractional extracellular volume (ECV) derived by cell volume measurement and equilibrium contrast imaging, with regression line and line of identity (dotted)

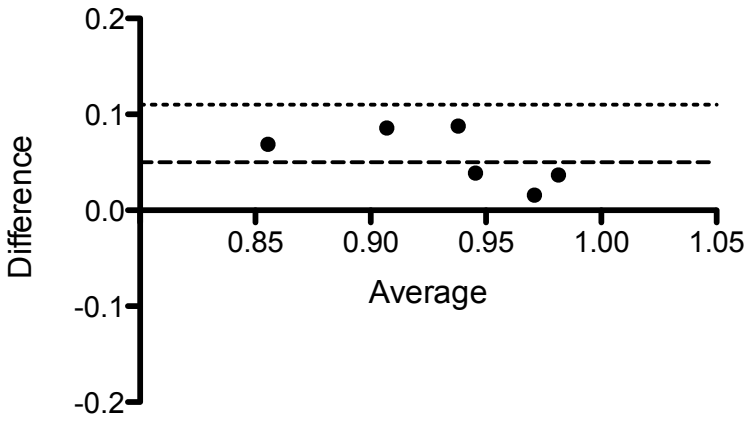

Figure 4.9 Bland-Altman comparison of ECV measurements

Bland-Altman comparison of cellular fraction measured directly ECVm and by EQ imaging ECVeq showing difference calculated by subtracting ECVeq from ECVm against mean ECV. Analysis demonstrates a bias of 0.05 (dashed line) with upper (dotted line) and lower (solid line) 95% limited of agreement.

4.5 Discussion

In this chapter I demonstrate initial use of a 3D engineered tissue model to interrogate estimation of extracellular volume fraction using equilibrium contrast imaging. EQ-MRI estimated ECV was strongly related to the fractional extracellular volume within tumouroids measured directly during their manufacture.

ECV measured using EQ imaging has promise as a biomarker of extracellular disease, and may be able to quantify extracellular expansion resulting from diffuse fibrosis (11-15), and amyloid protein deposition (16-17) within a range of organs. Although ECV has already been validated against specific reference standard measures of disease severity, to date there has been no specific verification of this volume fraction. By utilising a new 3-dimesional engineered tissue model I have been able to control the fractional cellular volume within a tissue and demonstrate in 6 collagen gels, that EQ-MRI provides good prediction of extracellular fraction.

ECV quantified by direct measurement might be expected to be equivalent to that by EQ-MRI, and for the regression line to overlie the line of identify. However Bland-Altman analysis demonstrated a bias, with ECV estimated by direct measurement consistently 5% greater than that by EQ imaging (also seen as a Y-axis intercept of 5% on the regression plot). This consistent discrepancy may in part reflect the volume occupied by collagen protein fibres, but other factors such as magnetization transfer (18) or differential relaxivity of the contrast agent in tissue rather than solution may contribute. A similar overestimate is suspected clinically where ECV in myocardial amyloid may appear very high (e.g. 0.7) (1).

This initial experiment has a number of limitations. The range of fractional extracellular volume across which EQ-MRI was tested was relatively small. Previous studies have shown myocardial ECV can increase from approximately 25% in healthy individuals to 40% in severe fibrosis (1) and up to 60% (4) in Amyloidosis, although the ECV in skeletal muscle may be much lower (10%). The tumouroid ECV range of 89-100% tested here was limited by the fraction of cells that could be incorporated into the collagen gels. At higher cell fractions, failure of preparations to solidify is likely the result of an inadequate supporting collagen matrix. Future development of these engineered models with more complex extracellular components will support cell packing, cell-cell and cell-matrix interactions which better represents biological tissue.

Future 3D engineered tissue models may incorporate higher amounts of collagen (19) in a more complex matrix able to support higher, more physiological cell fractions. Thus the relationship between ECV(m) and ECV(EQ) over a wider range, and the effect of varying extracellular collagen quantity may be investigated. Only 6 collagen gels were included in this initial proof of concept study and demonstration of the expected 1:1 relationship between ECV(m) and ECV(EQ) over this wider range will require an appropriately powered study.

A significant drop in oxygen level has been demonstrated inside tumouroid model specimens in the 24 hour period after manufacture (9). This reduced oxygen tension is likely to have an effect on cell metabolism, membrane permeability and cell volume, although this was not measured in this current study. The 2 compartment model assumes that all water (intracellular and extracellular) is relaxed by the contrast agent – ie that water exchange is in the fast exchange regime (5). However, transcytolemmal water exchange is in part an active process, and ischaemia (especially if cells are large and contrast agent doses are high) may push the model into the slow exchange regime. To minimise this in future, studies should be designed to reduce this 'wait' time. Some delay is however necessary due to the need for cells to equilibrate in the 3D environment, and attach to the collagen matrix.

The reference standard of cell fractional volume estimation involved separation of cells from medium supernatant by centrifugation to allow direct volume measurement. It is likely that a small volume of medium remained around the cells following centrifugation, but this volume is unlikely to be significant compared with volume measurement error.

Several practical issues arose during MRI imaging. Accurate T1 mapping necessitated use of the reference standard inversion recovery method, which allowed only acquisition of a single slice. Collagen gels were free floating within media to allow even, rapid contrast diffusion but this also allowed tumouroid motion. Whilst stationary during the 6 hour imaging experiment, the pots were subject to vibrations from the MRI scanner likely resulting in small through plane movement of tumouroids.

Repeatability of T1 and ECV measurements was not evaluated due to limitations on clinical scanner time (each measurement took approximately 20 minutes) but future extension of the work should include repeatability and reproducibility evaluation across scanner platforms, T1 mapping methods and at a 1.5T field strength.

MR imaging of this engineered tissue, may also provide a powerful model for exploration of imaging biomarker of other tissue properties. By incorporating elements such as blood cells, fat and calcium, specifically engineered tissue phantoms may allow improved MR microstructural tissue assessment.

In this initial exploratory experiment, I demonstrate use of a 3-dimension engineered tissue model as a platform to evaluate non-invasive tissue characterisation by equilibrium MRI. The results support the principles underpinning extracellular volume fraction estimation but future development of this model may allow validation over a wider, more physiological ECV range and a greater understanding of the effect of tissue extracellular protein burden on ECV.

5 EQUILIBRIUM MRI MEASUREMENT OF LIVER AND SPLEEN ECV IN SYSTEMIC AMYLOIDOSIS

5.1 Author declaration

The experiments presented in this chapter were completed, and the data analysed and presented by the author under the supervision of Prof. James Moon and Prof. Stuart Taylor. Dr. Daniel Sado provided comparator healthy volunteer data. This work was published in the journal article: 16. Bandula S, Banypersad S, Sado D et al. Measurement of Tissue Interstitial Volume in Healthy Patients and Those with Amyloidosis with Equilibrium Contrast-enhanced MR Imaging. Radiology. 2013;268(3).

5.2 Introduction

Systemic AL Amyloidosis causes multiorgan dysfunction through interstitial expansion (1). The presentation is usually non-specific and diagnosis is often difficult and delayed (2) – a major reason for this is an inability to reliably and accurately quantify interstitial expansion. The reference standard of invasive tissue biopsy is limited by its technical difficulty and complication rate; and although quantitative estimation of congo red birefringence is possible, the large sampling error limits clinical utility (3).

As discussed in chapter 1, amyloidosis is eminently suited for evaluation using equilibrium imaging techniques. Indeed equilibrium contrast imaging has been used to explore cardiac interstitial expansion (5-6)(8-9) mainly by diffuse fibrosis, but also in cardiac amyloidosis (4) where interstitial expansion is caused by the deposition of extracellular amyloid fibrils. Interstitial expansion in amyloidosis can be massive and difficult to

measure (7) – the only widely used non-invasive quantitative test being serum amyloid P (SAP) scintigraphy (10) which is ineffectual in the heart (11).

When the heart is at contrast equilibrium, so too are other tissues in the body, excluding privileged sites such as structures behind the blood:brain barrier. This raises the possibility of extending the equilibrium imaging technique beyond the heart ie EQ-MRI to evaluation of a range of tissues and organs.

The purpose of work within this chapter was too to investigate equilibrium contrast MRI (EQ-MRI) measurement of extracellular volume fraction (ECV) within healthy abdominal tissues; and test the hypotheses that tissue ECV in systemic AL Amyloidosis is greater than in health; and that this increase tracks organ amyloid burden.

5.3 Materials and Methods

Local ethics committee approval was obtained (see chapter 1) and all participants provided informed written consent.

5.3.1 Preliminary Evaluation of Tissue Equilibrium

Previous studies described in chapter 1 have confirmed contrast equilibrium within the myocardium (8). As static contrast steady state has been previously verified only in the heart, before applying the EQ technique to other organs I performed a preliminary experiment to test if the gadolinium bolus plus infusion (B/I) protocol described would also produce contrast equilibrium within the liver, spleen and skeletal muscle.

2 healthy volunteers (both male; aged 35 and 42 years) were given a bolus of 0.1 mmol/kg Gd-DTPA (Dotarem; Guerbet) with a 20ml normal saline flush at 3ml/s. After a 15-minute pause, an infusion of Gd at 0.0011

mmol/kg/min (equivalent to 0.1 mmol/kg over 90 minutes) was started as described by Flett et al. (8).

For comparison a further healthy volunteer (male; aged 41) received only a bolus of 0.1 mmol/kg Gd-DTPA with a 20ml normal saline flush at 3ml/s.

MRI was then used to measure the change in tissue signal intensity for a period of 55 minutes from the point of bolus injection:

Axial, sagittal and coronal plane localisers were used to plan an axial slice through the upper abdomen to include the largest section of liver and spleen and a 4 chamber view of the heart.

For rapid within-subject T1 measurement, a TI (time to inversion) scout steady-state free precession sequence was used (TR=1.27; TE=1.27ms; slice thickness 8mm, flip angle 30°; TI= 105 to RR interval) to measure TI' (TI prime, the TI without heart rate or readout correction (i.e. a reliable reflection of intrasubject T1 variation over time), at the selected slice every 5 minutes. TI' signal intensity was measured within regions of interest (ROI) drawn in the blood, myocardium, liver and biceps muscle (see EQ-MRI ECV measurement (section 5.3.3) for ROI drawing method). Steady state was defined within a tissue as a variation in signal intensity of less than 5% between 3 consecutive TI' readings.

5.3.2 Recruitment

Healthy volunteers were recruited as part of ongoing studies looking at ECV in health and disease at our institution. Amyloid patients were recruited specifically for this and a parallel study examining EQ-CMR in the heart (work outside of this thesis, results published elsewhere (12)). Recruitment took place between November 2010 and January 2012. Forty healthy volunteers (18 male; 22 female; median age 43; range 24-88 years) were recruited through advertising within the hospitals, university and general practitioner surgeries. Healthy subjects had no previous history of cardiac or liver disease.

Consecutive patients with systemic AL amyloidosis (n=90) were identified from the National Amyloidosis Centre clinic. Inclusion criterion was biopsy proven AL amyloidosis demonstrated by Congo red and immunospecific staining. Biopsies were from various sites including kidney, heart, liver and soft tissue depending on the individual patient's clinical presentation.

Exclusion criteria were renal impairment defined as an estimated glomerular filtration rate (eGFR) <30ml/min or a contraindication to standard MRI. 18 patients were excluded due to abnormal renal function, 4 had pacemakers, and 1 suffered with claustrophobia. The remaining 67 patients (43 male; 24 female; median age 65 years, range 38-81) were recruited to the study. Subjects in the amyloidosis group contained a greater proportion of men and were on average older (P<0.0001) than the healthy volunteer group.

5.3.3 EQ-MRI ECV Measurement

EQ-MRI was performed using a 1.5T magnet (Siemens medical solutions, Avanto, 16 channel coil). T1 was measured using an inversion recovery technique previously used and validated by Flett et al (8). This is a multi–breath-hold, spoiled gradient echo, fast low angle shot (FLASH) inversion recovery (IR) sequence with the following parameters: slice thickness 8mm, TR 2000ms, TE 3.15ms, flip angle=21°, field of view 400x260mm, increasing inversion times (TI) per breath-hold of 140 ms, then 200 to 1000 ms in 100-ms increments subsequently corrected for repeat time (8) – Table 5.1.

Sequence	FLASH Gradient Echo
Plane	Axial
Slices	1
TR	2000ms
TE	3.15ms
Flip angle	21°
FoV read / phase	400 / 260mm
Slice thickness	8mm
Inversion times	140, 200-1000ms
Acquisition time per TI	14s
Acquisition time for slice T1 map	Approx. 6mins
Image matrix	256 x 168
Breathing	Breath hold
Saturation bands	None

Table 5.1 Sequence parameters for IR T1 measurement

Sequence parameters for Inversion Recovery FLASH based measurement and mapping of T1 relaxation times

Immediately prior to the EQ-MRI a sample of blood was drawn and sent for complete blood count (CBC) analysis, and the subject briefed on consistent breath holding. A member of the research team used axial, sagittal and coronal plane localisers to plan an axial slice through the upper abdomen to include the greatest area of liver and spleen. Pre-contrast FLASH images were acquired at this location for T1 measurement with inversion times increasing from 140 to 200ms and then to 1000ms in 100ms increments.

A bolus and infusion of contrast was then administered to achieve equilibrium using parameters validated previously (8). A bolus of 0.1 mmol/kg Gd-DTPA (Dotarem; Guerbet) was used with a 20ml normal saline flush at 3ml/s, after which the subject was allowed to leave the scanner table to sit in a chair. Following a 15-minute pause, an infusion of

Gd at 0.0011 mmol/kg/min (equivalent to 0.1 mmol/kg over 90 minutes) was started. At 45 to 55 minutes post bolus, i.e. during contrast equilibrium (EQ), the patient was returned to the scanner and a further set of FLASH images acquired for T1 measurement (TI 200 to 600ms) at a similar location to the pre-contrast images – Figure 5.2.

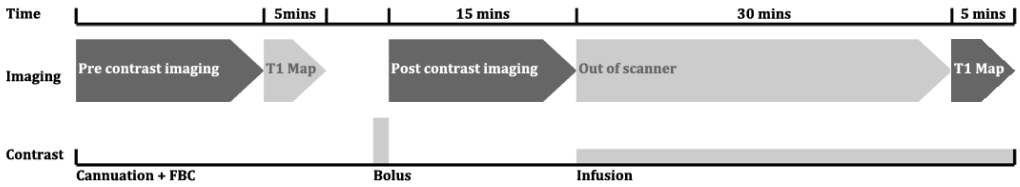

Figure 5.2 EQ-MRI scan protocol schematic

EQ-MRI protocol including contrast administration and imaging components

Matching of slice locations was done visually by the author. Mean tissue T1 relaxation time was then measured within the selected tissues at both time points as described below. Scan analysis was performed by the author, who was blinded to all clinical data. Region of interest (ROI) analysis was performed using OsiriX (Pixmeo SARL, Switzerland). Beginning with the equilibrium phase data, the image with the greatest soft tissue contrast was visually selected. Single ROIs were then drawn in each of the 4 tissues of interest. A circular ROI was drawn in the abdominal aorta (mean=136mm2, range 81-358mm2) so as to include the greatest area of lumen, but not include aortic wall – frequently thickened by atheroma. In the liver, a single large peripherally based, wedge shaped polygonal ROI was drawn in liver segment 6 and 7 (mean= 2938mm2, range 1268-3281mm2) so as to include the maximum area of liver tissue but avoid visible hepatic and portal veins. Elliptical ROIs were also drawn in the spleen (mean= 672mm2, range 213-842mm2) and paravertebral muscle (mean= 92mm2, range 35-104mm2) to include the maximum area of tissue and void adjacent vessels and fat – Figure 5.3. The 4 ROIs were then copied to the other EQ phase FLASH images and mean signal

intensity within each tissue at each inversion time recorded. Mean tissue signal intensities were then plotted against inversion time. The inversion time producing the lowest signal intensity was identified and the sign of signal intensities plotted to the left of this point made negative. This allowed reconstruction of the full range of the T1 signal intensity inversion recovery curve. A second-order polynomial curve-fitting technique was used to find the null point – Figure 5.4. A previously validated (8) algorithm was then used to correct for incomplete longitudinal recovery giving a corrected T1.

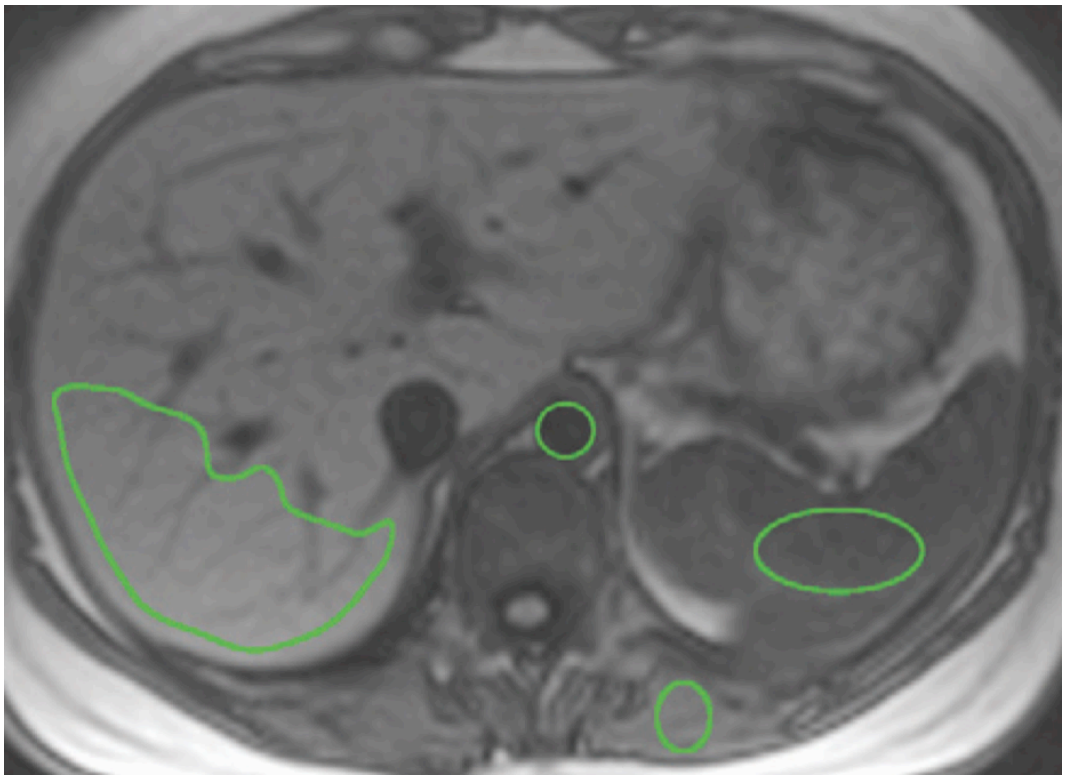

Figure 5.3 Example regions of interest

Example precontrast axial MR image (inversion time, 800 msec) showing sample regions of interest drawn within the abdominal aorta, spleen, liver and paravertebral muscle

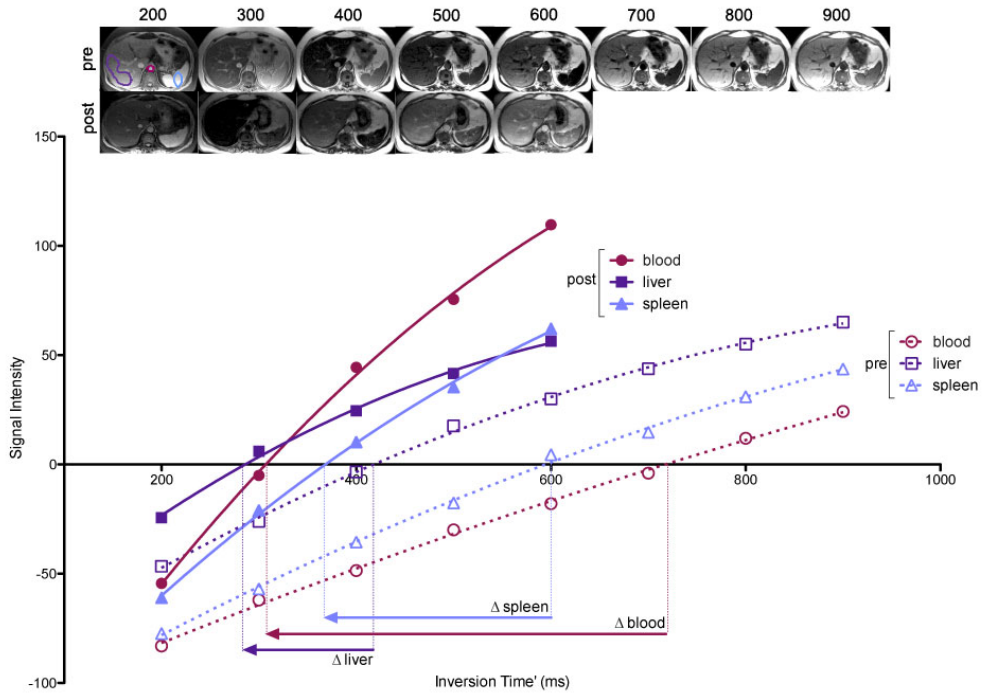

Figure 5.4 Signal intensity vs inversion time curves

FLASH images acquired at increasing inversion times and tissue signal intensity plotted with phase restored. From the inversion recovery curves, change in TI' can be determined, allowing ECV for that tissue to be calculated.

Following measurement of tissue T1 at the EQ phase, ROIs were copied to the pre-contrast images with manual adjustment of the ROI position where needed.

Where an organ was incompletely scanned on either phase, or images degraded by breathing or wrap around artefact such that measurement of reliable signal intensity was deemed not possible by the observer, data for the organ in that individual was excluded.

Using the pre-contrast and EQ phase mean T1 relaxation times, and hematocrit measured from the CBC, ECV fraction within each tissue was calculated using the formula: ECV = (1-haematocrit) x (Δ R1tissue ÷ Δ R1blood)

where Δ R1=(1÷T1)EQ phase - (1÷T1)pre contrast

5.3.4 SAP Scintigraphy

All patients with amyloidosis underwent amyloid I 123-labelled SAP scintigraphy as part of their routine assessment at the National Amyloidosis Centre – see chapter 1.20 (13). SAP imaging was performed within 8 weeks of the EQ-MRI. As described in chapter 1.20, weight-adjusted dose of purified human SAP component, radiolabelled with 200MBq of 123I is injected into the patient. Anterior and posterior whole body images and were acquired using a GE Infinia gamma camera and medium energy collimator, 24 hours after administration of 200 MBq 123I-SAP.

Total body, liver and splenic amyloid burden were scored by visual assessment (14) by a single physician (PH) with over 25 years experience in SAP imaging – see chapter 1.20.

- **None** – No tracer uptake into organs. Normal blood pool signal.
- **Small** – tracer uptake into organs with blood still clearly visible
- **Moderate** – organ tracer uptake with blood pool only just visible
- **Large** – Tracer uptake into organs with no blood pool visible

5.3.5 Statistical analyses

The Prism statistical package: version 5 (Graphpad Software Inc., San Diego, CA) was used for all data analysis. Normal distribution was assessed using the Kolmogorov-Smirnov test.

Variation in ECV between matched organs was assessed using the Friedman test for both the healthy subjects and patients with amyloidosis.

Liver, spleen and muscle ECV measurements in healthy volunteers followed a non-Gaussian distribution and were compared with those in the amyloidosis population using a Mann-Whitney U test.

Variation in ECV across SAP scores was assessed using a Kruskal-Wallis test for both the liver and spleen, with Dunn's multiple comparison between SAP gourps. In order to examine for an association between ECV and SAP score in the liver and spleen I performed Spearman correlation analysis, computing a one tailed P-value. A P value less than or equal to .05 was considered significant.

5.4 Results

5.4.1 Confirmation of Tissue Contrast Equilibrium

In the preliminary experiment, contrast equilibrium was achieved in the liver, biceps muscle, blood and myocardium in both volunteers with bolus and infusion by 25 minutes. In comparison, the volunteer given only a bolus of contrast failed to reach equilibrium within the blood, muscle and myocardium. After a steep fall immediately following the contrast bolus injection, TI' rose steadily back towards its pre-contrast value. A similar pattern was seen in the liver but the increase was slow compared to other organs, and from 25 minutes the change in TI' was less than 5% between consecutive time points – Figure 5.5.

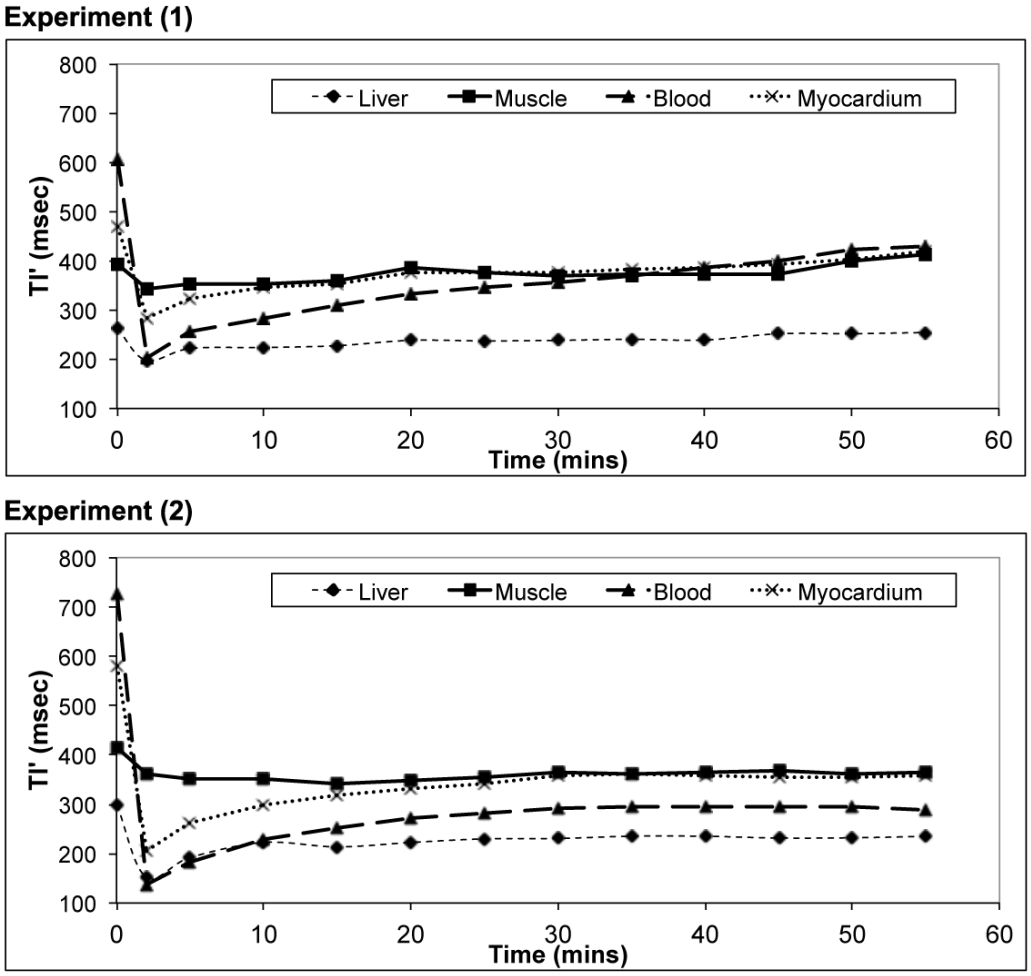

Figure 5.5 Confirming tissue contrast equilibrium

Blood and tissue TI' measured following (1) contrast bolus only and (2) bolus plus infusion in 2 different healthy subjects. The plot demonstrates the effect of the infusion on TI' – which directly relates to T1 and therefore maps contrast concentration change over time.

5.4.2 Clinical Validation

EQ-MRI was attempted in all 40 volunteers and 67 amyloidosis patients (see section 5.3.2 for patient characteristics). Due to scan time limitations, patient discomfort, breathing and wrap around artefacts and previous surgical resections, complete imaging was available for the liver, spleen and paravertebral muscle in 35, 32 and 34 healthy volunteers; and 56, 48 and 53 amyloidosis patients respectively. Imaging of all 3 tissues was available in 30 healthy volunteers and 46 amyloidosis patients.

EQ-MRI demonstrated a significant difference ($p<0.0001$) in median ECV between healthy liver, spleen and paravertebral muscle (median[IQR]= 0.29[0.27-0.33], 0.34[0.32-.35] and 0.09[0.08-0.14] respectively - Figure 5.6.

In amyloidosis the median ECVs also varied significantly ($p<0.0001$) between liver, spleen and paravertebral muscle (median[IQR]= 0.32[0.28-0.37], 0.39[0.35-0.51] and 0.16[0.13-0.22] respectively).

There was a statistically significant ($P_{spleen}<0.0001$, $P_{liver}=0.0136$, $P_{muscle}<0.0001$) increase in the ECV of all organs in the amyloidosis group compared with health volunteers - Figure 5.7.

56 patients underwent matched liver EQ-MRI ECV measurement and SAP scintigraphy. 16 of these cases were excluded - in 15 cases SAP imaging demonstrated a congested liver pattern, i.e. an increased blood-pool signal associated with cardiac failure, and in 1 case localization of the tracer was equivocal. 29 patients scored 0 on SAP; 5 scored 2 and 6 scored 3.

48 patients underwent matched splenic ECV measurement and SAP scintigraphy. 6 cases were excluded as SAP activity was scored as equivocal. 22 patients scored 0 on SAP; 8 scored 1; 7 scored 2 and 5 scored 3.

There was a significant difference in ECV between SAP scores in both the liver ($P=0.0005$) and spleen ($P=0.0014$). ECV increased with SAP score in both the liver and spleen. There was a positive correlation between ECV and SAP score in both the liver ($rs=0.54$,) and spleen ($rs=0.57$) - Figure 5.8.

Dunn's multiple comparison test showed that in the liver, only ECV in the SAP 0 vs 3 groups; and in the spleen SAP 0 vs 3 and SAP 1 vs 3 vaired

significantly. There was no significant difference between ECV in the healthy group and SAP 0 in the amyloid group for each organ.

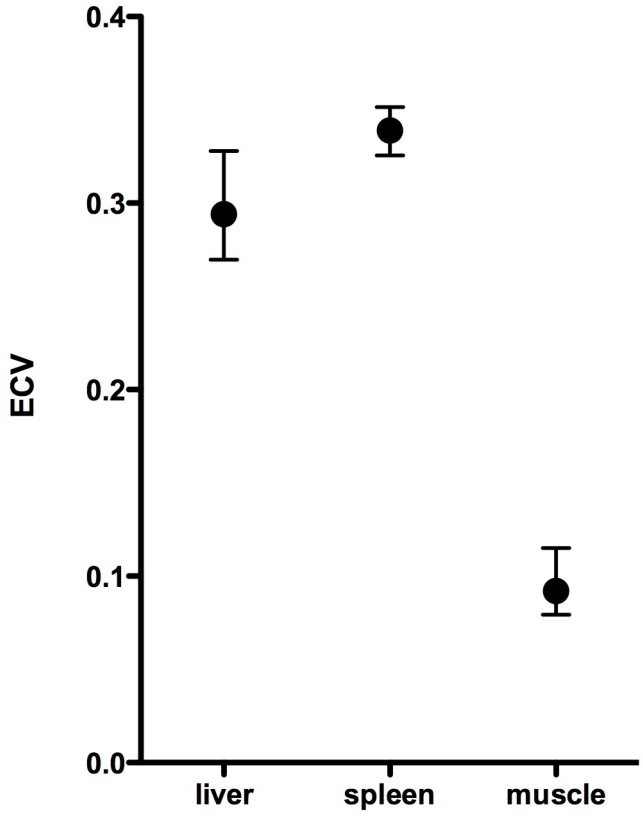

Figure 5.6 Tissue ECV (median and IQR) in healthy volunteers

Plot showing median and interquartile range of ECV measure with the liver, spleen and skeletal muscle of healthy volunteers. ECV varied significant between the difference tissues ($p<0.0001$).

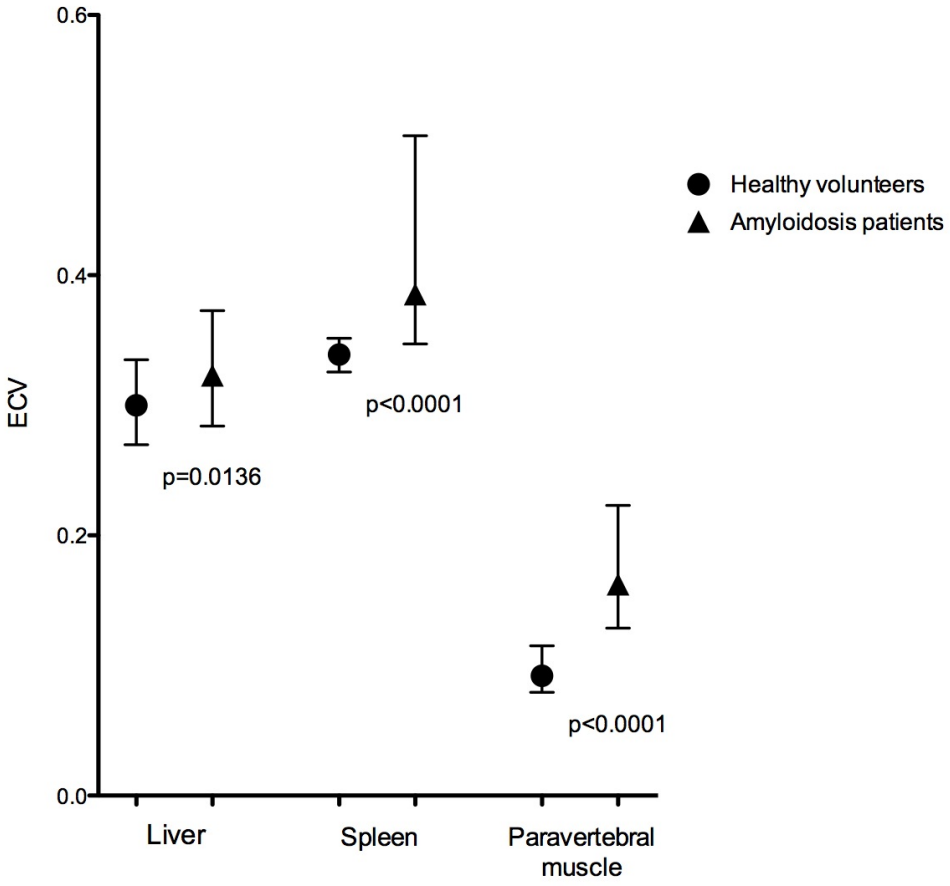

Figure 5.7 Comparison of ECV in health and amyloidosis

Comparison of healthy subjects and amyloidosis patient ECV (median and IQR) measured in the liver, spleen and paravertebral muscle.

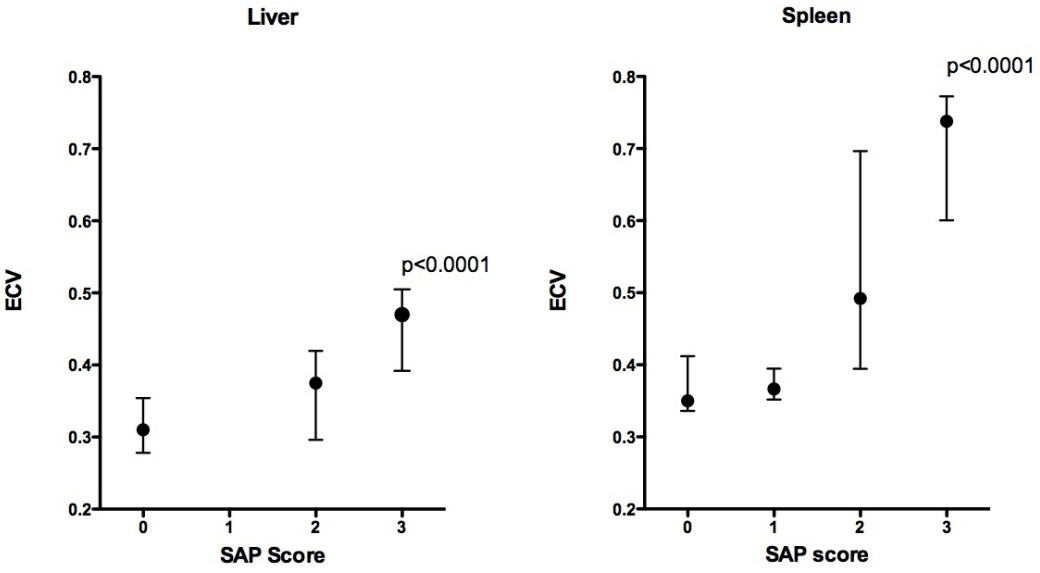

Figure 5.8 Confirming tissue contrast equilibrium

Blood and tissue TI' measured following (1) contrast bolus only and (2) bolus plus infusion in 2 different healthy subjects. The plot demonstrates the effect of the infusion on TI' – which directly relates to T1 and therefore maps contrast concentration change over time.

5.5 Discussion

In this chapter I have used EQ-MRI to define ECV in healthy tissues; and document variation in ECV between tissues. Such data is vital if ECV is to be used to detect pathological processes. I have then shown significant differences in a disease process that exemplifies expansion of the extracellular space - systemic AL amyloidosis. This provides strong proof of concept that the equilibrium techniques can be successfully applied outside the heart.

Although evidence exists that changes in the extracellular space may be a useful indicator of disease severity and treatment response (15), few existing techniques are able to quantify this space.

The ideal comparator for this study would have been histological assessment of the extracellular space. Histological techniques do exist to

quantify extracellular collagen matrix; and when applied to the liver, automated collagen proportionate area measurement has shown good association with other indices of diffuse liver fibrosis (16). However collagen proportionate area measurements in the healthy liver are in the order of 2-3% (17) – much lower than our ECV estimate. This difference is likely to be due to the fact that the extracellular collagen matrix occupies only part of the extracellular space within the liver. Current histological techniques are unable to directly measure the ECV as the process of tissue sampling and preparation almost certainly alters tissue ECV.

As many pharmaceutical products distribute exclusively within interstitial space, some pharmacokinetic model based ECV estimates exist. Levitt (18) collected data from earlier experiments to produce a physiologically based pharmacokinetic model; estimating the EC fraction in organs of a hypothetical standard human. He estimated the EC fluid fraction with the liver and muscle to be 0.23 and 0.15, which is broadly similar to the equilibrium imaging data.

DCE-MRI has been used more recently to quantify the extracellular space and evaluate changes in response to treatment using a tumour disease model (19). DCE-MRI is however a complex technique, prone to substantial measurement error and application is limited to only one tissue site (20). A direct comparison of EQ-MRI and DCE-MRI ECV quantification has yet to be made, however other authors using DCE-MRI have reported ECV in the healthy liver as 0.2-0.3 (15) and skeletal muscle as 0.106-0.115 (21). The estimates of ECV from pharmacokinetic modelling and DCE-MRI are thus broadly consistent with each other, and with our EQ-MRI results.

In this chapter, comparison is made with a disease specific in vivo probe for extracellular (amyloid) protein deposition. Serum amyloid P component scintigraphy is the current reference standard method for evaluation of systemic amyloidosis and has enabled wider assessment of organ amyloid

involvement. Unlike histology, it can be used to track changes in whole organs over time. These results demonstrate that an increase in tissue amyloid burden assessed by SAP scintigraphy is associated with an increase in tissue ECV. ECV between SAP groups showed some overlap particularly in the lower disease burden range, with ECV unable to distinguish between SAP 0 and 2. Improvements in measurement precision in this disease range will then be required before EQ-MRI can provide a useful non-invasive tool for early amyloid diagnosis, disease assessment and therapeutic monitoring.

Disease evaluation and quantitation using SAP scintigraphy however requires specific expertise and is only available in highly specialized centres. The high atomic mass of the SAP molecule (125 kDa) also favours evaluation in tissues with a fenestrated endothelium (such as the liver and spleen), where the large molecule is able to pass into the interstitium. Hence SAP scintigraphy provides little information about amyloid deposition in tissues such as skeletal muscle and myocardium.

This experiment had several limitations. The FLASH IR based T1 mapping technique used was complicated, time consuming and prone to error. To minimise possible variation in slice position during the multi breath hold acquisitions, careful subject coaching was necessary. Other sources of error were copying of ROIs, which required individual adjustment; and the restoration of signal intensity phase around the null inversion time, which was subjectively assessed to match the curve fit. Technical improvements in T1 mapping, for example the ‘Shortened Modified Look Locker Inversion recovery’ sequence (22) allows faster and more robust tissue ECV mapping; albeit within a single slice per breath hold. Although the bolus plus infusion protocol used in this study provided steady state equilibrium in all tissues of interest, prolonged contrast infusions are not practical for clinical imaging. Preliminary experimental findings concur with other authors (8) in showing steady state equilibration is reached approximately 15 to 20 minutes after administration of contrast bolus plus infusion. Future

protocols may then incorporate equilibrium phase imaging after a shorter delay than was used here.

EQ-MRI evaluation of ECV is also not specific to disease aetiology. As well as amyloid deposition and diffuse fibrosis, tissue ECV may be elevated by interstitial edema or an inflammatory infiltrate. Although these potential confounders could not be specifically excluded in this study, cases demonstrating a congested pattern of activity on SAP scintigraphy were excluded from the SAP/ECV correlation.

It is noted that healthy volunteer and amyloidosis patients groups were not age and gender matched. Sado et al. (24) showed that mean myocardial ECV in healthy females was 4% higher than in healthy men; with no change with age. This has not been assessed in other organs. In this study, the higher female proportion in the healthy group compared with the amyloidosis group (see section 5.3.2) may have reduced the difference in mean ECV measured between these groups. In order to minimise such bias, future studies should ensure that groups are gender matched.

Having assessed EQ-MRI in one disease, it is worth noting that amyloidosis forms a relatively small part of a larger set of conditions where EC disruption and expansion leads to organ dysfunction. Diffuse fibrosis is a ubiquitous process of interstitial collagen deposition, occurring in response to diffuse tissue injury as well as in senescence. Many of the conditions where this process can be identified histologically; for example diffuse myocardial fibrosis and liver cirrhosis, have huge population significance. The application of EQ imaging in these organs could potentially provide a new biomarker for disease evaluation and is the topic of subsequent chapters.

6 DEVELOPMENT OF EQUILIBRIUM CONTRAST COMPUTED TOMOGRAPHY (EQ-CT)

6.1 Author declaration

The experiments presented in this chapter were performed, and the data analysed and presented by the author under the supervision of Dr. Shonit Punwani, Prof. James Moon and Prof. Stuart Taylor. This work was published in the journal article: 1. Bandula S, White SK, Flett AS, Lawrence D, Pugliese F, Ashworth MT, et al. Measurement of myocardial extracellular volume fraction by using equilibrium contrast-enhanced CT: validation against histologic findings. Radiology. 2013 Nov;269(2):396–403.

6.2 Introduction

We have seen in previous chapters that developments in magnetic resonance imaging have permitted non-invasive quantification of tissue extracellular volume (ECV)(1), with validation against histological measures of diffuse fibrosis in the myocardium. These “equilibrium” techniques rely on three principles laid out in chapter 1: firstly, the measurement of global myocardial and blood T1 signal before intravenous contrast administration; secondly, re-measurement of T1 signal during sufficient contrast equilibrium to negate contrast kinetics as a contributor to signal change, (2); and thirdly, a direct measurement of the blood contrast volume of distribution (1-hematocrit). However, there are a number of limitations to the EQ-CMR approach. CMR availability is limited and T1 mapping as a technique is immature. Contrast agent induced signal change in CMR is complex, and potentially non-linear in tissue (3-4).

Together, these act as significant barriers to widespread clinical implementation

Iodinated computed tomography (CT) contrast agents are also extracellular tracers (5), and so theoretically behave similarly to CMR contrast agents. Although CT is associated with exposure to ionising radiation, the potential advantages of CT over CMR for measuring the interstitium include less complex measurements, faster, more widely available and cheaper imaging, and the potential for sub-millimetre resolution. Such an approach could allow measurement to be performed in almost any organ or tissue in the body (outside the blood-brain barrier) in almost any hospital, using conventional equipment and contrast agents.

The pharmacokinetics of iodinated contrast agents were described some time prior to the advent of CT imaging (6). Most recently, Nacif et al. described an EQ-CT technique (9) to measure myocardial ECV using a bolus only equilibrium contrast protocol (i.e. without contrast agent infusion), showing good agreement with ECV measured using conventional EQ-CMR.

In order to quantify extracellular volume using a bolus of contrast agent, a dynamic state of equilibrium is assumed, where tissue contrast enhancement parallels that of the blood. This dynamic state however requires rapid equilibration of contrast between the intra and extravascular EC spaces - kinetics which are dependent on tissue blood flow, capillary permeability, rate of diffusion and extravascular volume. A bolus only protocol has shown good ECV estimation in selected tissues such as myocardium, liver and spleen (7-9), although these measurements have yet to be validated against a histological standard. Furthermore, tissue perfusion or permeability, or disease states with interstitial expansion, will increase disequilibrium between plasma and the interstitium after a bolus of contrast. A steady state equilibrium, where a continuous infusion replaces renal and other losses produces a period of constant plasma

concentration (1)(10), which allows equilisation with the interstitium in all tissues (outside of the blood-brain barrier). The plasma and interstitum can then be treated as one extracellular compartment allowing measurement of ECV without knowledge of tissue perfusion or vascular permeability. For the initial validation of EQ-CT, the bolus/ infusion approach was deemed to be more robust than a single injection approach.

The work within this chapter aims to develop and validate steady state equilibrium contrast computed tomography (EQ-CT) as a measure of myocardial extracellular volume fraction (ECV) using a histological reference standard, and to compare with equilibrium contrast MRI (EQ-MRI).

6.3 Materials and Methods

Local ethics committee approval was obtained for each part of the study – see chapter 1. All participants provided informed and written consent.

EQ-CT development was approached in three stages. Firstly, in order to remove contrast kinetic effects, a protocol of primed iodinated contrast infusion (bolus plus maintenance infusion) that generated steady state equilibrium contrast conditions was developed, demonstrating this first in blood and later in blood and tissue. Secondly, a CT scanning and analysis protocol that could measure cardiac muscle and blood pool attenuation with an adequate signal to noise ratio was developed. Thirdly, this EQ-CT method was validated against human myocardial tissue obtained by surgical biopsy in patients with severe aortic stenosis where diffuse fibrosis is known to occur (21). Lastly EQ-CT measurement of ECV was compared with measurement using EQ-MRI.

6.3.1 Blood Contrast Equilibrium

A contrast infusion and bolus protocol to achieve equilibrium in the blood was developed in 15 individuals (12 healthy volunteers and 3 patient volunteers; mean age 44.2, range 27-76). An unpaired t-test demonstrated no significant difference in mean age between the 9 males (mean 41.8; range 27-76 years) and 6 females (mean age 47.0; range 27-71 years) in this group.

In order to achieve contrast equilibrium rapidly a primed infusion technique (bolus followed by slow continuous infusion) was developed to achieve steady state equilibrium consistently within 30 minutes. The parameters required for to reach contrast equilibrium in this time frame were identified using an iterative approach, first in healthy volunteers (n=12) then in patient volunteers (n=3), based on those previously validated in EQ-MRI (1).

Volunteers had a intra venous cannula placed in both antecubital fossae (one for contrast administration, and the other for blood sampling). The initial contrast protocol consisted of a bolus volume of 1mg/kg of Iohexol (Omnipaque 300; Nycomed Amersham, Oslo, Norway; 300 mg of iodine per millilitre) administered a rate of 3mls/sec. This initial infusion rate was based on similar work using MRI contrast agents (1). 3ml blood samples were taken at 0, 1, 3, 7, 10, 15, 20, 30, 45, 60 minutes after bolus injection and plasma iodine concentration measured using high performance liquid chromatography (HPLC) (11) – see methods Chapter 3. In the second volunteer a 1mg/kg bolus was given at 3ml/s followed after a 15 minutes delay by an infusion of Iohexol at 2.4ml/kg/hr (with a maximum contrast volume of 200mls). Three parameters: bolus volume; infusion start time and infusion rate were then varied iteratively after each experiment based on the derived plasma iodine concentration curve. Contrast equilibrium was defined as a plasma concentration variation in consecutive measurements of < 5% over 10 minutes. At the end of the iterative

development, a protocol consisting of 1mg/kg bolus at 3ml/s, followed immediately by an infusion of 1.88ml/kg/hr was found to provide the most rapid and consistent steady state equilibrium – Figure 6.1.

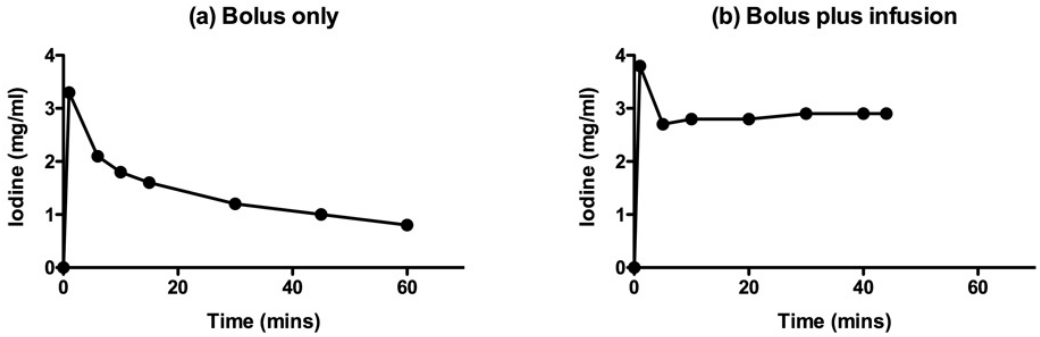

Figure 6.1 Iodinated contrast concentration curves

Blood iodine concentration measured using HPLC in 2 normal volunteers following (a) 80ml bolus and (b) 80ml bolus followed immediately by an infusion at 2.5ml/min of Iohexol (300mgI/ml).

6.3.2 Confirmation of Tissue contrast equilibrium

Following derivation of the contrast bolus and infusion protocol, blood and tissue equilibrium was assessed using CT imaging in consenting patient volunteers (n=5; 3 male, 2 female) referred for abdominal imaging for non-specific symptoms. Imaging examinations were performed using a multi detector 64-row CT scanner (SOMATOM Sensation 64, Siemens Medical Solutions, Erlangen, Germany). A topogram was used to plan a spiral CT volume of the lower chest from the level of the aortopulmonary window to just below the inferior aspect of the heart. Scans (tube voltage 120kV, tube current-time product 160mAs, slice collimation 64mm×1.2mm, gantry rotation time 330ms) were acquired using retrospective ECG gating at 4 time points (pre contrast, 10, 15 and 25 minutes post-primed infusion) to confirm equilibrium was achieved within cardiac tissue. Retrospective gating required continuous data acquisition through multiple cardiac cycles with simultaneous ECG recording, allowing reorganisation of the

reconstruction to the desired phase (65-75% of the RR interval). Heart rate was recorded at the beginning of the pre-contrast acquisition. Axial images were reconstructed with a slice thickness of 5mm using a B20f kernel.

Regions of interest (ROI) were drawn using OsiriX v4.1.2 (Pixmeo, Switzerland) by the author who was blinded to all other study data. An axial slice was selected that visually contained the greatest area of myocardial septum. On this slice an elliptical ROI was drawn in the left ventricular chamber so as to include the largest area of blood pool but not including papillary muscle; and a polygonal ROI was drawn in the myocardial septum to include the maximum area of myocardium but avoiding the endocardium.

Initially blood pool attenuation was measured in the descending aorta, however ROIs here were affected by streak and beam hardening artefact (see chapter 9.4.1) from adjacent dense vertebral endplates and aortic wall calcification leading to significant variation in measured attenuation. To overcome this, blood attenuation was measured within the left ventricular blood pool adjacent to the myocardial septum (the ventricular blood pool lies further away from the vertebra, is less affected by artefact, and given the proximity of the myocardial septum and ventricular blood pool, any artefact present was likely to affect both ROIs in a similar way).

The mean HU was measured in each ROI and plotted against time. Steady state equilibrium was confirmed in all 5 volunteers by a change in mean HU attenuation within myocardial and blood ROIs between successive time points of < 10% (reflecting the increased noise associated with CT attenuation measurement) - Figure 6.2.

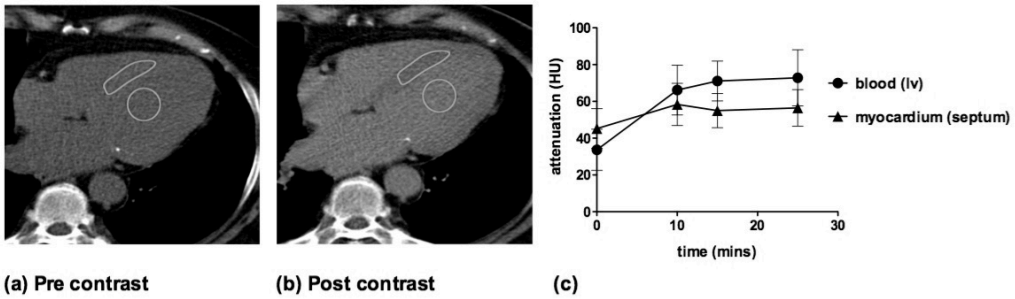

Figure 6.2 CT confirmation of tissue equilibrium

Left – pre contrast CT; middle – post contrast at 25 minutes; right - CT attenuation plots of blood and myocardial equilibrium. Pre contrast blood and myocardium are visually iso-dense; post contrast, both have increased attenuation but now a blood:myocardial boundary is visible with blood brighter – therefore blood visually has the larger ECV.

6.3.3 Clinical Validation

Recruitment took place at UCLH between July 2010 and February 2012. Patient inclusion criteria were severe aortic stenosis with elective open valve replacement planned within 4 weeks. Exclusion criteria were uncontrolled arrhythmia; impaired renal function (estimated glomerular filtration rate, eGFR< 60 ml/min) or contraindications to MRI (e.g. implanted devices). 2 patients were excluded with atrial fibrillation; 2 with impaired renal function and 1 due to severe claustrophobia.

EQ-CT was performed pre-operatively using the contrast and scan parameters defined in the preliminary experiment (bolus 1ml/kg, no delay, infusion 1.88ml/kg/hr) and tube current 300-650mAs depending on patient body habitus. Prior to the scan, following insertion of an intravenous cannula, a 2ml blood sample was collected and sent for complete blood count (CBC) analysis. CT images were acquired pre contrast and 25 minutes post contrast bolus (i.e. during static equilibrium). In order to reduce inter-slice dose variation, which would lead to variation in image noise and attenuation measurement standard error, the proprietary dose modulation function (CARE Dose) was not used. Careful attention was paid to ECG gating and breath hold instructions to ensure consistency

between scan phases and reduce image misregistration. CT datasets were reconstructed into 5mm thick axial slices. The scanner measured total Dose Length Product for each examination an effective dose was calculated using a conversion factor of 0.014 (12).

The author who was blinded to the rest of the study data performed the CT analysis. The slice with the greatest area of myocardial septum was selected for ROI analysis from the images acquired during steady state equilibrium (EQ phase images) and the matching pre contrast slice identified visually. ROIs were drawn first on to the EQ phase image; as in the preliminary experiment within the left ventricular chamber (mean area 3.1cm2; range 1.7-5.3cm2) and myocardial septum (mean area 4.3cm2; range 2.1-8.8cm2). ROIs were then copied to the pre contrast image. Mean attenuation in Hounsfield units (HU) at each phase was then recorded and myocardial ECV calculated using the formula:

$ECV_{myocardium} = (1\text{-haematocrit}) \times (\Delta HU_{myocardium} \div \Delta HU_{blood})$

;where ΔHU = HU EQ phase- HUpre contrast

EQ-MRI was performed pre-operatively and within 48 hours of the EQ-CT to quantify myocardial ECV. A previously validated protocol (1) consisting of 0.1 mmol/kg Gd-DTPA bolus (Dotarem; Guerbet), followed by a 15-minute pause, then an infusion at a rate of 0.0011 mmol/kg/min was used. Tissue T1 relaxation time was measured using a Shortened Modified Look-Locker Inversion Recovery (ShMOLLI) (13) sequence – which provided a single slice T1 map in a breath hold. Using multi-plane localisers to plan, an axial T1 map was acquired through the heart to include the largest area of myocardial septum. Images were acquired at the same position before and during contrast equilibrium, with position matching performed visually by a researcher supervising the scans (Steven K. White – Cardiology Fellow UCLH). A standard cardiac MRI late Gadolinium enhancement (LGE) technique(2) was included in the protocol to exclude focal myocardial fibrosis.

MRI data was analysed independent of the CT and histology data by a Cardiologist with 3 years experience in cardiac MRI (Steven K. White – Cardiology Fellow UCLH). Beginning with the EQ phase T1 map, single ROIs were draw within the ventricular blood pool and myocardial septum using the method described above for CT and copied to the pre contrast T1 map and mean T1 relaxation times recorded as previously published(4). Myocardial ECV was then calculated using the formula:

$$ECV_{myocardium} = (1\text{-hematocrit}) \times (\Delta R1_{myocardium} \div \Delta R1_{blood})$$

;where $\Delta R1 = (1 \div T1_{EQ\ phase}) - (1 \div T1_{pre\ contrast})$

Aortic valve surgery took place no more that 7 days after imaging – typically within 24 hours. Intra-operative myocardial septal tissue specimens (1cm cores) were collected during cardioplegia using a 14-gauge coaxial needle system at the time of aortic valve replacement by the senior attending surgeon who had been briefed by a member of the research team. The myocardial septum was agreed as a safe site for biopsy by the cardiothoracic surgical team. Samples were immediately fixed in 10% buffered formalin, embedded in paraffin, and stained with picrosirius red. Collagen volume fraction was measured as previously described in chapter 3.

6.3.4 Statistical analysis

The Prism statistical package: version 5 (Graphpad Software Inc.) was used for all data analysis. Normal distribution was assessed using the Kolmogorov-Smirnov test.

EQ-CT derived myocardial ECV was compared with histological CPA using Pearson correlation. The EQ-MRI data was similarly compared with histology.

The relationship between myocardial ECV measured using EQ-CT and EQ-MRI was assessed using Pearson correlation. Agreement between these measures was assessed using Bland-Altman comparison (14).

6.4 Results

6.4.1 Clinical Validation

23 eligible pre-operative patients (male=16; female=7; mean age=70.8; SD=8.3) with severe aortic stenosis were recruited – Table 6.3.

All 23 patients underwent EQ-CT prior to surgery. The mean heart rate at the beginning of the examination was 69 beats/minute. The mean total calculated effective radiation dose for the EQ-CTs was 10.7mSv (+\- 3.4mSv), with a mean total Iohexol volume of 143.2ml (+/- 22.7ml).

19 of the 23 patients underwent EQ-MRI (including a standard LGE technique) prior to surgery. Mean total dose of Gd-DOTA was 10.7mmol (+/- 1.8mmol). Of the 4 patients who failed to undergo MRI; one became acutely unwell prior to scanning; one was found to have a non-MRI safe device in-situ; one had a metallic eye foreign body and 1 scan was cancelled after the patients operation was brought forward. None of the scanned patients were found to have late gadolinium enhancement.

All 23 biopsy procedures during aortic valve replacement surgery were uneventful. Four biopsies were unsuitable for analysis as they contained only superficial endocardium, and two were fragmented. In the remaining 17 biopsies the mean histological CVF was 18% (intersubject range 5% to 40%) – Figure 6.4.

In the 23 patients, the ECV measured by EQ-CT had a mean of 0.31 and range of 0.18-0.44. ECV measured by EQ-CT correlated with CVF: $r=0.71$, $p<0.001$ (Figure 6.5) in the 17 patients with comparative data.

In the 19 patients that underwent EQ-CMR, ECV had a mean of 0.30 and range of 0.25 to 0.41. There was a good correlation between EQ-CMR measured ECV and CVF: r=0.84, p<0.0001 (Figure 6.6) in the 15 patients with comparative data.

In 19 cases, myocardial ECV was measured using both EQ-CT and EQ-CMR. Pearson correlation demonstrated a good linear relationship between these two measures: r=0.73, p=0.0002 (Figure 6.7), Bland-Altman analysis demonstrated little bias (-1.4% with no slope) but with relatively wide confidence limits (95% limits -34.7 and 31.9%) - Figure 6.8.

Volunteer Characteristics for Healthy and Aortic Stenosis Groups				
	Group	**Male**	**Female**	**P value**
Healthy volunteers				
Number [%]	**15**	**9 [60]**	**6 [40]**	
Age (y)	**44.2 (18.9)**	**41.8 (20.0)**	**47.0 (19.4)**	**0.675**
Aortic stenosis patients				
Number [%]	**23**	**16 [70]**	**7 [30]**	
Age (y)	**70 (8)**	**70.9 (8.3)**	**69.9 (7.6)**	**0.785**
Heart rate (beats/min)	**68.9 (9.1)**			
Estimate glomerular filtration rate (ml/min/1.73m^2)	**76.9 (13)**			
Hematocrit (%)	**40.2 (5)**			

Table 6.3 Volunteer characteristics

Volunteer characteristics for healthy and aortic stenosis groups. Data are mean values (+/- standard deviation)

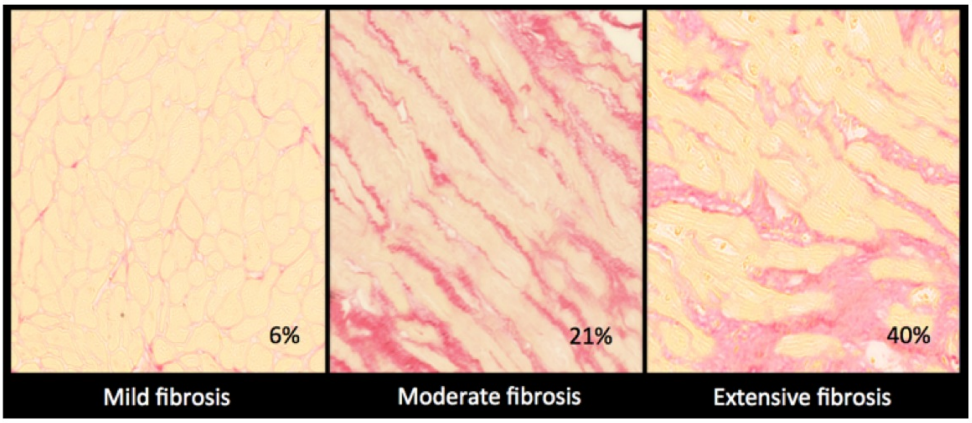

Figure 4:

Figure 6.4 Histological stages of fibrosis

Example histological samples with collagen stained red with picrosirius red. Slides show mild, moderate and severe myocardial fibrosis, with digital image analysis measurement of collagen proportionate area of 6, 21 and 40% respectively..

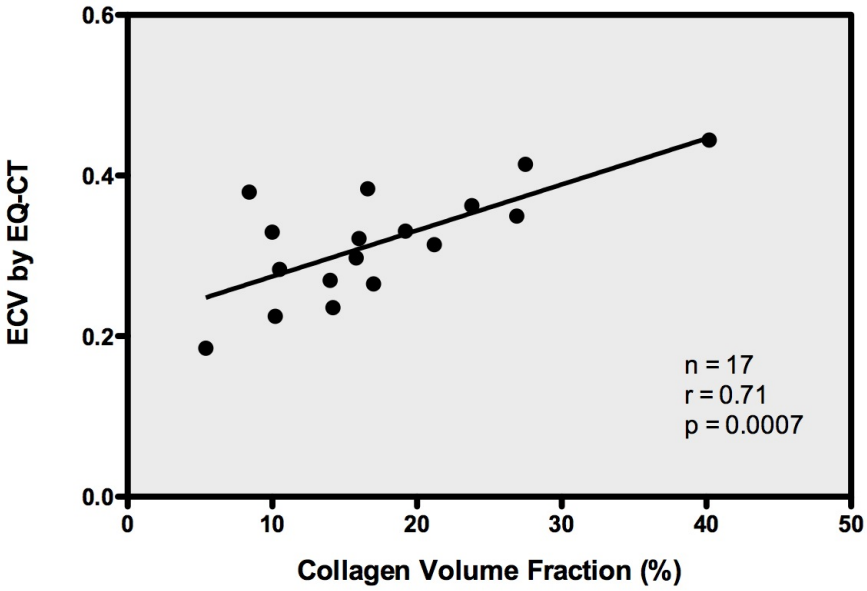

Figure 6.5 ECV by EQ-CT vs CVF

Scatter plot of ECV measured by EQ-CT against histological CVF with regression line

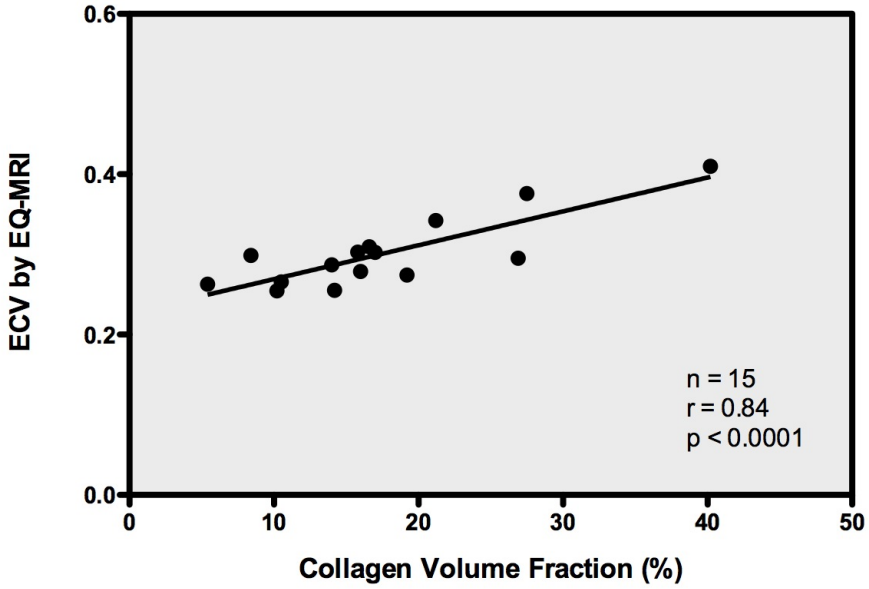

Figure 6.6 ECV by EQ-MRI vs CVF

Example histological slides showing mild, moderate and severe myocardial fibrosis.

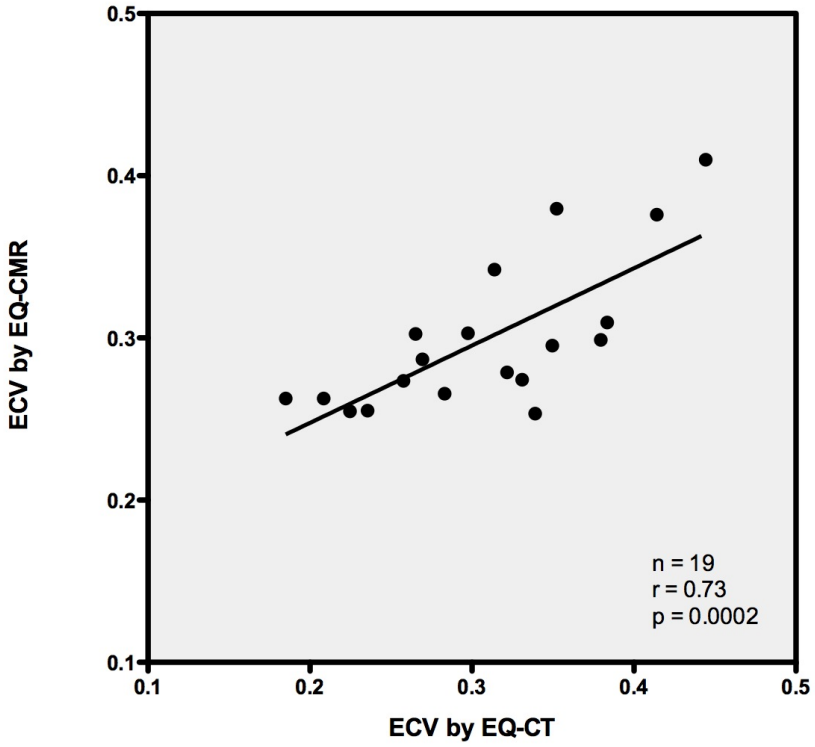

Figure 6.7 ECV by EQ-MRI vs EQ-CT

Plot of ECV measured by EQ-CT against ECV measured by EQ-CMR

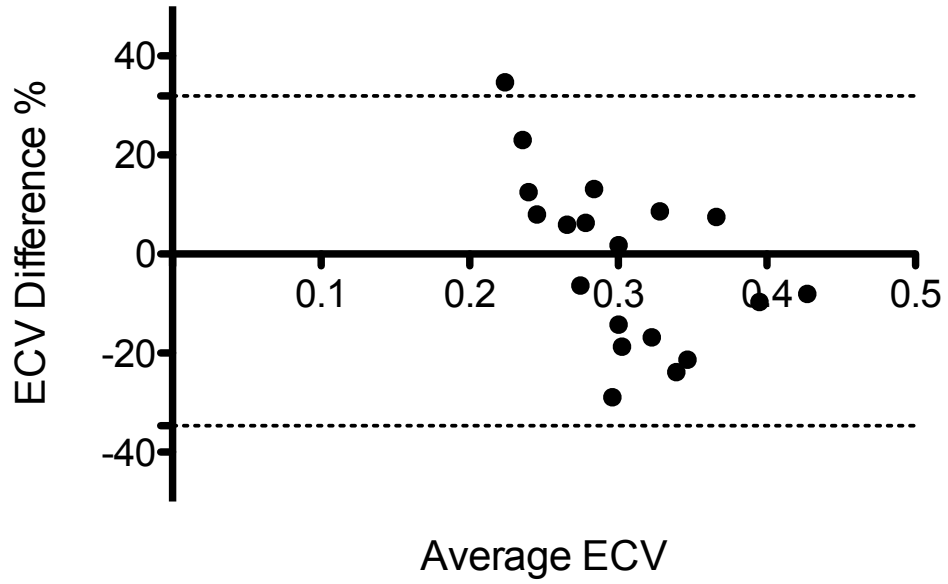

Figure 6.8 Bland-Altman evaluation of ECV measures

Bland-Altman comparison of ECV measurement method shows ECV difference expressed as a percentage (calculated by subtracting ECV measured with equilibrium CT from ECV measured with equilibrium MR imaging) against mean ECV (solid line), with lower (bottom dotted line) and upper (top dotted line) 95% limited of agreement

6.5 Discussion

The work within this chapter supports the use of CT for the non-invasive quantification of tissue extracellular space, measured as the Extracellular Volume (ECV). Here, diffuse fibrosis quantified histologically from human myocardial biopsies in severe aortic stenosis is used as the reference standard for validation, with a secondary comparator of ECV measured by EQ-MRI.

Our group and others have used T1 mapping based contrast techniques to measure ECV with cardiac MRI(1)(3)(15). An important assumption of the equilibrium model is that the extracellular space with tissue consists only of a single compartment. In reality, the tissue extracellular space consists

of an intravascular extracellular component in addition to the extravascular extracellular space we describe as the interstitium. Where the tissue vascular volume is large, for example in the liver, this intravascular extracellular component may introduce error into ECV measurement using the equilibrium technique (see chapter 1.10).

A steady state contrast equilibrium technique - achieved here using a bolus followed by a slow contrast infusion - was chosen in preference to the bolus only dynamic equilibrium protocol used by other authors (2) (7) as a method to eliminate the effect of contrast kinetics. A steady state protocol allows ECV measurement in tissues irrespective of permeability or blood flow and has been validated a histological reference (1). It is recognised that a steady state infusion method has disadvantages over a contrast bolus based method – i.e. is more time consuming, and would be additional to standard diagnostic images. However, in this work I sought to lay out an optimal method against which future abbreviated estimations of ECV could be compared. White et al. (16) recently compared bolus only and primed infusion methods for myocardial ECV measurement using CMR, demonstrating good agreement between techniques in aortic stenosis. This bolus only approach is explored in subsequent chapters.

Using this EQ-CT methodology to measure tissue ECV, the correlation with histological fibrosis obtained in this proof of principle study was reasonable (r=0.71) but lower than found with CMR in this study and by other authors (r=0.84 and 0.93)(1). There are several possible underlying explanations.

The use of ionising radiation necessitates a dose that is as low as reasonably possible – thus CT attenuation SNR was lower than the changes found using MRI (17). Additional noise in the CT images stemmed from streak and beam hardening artefacts originating from dense vertebral endplates and vessel wall calcification – Figure 6.9. To minimise these effects, blood attenuation was instead measured within the

left ventricular chamber. Applying tailored reconstruction algorithms (18, 19) may reduce these effects and allow accurate aortic blood pool attenuation measurement. I address the subject of CT artefacts in chapter 9.

Examination dose for the EQ-CT study was comparable to local Dose Reference Levels for a similar multiphasic body CT examination.

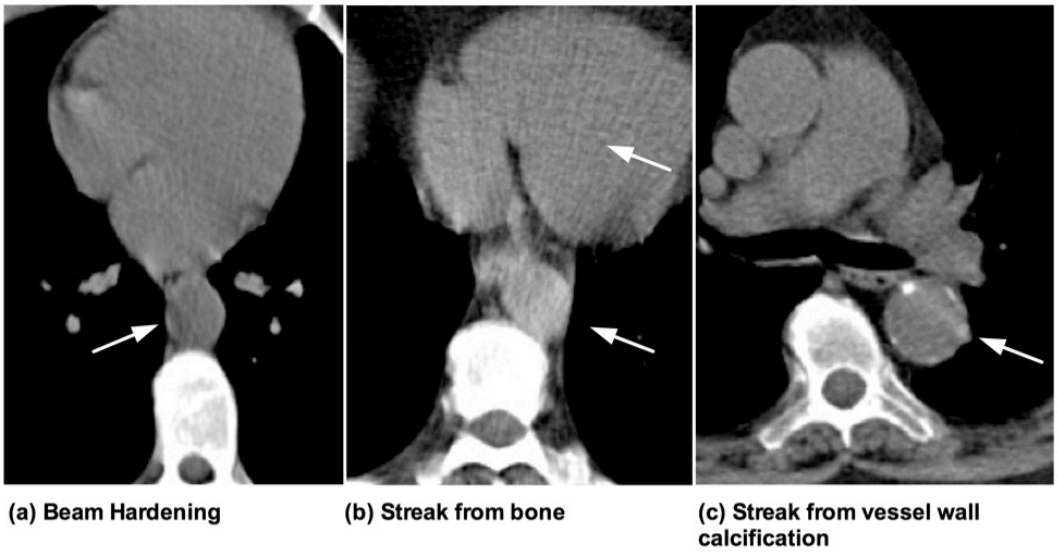

Figure 6.9 CT artefacts

Inter-related artefacts affecting pre contrast blood attenuation measured within the descending aorta. Ventricular blood pool suffers less from these. All figures have all artefact types – but each has a different predominance: (a) beam hardening; (b) brighter aortic vs myocardial blood pool (streak from the adjacent vertebral body); (c) streak from focal aortic wall calcification.

It is noted that myocardial radio-density did not alter post contrast to the same degree as T1 weighted signal intensity following gadolinium. Low voltage and dual energy techniques may improve this contrast, and while the effective radiation dose for this EQ-CT protocol lay with acceptable limits, could be included in a dose minimisation strategy.

Additionally, despite choosing a disease (aortic stenosis) with homogeneous diffuse fibrosis and optimal sampling method (surgical biopsy), comparison of either EQ-CT or EQ-MRI with a reference standard of biopsy is imperfect because of the potential for sampling error. In this

study, precise matching of pre-operative CT and MRI ROI placement with the site of biopsy was not possible. Surgical specimens were collected without image guidance making precise localisation within the myocardial septum difficult.

Further potential technical improvements include additional processing of image data with application of automated segmentation methods, which may reduce reliance on expert interpretation, and increase the speed of image data processing. Co-registration of pre and EQ phase images has been used to compute a pixel-by-pixel ECV map (20) showing regional tissue ECV variation. This may aid clinical interpretation and comparison with assessment other imaging modalities – for example ultrasound / echocardiography.

Although correlation between CT and MRI measures of ECV demonstrated a good linear relationship, the Bland-Altman limits of agreement between the two techniques were relatively wide. This may result from the small sample size used, but may also reflect technical differences in the two imaging modalities. Whether the strength of correlation between ET-CT derived ECV and histological fibrosis demonstrated here translates into a meaningful clinical tool remains unknown. Larger cohorts studies are need to test the ability of EQ-CT to differentiate between clinically important disease states (e.g. mild vs severe fibrosis) and if indeed EQ-CT findings can prognosticate on disease outcome and guide therapeutic decision-making.

This chapter demonstrates proof of principle of EQ-CT measurement of ECV against a histological standard in a common cardiac disease. Further work will be required to pursue potential technical improvements to the method, but the use of conventional CT equipment and contrast agents suggests wide potential clinical applicability. This work will provide the basis to explore the utility of EQ-CT in other organs and diseases where

diffuse interstitial expansion plays a key role, such as the liver, bowel wall, bladder, or nerves.

7 EQUILIBRIUM CONTRAST CT TO EVALUATE HEPATIC FIBROSIS

7.1 Author declaration

The experiments presented in this chapter were performed, and the data analysed and presented by the author under the supervision of Dr. Shonit Punwani, Prof. James Moon, Prof. Stuart Taylor and Prof. William Rosenberg. This work was published in the journal article: 14. Bandula S, Rosenberg WM, Hall AR, Moon JC, Taylor SA. Equilibrium Contrast-enhanced CT Imaging to Evaluate Hepatic Fibrosis : Initial Validation by Comparison with Histopathologic. 2015;000(0):1–8.

7.2 Introduction

Chronic liver disease is a major worldwide public health issue (1), with an estimated 1.29 million deaths worldwide in 2010 from viral hepatitis alone (2). Regardless of etiology, sustained liver injury eventually leads to diffuse interstitial fibrosis and expansion of the extracellular space by collagenous scar that distorts the normal architecture, impairs hepatic function and is the hallmark of cirrhosis. Evaluation of hepatic fibrosis plays a key role in disease management, facilitating prognostication and guiding therapies such as antiviral agents, which in some instances may reverse the fibrogenic process (3). Staging of liver fibrosis allows clinical risk stratification, assessment for treatment eligibility and evaluation of treatment effect. Histopathological evaluation of biopsy samples remains the reference standard test for assessment of diffuse hepatic fibrosis, but has a number of well documented limitations, including its invasive nature and associated small but significant risk of complications (4). Furthermore, it examines only a tiny fraction of the organ (5) and is therefore prone to

sampling error(6). These deficiencies have fueled the development of non-invasive techniques for fibrosis quantification. As discussed in chapter 1, liver stiffness measurement by transient elastography is well validated (7) but requires dedicated equipment and is of limited use in obese patients, and those with ascites or narrow intercostal spaces (8). Serum biomarkers such as the enhanced liver fibrosis (ELF) test are sufficiently related to liver fibrosis that they are clinically useful (9), but are not liver specific (10), and some have other influences such as renal function that reduce their discrimination between mild and moderate fibrosis (11-12).

Both MRI (15) and CT (see chapter 6) have now been applied successfully to quantify myocardial ECV as a surrogate marker for diffuse fibrosis. In chapter 5 I also applied the technique in the liver using MRI to quantify amyloid deposition. Intuitively the technique may have a role in assessing diffuse liver fibrosis and indeed Varenika et al. (17) have recently described a strong correlation between hepatic ECV and histological fibrosis area in a rodent model of chronic liver disease. Early retrospective studies suggest this observation may translate into humans (18). To date there has been no validation of EQ imaging assessment of diffuse liver fibrosis against a histopathological reference, and in particular a robust morphometric quantitation of collagen in an appropriate spectrum of patients with a range of disease severity.

In this chapter, I prospectively evaluate hepatic ECV measurement by equilibrium CT (EQ-CT) against fibrosis quantified histologically and against the enhanced liver fibrosis panel (ELF) (9) in a cohort of patients with chronic hepatitis.

7.3 Materials and Methods

Between April 2011 and July 2013, 40 patients with serologically confirmed hepatitis B or C undergoing clinically indicated liver biopsy were recruited prospectively from outpatient clinics at the Royal Free Hospital -

London. Exclusion criteria were: contraindication to contrast enhanced CT (iodinated contrast allergy; estimated glomerular filtration rate less than 60ml/min);, previous liver transplantation or risk factors for other casues of liver fibrosis including HIV co-infection and a history of significant alcohol consumption (>3-4 units/day for men; >2-3units/day for women). All patients gave fully informed written consent.

7.3.1 Histology

Liver biopsies were performed following local guidelines as part of the patient's routine clinical care. Percutaneous biopsy was performed using a Menghini technique (19) with a 16-gauge needle from the right lobe. Transjugular biopsy samples were collected with up to 4 passes of a 19-gauge needle through either the right or middle hepatic vein wall (20).

To ensure reliable histopathological evaluation, only biopsies samples with a total length ≥ 12mm were included in the analysis (21). Samples were formalin fixed, paraffin embedded and stained with hematoxylin and eosin, and Gordon and Sweet staining for reticulin. The reference standard fibrosis stage was evaluated by an experienced hepatopathologist (Prof. P. Dhillon – Department of Histopathology, Royal Free Hospital) according to the Ishak system - see chapter 1.4.1 (22). A further tissue section was stained with picro-Sirius red for collagen proportionate area (CPA) quantification by digital image analysis (DIA). CPA as been show to be a objective continuous quantitative measure of fibrosis with recognized prognostic value, but has not yet been widely adopted for clinical use – Germani et al. Histopathology 2010. DIA was performed independent of fibrosis staging by a single operator (Andrew Hall – Department of Histopathology, Royal Free Hosptial) using the method described in chapter 3.8 (23)-. A digital camera (Canon Powershot A640) was used for image capture and digital image analysis was performed using Zeiss KS300 software.

7.3.2 Equilibrium Contrast Computed Tomography

The principals underpinning equilibrium contrast imaging have been laid out in chapter 1 and tested in chapter 2. In this initial exploratory study of use in liver fibrosis, as in chapter 6, a steady state contrast equilibrium protocol was used based on contrast bolus injection followed by an infusion. This method was again chosen to minimize potential error resulting from inter subject haemodynamic or contrast kinetics variation that could arise from a single bolus technique (13).

EQ-CT was performed using a 64-detector row CT scanner (Somatom Sensation 64; Siemens Medical Solutions, Erlangen, Germany) no more than 2 weeks prior to liver biopsy. Prior to CT scanning, two 5ml blood samples were collected. The first was sent for complete blood count (CBC) to obtain blood hematocrit, and the second for ELF analysis (see below).

A pre contrast scan was acquired through the upper abdomen to include the whole liver using the parameters: effective tube current-time product 250mAs, pitch 0.8, tube voltage 120 kV, slice collimation 24x1.2mm, gantry rotation time 500ms and reconstructed to a slice thickness of 10mm using a soft tissue convolution kernel (B20f). The iodinated contrast agent iohexol (Omnipaque 300, GE Healthcare) was then administered as a bolus dose of 1ml/kg at 3ml/s; followed immediately by an infusion of 1.88ml/kg/hr based on prior development work demonstrating contrast steady state on sequential plasma iohexol measurements and CT scan attenuation measurements (see chapter 6). After 30 minutes of infusion, the scan volume through the upper abdomen was repeated using the same parameters. Scanner generated dose length product (DLP) for each examination was used to calculate effective dose using a conversion factor of 0.015 (25).

Image analysis was performed using OsiriX v4.1.2 (Pixmeo, Switzerland) by the author, blinded to biopsy findings.

On 3 contiguous slices reconstructed to a thickness of 10mm, a peripherally based wedge shaped region of interest was drawn in segment VII of the liver (mean area 34.5cm^2) to include the greatest area of liver parenchyma whilst avoiding visible vessels or incidental hepatic lesions such as cysts. Because the exact liver segment from which the biopsy samples were collected was not known in all cases, imaging-biopsy matching was at the level of the right lobe only. A further elliptical region of interest was drawn on the same slice within the abdominal aorta (mean area 1.6cm^2) avoiding the aortic wall and any atheromatous plaque. ROIs were drawn on the post contrast images and then copied to the matching slices on the pre contrast images. Mean attenuation (in standard CT Hounsfield units [HU]) for liver parenchyma and blood were derived and liver ECV calculated using the formula:

ECV_{liver} = (1-hematocrit) x ($\Delta HU_{liver} \div \Delta HU_{blood}$)

;where $\Delta HU = HU_{EQ\ phase} - HU_{pre\ contrast}$

Where visible, mean attenuation within the gallbladder was also measured on the pre and post contrast images to assess for vicarious biliary excretion of contrast.

7.3.3 ELF Test Biomarker

Patient serum was separated from blood collected prior to the CT and stored at -80°C before being sent to an independent laboratory (iQur Limited, London). Proprietary assays (Siemens Healthcare Diagnostics, Tarrytown, USA) were used in conjunction with an Advia Centuar automated analyser (Siemens Healthcare Diagnostics, Tarrytown, USA) in accordance with the manufacturer's instructions to determine levels of tissue inhibitor of matrix metalloproteinase 1 (TIMP-1), hyaluronic acid (HA) and amino-terminal propeptide of type III collagen (PIIINP). Results were combined via an algorithm to generate a fibrosis score (9).

7.3.4 Statistical Analysis

Statistical analyses were performed using Prism 5.0 software (Graphpad, San Diego, CA). Kolmogorov-Smirnov analysis was used to test for normality. Non-Gaussian distributed data were expressed as a median and interquartile range. Correlation between variables was evaluated by using Spearman correlation, with one sided significance testing set to <= 0.05. Linear regression was used to evaluate the ability of ECV, ELF and a model combining ECV and ELF score to predict CPA. The R and R^2 values were used to assess the strength of correlation, and P values less than 0.05 were considered to indicate a significant difference.

Histological stage was divided into low (S0-1), moderate (S2-4) and severe (S5-6) groups, and ECV, CPA and ELF score were compared with fibrosis stage by using the Kruskal-Wallis nonparametric analysis of variance test.

7.4 Results

Of the 40 patients fulfilling the eligibility criteria, complete sets of data (ECV, CPA and ELF score) were collected in 33 cases (4 histology samples were fragmented or measured less than 12mm; 2 patients had pre-CT eGFRs <60mls/min; and 1 patient withdrew consent – see table 7.1 for demographic data. Figure 7.2 shows an example patient's EQ-CT imaging with corresponding biopsy specimen. Of the 33 patients, a diagnosis of hepatitis C virus infection had been made in 23 cases and hepatitis B in 10. 24 tissues samples were collected by ultrasound guided biopsy and 9 by transjugular biopsy. Demographic and ELF details are summarized in table 7.1.

	Total
Patient number (%)	33 (19M/14F)
age (y) mean	49.9 (48.8M/51.4F)
age (y) range	22 – 68
Biopsy method (US / TJ)	25 / 8
Hematocrit	0.428 +/- 0.041
Serum creatinine conc. (µmol/L)	89.5 +/- 22
International Normalized Ratio	1.22 +/- 0.42
Bilirubin μ mol/L	16.6 +/- 10.6

Table 7.1 Demographic data

Summary of demographic and clinical data. Values are mean +/- SD

EQ-CT examination SSDE had a mean (+/-SD) of 38.8mGy (+/-8.2). The region of interest volume was approximately 500 times that of the each biopsy (10.4mls vs 0.02mls) average. The mean (and range) attenuation within the liver and aorta pre contrast was 50HU (24-62) and 41HU (32-51); and at equilibrium phase was 67HU (38-78) and 80HU (71-94).

The gallbladder was present in 24 of the 33 patients analysed, and mean attenuation within the gallbladder lumen was 9HU (range 2-25) pre contrast and 11HU (range 2 to 24HU) post contrast. Paired t-test confirmed no significant difference ($p = 0.08$) in gallbladder lumen attenuation between the pre contrast and equilibrium phase images (mean difference 1.1HU).

Fractional ECV measured in the liver had a median (IQR) of 0.26 (0.24 – 0.29) and a range of 0.17 – 0.47; CPA a median (IQR) of 5.0 (3.0 – 15.0) and a range of 1.8 – 28.3; and ELF score a median (IQR) of 9.71 (8.14 – 10.92) and a range of 7.27 – 12.43.

Fractional ECV showed good association with CPA ($r = 0.64$, $p < 0.0001$) and ELF score ($r = 0.38$, $p = 0.0272$) – figure 7.3 (a) and (b), with no significant difference in the strength of the correlations ($p = 0.177$). A significant association was also found between ELF score and CPA ($r = 0.46$, $p = 0.0075$) – figure 7.3c.

Multiple regression analysis showed that both ECV ($p<0.0001$) and ELF ($p=0.0062$) were significant independent predictors of CPA, with a t statistic for ECV and ELF of 5.20 and 2.94 respectively. The regression model (80 x ECV + 1.8 x ELF -30.4) was a better predictor of CPA ($R^2 = 0.67$; $p<0.0001$) (figure 7.3d) than either ECV ($R^2=0.56$; $p<0.0001$) or ELF ($R^2=0.35$; $p = 0.0168$) alone.

ECV ELF and CPA demonstrated comparable discrimination between Ishak score S0-1 vs S5-6 and S2-4 vs S5-6 ($p=0.0126$, $p=0.0160$ and $p=0.0008$ respectively). Neither of the three was able to significantly distinguish S0-1 and S2-4 ($p>0.05$).

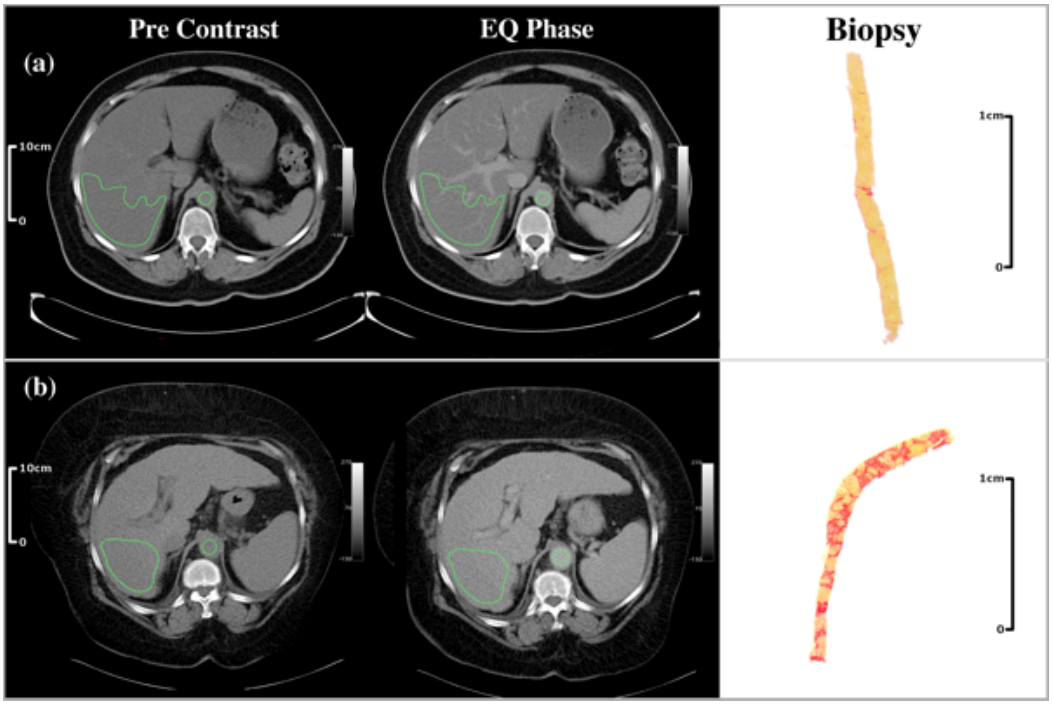

Figure 7.2 EQ-CT images and corresponding biopsy specimens

EQ-CT and biopsy specimen (picro-Sirius red stain; macro view) images from a patients with (a) no significant fibrosis (ECV=0.21; CPA=3,) and (b) severe fibrosis (ECV=0.31; CPA=24). Sampled volumes between EQ-CT and biopsy differ by approximately x1500. Note that the IVC and right portal vein branches in (b) are less visible than in (a) - as liver ECV approaches that of the blood

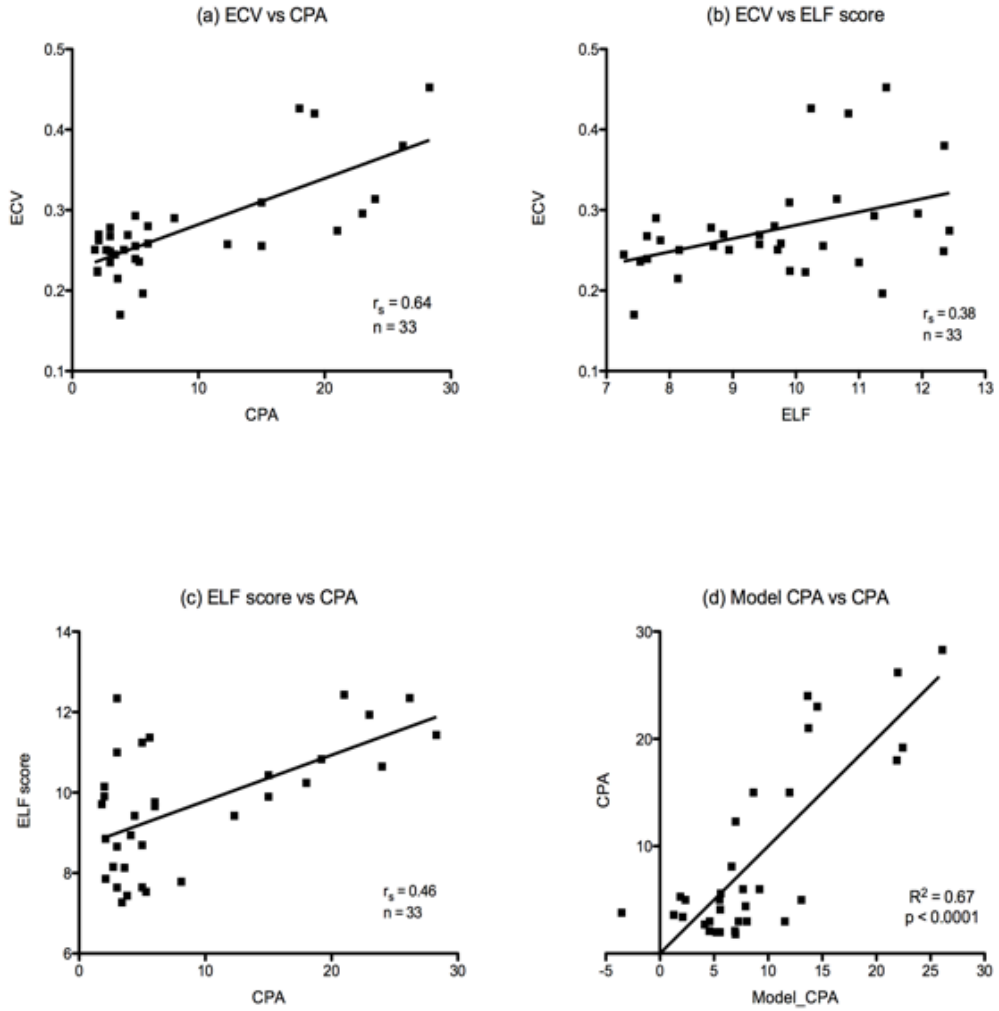

Figure 7.3 Scatterplots comparing ECV, ELF and CPA

a, b & c. Scatterplots showing correlation between extracellular volume measured using EQ-CT, histological collagen proportionate and ELF score, with lines of best fit. 2d. Multiple regression model combining EVC and ELF to predict CPA

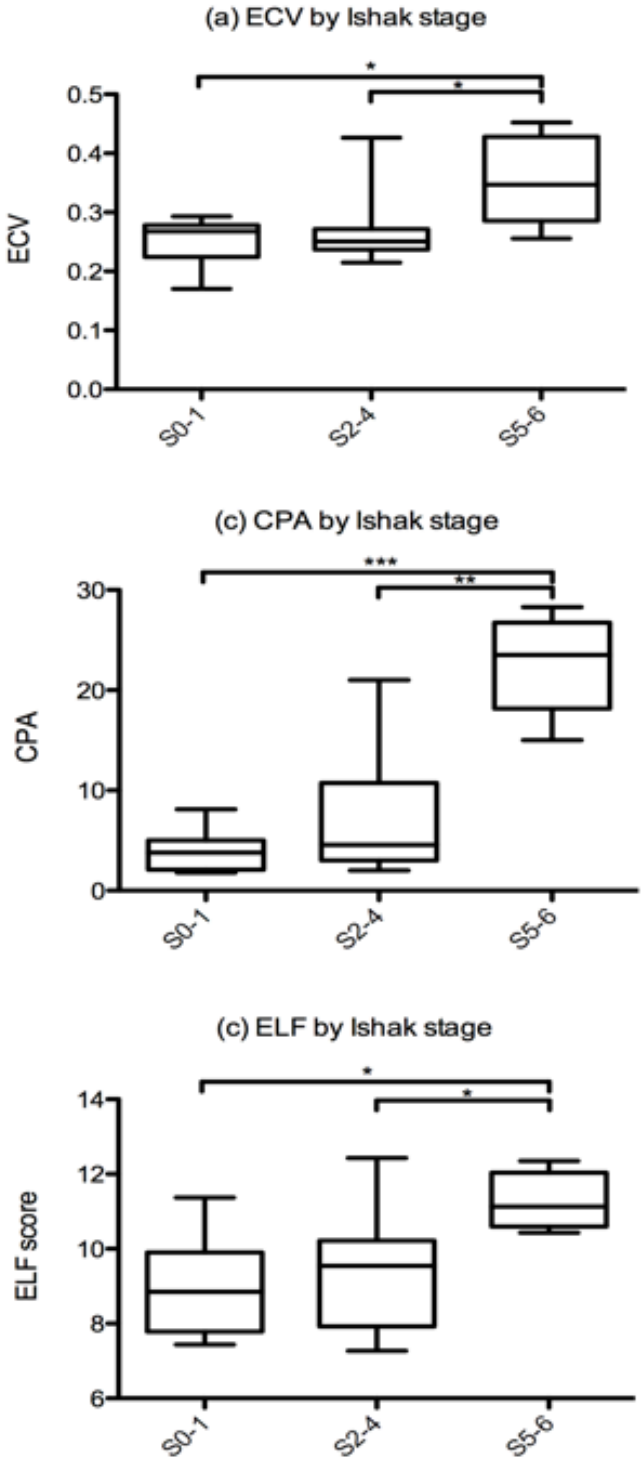

Figure 7.4 Bland-Altman evaluation of ECV measures

Bland-Altman comparison of ECV measurement method shows ECV difference expressed as a percentage (calculated by subtracting ECV measured with equilibrium CT from ECV measured with equilibrium MR imaging) against mean ECV (solid line), with lower (bottom dotted line) and upper (top dotted line) 95% limited of agreement

7.5 Discussion

In this prospective exploratory experiment I measured the hepatic extracellular volume fraction (ECV) using equilibrium contrast CT. The ECV was found to track liver fibrosis, measured either by collagen proportionate area or by Ishak fibrosis stage. These results are consistent with preliminary studies using animal models (17) and tentatively suggest that a CT scan using widely available equipment and contrast agents could be used to evaluate hepatic fibrosis, reducing the need for invasive biopsy.

Automated morphometric fibrosis quantification was used as the primary histologic comparator. As a continuous measurement, this largely eliminated limitations of traditional categorical staging. Data suggests CPA is a better predictor of future clinical decompensation than Ishak stage (25) and shows strong correlation with hepatic venous pressure gradient (HVPG) – a good prognostic index in relation to survival and complications (27). However CPA suffers the limitations of biopsy, with accuracy dependent on aetiology of cirrhosis and biopsy specimen size (21).

EQ-CT derived ECV was compared with a biochemical marker - the ELF test. The ELF score is a well-validated marker of hepatic fibrosis, incorporating levels of extracellular matrix components and enzymes involved in their regulation, and is a strong predictor of clinical outcome in chronic liver disease (28). Previous work has shown association between ELF score and histological fibrosis stage - confirmed by our current study. ECV correlated with ELF suggesting ECV does reflect underlying damage and fibrosis, although the strength of association was lower than with CPA. Neither ECV nor ELF suffers the limitations of histological staging and CPA, imposed by reliance on liver biopsy. It may be that their ability to sample the whole liver volume reduces sampling error and may improve repeatability. Although ELF was primarily used to test the ability of EQ-CT to assess liver fibrosis, regression analysis showed them to be

independent predictors of CPA and indeed when ELF and ECV were combined they better predicted CPA than either in isolation. The combination of two non-invasive tests to accurately predict liver fibrosis is clearly an attractive proposition and validation in a new cohort is now required.

The CT work in chapter 6 and MRI work by other authors (15,13,29) using equilibrium imaging has provided evidence for an association between elevated ECV and diffuse fibrosis in the heart. There are however limitations of EQ imaging for fibrosis assessment. The principle behind its use is that accumulation of extracellular collagenous matrix is accompanied by expansion in the extracellular water volume into which contrast agents distribute. There are however several other processes which may affect this volume and confound fibrosis measurement which may be more problematic in the liver. Oedema arising from inflammation or venous congestion for example may expand ECV, while hepatocellular swelling arising from steatosis may compress the extracellular volume. A further important point to emphasize is that the ECV measures the extracellular volume in the whole tissue; parenchyma and enclosed vasculature – i.e. both interstitial fluid and the interstitial (plasma) blood compartment. This is small in tissues such as the myocardium but much larger and potentially independently varying with disease in the liver. A further potential confounder in the liver is the vicarious uptake of contrast agents by hepatocytes seen following delayed contrast administration. This phenomenon is thought to be associated with impaired renal function, but has been described in patients with normal kidneys (31). Contrast uptake by hepatocytes and excretion via the biliary tree would lead to increased hepatic enhancement relative to blood and an overestimation of liver ECV. The lack of a discernible increase in the attenuation of bile in the gallbladder suggests that in this small group, significant vicarious excretion had not occurred following the 30 minute infusion. It should be noted that patients with significant renal impairment were excluded from

the study, thus lessening the risk of confounding the fractional hepatic ECV estimates by vicarious excretion.

I used standard CT acquisition and reconstruction techniques, which are widely available. Modern multidetector scanners and reconstruction techniques may reduce image artefacts and noise leading to more precise and accurate ECV quantitation while reducing the dose of ionizing radiation (32,33). Mean SSDE for liver EQ-CT in this study was comparable to that of a standard clinical CT examination of the liver and equivalent to 4 years of natural background radiation in the UK – background radiation dose data from Public Health England, 2011. The theoretical risk associated with this exposure (35) needs to be weighed against the sampling error and complication risks associated with biopsy and operator dependence and patient limiting factors associated with transient elastography.

The reference steady state equilibrium method used in this study involves establishing a constant plasma concentration of contrast via a prolonged infusion. Although time consuming and somewhat impractical, it was, at the time of study design, considered the most robust methodology. A further limitation of the infusion technique is the relatively low level of enhancement with the aorta and liver during the delayed equilibrium phase. Even with large ROIs, the contrast to noise ratio at this level of enhancement is relatively low. More recently validated equilibrium MRI contrast protocols employ a bolus only method (36), which for tissues with rapid kinetics such as the myocardium produces a dynamic equilibrium of changing but related plasma/interstitial contrast concentrations. This dynamic steady state may allow ECV estimation of sufficient accuracy to replace less practicable protocols using prolonged infusions, and is explored in chapter 8. By using a bolus/infusion technique I ensured contrast equilibrium within the liver. Simple integration of whole liver ECV quantitation into clinical CT, supplementing anatomical assessment and

focal lesion detection is clearly desirable and a future study is now indicated.

There were additional limitations to this experiment. Patient selection resulted in a relatively high proportion of patients with mild fibrosis - 70% of our patient cohort had CPA values clustered between 2 and 8.1. Future studies should endeavour to recruit a patient cohort equally distributed across the range of fibrosis severity. I used a uniform aetiology of viral induced hepatitis to ensure homogeneity in our data. However we cannot assume the results can be extrapolated to other aetiologies such as alcohol or steatosis.

As noted above, factors thought to affect hepatic extracellular volume fraction such as hepatic inflammation, steatosis, hepatic venous congestion and portal venous flow were not controlled for in this study, and future studies may examine the influence of these confounders on hepatic ECV.

Although comparison is made here with the current reference standard of histology, other techniques have shown strong association with clinical markers of liver cirrhosis, and were not included. HVPG and transient elastography are both well validated against histology and are predictive of decompensation and portal-hypertension related complications (37). Future studies should include comparison of ECV with liver stiffness measurement and HVPG.

This study provides biopsy-controlled evidence for a relationship between extracellular volume and diffuse liver fibrosis in man; and provides basis for a larger study to examine the diagnostic performance of EQ imaging for non-invasive monitoring of liver disease severity. Combination of two non-invasive tests (EQ-CT ECV and ELF) to accurately predict liver fibrosis is potentially very powerful and validation studies are now indicated.

8 DYNAMIC CONTRAST EQUILIBRIUM COMPUTED TOMOGRAPHY FOR MYOCARDIAL EXTRACELLULAR VOLUME MEASUREMENT

8.1 Author declaration

The work contained in this chapter was completed by the author (in partnership with Dr Thomas Treibel Cardiology Fellow - UCLH) including the pseudo-equilibrium protocol design; volunteer recruitment; CT image data acquisition; and data analysis. Statistical analysis and graphs were prepared by Dr Treibel. Primary supervisors were Prof. Stuart Taylor and Prof. James Moon. The intention was for the author to jointly lead publication with Dr. Treibel, however this was not allowed by the accepting journal: Treibel, T. A., Bandula, S., Fontana, M., White, S. K., Gilbertson, J. a., Herrey, A. S., Moon, J. C. (2015). Extracellular volume quantification by dynamic equilibrium cardiac computed tomography in cardiac amyloidosis. Journal of Cardiovascular Computed Tomography, 9(6), 585–92. doi:10.1016/j.jcct.2015.07.001

8.2 Introduction

The experiment in this chapter was designed to simplify the steady state equilibrium contrast CT method developed in chapter 6, by using a bolus-only approach (DynEQ-CT) and apply it to an important clinical problem: the non-invasive diagnosis and quantification of cardiac amyloid burden. As laid out in chapter 6, the steady state protocol was designed to allow sufficient time for equilisation of plasma/interstitial contrast concentrations (static equilibrium) – thereby eliminating the effects of contrast kinetics and

allowing robust ECV estimation. The required prolonged contrast infusion was however time consuming - a hurdle to clinical implementation. However in tissues like the myocardium and liver where diffusion kinetics are rapid, the concentration of contrast within the plasma and interstitium following a contrast bolus are changing, but have a fixed relationship – ie are in dynamic equilibrium. The objectives in this chapter were to evaluate the feasibility and optimal contrast timing for dynamic equilibrium with iodinated contrast; to assess the ability of DynEQ-CT to quantify myocardial amyloid against conventional semi-quantitative methods (bone scintingraphy) (1) and compare against ECV quantification by EQ-CMR as the current imaging standard of reference.

8.3 Materials and Methods

All research was carried out at University College London Hospital and the Royal Free NHS Trusts, London, UK, between January 2013 and December 2013. All subjects gave written informed consent to participate in the study. A total of 53 patients were recruited: 26 with systemic amyloidosis (ATTR and AL) and 27 comparator controls with aortic stenosis (23 of these patients were described in the experiment in chapter 6) in whom amyloid could be histologically excluded.

Exclusion criteria were uncontrolled arrhythmia, impaired renal function (estimated glomerular filtration rate <60 mL/min), or contraindications to MR imaging (e.g., implanted devices).

ATTR amyloid patients. Eighteen patients had ATTR amyloidosis (16 male, age 68 +/- 8 years). All patients underwent sequencing of exons 2, 3, and 4 of the *TTR* gene: 14 had senile systemic amyloid (SSA) and four TTR patients were familial (V122I [n = 1], V30M [n = 1], E54G [n = 2]). Cardiac status (cardiac involvement, possible cardiac involvement, no cardiac involvement) was determined by myocardial biopsy or DPD scintigraphy (see chapter 3.6). Cardiac retention of 99mTc-DPD was visually scored as: Grade 0: no myocardial uptake; Grade 1: mild cardiac

uptake with no significant attenuation of normal bony uptake; Grade 2: moderate cardiac uptake with some attenuation of the bone signal; Grade 3: strong cardiac uptake with little or no bone uptake.

AL amyloid patients. Eight patients (5 male, age 56 +/- 12 years) had biopsy proven systemic AL amyloid with biopsies from the myocardium or other tissues. Cardiac categorization was performed by Dr. Treibel based on modified international consensus criteria (2) defined as:

1) definite cardiac involvement: LV wall thickness of >12 mm in the absence of any other known cause or RV free wall thickening coexisting with LV thickening in the absence of systemic or pulmonary hypertension;
2) possible cardiac involvement: LV wall thickening in the presence of hypertension; RV thickening in the presence of pulmonary hypertension or normal wall thickness with diastolic dysfunction and raised serum bio-markers;
3) no suspected involvement: normal wall thickness with normal serum biomarkers.

All amyloid patients underwent DynEQ-CT and EQ-MRI as described in the following section. The 2:1 recruitment of ATTR s AL patients reflected a significant prevalence of eGFR <60 (cut-off point requested by the ethics committee for this study) in the AL cohort.

Comparator group. In twenty-seven patients with severe aortic stenosis (19 male, age 68 +/- 8 years) cardiac amyloid was excluded histologically on myocardial biopsy taken during aortic valve surgery as part of the study described in chapter 6. These patients also then underwent DynEQ-CT (n=27) and EQ-CMR (n=22 due to 7 patients suffering claustrophobia and 15 with pacemakers).

DynEQ-CT protocol. Imaging examinations were performed by using a 64–detector row CT scanner (Somatom Sensation 64; Siemens Medical Solutions, Erlangen, Germany). To limit radiation exposure, a topogram was used to plan CT volumes of the lower chest from the level of the aortic valve to just below the inferior aspect of the heart. Cardiac scans (tube

voltage, 120 kV; tube current–time product, 160 mAs; section collimation, 64 detector rows and 1.2-mm section thickness; gantry rotation time, 330 msec) were acquired with prospective electrocardiographic gating (65%–75% of the R-R interval). The proprietary dose modulation function (CareDose; Siemens Medical Solutions) was switched off so pre and post contrast scans were identical for ECV calculation. CT datasets were reconstructed into 3-mm-thick axial sections with a B20f kernel.

The DynEQ-CT protocol was consisted of three steps: firstly, dynamic equilibration achieved by delayed post-bolus measurement to remove the effect of contrast kinetics; secondly, measuring the ratio of tissue and blood CT attenuation change measured in Hounsfield units (ΔHU); thirdly, direct measurement of the blood volume of contrast distribution. CT-ECV was calculated as: $ECV = (1\text{-Haematocrit}) \times (\Delta HU_{tissue} / \Delta HU_{blood})$

Optimal timing of the post contrast scan was unknown: too early and equilibrium may not have occurred; too late and the signal to noise ratio may have been poor. Accordingly, imaging was performed at pre- and at 5- and 15-minutes following a bolus of Iodixanol (652mg/mL) at a dose of 1mL/kg, in order to establish the best timing of post contrast imaging. An additional scan at 1-minute was introduced in the amyloid cohort to aid segmentation of blood and myocardium which was not easily visible at the later time points. Radiation exposure was derived from the dose-length product multiplied by a chest conversion coefficient (κ=0.014mSv/mGy) (10).

EQ-CMR protocol. EQ-CMR was performed either after or at least 24 hours prior to the CT to allow enough time for gadolinium contrast to be cleared and not act as a CT contrast agent. Standard EQ-CMR examinations were performed in all patients using a 1.5-T scanner (Avanto; Siemens Medical Imaging, Erlangen, Germany) using the contrast protocol described in chapter 5, with T1 mapping for CMR ECV quantification performed using ShMOLLI (Shortened Modified Look-Locker Inversion recovery) (11), providing single-section T1 map in one breath hold. Images were acquired at positions visually matched by the operator

(Cardiology Fellow - Dr. Thomas Treibel or Steve White) before and during contrast material equilibrium – Figure 8.1. Standard CMR inversion recovery late gadolinium enhancement was included in the protocol to exclude focal myocardial fibrosis. Signal-to-noise ratios (SNR) was measured in ROIs on 3 sequential transverse images in the myocardial septum as the ratio of the average signal intensity (SI) to the standard deviation of the SI. Background image noise was not measured as this was reduced automatically by scanner system.

The CMR-ECV was calculated by:

$ECV = (1–haematocrit) \times (1/\Delta T1_{tissue}) / (1/\Delta T1_{blood})$.

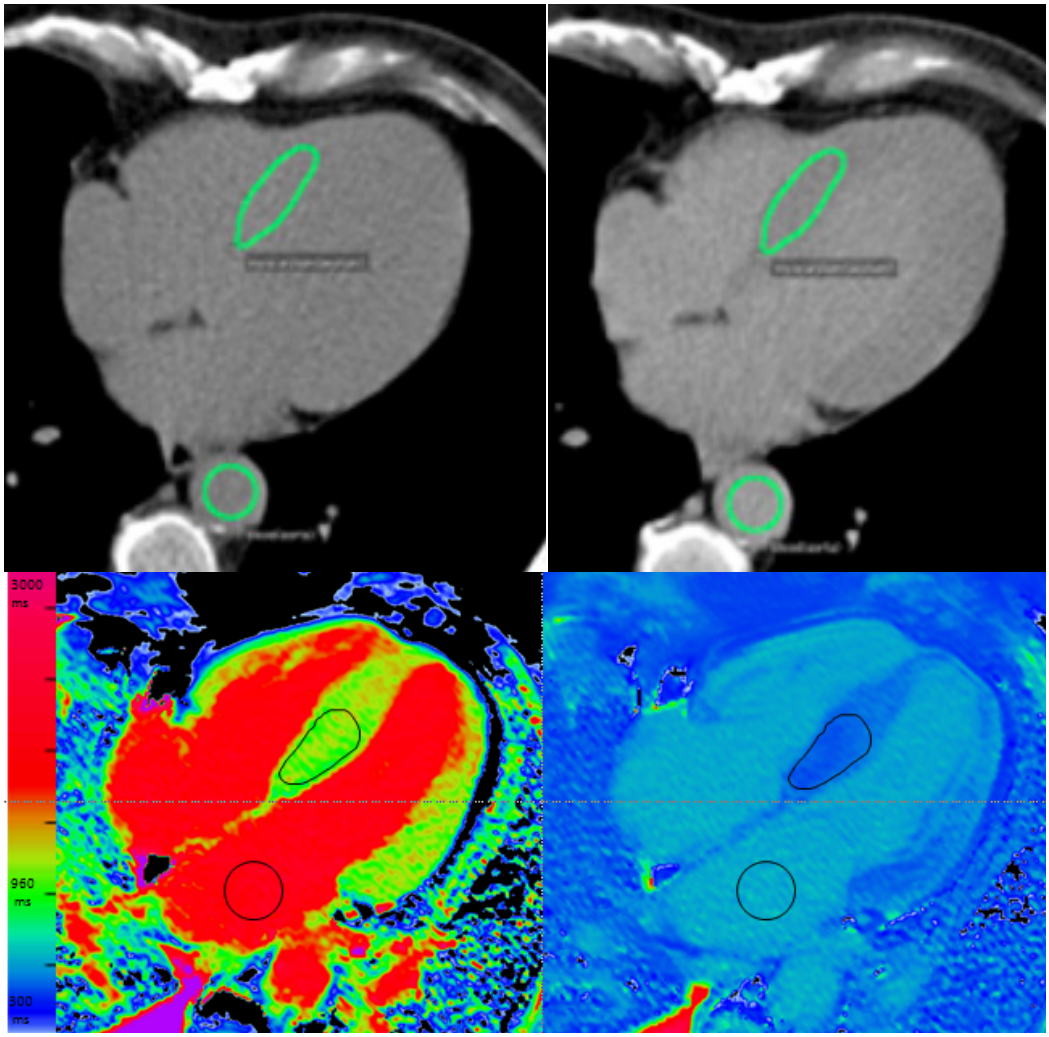

Figure 8.1 Example EQ-MRI and EQ-CT imaging

Examples of ROIs in ShMOLLI (bottom row) and CT (top row); pre-contrast (left) and post-contrast (right) with ROIs drawn in the basal septum and blood pool.

.

8.4 Results

8.4.1 DynEQ-CT ECV

Comparison of the SNR at the individual time points (pre contrast, 5 and 15 minutes following contrast) showed that the highest SNR was achieved at 5 minutes post contrast ($p<0.001$; paired sample T-Test, Figure 8.2).

The mean total calculated effective radiation dose for the complete DynEQ-CT protocol (including both post contrast time points) was 1.56 mSv ± 0.58 mSv, with a mean administered total Iodixanol (Visipaque) volume of 78 mL ± 11 mL

In the systemic amyloid group, ECV at 5min by DynEQ-CT showed a strong and significant correlation with that derived using CMR (r^2 = 0.73, *p<0.001*), which worsened at 15 minutes (r^2 = 0.55 at 15 minutes *p<0.001*; Figure 8.4).

Bland-Altman comparisons of ECV measurement methods by EQ-CMR and DynEQ-CT in the amyloid group demonstrated no bias at 5 minutes post contrast, with slight bias at 15 minutes (4% with no slope), but the confidence limits were twice as wide at 15 minutes (95% confidence limits: -19%, 28%; Figure 8.5).

8.4.2 Diagnosis of cardiac amyloid by ECV

Myocardial ECV by CT was significant higher in patients with amyloidosis than aortic stenosis (0.48 +/- 0.15 versus 0.28 +/- 0.04, *p<0.001*; Figure 8.3). The difference in ECV between AL and TTR amyloid only reached significance with DynEQ-CT at 5 minutes (0.42 +/- 0.11 versus 0.53 +/- 0.13, *p<0.04*) - Figure 8.4. In ATTR amyloid, all patients had at least Grade 1 uptake on DPD. ECV by EQ-CT tracked amyloid burden semi-quantitatively measured by DPD bone scintigraphy (p<0.001) – see Figure 8.6.

.

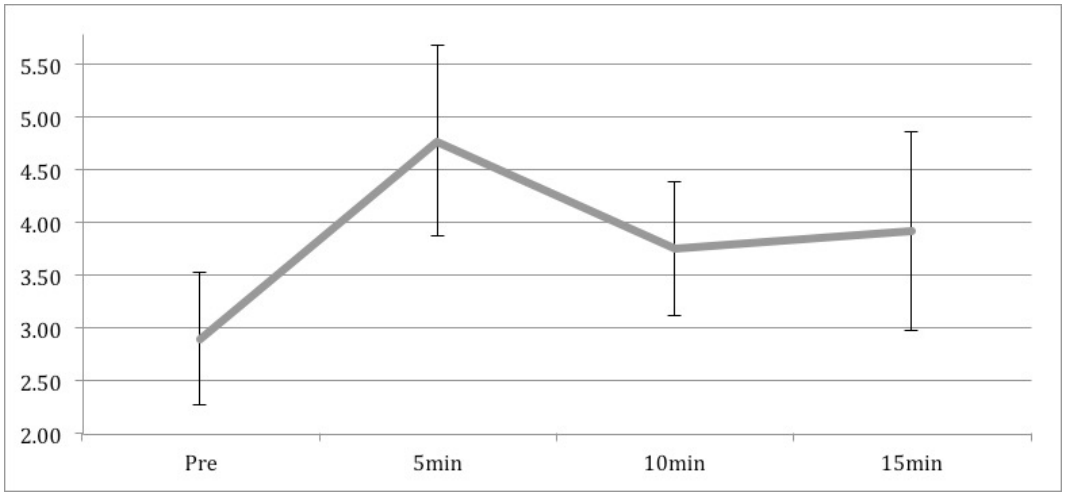

Figure 8.2 Image Signal to Noise Ratio at 4 time points

Signal-to-Noise ratio pre-contrast, at 5 minutes, 10 minutes and 15 minutes post contrast for regions of interest drawn in the myocardium (with standard deviations).

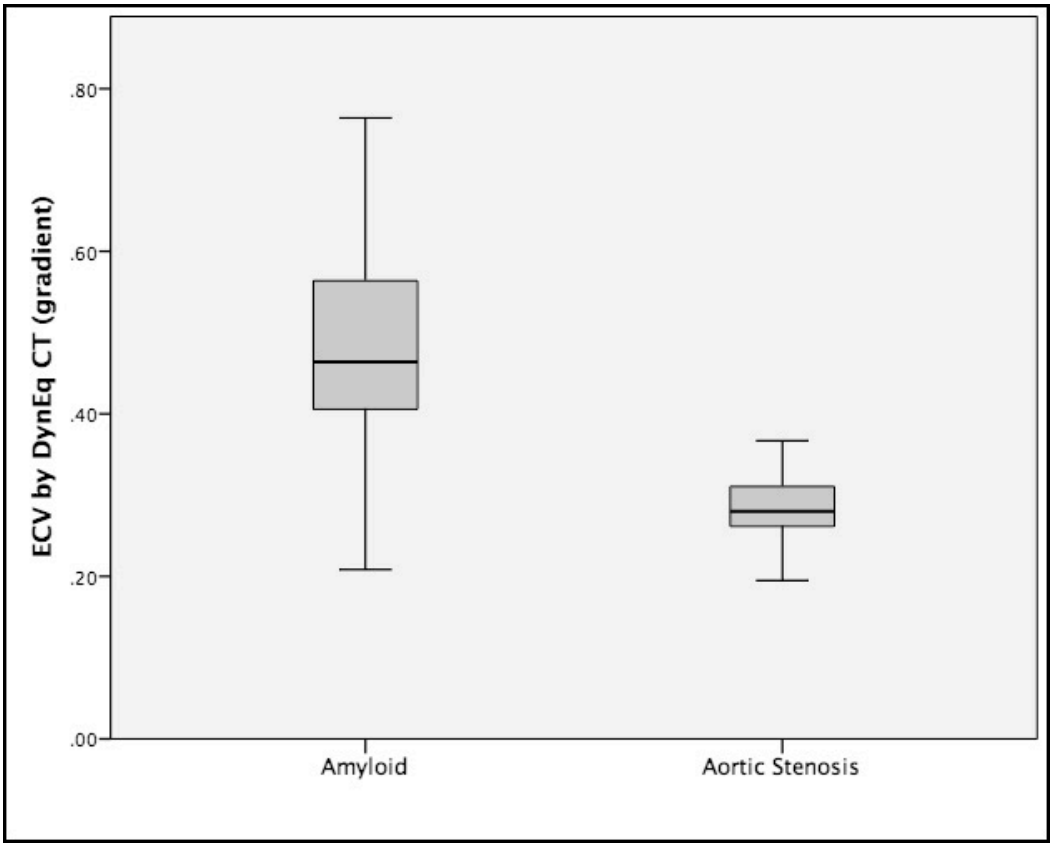

Figure 8.3 Myocardial ECV by DynEQ CT

Myocardial ECV by CT was significant higher in patients with amyloidosis than aortic stenosis (0.48 +/- 0.15 versus 0.28 +/- 0.04, p<0.001).

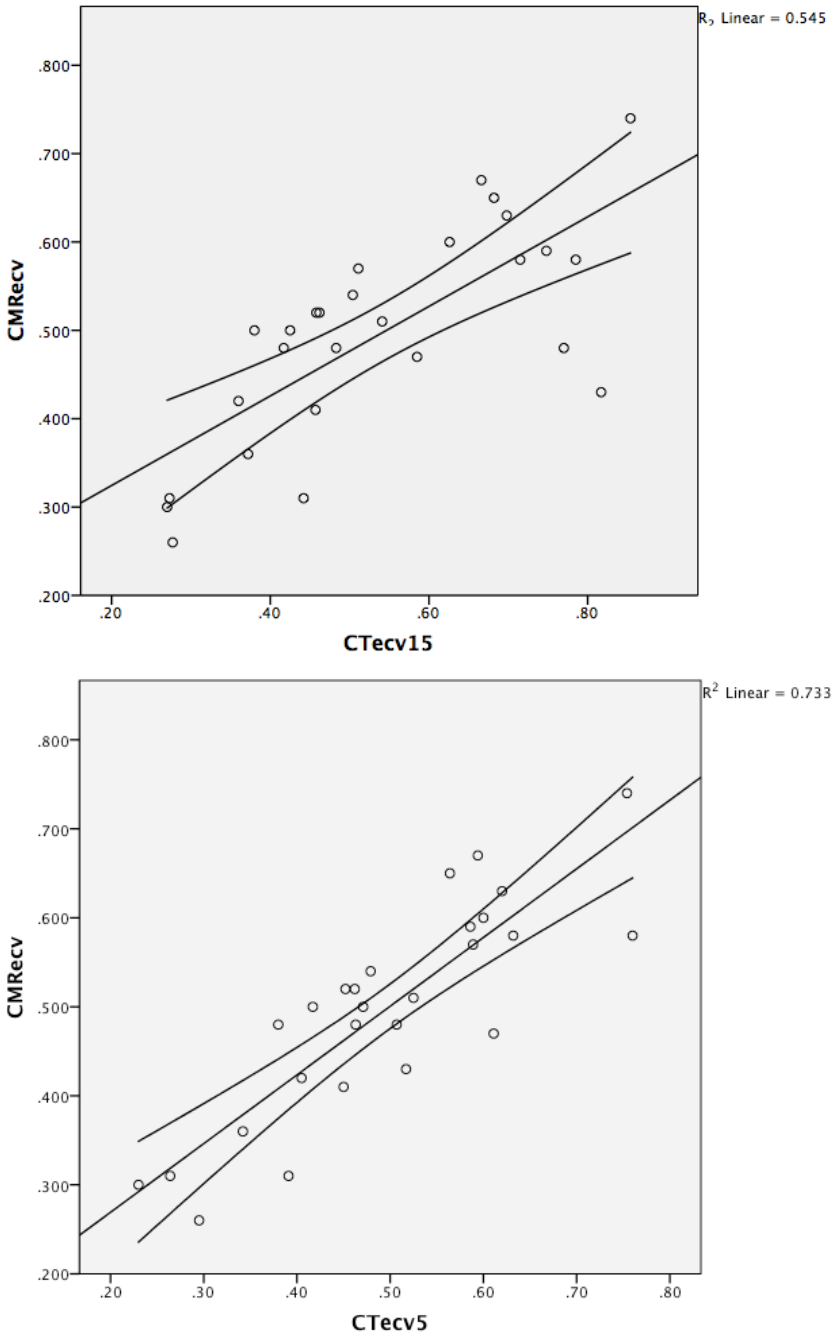

Figure 8.4 Correlations CMR ECV vs CT ECV

Association between myocardial ECV measured using EQ-CMR and EQ-CT in systemic amyloidosis. Top uses 5 minute and bottom uses 15 minute post contrast EQ-CT phase images for ECV estimation.

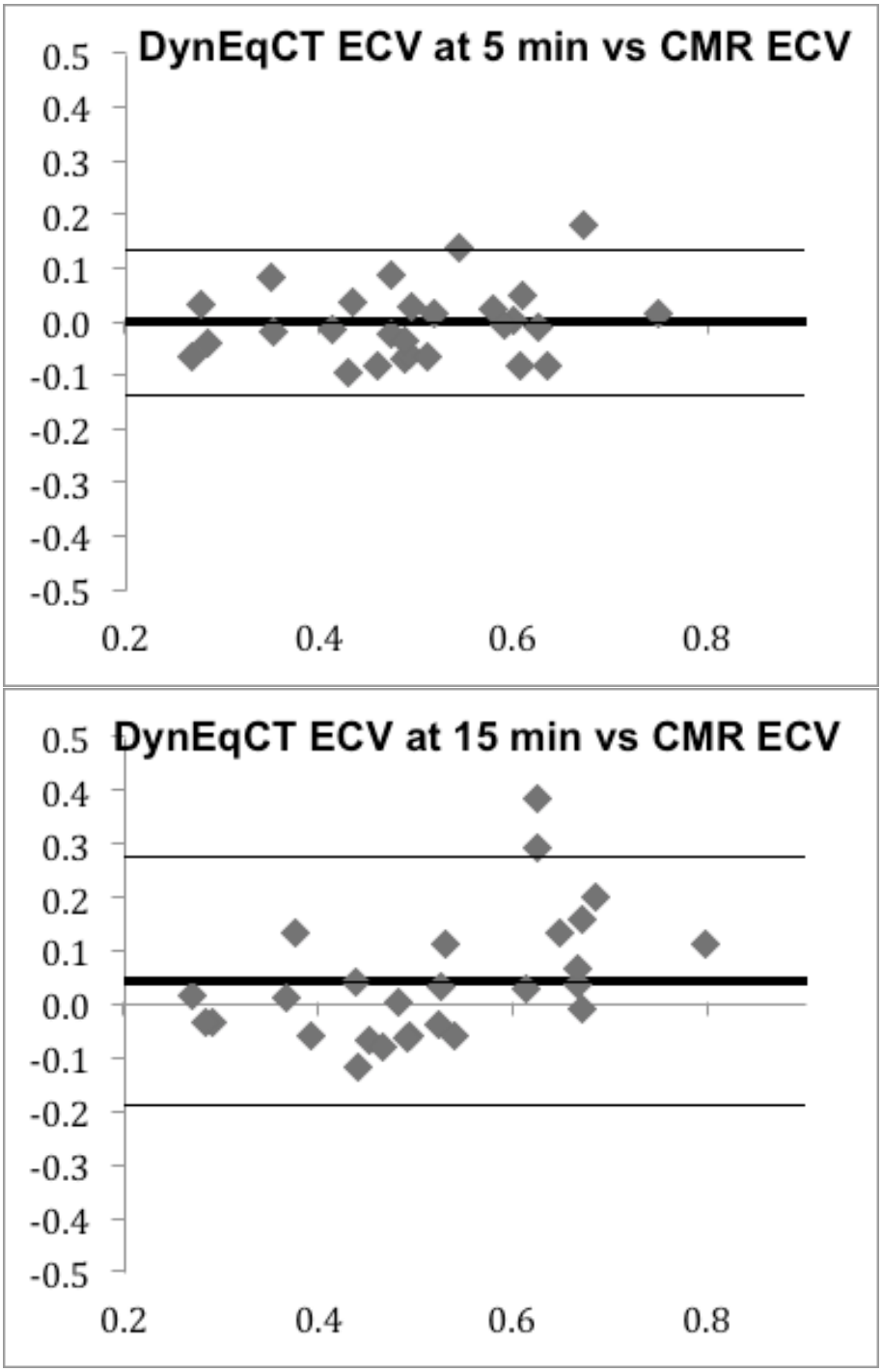

Figure 8.5 Bland-Altman analysis of EQ-CT at 5 and 15 mins

Bland-Altman comparisons of myocardial ECV measurement method in systemic amyloidosis shows ECV difference expressed as a percentage, calculated by subtracting ECV measured with DynEq-CT from ECV measured with EQ-CMR) against mean ECV (solid thick line), with lower (bottom thin line) and upper (top thin line) 95% limits of agreement.

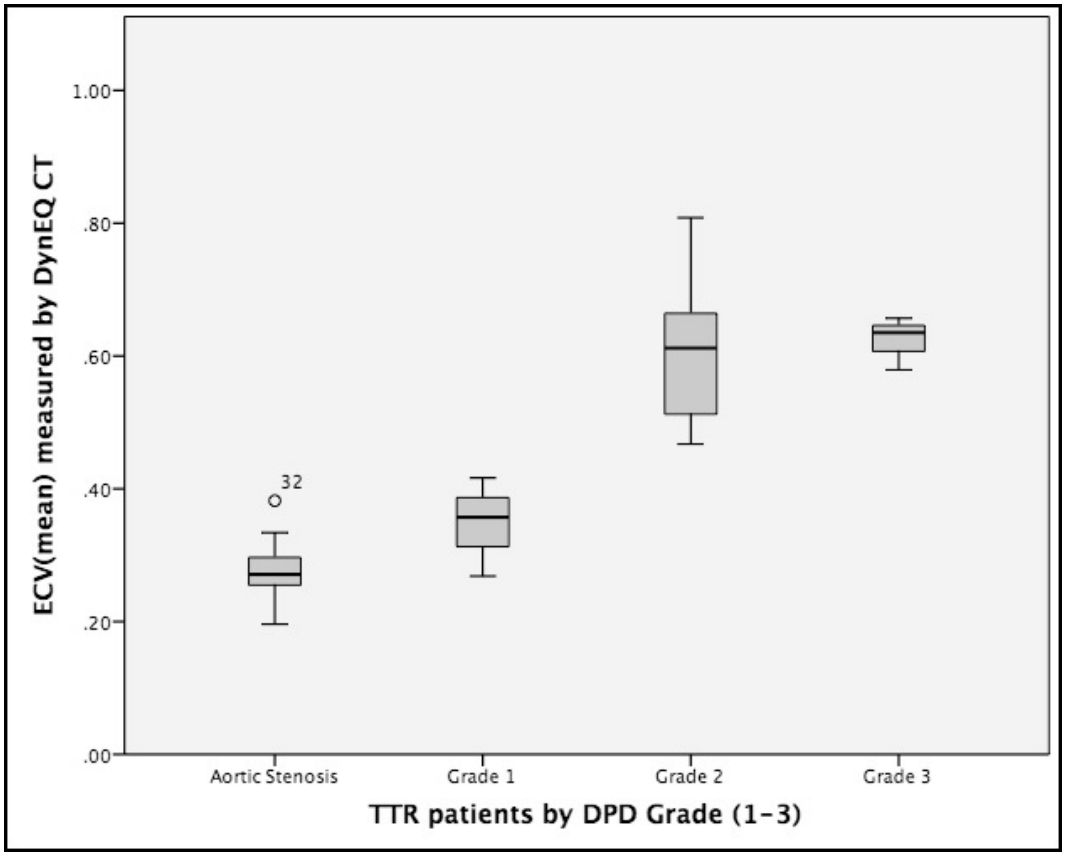

Figure 8.6 ECV vs DPD grade

ECV vs DPD grade (aortic stenosis cohort used as control – no evidence of cardiac involvement on intra-operative myocardial biopsy).

8.5 Discussion

The work in this chapter has showed that a simple 5-minute, gated three phase CT protocol can diagnose cardiac amyloid burden and track disease severity. This new more rapid protocol can simply be added to routine CT coronary angiography protocols with only a minimal increase in radiation (equivalent of repeating the pre-contrast coronary calcium score

scan), but offer a new insight into the myocardial interstitium and is informative for an under-diagnosed and now treatable cause of LVH and heart failure: cardiac amyloidosis.

The steady state protocol developed in chapter 6 using a primed infusion to reach contrast equilibrium was logistically cumbersome and time consuming, therefore development of a bolus-only approach brings ECV, as a promising novel biomarker, a step closer to routine clinical applicability.

As part of the technical development, I established that acquisition of the post contrast images at 5 minutes was superior to acquisition at 15 minutes, resulting in the better signal-to-noise, contrast-to-noise ratios, and higher DynEQ-CT ECV correlation with ECV by CMR. Peculiar to cardiac amyloid with an extremely high ECV, is the lack visible interface between myocardium and blood even in post contrast images at 5 minutes, as the ECV in myocardium equals that of the blood. This necessitated the addition of a low dose, early arterial phase scan to facilitate blood myocardial segmentation. The overall radiation dose for this scan was within acceptable limits and lower than the conventionally used DPD scintigraphy.

From a diagnostic perspective, myocardial ECV by DynEQ-CT was higher in patients with cardiac amyloidosis than the comparator group with LVH due to AS. Furthermore, ECV by CT tracked established markers of cardiac amyloid severity as measured by DPD scintigraphy (ATTR patients only).

In this study, the DynEQ-CT technique was compared to the best, currently available non-invasive techniques for the quantification of ECV (EQ-CMR) and TTR amyloid burden (DPD scintigraphy), but no invasive biopsy data was available for this validation, though with the patchy distribution of cardiac amyloid deposits, biopsy data may not be superior.

The data presented here is from a small study in a single specialised centre, aimed to be hypothesis generating, and a larger study is required

to test these and develop this test further. The 64-slice-CT-system employed may reflect the most commonly available systems available, but does not take advantage of the newer systems that offer a variety of iterative reconstruction algorithms, dual energy acquisition and larger detector arrays that allow acquisition of isotropic volumes of the entire heart in one heart beat and at low radiation dose. In conjunction with 3D image registration and processing, this allows creation of whole heart ECV maps.

8.6 Conclusion

A simple 5-minute, gated, contrast-enhanced CT scan can diagnose cardiac amyloid burden, track disease severity and distinguish cardiac amyloid from aortic stenosis, another cause of LV hypertrophy. DynEQ-CT is able to quantify interstitial expansion in the heart, and offers to be a simple, technique to diagnose amyloidosis, because it is ubiquitously available, cheaper and faster than MRI and an alternative for patients with claustrophobia or metallic implants.

9 QUANTITATIVE COMPUTED TOMOGRAPHY

9.1 Author declaration

The experiments presented in this chapter were performed, and the data analysed and presented by the author under the supervision of Dr. Shonit Punwani and Prof. Stuart Taylor.

9.2 Introduction

The EQ-CT technique described in chapters 6, 7 and 8 is reliant on accurate and precise attenuation measurement. Computed tomography development has however focused on delivering high image quality and fast processing, allowing rapid and accurate diagnosis of disease. Other clinical quantitative CT techniques have been slow to implementation compared with other modalities such as MRI and PET, largely as a result of the concerns about radiation dose exposure, but CT HU measurement is now routinely used in clinical practice to assess suitability of renal stones for extracorporeal treatment (1), to evaluate adrenal nodules (2) and to evaluate the composition of body fluids.

Quantitative tissue characterisation using computed tomography relies on accurate representation of tissue properties within the created image. By measuring the attenuation of a rotating X-ray beam, CT scanners produce an image map of Hounsfield Units (CT number) – a linear transformation of the linear attenuation coefficient; in which distilled water at standard pressure and temperature is assigned a value of zero Hounsfield units (HU), while air a value of 1000HU (3).

$HU = 1000 \times (\mu - \mu_{water} / \mu_{water})$.

The exact relationship between imaged material and CT number is complex. Firstly attenuation is dependent on the incident photon energy, although CT systems utilise a polychromatic spectrum of X-ray energies with operator variable effective energy. Photon energies are subject to both photoelectric (pe) and Compton (c) interactions, and the total attenuation coefficient (μ) is the sum of these effects i.e. $\mu = \mu_{pe} + \mu_c$, with μ_{pe} strongly dependent on atomic number as well as electron density. Reconstructed CT number values are also dependent on reconstruction kernel and post-processing filters. Failure of the reconstruction process leads to image artefacts and error in affected areas of the map. Artefacts can also result from a number of physics, geometric, patient and processing effects. In addition, the obligation to minimise ionising radiation exposure results in a level of noise within the image data known as quantum mottle and a degree of uncertainly in CT number that cannot be overcome by technological refinement.

Initial development of equilibrium CT involved quantifying attenuation within tissue from scan data. During the analysis, significant unexpected variations in CT number were noted which did not correspond to anatomical structures or pathological processed. In this chapter, these effects are investigated with descriptive and quantitative evaluation (4).

The hypothesis explored in this chapter is that unexpected variations in measured CT number are due to system artefacts; and application of advanced methods to reduce artefacts will lead to a reduction in this variation.

9.3 Method

To understand the artefacts underlying unexpected attenuation variations in CT scan data, 25 EQ-CT datasets acquired using scanner A (table 9.2) as part of experiments in chapter 8 were analysed. Mean (+SD) attenuation was measured within the whole imaged descending thoracic

and abdominal aorta at equilibrium contrast phase using the open source image analysis tool Osirix (OsiriX v4.1.2; OsiriX Foundation, Geneva, Switzerland). Elliptical regions of interest were drawn so as to incorporate the maximum area of blood, but avoid aortic wall atherosclerotic plaque or calcifications. Intra-slice attenuation statistical variance was compared with the variance of attenuation values between slices. Mean attenuation was plotted against slice number for each scan (Figure 9.1) and the mean and standard deviation (SD) attenuation for the whole segmented blood pool volume was calculated (as the ROI area within each slice was equal and the same number of slices sampled; a pooled standard deviation could be calculated).

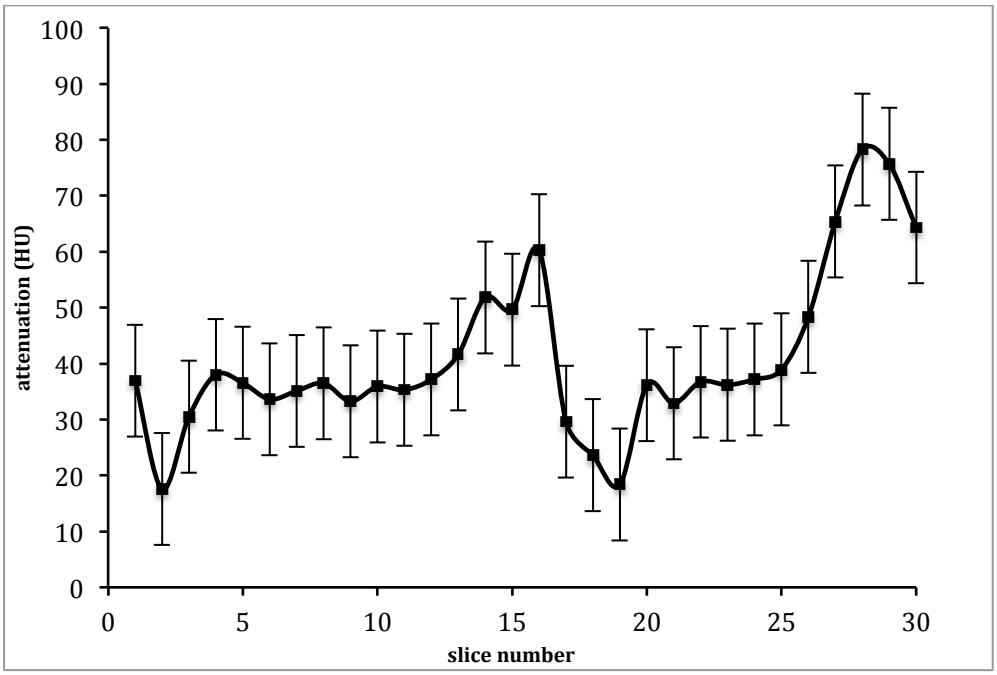

Figure 9.1 EQ-CT Blood attenuation measured within sequential slices

Example of attenuation (mean + SD) drawn within the aorta from thorax to abdomen within scan acquired using scanner A. The diaphragm lies between slice 12 and 24.

Instances where slice attenuation varied by greater that 2 standard deviations from the scan mean were identified. Individual instances could involve multiple slices, as long as affected slices were consecutive.

Artefact images were subjectively analysed by the thesis author and the type of artefact categorised as beam hardening; metal; motion; or helical interpolation (5). These are and listed below and discussed further in later sections:

1. Beam Hardening. Mean beam photon energy increases due to absorption of low energy photons as the beam passes through an object. This can lead to so-called cupping artefacts as central parts of the beam are hardened more that than those passing through the edges; and streaks and bands caused by variations in beam hardening occurring with CT tube position.

2. Metal: Metal density is beyond the normal range that can be handled by the reconstruction method, resulting in incomplete attenuation profiles, and severe streaking.

3. Motion: Misregistration caused by motion produced shading, streaks and image ‘smearing’.

4. Helical interpolation: This is caused by mutidetector scanners operating at higher pitch. Several rows of detectors intersect the plane of reconstruction during each rotation. The result is a windmill-like spiral artefact, with increasing vanes at higher pitch.

For comparison, equilibrium contrast phase data from a further new cohort of 30 EQ-CT patient scans acquired using a more recent CT system implementing the latest reconstruction and data correction methods (scanner B – Table 9.2) were analysed using the same methodology. As in previous chapters, these patients were recruited from the outpatient clinic at the national amyloid centre, with a histological or imaging diagnosis of either AL or ATTR amyloidosis (see Table 9.3). Exclusion criteria included an estimated glomerular filtration rate of less than 45ml/min and allergy to iodinate contrast agents. All patients provided written informed consent.

	Scanner A	Scanner B
Model release date	2004	2010
CT generation	3rd	3rd
No. slices	64	320
Imaging reconstruction	Filtered back projection	Iterative (AIDR)
Corrections	None	Beam hardening

Table 9.2 CT scanner specifications

Summary of technical specifications of CT scanners used in this chapter

	Total
Patient number (%)	30 (20M/10F)
age (y) mean	65.6 (63.3M/65.8F)
age (y) range	43-83
Amyloid AL/ATTR	20/10

Table 9.3 Demographic data – comparison amyloid cohort

Summary of amyloid patient demographic and clinical data. Values are mean +/- SD

To investigate the specific effect of improved reconstruction on beam hardening artefacts, a beam hardening algorithm and iterative algorithm at 3 levels (low, medium and high) were separately applied to a sample of 6 clinical scans of the chest and abdomen; 3 acquired and reconstructed using scanner A and 3 using and scanner B; in addition to filtered back projection reconstruction. ROI analysis of blood attenuation within the aorta was performed as described in the earlier part of this methods section.

9.4 Results

Data from Cohort 1 scanned using scanner A contained 25 patients (21 men, 4 women; median age, 65 years; range, 41-87 years); and Cohort 2 using scanner B contained 30 patients (11 men, 19 women; median age, 74 years; range, 49-85 years). The pooled SD for scanner A was 7.50 and scanner B was 5.28 [P<0.0001] – see Figure 9.4.

Evaluation of the 55 equilibrium scans demonstrated 20 instances from scanner A and 5 instances from scanner B where EQ phase blood pool attenuation varied by greater than 2 standard deviations. These instances had a mean magnitude of 32HU (range 22-78HU). Subjective evaluation of the causes of the artefacts with frequencies are summarised in Table 9.5.

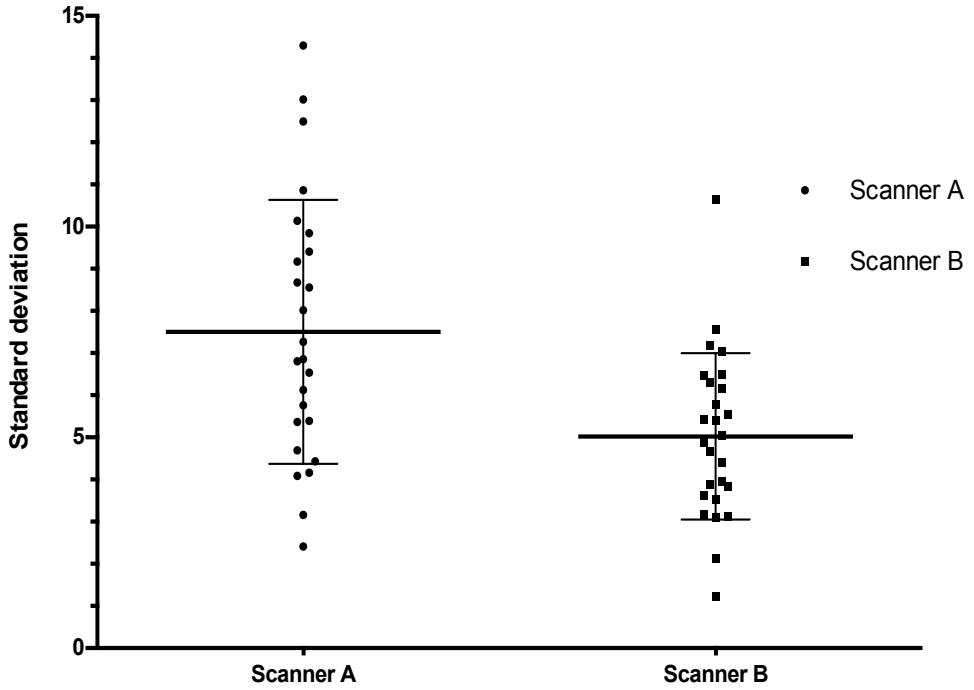

Figure 9.4 Scatter plot of blood attenuation SD

Scatter plot of scan EQ-CT blood pool standard deviation measured within patient cohorts scanned using scanner A and B. Horizontal lines indicate mean and standard deviation.

Artefact	Frequency in cohort A	Frequency in cohort B	Total
Beam hardening artefact	10	3	13
Motion artefact	7	1	8
Metal artefact	3	1	4
Helical interpolation	0	0	0
Total			25

Table 9.5 Summary of artefacts

Summary of the type and frequency of artefacts resulting in attenuation variation of 2 standard deviations of more from mean aortic blood attenuation.

Beam hardening effects were the most common artefacts seen within both datasets; with a total of 13 occurrences. These were caused by areas of increased density within the scan volume, related to: aortic wall calcification (4); vertebral osteophytes (3); dense vertebral end plates (2) and contrast that had pooled within the renal pelvis (2). In 2 cases, an underlying anatomical source of the artefact was not identified. The resulting bright and dark bands projected over the aorta resulted in significant attenuation variation.

Motion artefacts were seen around the diaphragm in 8 cases, causing image blurring and a reduction in CT number in the upper abdominal and lower thoracic region – Figure 9.6 Figure 9.7.

Metal artefact was seen in 4 cases relating to pacemaker wires.

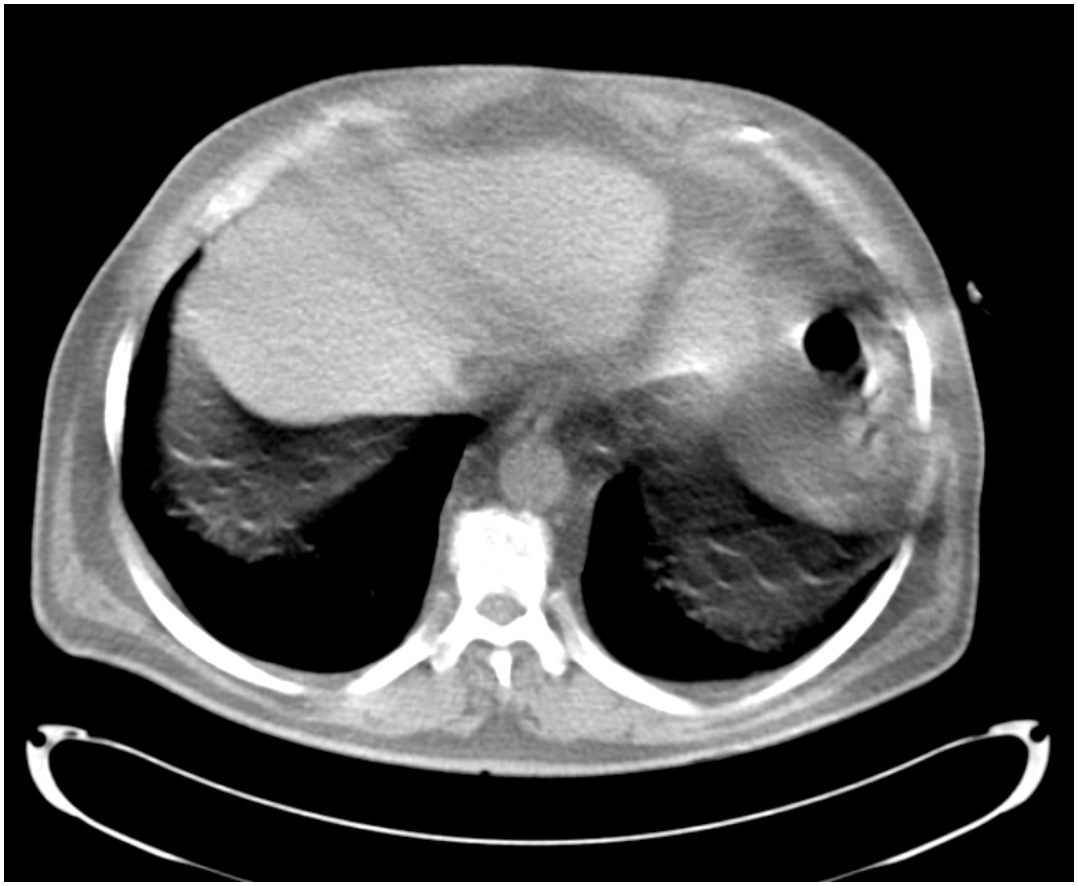

Figure 9.6 Example CT image showing motion artefact

Motion artefact caused by motion of the diaphragm during the scan acquisition. The image has been windowed to allow visualisation of the blurred lung as well as upper abdominal structures. A thick artefactual band of decreased attenuation is projected across the aorta and liver.

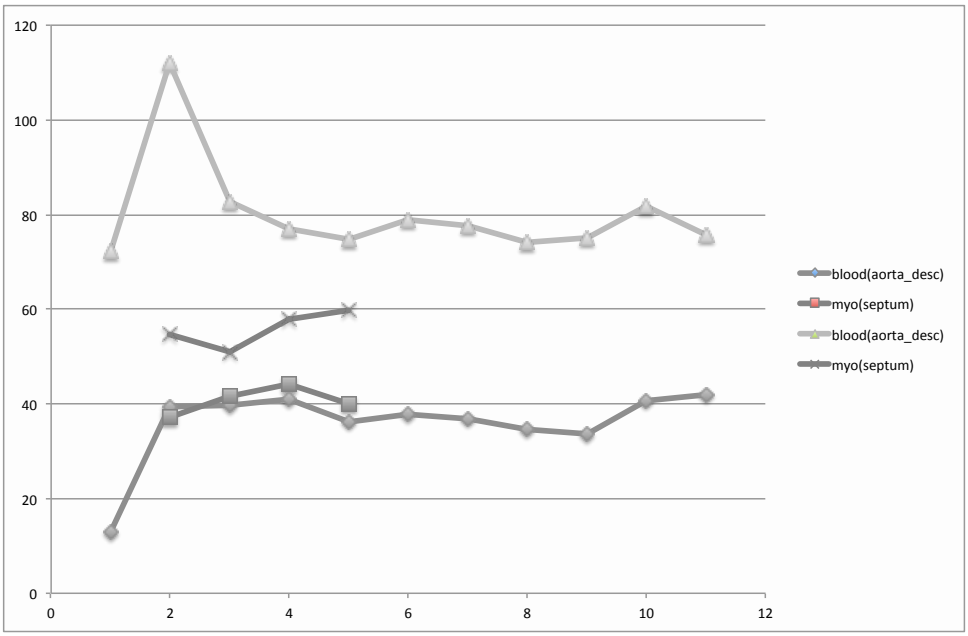

Figure 9.7 Variation in attenuation within an example EQ-CT dataset

Example of variation in CT Hounsfield number. Attenuation measured within structures within the thorax, before and after equilibrium contrast. The X-axis represents slice number, moving cranially from the level of the diaphragm; and Y-axis CT number. Around the diaphragm (slice 1-4), motion artefact results in streaks of decreased attenuation on the pre-contrast phase and increased attenuation on the post contrast images. Pre contrast aorta and myocardium are given in blue and red; and post contrast in green and purple.

9.4.1 Beam Hardening

Beam hardening is seen with polychromatic X-ray sources such as that used in CT and can produce dark streaks around high attenuation objects (5) – Figure 9.8Figure 9.9; Figure 9.10Figure 9.11Figure 9.12. As X-rays pass through the body, low energy photos are attenuated more easily by dense structures, leaving high-energy photos, which are not attenuated as easily. Beam transmission then does not follow simple exponential decay as seen with monochromatic sources. High-energy attenuation is primarily due to Compton scatter, which causes X-ray photons to change direction (and energy) and thus end up in at a different detector. High pass filters used in FBP also exaggerates difference between adjacent detectors producing bright streaks in other directions. Evaluation of the attenuation

plot within the aorta within several scans revealed small periodic areas of reduced attenuation, which coincided with vertebral endplates (most marked when an endplate was also associates with dense osteophytes) and with aortic wall calcification.

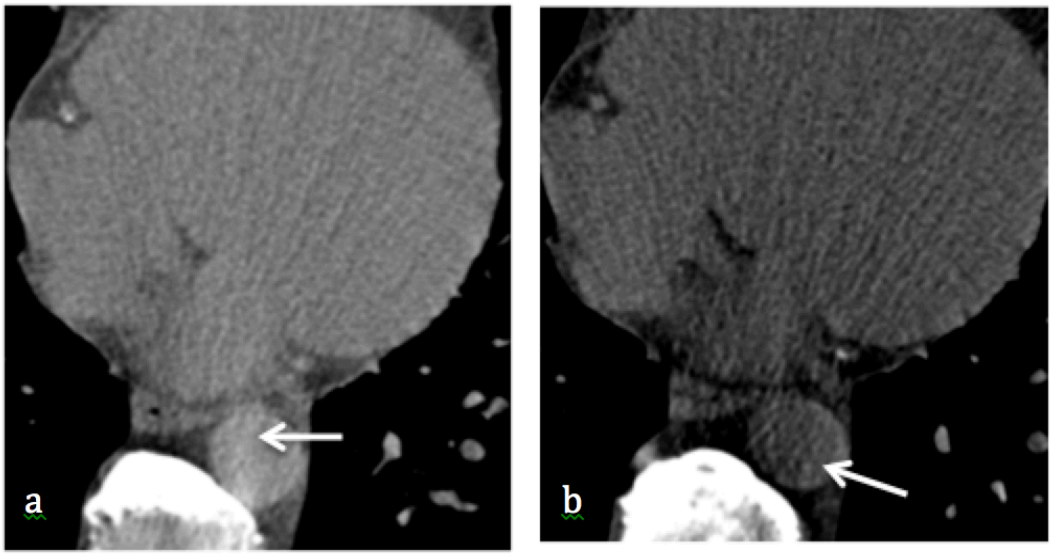

Figure 9.8 Example CT images showing beam hardening effects

An example of beam hardening caused by dense vertebral osteophytes causing a bright streak through axial image (a) and a dark streak through the image (b)

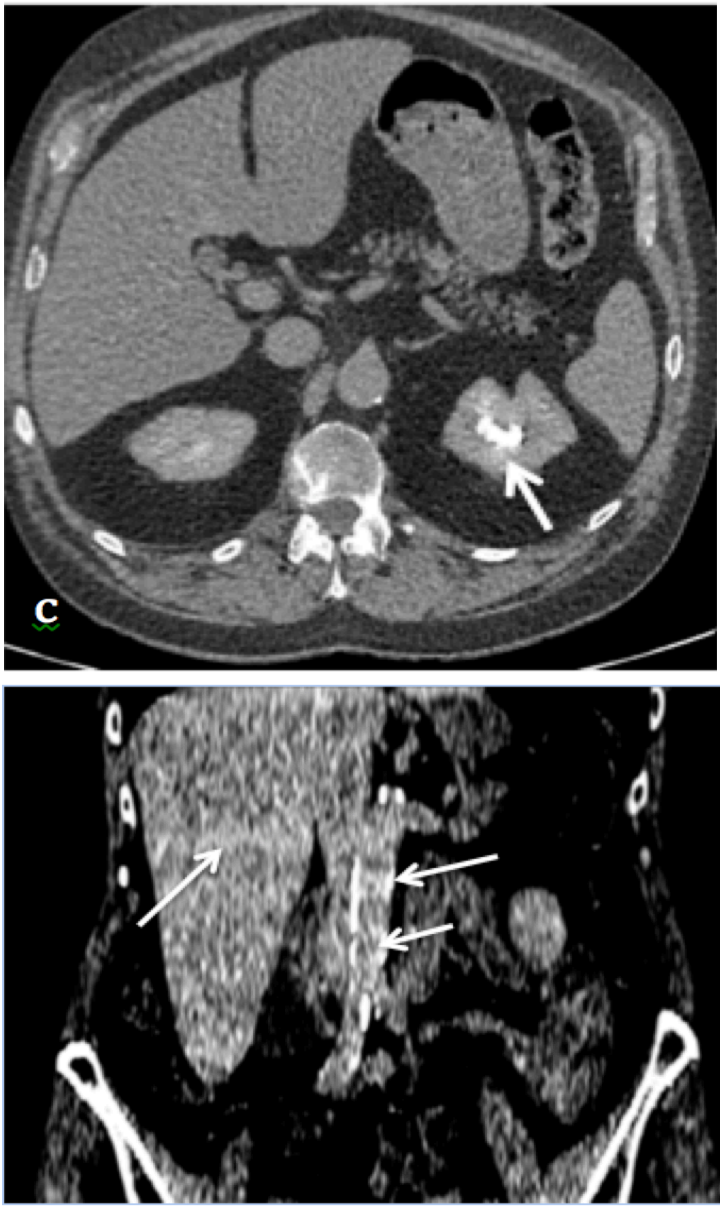

Figure 9.9 Example CT images showing beam hardening effects (II)

Dense contrast pooling in the renal collecting system causes beam hardening with bright bands through the affected slices – upper 2 white arrows.. A further dense band is seen at the level of the inferior abdominal aorta caused by dense aortic wall calcification – lower white arrow

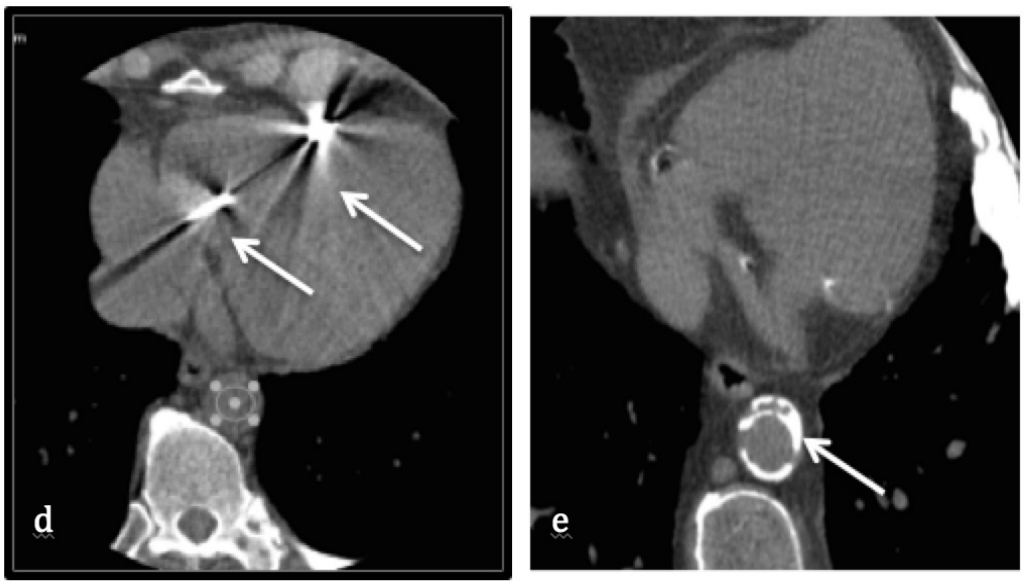

Figure 9.10 Example CT images showing metal artefact

Metal seen as severe streaking caused by pacemaker wires and (e) heavy circumferential calcification involving the aortic wall

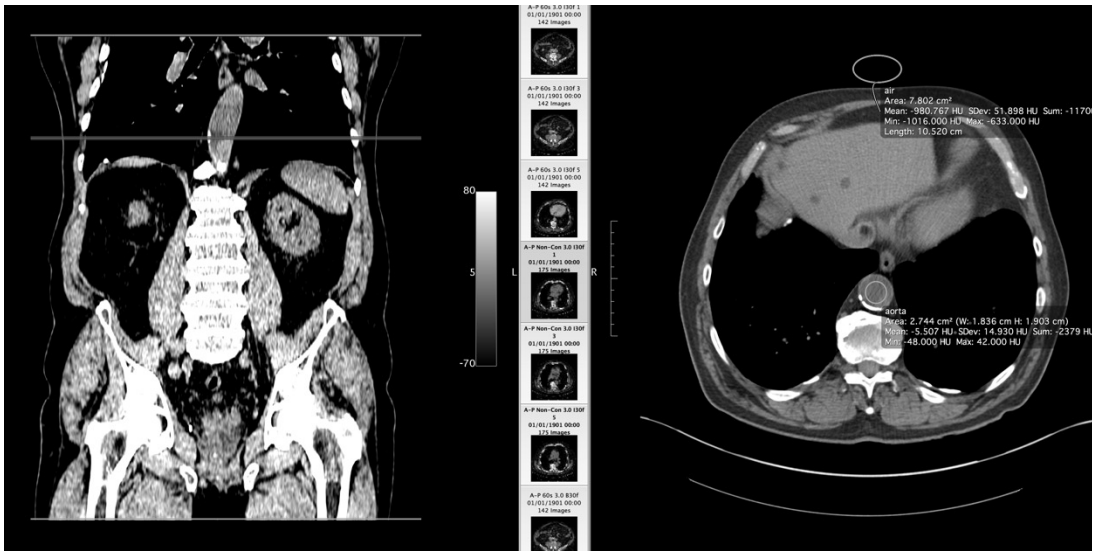

Figure 9.11 Example CT images showing artefactual hypo-attenuation

Coronal and axial images through an area of artefactual reduced density with ROI data caused by a series of large vertebral osteophytes.

Figure 9.12 Magnified view of artefact

Magnified view of this area. Bands of low density coincide with beam hardening artefact arising from dense vertebral osteophytes immediately posterior to the aorta

9.4.2 Reducing beam hardening

Beam hardening correction methods can roughly be subdivided into four classes: hardware filtering, dual energy, statistical polychromatic reconstruction, and linearization. Various correction schemes have been implemented by vendors, including high effective kV scanning, filtration, calibration correction and beam hardening correction. Filtration produces ‘pre hardening’ of the xray beam before it enters the patient and a ‘bowtie’ filter can be used to further harden the edges of the beam that will pass through the thinner tissues at the edges of the patient. Manufacturer calibration is performed with patient area specific phantoms, which allow specific elimination of ‘cupping’ artefacts. Modern scanners employ a software-based beam hardening correction that assumes an average degree of hardening for the given measured attenuation. Application of beam hardening correction to the sample of 6 clinical CT scans however

produced no significant effect on the noted attenuation variation – Figure 9.13.

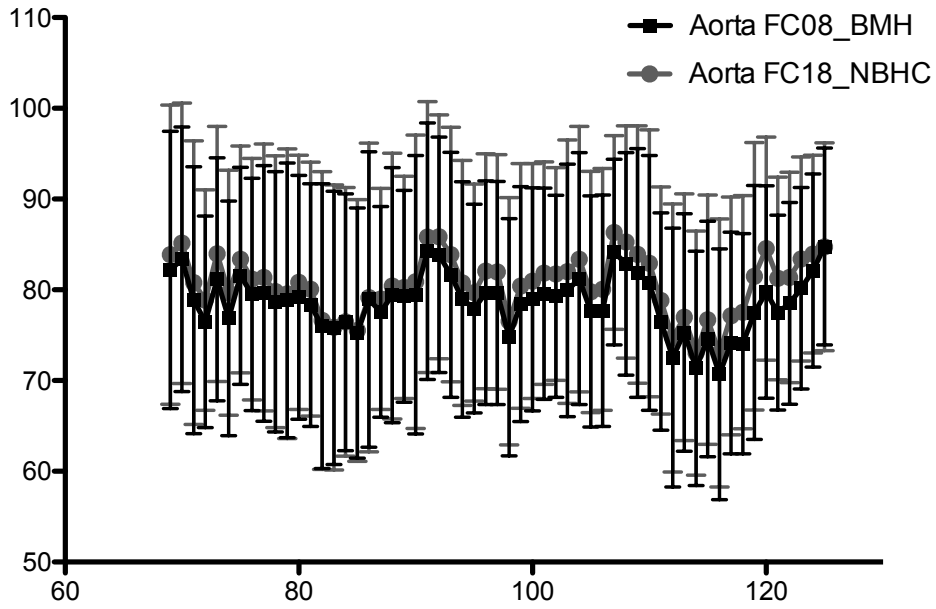

Figure 9.13 Example CT urogram showing effect of beam hardening algorithm

Effect of using a beam hardening correction algorithm. Example showing depression in aortic attenuation (position 115-120) corresponding to significant beam hardening artefact arising from a vertebral osteophyte. Images were reconstructed with the standard algorithm and with the addition of a beam hardening correction algorithm (FC08 – Toshiba Medical Systems).

Iterative reconstruction can also include custom correction into forward projected data – Figure 9.14; Figure 9.15; Figure 9.16; Figure 9.17; Figure 9.18. Iterative algorithms use multiple reconstruction repetitions to converge on an improved representation. Schemes can incorporate physical models that allow more intuitive and natural image reconstruction - resulting in fewer artefacts. Dual energy CT can be used to derive virtual monochromatic images, which do not suffer from beam hardening, however this reconstruction assumes an idealised X-ray absorption curve without k-edges and is therefore only an approximation.

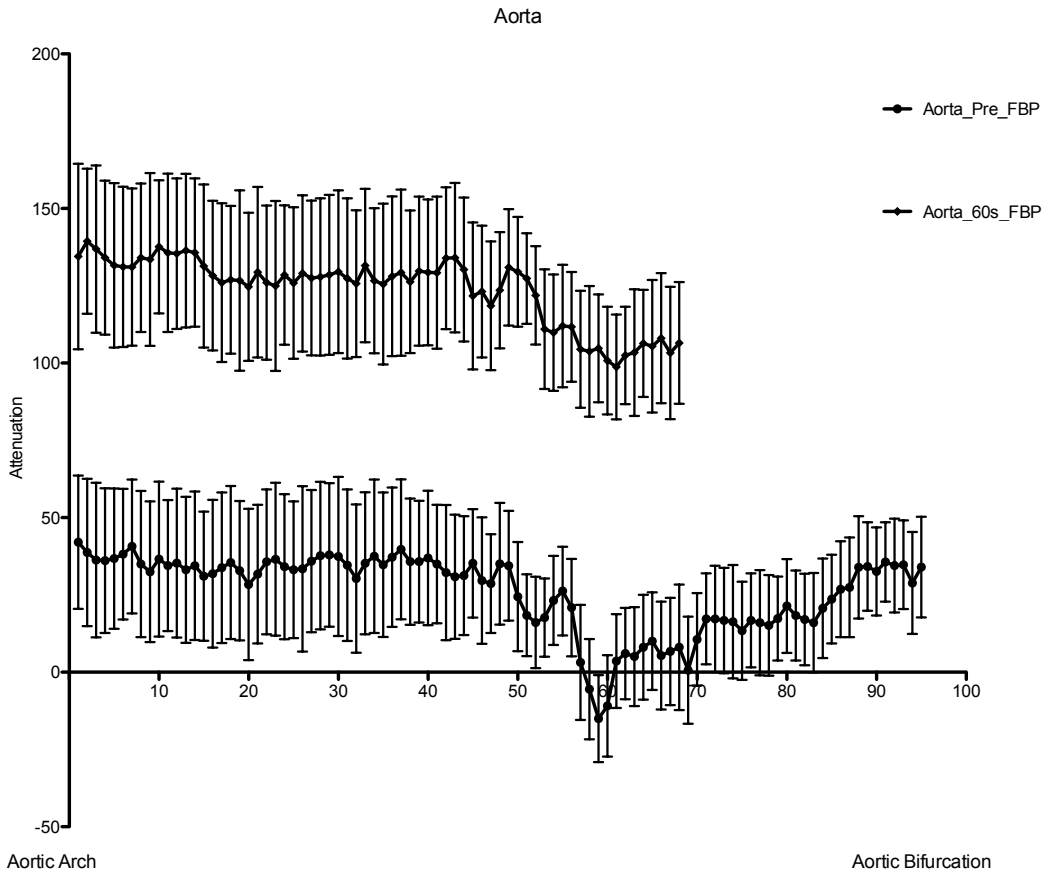

Figure 9.14 Plot of attenuation vs slice number with an example dataset

Plot illustrating the effect of focal dense vertebral osteophytes on aortic blood pool attenuation on a standard clinical scan. Attenuation measured within regions of interest draw within the aorta on serial slices though a scan (pre and post contrast) from the aortic arch caudally to the aortic bifurcation. Note the marked drop in attenuation seen within the centre of the scan data, which coincides with the thoracolumbar junction and an area of marked bridging osteophytes.

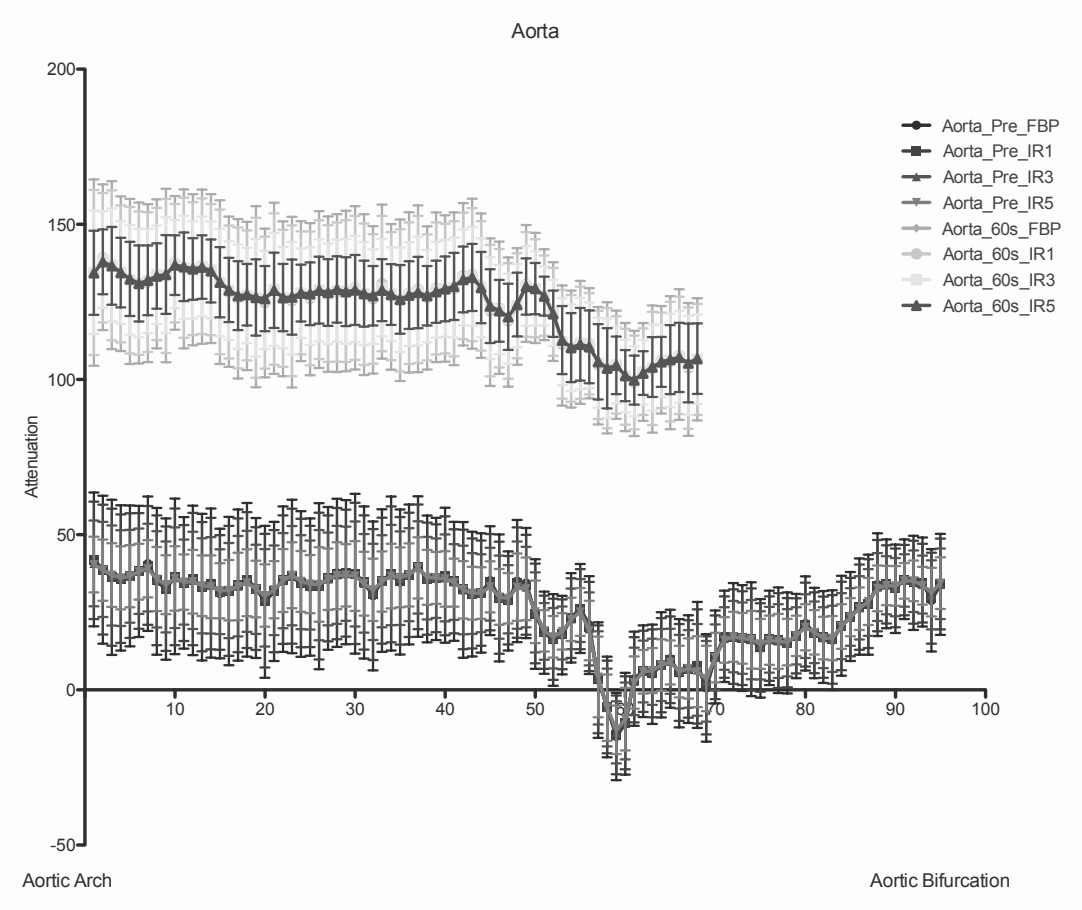

Figure 9.15 Plot showing effect of iterative reconstruction

Plot showing the same scan data as figure 9.12 but with superimposed data reconstructed using increasing degrees of iterative reconstruction (SAFIRE - Siemens). There remains a dip in measured attenuation at the level of the osteophytes with no change in mean attenuation. However with increasing levels of SAFIRE, the standard deviation (noise) within attenuation measurements falls – ie error bars become narrower.

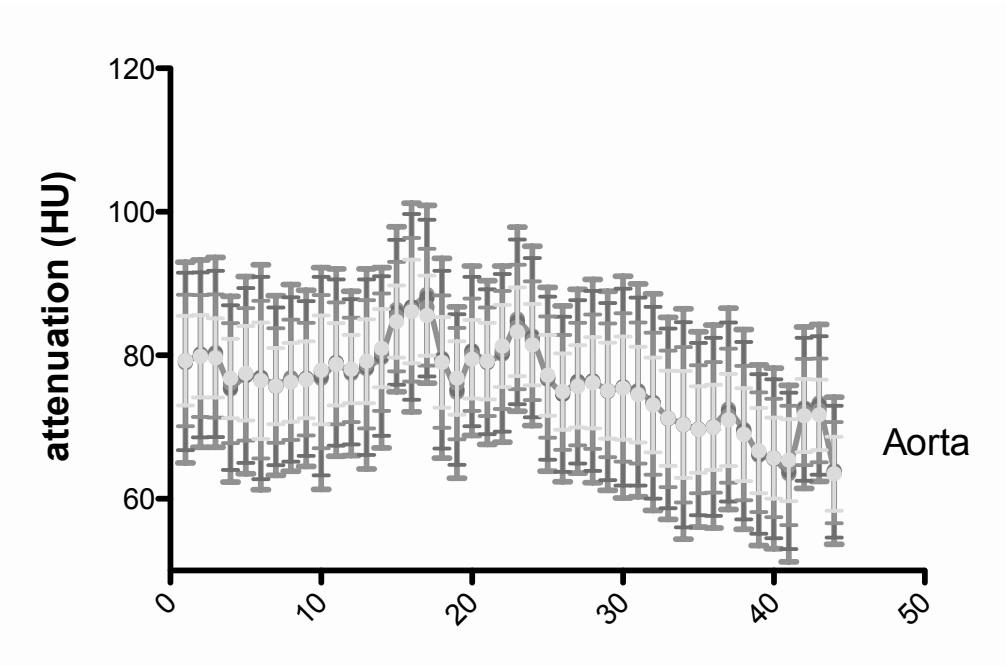

Figure 9.16 Example CT urogram attenuation plot with iterative reconstruction

Plots of attenuation measured on axial section within the abdominal aorta measured on a CT urogram, from the diaphragm moving inferiorly to the bifurcation. There are two artefactual peaks of increased density within the centre of the plot which are unaffected by increasing amounts of iterative reconstruction. Blue plot shows filtered back projection data; purple low, red medium and green high level of iterative reconstruction.

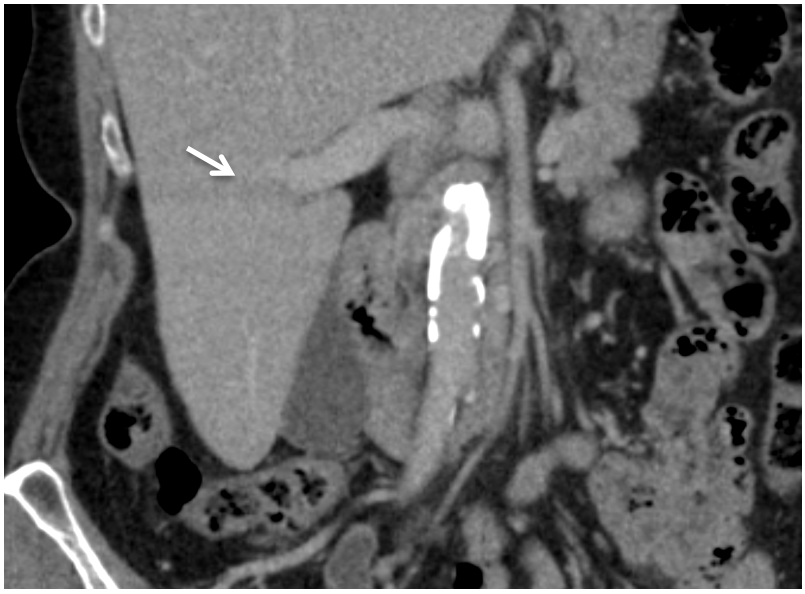

Figure 9.17 Example CT urogram coronal image

Bands of high and low density affected a transverse area of the scan – seen on coronal reconstruction, correspond to areas of densely calcified aortic wall.

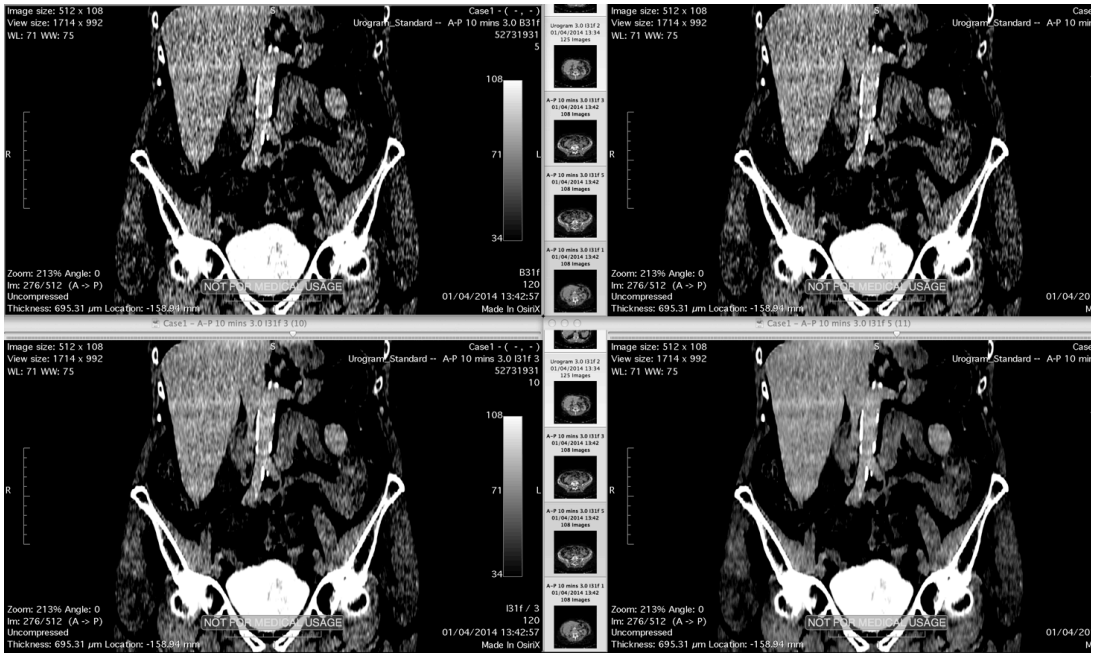

Figure 9.18 Example CT urogram images with iterative reconstruction

Images of the beam-hardening artefact, with increasing levels of iterative reconstruction applied. The artefact is still clearly visible, but there is progressively less noise within the images. Top left – filtered back projection reconstruction; top right – low; bottom left- medium; bottom right – high level of iterative reconstruction.

Iterative reconstruction applied to the sample of 3 clinical scans produced an overall reduction in image noise (lower noise with increasing amount of iterative reconstruction) however the variations caused by beam hardening artefact did not change – Figure 9.16.

9.4.3 Helical Interpolation Error

Helical interpolation errors create streaks of both increased and decreased attenuation, with an element of rotation. In helical mode, as the patient is advanced through the scanner the reconstruction alternates between measurements from adjacent detector rows, with interpolation between rows. Windmill or helical interpolation artefact occurs when a high contrast edge (e.g. diaphragm) falls between two detector rows and the interpolated values become inaccurate. The effect is most marked when there is movement, such as around the diaphragm. This is essentially an

aliasing effect that arises as a result of under sampling in the patient longitudinal direction (6). The effect is not seen in step-and-shoot or 'volume' modes but these are significantly slower to acquire and impart a higher dose.

9.4.4 Reducing measurement errors from artefacts

Simple methodological steps can be implemented to reduce attenuation error caused by artefacts. Visual evaluation of the image data and attenuation plot allows identification of significant artefacts. A more systematic and reproducible approach to identifying artefacts would be to assign an arbitrary threshold for the attenuation range within an anatomically homogenous tissue. For example, within a tissue spanning multiple slices (e.g. blood within the aorta), the range of mean HU should be less than the HU standard deviation within the tissue volume (from the law of total variance, assuming equal sized ROI samples throughout structure, the $\Sigma(\sigma)$

1. Exclusion of affected slices. Artefacts are often difficult to visually identify and can affect slices adjacent to the causative structure. In order to exclude these areas, graphically plotted attenuation data should be evaluated

2. The effect of artefacts can be 'smoothed' by calculating the average attenuation measured over multiple slices

9.5 Conclusion

As CT technology develops, quantitative methods are emerging which augment subjective visual image assessment. Attenuation measurement for characterisation of renal stones, adrenal nodules and fluid collections/cysts is well established, but newer quantitative techniques such as perfusion CT; equilibrium CT, and dual energy material

decomposition are emerging which required accurate and reliable measurement of attenuation. Modern scanners and reconstruction are not however geared towards quantitative evaluation and development up to now has been focused on delivering subjective image quality, with good contrast between healthy tissue and disease.

In this chapter I have identified significant variation in measured attenuation within homogenous tissue structures with no intrinsic anatomical explanation. These variations have a magnitude of up to 78HU from the adjacent tissue mean attenuation and if included in any quantitative analysis would have a marked deleterious effect. Evaluation of these abnormalities was performed subjectively, and in several the underlying cause was not clear, but either beam hardening or interpolation artefacts were responsible in the majority of cases.

Manufacturers have worked hard to improve the quality of reconstructed images and many schemes exist to reduce image artefact. Beam hardening, the result of preferential attenuation of high-energy photons and scatter is thought to improve with the use of iterative (6,7) and tailored beam hardening correction reconstruction algorithms, but this was not observed in our small test sample.

With the development of quantitative CT biomarkers such as perfusion and equilibrium CT, the issue of attenuation measurement precision, and parameter repeatability and reproducibility needs to be specifically addressed by system vendors. This may require specific acquisition modes and reconstruction kernels that prioritise absolute attenuation number over image spatial and contrast resolution. These developments may improve measurement precision and allow biomarkers like ECV to distinguish earlier stages of disease. In the meantime, data analysis,

interpretation of results, and clinical application should also be cognisant of these limitations.

10 QUANTIFICATION OF SKELETAL MUSCLE INVOLVEMENT IN SYSTEMIC AMYLOIDOSIS USING ^{99M}TC-DPD SCINTIGRAPHY AND EQUILIBRIUM CONTRAST MRI

10.1 Author declaration

The work contained in this chapter was completed by the author, including experimental design, MRI data analysis, statistical analysis and manuscript preparation. David Hutt of the National Amyloidosis Centre (NAC) designed the DPD scoring system and analysed the DPD data. The work was additionally supervised by Dr. Ashutosh Wechlekar and Prof. Philip Hawkins of the National Amyloidosis Centre.

10.2 Introduction

As discussed in previous chapters, amyloidosis is a disease characterised by extracellular accumulation of abnormally folded insoluble proteins within a range of organs including the heart, kidneys, liver, and muscle (1-3). Amyloid myopathy, in which abnormal protein accumulates around muscle fibers and small blood vessels leading to progressive proximal weakness, muscle pseudohypertrophy and elevated creatine kinase levels is well described but is rarely the sole or dominant presentation (3). Weakness is however a common symptom in systemic amyloidosis. Current methods do not allow assessment of skeletal muscle involvement without invasive biopsy - hence its frequency and clinical significance has not been studied, and is poorly understood. With the development of new therapies that may halt and potentially reverse the deposition process (4), assessment of

skeletal muscle involvement and its association with symptoms is required.

Technetium-99m-3,3-diphosphono-1,2 propanodicarboxylic acid (99mTc-DPD) scintigraphy is a sensitive method for imaging cardiac muscle involvement in transthyretin (ATTR) amyloid – with visual scoring based on cardiac uptake and an apparent parallel reduction in bone uptake. Recently Hutt et al. however found that rather than a competitive reduction in bone uptake, localization to bone was being masked by a consistent specific pattern of tracer uptake within skeletal muscles of patients with ATTR amyloidosis . This pattern was most pronounced and characteristic in wild-type non-hereditary TTR amyloidosis (ATTRwt, senile systemic amyloidosis) and the V122I variant of TTR (5). Blinded assessment of soft tissue uptake pattern in 150 patients demonstrated a sensitivity of 99% and specificity of 100% for ATTR amyloidosis with a cardiac uptake of at least grade 2 or 3. These findings suggest skeletal muscle is a significant target organ in ATTR amyloidosis, and post mortem of a single patient from this cohort indeed confirmed widespread muscle involvement. Further elucidation of this phenotypic extension is needed.

In previous chapters I have established equilibrium contrast (EQ) imaging as a technique that allows non-invasive interrogation of tissue extracellular volume fraction (ECV) in the heart and the liver. Specifically in chapters 5 and 8 I demonstrate that EQ-MRI and EQ-CT are able to track the degree of amyloid involvement, measured used conventional means ($P<0.001$). ECV can then act as a surrogate measure of amyloid tissue burden without the need for invasive biopsy.

In this chapter I move beyond validating EQ-MR as a tool to quantify the burden of tissue amyloid deposition to using it as a standard of reference for another technique. Specially I propose a method for quantifying skeletal muscle uptake on 99mTc-DPD in ATTR amyloidosis, and test the hypotheses that muscle tracer uptake reflects the degree of diffuse muscle

amyloid infiltration, quantified non-invasively using equilibrium contrast imaging; and that skeletal muscle uptake score follows the grade of cardiac involvement.

10.3 Materials and methods

All participants provided informed written consent.

57 patients (51 men, 6 women; median age 78 years; age range, 40–88 years) with either clinically suspected or proven wild type TTR ($ATTR_{wt}$) or familial amyloid polyneuropathy ($ATTR_{FAP}$) amyloidosis attending the outpatient clinic at the National Amyloidosis Centre (NAC) were recruited. Included patients had undergone both 99mTc-DPD and cardiac EQ-MRI to assess cardiac amyloid burden with an interval of less than 12 months as part of their standard clinical workup at the NAC. Where possible, a diagnosis of ATTR amyloidosis was confirmed by the presence of characteristic histological staining with Congo red under polarized light or by immunohistochemical staining.

10.3.1 Skeletal muscle ECV measurement

In order to measure skeletal muscle ECV, the EQ-MRI with a steady state equilibrium contrast method via the contrast agent Gadoterate meglumine (gadolinium-DOTA, marketed as Dotarem, Guerbet S.A., Paris, France) as described in chapter 5.3.3 was analysed. The equilibrium steady state contrast protocol comprised a bolus dose of 0.1 mmol/kg followed after a 15 minutes delay by an infusion at 0.0011 mmol/kg/min for a minimum of 30 minutes, to achieve a constant blood and tissue contrast (7,9).

As part of the cardiac-EQ-CMR protocol, single slice transverse section T1 maps were acquired through the thorax at the level of the mid cardiac septum, using a shortened look locker inversion recovery (ShMOLLI) sequence on a 1.5T MR scanner (Avanto, Siemens Medical Solutions,

Ehrlangen, Germany). T1 maps (table 10.1) were made before and after contrast equilibrium at an equivalent slice location.

Sequence	FLASH Gradient Echo
Plane	Axial
Slices	1
TR	2000ms
TE	3.15ms
Flip angle	21°
FoV read / phase	400 / 260mm
Slice thickness	8mm
Inversion times	140, 200-1000ms
Acquisition time per TI	14s
Acquisition time for slice T1 map	Approx. 6mins
Image matrix	256 x 168
Breathing	Breath hold
Saturation bands	None

Table 10.1 ShMOLLI MRI sequence parameters

Summary of sequence parameters for Shortened Modified Look-Locker Inversion recovery T! mapping

Skeletal muscle was assessed with elliptical regions of interest (ROI) drawn within the left biceps muscle (as this comprised the largest muscle included within the imaged volume) (mean;range area 63mm2; 28-94mm^2) and within the left ventricular blood pool (mean;range area 417mm^2; 342-683mm2) by the author. ROIs were drawn to include the maximum areas of muscle and blood, but avoid adjacent fat and myocardium with a margin of at least 2mm. ROIs were drawn first on the pre-contrast T1 maps and copied to the post contrast T1 image.

A hematocrit was taken in all subjects immediately before the MRI study. The ECV was calculated as:

ECV_{muscle} = (1-hematocrit) x ($\Delta R1_{muscle}/\Delta R1_{blood}$), where R1 = 1/T1

ECV within the biceps muscle was then compared with comparable data (already described in chapter 5 section 4.2) in 67 patients with AL amyloidosis and in a group of 40 healthy volunteers (6). Patients were scanned using an identical steady state contrast equilibrium and T1 mapping technique, and ROI analysis was performed as described above. Of the 40 healthy volunteers and 67 patients with AL amyloidosis who underwent EQ-CMR, limited field of view, and wrap-around artefact limited assessment of the biceps muscle to 34 healthy volunteers and 42 AL amyloidosis patients. A summary of patient characteristics is given in Table 10.2.

Group	ATTR	AL	Healthy
Recruited	57	67	40
Cases in which biceps ECV successfully measured	46	42	34
Age mean (range)	75 (40-88)	67(40-81)	45 (27-88)
Male / female	42/4	29/13	14/20

Table 10.2 Patient characteristics

Summary of patient characteristics for ATTR and AL amyloid groups, and healthy volunteers

10.3.2 99mTc-DPD scintigraphy

DPD scintigraphy was performed as part of the routine clinical investigation for patients with suspected or confirmed ATTR amyloidosis. Scanning was performed on one of two General Electric (GE) Medical Systems hybrid SPECT-CT gamma cameras (Infinia Hawkeye 4 and Discovery 670) after intravenous injection of 700 MBq of 99mTc-DPD. Whole body planar images were acquired 3 hours post-injection followed by cardiac SPECT-CT (single photon emission computed tomography with

a low-dose, non-contrast CT scan). The soft-tissue reconstruction was loaded into the Myovation programme on the Xeleris workstation to perform the attenuation correction on the SPECT data. The SPECT data were reconstructed using filtered back projection. Data were prefiltered using a Butterworth filter with a critical frequency of 0.4 cycles/cm and a power of 10. It was then reconstructed with a quantitative ramp filter.

10.3.3 Quantification of tissue tracer uptake

The data by Hutt el al. showed that across the range of ATTR disease severities, the intensity of the peak uptake seen within bone on Tc-DPD remained relatively stable, despite variation in soft tissue uptake. Apparent loss of bone signal in higher-grade disease occured due to a progressive increase in the adjacent muscle uptake. This pattern was most clearly demonstrated in the thigh where large muscle groups surround the femur. Signal to noise ratio within the smaller biceps muscle (corresponding to the area imaged with MRI) was significant lower, but as tracer uptake was diffuse, muscle involvement was assumed to be uniform and uptake quantified in the lower limb where signal was strongest. In order to quantify muscle uptake, line count profiles were created by drawing a 4.5cm wide region of interest (ROI) across the mid thigh on the anterior whole body planar image – figure 10.3. The femoral peak and adjacent soft tissue uptake were identified visually. The maximum (peak) uptake within the femur and the mid-range (mean of the largest and the smallest values) of uptake within the soft tissue on either side of the femur were recorded for each leg, and the average of each calculated. The femoral uptake was used as reference, and relative soft tissue uptake (ST score) was then derived using the formula:

DPD_{muscle} ST score = F_{max} / ST_{avg}

where F_{max} is the mean of the maximum femoral uptake measured within both legs; and ST_{avg} is the mean of the midrange uptake within the 4 soft tissue compartments sampled (bilateral medial and lateral).

Cardiac retention of 99mTc-DPD was visually scored using a modification of the grading devised by Perugini et al., with cardiac uptake visualized on SPECT-CT but not on planar imaging additionally classified as Grade 1:

score 0, absent cardiac uptake and normal bone uptake

score 1, mild cardiac uptake, inferior to bone uptake or cardiac uptake on SPECT-CT but not on planar imaging

score 2, moderate cardiac uptake accompanied by attenuated bone uptake

score 3, strong cardiac uptake with mild/absent bone up- take

10.3.4 Statistical analyses

Data analyses were performed by using statistical software (prism version 5; Graphpad Software, San Diego, Calif). Normal distribution was assessed using the Kolmogorov-Smirnov test.

Differences in biceps ECV between the current ATTR group, the group of patients with AL amyloidosis and the group of healthy volunteers was assessed by using the Kruskal-Wallis test; with Dunn's post test comparison of groups.

The Kruskal-Wallis test was also used to compare DPD and ECV between cardiac DPD grade groups

Variation in ST score and ECV across cardiac DPD scores was tested by using a Kruskal-Wallis test. Spearman correlation analysis was performed to establish an association between ST score and ECV; and cardiac DPD grade using a one-tailed P value. A P value less than or equal to .05 indicated statistical significance.

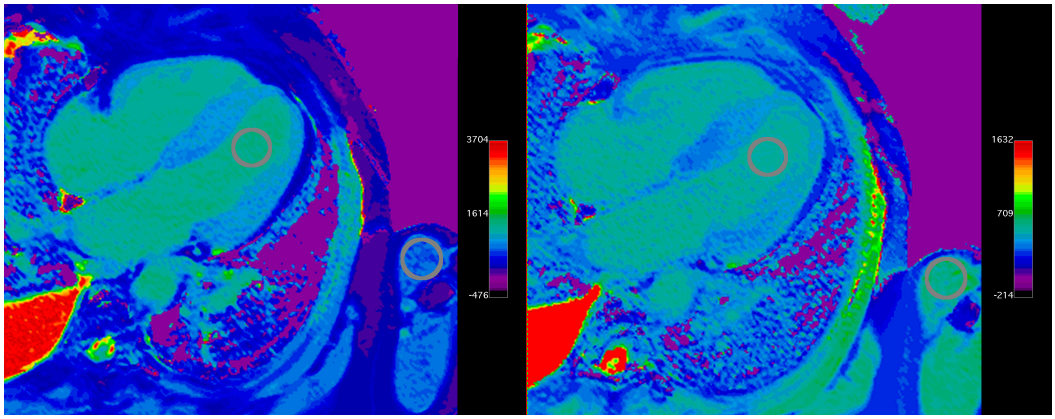

Figure 10.3 EQ-MRI Sh-MOLLI colour T1 maps

Images from EQ-MRI showing T1 colour maps before and after equilibrium contrast. Regions of interest have been drawn in the left ventricular blood pool and within the biceps muscle

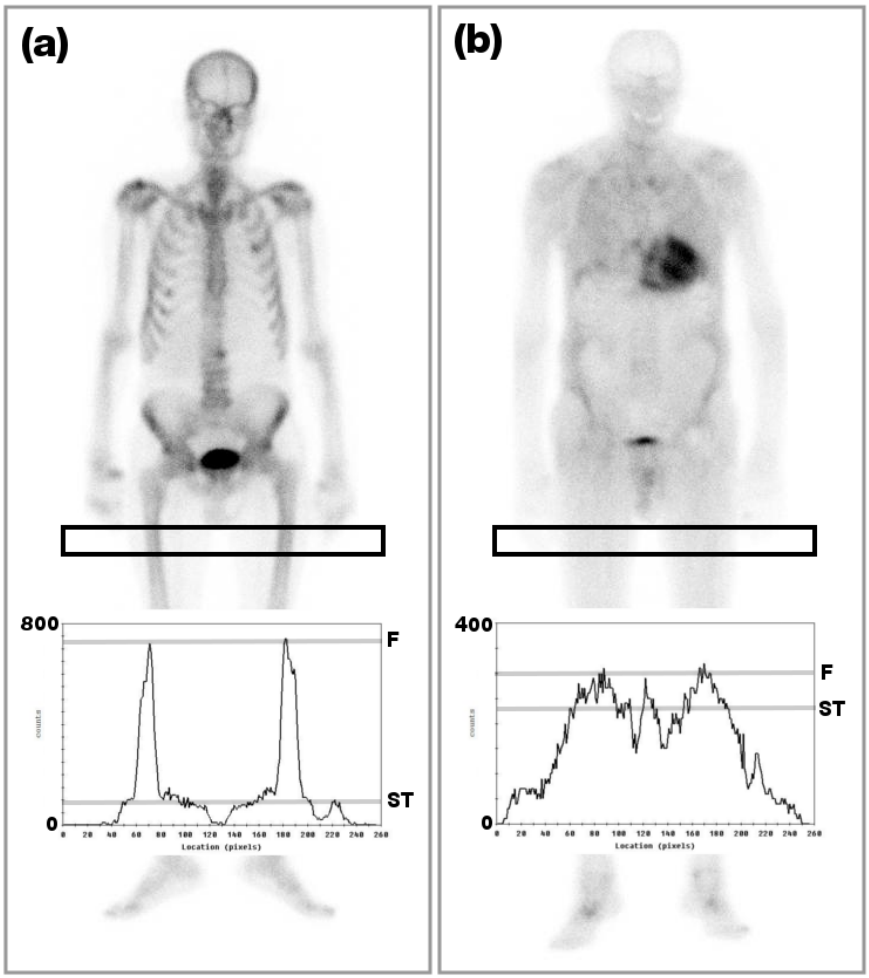

Figure 10.4 99mTc-DPD images with line count profiles

Anterior projection SPECT 99mTc-DPD images in ATTR patients with (a) grade 0 and (b) grade 3 cardiac involvement; with ROI drawn through the upper thigh and corresponding line count profiles. In case (a) clear high count femoral peaks (F_{max} – maximum femoral uptake) are seen with adjacent shouldering in the profile corresponding to soft tissue uptake (ST_{avg} – mean soft tissue uptake). Case (b) demonstrates increased diffuse soft tissue uptake with activity approaching that of the femora.

10.4 Results

Of the 57 patients recruited, paired cardiac and skeletal muscle DPD grade and biceps muscle ECV measurement were available in 46 cases. In 11 cases EQ-MRI did not allow adequate assessment of the biceps

muscle ECV due to artefact within T1 maps or incomplete coverage of the upper arm.

Of the 46 included cases, the diagnosis was wild-type non-hereditary TTR amyloidosis ($ATTR_{wt}$) in 36 cases; familial amyloid polyneuropathy ($ATTR_{mt}$ amyloidosis) in 8 cases and 2 included patients were eventually found not to have systemic amyloidosis.

The mean (range) interval between ^{99m}Tc-DPD and EQ-MRI was 0.4 months (range -10 to +11 months).

The median (and IQR) soft tissue DPD score was 0.51 (0.41 – 0.69) and biceps muscle ECV was 0.21 (0.18 – 0.32).

When compared with ECV data in a cohort of healthy volunteers and a group of patients with AL amyloidosis described in chapter 5 – summarised again in table 10.2, ECV with the biceps muscle in the ATTR group was not significantly different to that in the AL group, but biceps ECV in both the AL and ATTR group were elevated compare with the healthy volunteers ($P < 0.0001$) - see figure 10.5.

There was a statistically significant differences in both 99mTc-DPD soft tissue activity quantified by our soft tissue score ($p < 0.0001$), and biceps ECV ($p = 0.026$) according to cardiac DPD grade. There was a positive correlation between ST_DPD score ($r_s = 0.64$, $p < 0.0001$) and biceps ECV ($r_s = 0.43$, $p = 0.0013$); and cardiac DPD grade - figure 10.6. Regression analysis revealed ST_DPD score to be a predictor of biceps ECV (R^2=0.34) – figure 10.7.

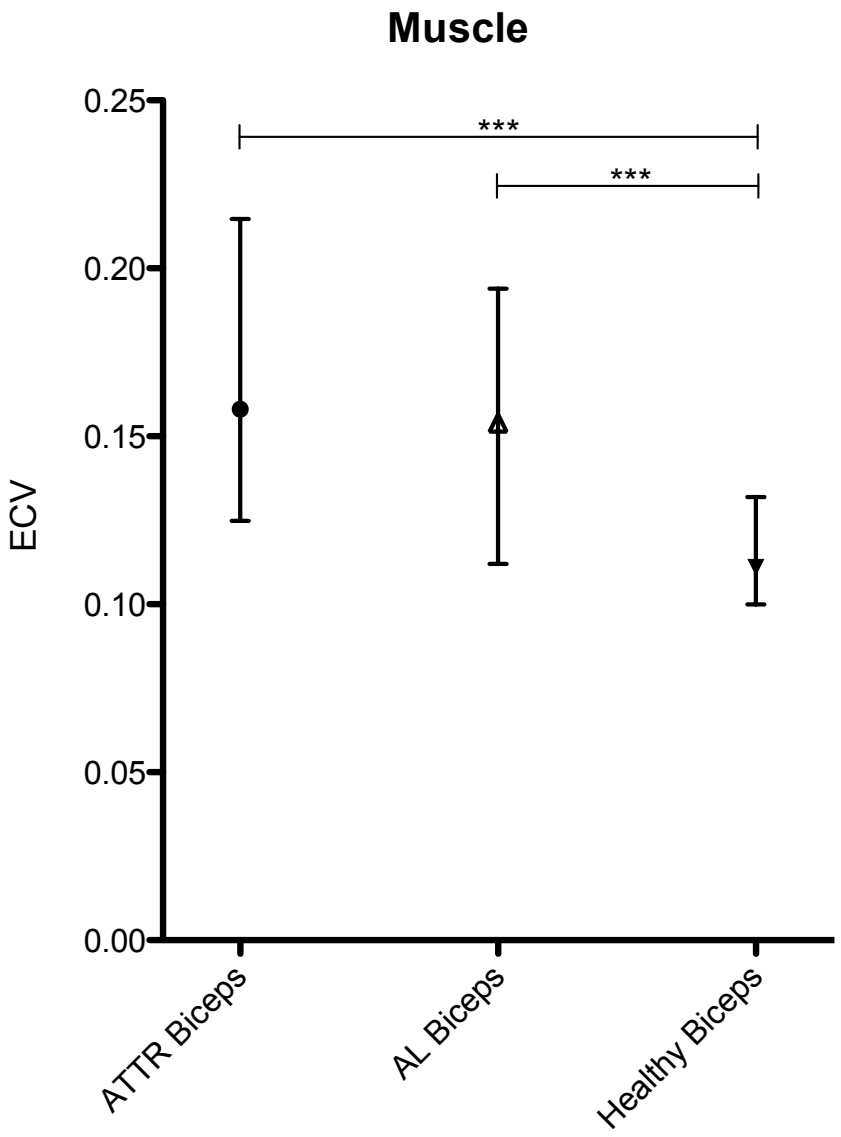

Figure 10.5 Box plot of skeletal muscle ECV

Box-and-whisker plot of median and IQR of biceps ECV measured within the current ATTR cohort, and similar measurements made in a patient group with AL amyloidosis and a group of healthy volunteers from chapter 5.

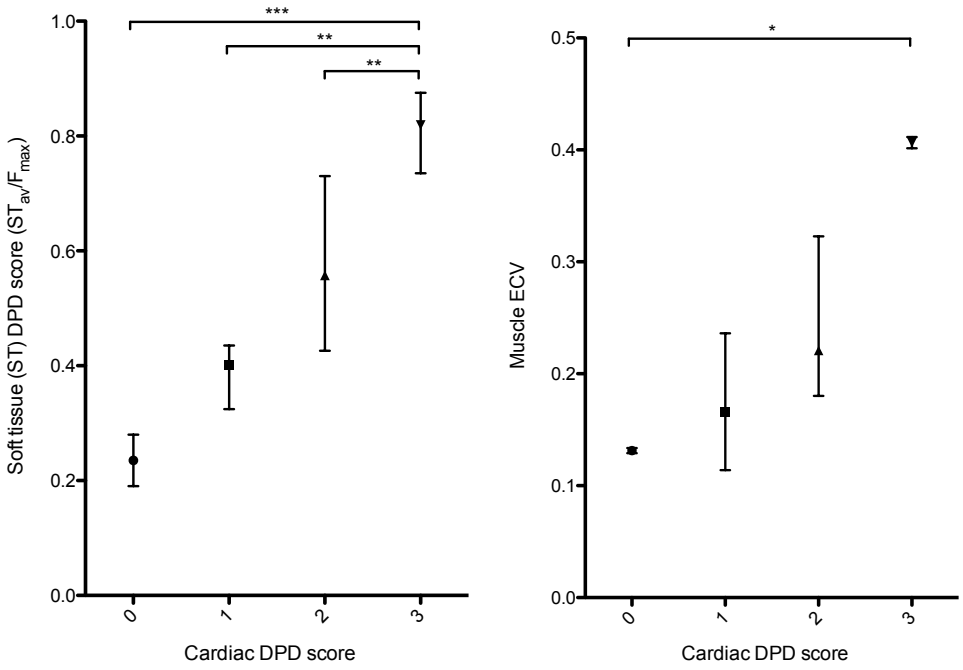

Figure 10.6 99mTc-DPD images with line count profiles

Box-and-whisker plot of median and IQR 99mTc-DPD soft tissue score (ST) showing (a) increasing ST and (b) biceps muscle ECV with greater cardiac DPD grade

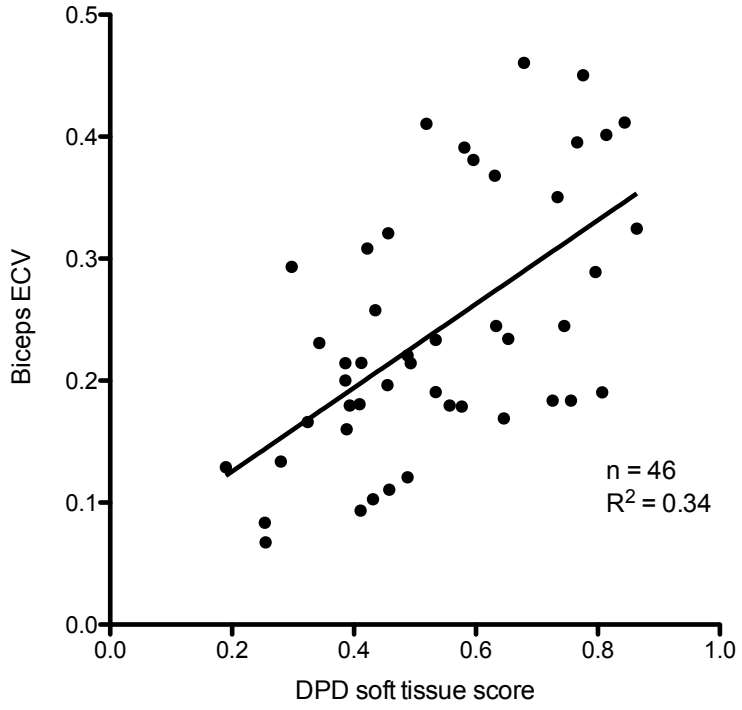

Figure 10.7 Scatter plot of soft tissue score vs ECV with regression line

Scatter plot of 99mTc-DPD soft tissue score versus ECV measured within the biceps on EQ-MRI – with regression line.

10.5 Discussion

Myopathy is rarely the principle sign of systemic amyloidosis, but non-specific complaints such as weakness and malaise are common. Biopsy evidence exists which suggests diffuse skeletal muscle amyloid infiltration (3), and this has recently been postulated as the cause of diffuse soft tissue uptake seen on 99mTc-DPD in ATTR amyloidosis (5). In this chapter I propose a method for quantifying this soft tissue uptake, and demonstrate an association with grade of cardiac involvement. Extracellular volume fraction measured within skeletal muscle by equilibrium contrast MRI was used as an independent reference technique to corroborate these findings. In this cohort of ATTR patients, biceps muscle ECV increased with both 99mTc-DPD soft tissue score and

cardiac grade, suggesting that diffuse infiltration of skeletal muscle occurs in addition to the myocardium with worsening disease.

I use two imaging techniques to explore skeletal muscle involvement in ATTR amyloidosis, showing that with worsening disease, skeletal muscle involvement is diffuse. This study makes no assessment of the possible clinical manifestation of this amyloid deposition. Symptoms of muscle weakness and malaise may be the result of skeletal muscle infiltration, cardiac dysfunction and a peripheral neuropathy. Non-invasive methods such as 99mTc-DPD scintigraphy and EQ-MRI; as well as blood markers like creatinine kinase and electrophysiological assessment with objective assessment of symptoms may allow us to evaluate the various contributions – and this should be the subject of future investigation.

This study had several further limitations. Although variations were subjectively apparent, quantification of 99mTc-DPD tracer activity within soft tissue was difficult. Absolute tissue uptake is influenced by multiple non-disease dependent variables, including tracer clearance, patient habitus and gamma camera setup. As a femoral activity peak is a constant finding (5), this was used as an internal control. However differences in femoral mineralization between individuals will lead to variations in tracer binding, and size of the femoral peak. Additionally, with extensive infiltration, surrounding soft tissue activity may conceal femoral uptake, leading to inaccurate scoring and an artificial plateau in scores at an upper threshold where soft tissues and femoral uptake are equivalent. Thirdly, the soft tissue and femoral parts of the line count profile were identified visually. However noise could make separately distinguishing these parts of the trace difficult, particularly when the two were similar.

In developing a soft tissue scoring system, I initially aimed to quantify uptake within the upper limb, matching the area assessed on MRI. The smaller size of the upper limb however produced uptake line profiles with significantly lower signal to noise, and visual separation of soft tissue and

bone was imprecise compared with the lower limb. Using soft tissue DPD scoring data from the lower limb and ECV data from the upper limb reduced the usefulness of technique comparison, but the modest association between the two (figure 10.7), highlights the diffuse nature of amyloid deposition.

This study provides initial evidence that skeletal muscle is a significant target organ in ATTR amyloidosis, with disease burden paralleling that of the myocardium. With the advent of therapies able to halt and even reverse tissue amyloid deposition (4), techniques to accurately assess overall and specific tissue involvement are required, to evaluate efficacy and monitor treatment response. 99m-Tc-DPD and EQ-MRI are tools that may be used to quantify diffuse amyloid deposition and the associated changes in ECV, but in future, pathological and clinic markers will be required to fully understand the clinical significance.

11 DISCUSSION

11.1 Summary of conclusions

This chapter concludes the thesis with a discussion of the main results and conclusions, and sets out the areas that require development in the future.

Non-invasive diagnosis has for the most part focussed on tissue morphological changes, with the latest techniques now beginning to probe tissue function and microstructural changes. Until recently the importance of cellular supporting elements and their role in disease was overlooked, largely as a result of our inability to probe these changes. Histopathologists have for centuries recognised that in several important disease processes, tissue volume is replaced by a protein matrix. This was however seen as a passive response to disease, rather than an intrinsic dynamic process within the pathophysiological pathway. Our understand of the interplay between cellular and extracellular tissue components in health and disease has been hindered by the lack of robust methods for evaluation. Despite advances in tissue collection and preparation, histological evaluation is still critically limited by sample artefacts which prevent accurate extracellular quantification. It is then the development of new non-invasive methods which has allowed improved understanding. Equilibrium contrast imaging is one such technique, that promises accurate whole organ extracellular volume assessment using existing technology and techniques. My aim throughout this work has been to initiate the process of development towards producing a robust, validated clinical test (figure 11.1), allowing ECV to become a clinically useful marker of extracellular disease.

This thesis provides stepwise development of the Equilibrium Imaging method for extracellular volume fraction measurement. After exploring the

structure, function and properties of the extracellular space, and its role in disease, I began by laying out the basic principles and assumptions of the EQ method. Due to the limitations discussed earlier, testing these principles against direct tissue measurements has not been possible. In chapter 4 I was however able to use engineered tissues with predetermined extracellular volume fractions to demonstrate for the first time an association with ECV measured by EQ-MRI. Since this experiment, three-dimensional engineered tissue models have continued to progress towards the complexity of the in vivo environment. Newer models now incorporate higher cell densities with rolled cylindrical structures, immune cells and vascular elements (1). These improvements will allow evaluation of EQ imaging at physiological cell densities with more complex cell-cell interactions and allow us to examine the effect of higher concentrations of tissue matrix proteins and tissue vascular volume, thereby testing the limits of the assumptions necessary for EQ imaging.

After initial development of EQ-CMR and early validation in aortic stenosis I was keen to explore the huge potential application of this technique in other organs. The liver, another important organ commonly affected by diffuse fibrosis, was an obvious target - although the sinusoidal blood volume is higher than in the heart. Before evaluating hepatic cirrhosis, to provide the best chance of proof of principle, I applied the EQ-MRI technique in systemic light chain amyloidosis, where hepatic extracellular expansion by amyloid protein deposition can be massive. The results presenting in chapter 5 showed a significant elevation of hepatic ECV which tracked disease burden measured by SAP. Identifying the interstitial expansion associated with amyloid deposition was then the first demonstration of the potential application of EQ imaging in the liver. EQ-MRI measured liver ECV was subsequently used as an endpoint in a first in man, phase 1 clinical trial evaluating a new drug, (R)-1-[6-[(R)-2-carboxy-pyrrolidin-1-yl]-6-oxo-hexanoyl]pyrrolidine-2-carboxylic acid (CPHPC). CPHPC acts to deplete plasma SAP, allowing specific targeting of SAP within amyloid deposits by therapeutic IgG anti-SAP antibodies.

The results of this study showed that in the group of patients who received sufficient therapy in relation to disease load, liver function improved with a significant reduction in liver ECV and tracer uptake on SAP scintigraphy (2).

Early development of EQ imaging used MRI, an imaging modality able to deliver high signal and contrast-to-noise. Although increasing in availability, the long imaging times and cost could limit potential use of this test. As discussed in chapter 4, the non-linear relationship between signal and contrast concentration, and effects of fast transcytolemmic water exchanged adds additional complexity to the MRI technique. Computed tomography offers faster, cheaper and more widely available imaging, albeit with of the use of ionising radiation. Translation to this platform required development of a new iodinated contrast administration protocol, which I was able to do in chapter 6 with the help of 15 volunteers, before evaluating myocardial ECV against histological collagen proportionate area, in an experiment mimicking the earlier EQ-CMR validation study by Flett et al (3). Although the association was not as strong as that shown with EQ-CMR, maintaining dose at an acceptable level meant that CT image noise was higher. This initial proof of concept experiment used a standard mid-3rd generation scanner, which lacked newer detector and reconstruction technologies. Some of these issues and possible solutions are explored in chapter 9, with a broad application to quantitative CT techniques. Although I was able to make observations and suggestions based on a subjective analysis of a small cohort, specific development of attenuation measurement by CT, in combination with scanner vendors, engineers and ionising radiation physicists is required in the future to allow quantitative CT techniques to achieve the necessary accuracy and precision. Subsequent work by our group in collaboration with a scanner vendor (Toshiba Medical Systems Europe, and Toshiba Medical Visualisation Systems), to be published in the future has already taken advantage of recent commercially available improvements to develop acquisition protocols with improved artefact correction and noise reduction.

In chapter 7 I applied development of EQ image to one of the modern worlds most prevalent diseases – hepatic cirrhosis. Until the development of Transient Elastography (EchoSens 2009) hepatic fibrosis had been exclusively managed using invasive biopsy, with sampling done either via a percutaneous or transjugular route. Transient Elastography provides a convenient bedside test with good sensitivity (90%) but fails in up to 18% of cases (4) and suffers from similar sampling error issues to biopsy. The proposed use of Equilibrium contrast CT in chapter 7 could potentially provide whole liver ECV assessment at the same time as morphological assessment of the liver and assessment of potential complications of the disease – such as varices and hepatocellular carcinoma. My initial proof of concept study described in chapter 7 showed modest diagnostic accuracy in a cohort of 33 patients ($r=0.64$, $p<0.0001$). This potentially exciting finding should be built upon in the future with refinement of the CT acquisition and contrast protocols. The diagnostic performance of EQ-CT at discriminating early stages of fibrosis, and crucially its ability to predict negative clinical outcomes in liver disease patients can then be explored in a larger cohort. Since completing this work, other techniques which utilise multiparametric MRI assessment of the liver, including T2* and native T1 mapping have developed. Pavlides et al. used one such implementation (LiverMultiScan, Perspectum Diagnostics, Oxford, UK) and showed a composite liver inflammation and fibrosis score generated by a proprietary algorithm was predictive of clinical outcome in patients with chronic liver disease (3). In the future, performance of EQ-CT, in addition to cost and clinical applicability should be compared with these emerging techniques.

In the final chapter 10, EQ-MRI is used a reference standard for interstitial expansion in systemic amyloidosis, probing changes in skeletal muscle hypothesised after diffuse soft tissue uptake was noted on 99mTc-DPD scintigraphy. The increase in skeletal muscle ECV has added to evidence that the soft tissues are a significant target for amyloid deposition in ATTR amyloidosis. Although an interesting application of the EQ technique, until corroborative clinical and biochemical markers are examined, the

significance of this deposition will remain unclear. In the meantime, EQ assessment of ECV remains available to those developing new anti ATTR amyloid agents.

This thesis has largely focused on technical development of the equilibrium technique with early comparison of ECV against histology and other markers of disease. Some limitations of this work have been the retrospective use of cohorts for additional analyses, introducing experimental constraints. For example, in chapter 10 we relied on muscles visible on EQ-CMR for comparison against a scintigraphic marker measured in the thigh. Within this development, importantly evaluation of ECV measurement precision has been omitted, with no incorporation of repeatability or reproducibility assessment steps. Before proposing use of ECV as a diagnostic tool, these attributes, including intra and inter user variation, and variation between scanners, vendors and locations must be evaluated. Biomarker reference ranges, test sensitivity and specificity, and linkage to clinical outcomes can then be defined. This work will form the basis of the next phase of EQ imaging development.

1. **Technical development**
2. **Comparison against histology**
3. **Comparison in disease vs health**
4. **Correlation with imaging markers**
5. **Correlation with blood biomarkers**
6. **Assessment in multiple clinical scenarios**
7. **Assessment in early disease or with aging**
8. **Ability to track change over time, and after Rx**
9. **Predictive/prognostic value**
10. **Test standardisation**
11. **Define normal reference ranges**
12. **Test as Surrogate trial endpoint**
13. **Clinical use and regulatory approval**
14. **Test improves clinical outcome**

Figure 11.1 Stages of development of a clinical test

Development stages through which a test such as EQ imaging must pass before it can be adopted in clinical practice.

11.2 Conclusions

Finally, in conclusion, this thesis has made stepwise methodological development of the Equilibrium Imaging technique, demonstrating early proof of the underlying principles, translation to a new imaging platform and utility in diffuse fibrosis and amyloidosis of the heart and liver. It is my hope that future work will continue development of this technique towards a robust non-invasive test, with real clinical utility.

Steve Bandula 2016

12 REFERENCES

12.1 Chapter 1

1. Järveläinen H, Sainio A, Koulu M, Wight TN, Penttinen R. Extracellular matrix molecules: potential targets in pharmacotherapy. Pharmacol Rev [Internet]. 2009 Jun [cited 2014 Sep 1];61(2):198–223.

2. Alberts B, Johnson A, Lewis J. Molecular Biology of the Cell. 4th edition. In: Molecular Biology of the Cell [Internet]. 2002.

3. Bosman FT, Stamenkovic I. Functional structure and composition of the extracellular matrix. J Pathol [Internet]. 2003 Jul [cited 2012 Nov 9];200(4):423–8.

4. Krishnan A, Li X, Kao W-Y, Viker K, Butters K, Masuoka H, et al. Lumican, an extracellular matrix proteoglycan, is a novel requisite for hepatic fibrosis. Lab Invest [Internet]. 2012 Dec [cited 2014 Sep 1];92(12):1712–25.

5. Ogston a G, Stanier JE. On the state of hyaluronic acid in synovial fluid. Biochem J [Internet]. 1950 Mar;46(3):364–76.

6. Cleland RL. Ionic polysaccharides. II. Comparison of polyelectrolyte behavior of hyaluronate with that of carboxymethyl cellulose. Biopolymers [Internet]. 1968;6(11):1519–29.

7. Kiani C, Chen L, Wu YJ, Yee AJ, Yang BB. Structure and function of aggrecan. Cell Res [Internet]. 2002 Mar;12(1):19–32.

8. Anderson KR, Sutton MG, Lie JT. Histopathological types of cardiac fibrosis in myocardial disease. J Pathol [Internet]. 1979 Jun [cited 2012 Jul 17];128(2):79–85.

9. Choudhury L, Mahrholdt H, Wagner A, Choi KM, Elliott MD, Klocke FJ, et al. Myocardial scarring in asymptomatic or mildly symptomatic patients with hypertrophic cardiomyopathy. J Am Coll Cardiol [Internet]. 2002 Dec;40(12):2156–64.

10. Hein S. Progression From Compensated Hypertrophy to Failure in the Pressure-Overloaded Human Heart: Structural Deterioration and Compensatory Mechanisms. Circulation [Internet]. 2003 Feb 10 [cited 2014 Oct 8];107(7):984–91.

11. Turto H, Lindy S, Halme J. Protocollagen proline hydroxylase activity in work-induced hypertrophy of rat muscle. Am J Physiol [Internet]. 1974 [cited 2012 Sep 5];226(1).

12. Weber KT. Cardiac interstitium in health and disease: the fibrillar collagen network. J Am Coll Cardiol [Internet]. 1989 Jun;13(7):1637–52.

13. Fielitz J, Hein S, Mitrovic V, Pregla R, Zurbrügg HR, Warnecke C, et al. Activation of the cardiac renin-angiotensin system and increased myocardial collagen expression in human aortic valve disease. J Am Coll Cardiol [Internet]. 2001 Apr;37(5):1443–9.

14. Davis KL, Mitra D, Medjedovic J, Beam C, Rustgi V. Direct economic burden of chronic hepatitis C virus in a United States managed care population. J Clin Gastroenterol [Internet]. 2011 Feb;45(2):e17–24.

15. Roberts HW, Utuama O a, Klevens M, Teshale E, Hughes E, Jiles R. The Contribution of Viral Hepatitis to the Burden of Chronic Liver Disease in the United States. Am J Gastroenterol [Internet]. Nature Publishing Group; 2014 Jan 21 [cited 2014 Feb 18];(June 2013):1–7.

16. Parola M, Robino G. Oxidative stress-related molecules and liver fibrosis. J Hepatol [Internet]. 2001 Aug;35(2):297–306.

17. Tarrats N, Moles A, Morales A, García-Ruiz C, Fernández-Checa JC, Marí M. Critical role of tumor necrosis factor receptor 1, but not 2, in hepatic stellate cell proliferation, extracellular matrix remodeling, and liver fibrogenesis. Hepatology [Internet]. 2011 Jul [cited 2012 Sep 11];54(1):319–27.

18. Yeh MM, Brunt EM. Pathology of nonalcoholic fatty liver disease. Am J Clin Pathol [Internet]. 2007 Nov [cited 2014 Nov 8];128(5):837–47.

19. Blancas-Mejía LM, Ramirez-Alvarado M. Systemic amyloidoses. Annu Rev Biochem [Internet]. 2013 Jan [cited 2014 Nov 11];82:745–74.

20. Bird NJ, Michell a R, Peters a M. Accurate measurement of extracellular fluid volume from the slope/intercept technique after bolus injection of a filtration marker. Physiol Meas [Internet]. 2009 Dec [cited 2012 Feb 29];30(12):1371–9.

21. Gilmore I, Burroughs A, Murray-Lyon I. Indications, methods and outcomes of percutaneous liver biopsy in England and Wales: an audit by the British Society of Gastroenteriology and the Royal College of Physicians of London. Gut [Internet]. 1995 Mar [cited 2012 Jul 17];36(3):437–41.

22. Bedossa P, Dargère D, Paradis V. Sampling variability of liver fibrosis in chronic hepatitis C. Hepatology [Internet]. 2003 Dec [cited 2012 Jan 28];38(6):1449–57.

23. Knodell RG, Ishak KG, Black WC, Chen TS, Craig R, Kaplowitz N, et al. Formulation and application of a numerical scoring system for assessing histological activity in asymptomatic chronic active hepatitis. Hepatology [Internet]. 1981;1(5):431–5.

24. Bedossa P, Poynard T. An algorithm for the grading of activity in chronic hepatitis C. The METAVIR Cooperative Study Group. Hepatology [Internet]. 1996 Aug;24(2):289–93.

25. James J, Bosch KS, Aronson DC, Houtkooper JM. Sirius red histophotometry and spectrophotometry of sections in the assessment of the collagen content of liver tissue and its application in growing rat liver. Liver [Internet]. 1990 Feb;10(1):1–5.

26. O'Brien MJ, Keating NM, Elderiny S, Cerda S, Keaveny AP, Afdhal NH, et al. An assessment of digital image analysis to measure fibrosis in liver biopsy specimens of patients with chronic hepatitis C. Am J Clin Pathol [Internet]. 2000 Nov;114(5):712–8.

27. Calvaruso V, Burroughs AK, Standish R, Manousou P, Grillo F, Leandro G, et al. Computer-assisted image analysis of liver collagen: relationship to Ishak scoring and hepatic venous pressure gradient. Hepatology [Internet]. 2009 Apr [cited 2012 Nov 13];49(4):1236–44.

28. Calvaruso V, Dhillon AP, Tsochatzis E, Manousou P, Grillo F, Germani G, et al. Liver collagen proportionate area predicts decompensation in patients with recurrent hepatitis C virus cirrhosis after liver transplantation. J Gastroenterol Hepatol [Internet]. 2012 Jul [cited 2014 Jan 20];27(7):1227–32.

29. Azevedo CF, Nigri M, Higuchi ML, Pomerantzeff PM, Spina GS, Sampaio RO, et al. Prognostic significance of myocardial fibrosis quantification by histopathology and magnetic resonance imaging in patients with severe aortic valve disease. J Am Coll Cardiol [Internet]. Elsevier Inc.; 2010 Jul 20 [cited 2014 Sep 21];56(4):278–87.

30. Zhang Y, Edgley AJ, Cox AJ, Powell AK, Wang B, Kompa AR, et al. FT011, a new anti-fibrotic drug, attenuates fibrosis and chronic heart failure in experimental diabetic cardiomyopathy. Eur J Heart Fail. 2012;14(5):549–62.

31. Zdolsek JH, Lisander B, Hahn RG. Measuring the size of the extracellular fluid space using bromide, iohexol, and sodium dilution. Anesth Analg [Internet]. 2005 Dec [cited 2012 Feb 29];101(6):1770–7.

32. Foucher J. Diagnosis of cirrhosis by transient elastography (FibroScan): a prospective study. Gut [Internet]. 2006 Mar 1 [cited 2014 Mar 21];55(3):403–8.

33. Yoon KT, Lim SM, Park JY, Kim DY, Ahn SH, Han KH, et al. Liver stiffness measurement using acoustic radiation force impulse (ARFI) elastography and effect of necroinflammation. Dig Dis Sci. 2012;57(6):1682–91.

34. Wai C-T, Greenson JK, Fontana RJ, Kalbfleisch JD, Marrero JA, Conjeevaram HS, et al. A simple noninvasive index can predict both significant fibrosis and cirrhosis in patients with chronic hepatitis C. Hepatology [Internet]. 2003 Aug;38(2):518–26.

35. Groves AM, Win T, Screaton NJ, Berovic M, Endozo R, Booth H, et al. Idiopathic pulmonary fibrosis and diffuse parenchymal lung disease: implications from initial experience with 18F-FDG PET/CT. J Nucl Med. 2009;50(4):538–45.

36. Roulot D, Czernichow S, Le Clésiau H, Costes J-L, Vergnaud A-C, Beaugrand M. Liver stiffness values in apparently healthy subjects: influence of gender and metabolic syndrome. J Hepatol [Internet]. 2008 Apr;48(4):606–13.

37. Fraquelli M, Rigamonti C, Casazza G, Conte D, Donato MF, Ronchi G, et al. Reproducibility of transient elastography in the evaluation of liver

fibrosis in patients with chronic liver disease. Gut [Internet]. 2007 Jul;56(7):968–73.

38. Gómez-Domínguez E, Mendoza J, Rubio S, Moreno-Monteagudo JA, García-Buey L, Moreno-Otero R. Transient elastography: a valid alternative to biopsy in patients with chronic liver disease. Aliment Pharmacol Ther [Internet]. 2006 Aug 1;24(3):513–8.

39. Talwalkar JA, Kurtz DM, Schoenleber SJ, West CP, Montori VM. Ultrasound-based transient elastography for the detection of hepatic fibrosis: systematic review and meta-analysis. Clin Gastroenterol Hepatol [Internet]. 2007 Oct;5(10):1214–20.

40. Friedrich-Rust M, Ong M-F, Martens S, Sarrazin C, Bojunga J, Zeuzem S, et al. Performance of transient elastography for the staging of liver fibrosis: a meta-analysis. Gastroenterology [Internet]. 2008 Apr [cited 2012 Feb 29];134(4):960–74.

41. Ferraioli G, Tinelli C, Lissandrin R, Zicchetti M, Dal Bello B, Filice G, et al. Controlled attenuation parameter for evaluating liver steatosis in chronic viral hepatitis. World J Gastroenterol [Internet]. 2014 Jun 7 [cited 2014 Jul 10];20(21):6626–31.

42. Stebbing J, Farouk L, Panos G, Anderson M, Jiao LR, Mandalia S, et al. A meta-analysis of transient elastography for the detection of hepatic fibrosis. J Clin Gastroenterol [Internet]. 2010 Mar;44(3):214–9.

43. Muthupillai R, Lomas DJ, Rossman PJ, Greenleaf JF, Manduca a, Ehman RL. Magnetic resonance elastography by direct visualization of propagating acoustic strain waves. Science. 1995;269(5232):1854–7.

44. Ichikawa S, Motosugi U, Morisaka H, Sano K, Ichikawa T, Tatsumi A, et al. Comparison of the diagnostic accuracies of magnetic resonance elastography and transient elastography for hepatic fibrosis. Magn Reson Imaging [Internet]. Elsevier Inc.; 2015;33(1):26–30.

45. Tofts PS, Brix G, Buckley DL, Evelhoch JL, Henderson E, Knopp M V, et al. Estimating kinetic parameters from dynamic contrast-enhanced T1- weighted MRI of a diffusable tracer: Standardized quantities and symbols [Internet]. Journal of Magnetic Resonance Imaging. 1999. p. 223–32.

46. Ocak I, Bernardo M, Metzger G, Barrett T, Pinto P, Albert PS, et al. Dynamic contrast-enhanced MRI of prostate cancer at 3 T: a study of pharmacokinetic parameters. AJR Am J Roentgenol [Internet]. 2007 Oct;189(4):849.

47. Hayes C, Padhani AR, Leach MO. Assessing changes in tumour vascular function using dynamic contrast-enhanced magnetic resonance imaging. NMR Biomed [Internet]. 2002 Apr;15(2):154–63.

48. Zhou L, Chen TW, Zhang XM, Yang Z, Tang HJ, Deng D, et al. Liver dynamic contrast-enhanced MRI for staging liver fibrosis in a piglet model. J Magn Reson Imaging. 2014;39(4):872–8.

49. Smith DS, Welch EB, Li X, Arlinghaus LR, Loveless ME, Koyama T, et al. Quantitative effects of using compressed sensing in dynamic

contrast enhanced MRI. Phys Med Biol [Internet]. 2011;56(15):4933–46.

50. Flacke SJ, Fischer SE, Lorenz CH. Measurement of the gadopentetate dimeglumine partition coefficient in human myocardium in vivo: normal distribution and elevation in acute and chronic infarction. Radiology. 2001;218(3):703–10.

51. Zemrak F, Petersen SE. Late Gadolinium Enhancement CMR Predicts Adverse Cardiovascular Outcomes and Mortality in Patients With Coronary Artery Disease: Systematic Review and Meta-Analysis. Prog Cardiovasc Dis [Internet]. Elsevier Inc.; 2011;54(3):215–29.

52. Ismail TF, Prasad SK, Pennell DJ. Prognostic importance of late gadolinium enhancement cardiovascular magnetic resonance in cardiomyopathy. Heart [Internet]. 2012 Mar;98(6):438–42.

53. Arheden H, Saeed M, Higgins CB, Gao DW, Bremerich J, Wyttenbach R, et al. Measurement of the distribution volume of gadopentetate dimeglumine at echo-planar MR imaging to quantify myocardial infarction: comparison with 99mTc-DTPA autoradiography in rats. Radiology [Internet]. 1999 Jun [cited 2012 Nov 29];211(3):698–708.

54. Tong CY, Prato FS, Wisenberg G, Lee TY, Carroll E, Sandler D, et al. Techniques for the measurement of the local myocardial extraction efficiency for inert diffusible contrast agents such as gadopentate dimeglumine. Magn Reson Med [Internet]. 1993 Sep [cited 2012 Nov 29];30(3):332–6.

55. Runge VM, Clanton JA, Herzer WA, Gibbs SJ, Price AC, Partain CL, et al. Intravascular contrast agents suitable for magnetic resonance imaging. Radiology [Internet]. 1984;153(1):171–6.

56. Elster a D, Sobol WT, Hinson WH. Pseudolayering of Gd-DTPA in the urinary bladder. Radiology [Internet]. 1990 Feb;174(2):379–81.

57. Flett AS, Hayward MP, Ashworth MT, Hansen MS, Taylor AM, Elliott PM, et al. Equilibrium contrast cardiovascular magnetic resonance for the measurement of diffuse myocardial fibrosis: preliminary validation in humans. Circulation [Internet]. 2010 Jul 13 [cited 2011 Jun 15];122(2):138–44.

12.2 Chapter 2

1. Banypersad SM, Sado DM, Flett AS, Gibbs SDJ, Pinney JH, Maestrini V, et al. Quantification of myocardial extracellular volume fraction in systemic AL amyloidosis: an equilibrium contrast cardiovascular magnetic resonance study. Circ Cardiovasc Imaging [Internet]. 2013 Jan 1 [cited 2014 Mar 24];6(1):34–9.

2. AL-Saedi M. Liver Amyloidosis Complicated with Liver Failure: A Case Report and Review of the Literature. J Gastrointest Dig Syst [Internet]. 2011 [cited 2014 Dec 2];S3.

12.3 Chapter 3

1. Rosenberg WMC, Voelker M, Thiel R, Becka M, Burt A, Schuppan D, et al. Serum markers detect the presence of liver fibrosis: A cohort study. Gastroenterology [Internet]. 2004 Dec [cited 2014 Mar 24];127(6):1704–13.

2. Ripoll C, Bañares R, Rincón D, Catalina M-V, Lo Iacono O, Salcedo M, et al. Influence of hepatic venous pressure gradient on the prediction of survival of patients with cirrhosis in the MELD Era. Hepatology [Internet]. 2005 Oct;42(4):793–801.

3. Mayo MJ, Parkes J, Adams-Huet B, Combes B, Mills AS, Markin RS, et al. Prediction of clinical outcomes in primary biliary cirrhosis by serum enhanced liver fibrosis assay. Hepatology. 2008;48(5):1549–57.

4. Parkes J, Roderick P, Harris S, Day C, Mutimer D, Collier J, et al. Enhanced liver fibrosis test can predict clinical outcomes in patients with chronic liver disease. Gut [Internet]. 2010 Sep [cited 2012 Feb 29];59(9):1245–51.

5. Abignano G, Cuomo G, Buch MH, Rosenberg WM, Valentini G, Emery P, et al. The enhanced liver fibrosis test: a clinical grade, validated serum test, biomarker of overall fibrosis in systemic sclerosis. Ann Rheum Dis [Internet]. 2014 Feb 1 [cited 2014 Jan 14];73(2):420–7.

6. Lichtinghagen R, Pietsch D, Bantel H, Manns MP, Brand K, Bahr MJ. The Enhanced Liver Fibrosis (ELF) score: normal values, influence factors and proposed cut-off values. J Hepatol [Internet]. European Association for the Study of the Liver; 2013 Aug [cited 2014 Apr 3];59(2):236–42.

7. Mafham MM, Niculescu-Duvaz I, Barron J, Emberson JR, Dockrell MEC, Landray MJ, et al. A practical method of measuring glomerular filtration rate by iohexol clearance using dried capillary blood spots. Nephron Clin Pract [Internet]. 2007 Jan [cited 2014 Nov 25];106(3):c104–12.

8. Look DC. Time Saving in Measurement of NMR and EPR Relaxation Times. Rev Sci Instrum [Internet]. 1970 [cited 2014 Jan 20];41(2):250.

9. Piechnik SK, Ferreira VM, Dall'Armellina E, Cochlin LE, Greiser A, Neubauer S, et al. Shortened Modified Look-Locker Inversion recovery (ShMOLLI) for clinical myocardial T1-mapping at 1.5 and 3 T within a 9 heartbeat breathhold. J Cardiovasc Magn Reson [Internet]. 2010 Jan [cited 2011 Aug 1];12:69.

10. Bulluck H, Maestrini V, Rosmini S, Abdel-Gadir A, Treibel TA, Castelletti S, et al. Myocardial T1 mapping. Circ J [Internet]. 2015;79(3):487–94.

12.4 Chapter 4

1. Sado DM, Flett a. S, Banypersad SM, White SK, Maestrini V, Quarta G, et al. Cardiovascular magnetic resonance measurement of myocardial extracellular volume in health and disease. Heart. 2012;98:1436–41.

2. Flett AS, Hayward MP, Ashworth MT, Hansen MS, Taylor AM, Elliott PM, et al. Equilibrium contrast cardiovascular magnetic resonance for the measurement of diffuse myocardial fibrosis: preliminary validation in humans. Circulation [Internet]. 2010 Jul 13 [cited 2011 Jun 15];122(2):138–44.

3. White SK, Sado DM, Fontana M, Banypersad SM, Maestrini V, Flett AS, et al. T1 mapping for myocardial extracellular volume measurement by CMR: bolus only versus primed infusion technique. JACC Cardiovasc Imaging [Internet]. 2013 Sep [cited 2014 Mar 24];6(9):955–62.

4. Banypersad SM, Sado DM, Flett AS, Gibbs SDJ, Pinney JH, Maestrini V, et al. Quantification of myocardial extracellular volume fraction in systemic AL amyloidosis: an equilibrium contrast cardiovascular magnetic resonance study. Circ Cardiovasc Imaging [Internet]. 2013 Jan 1 [cited 2014 Mar 24];6(1):34–9.

5. Landis CS, Li X, Telang FW, Molina PE, Palyka I, Vetek G, et al. Equilibrium transcytolemmal water-exchange kinetics in skeletal muscle in vivo. Magn Reson Med [Internet]. 1999 Sep;42(3):467–78.

6. Ohno N, Terada N, Saitoh S, Ohno S. Extracellular space in mouse cerebellar cortex revealed by in vivo cryotechnique. J Comp Neurol. 2007;505(October 2006):292–301.

7. Hirokawa N, Kirino T. An ultrastructural study of nerve and glial cells by freeze-substitution. J Neurocytol. 1980;9:243–54.

8. Khajotia SS, Smart KH, Pilula M, Thompson DM. Concurrent quantification of cellular and extracellular components of biofilms. J Vis Exp [Internet]. 2013;(December):e50639.

9. Nyga A, Loizidou M, Emberton M, Cheema U. A novel tissue engineered three-dimensional in vitro colorectal cancer model. Acta Biomater [Internet]. Acta Materialia Inc.; 2013 Aug [cited 2013 Aug 29];9(8):7917–26.

10. Brown RA, Wiseman M, Chuo CB, Cheema U, Nazhat SN. Ultrarapid engineering of biomimetic materials and tissues: Fabrication of nano- and microstructures by plastic compression. Adv Funct Mater. 2005;15:1762–70.

11. Bandula S, White SK, Flett AS, Lawrence D, Pugliese F, Ashworth MT, et al. Measurement of myocardial extracellular volume fraction by using equilibrium contrast-enhanced CT: validation against histologic findings. Radiology [Internet]. 2013 Nov [cited 2014 Mar 24];269(2):396–403.

12. Nacif MS, Kawel N, Lee JJ, Chen X, Yao J, Zavodni A, et al. Interstitial myocardial fibrosis assessed as extracellular volume fraction with low-radiation-dose cardiac CT. Radiology [Internet]. 2012 Sep [cited 2014 Mar 24];264(3):876–83.

13. Bauner KU, Biffar A, Theisen D, Greiser A, Zech CJ, Nguyen ET, et al. Extracellular Volume Fractions in Chronic Myocardial Infarction. Invest Radiol. 2012;47(9):538–45.

14. Bandula S, Rosenberg WM, Hall AR, Moon JC, Taylor SA. Equilibrium Contrast-enhanced CT Imaging to Evaluate Hepatic Fibrosis : Initial Validation by Comparison with Histopathologic. 2015;000(0):1–8.

15. Yoon JH, Lee JM, Klotz E, Jeon JH, Lee K, Han JK, et al. Estimation of Hepatic Extracellular Volume Fraction Using Multiphasic Liver Computed Tomography for Hepatic Fibrosis Grading. Invest Radiol [Internet]. 2015;00(00):1.

16. Bandula S, Banypersad S, Sado D. Measurement of Tissue Interstitial Volume in Healthy Patients and Those with Amyloidosis with Equilibrium Contrast-enhanced MR Imaging. Radiology [Internet]. 2013 [cited 2014 Feb 5];268(3).

17. Deux J-F, Mihalache C-I, Legou F, Damy T, Mayer J, Rappeneau S, et al. Noninvasive detection of cardiac amyloidosis using delayed enhanced MDCT: a pilot study. Eur Radiol [Internet]. 2015;

18. Robson MD, Piechnik SK, Tunnicliffe EM, Neubauer S. T1 measurements in the human myocardium: The effects of magnetization transfer on the SASHA and MOLLI sequences. Magn Reson Med. 2013;70:664–70.

19. Magdeldin T, López-Dávila V, Villemant C, Cameron G, Drake R, Cheema U, et al. The efficacy of cetuximab in a tissue-engineered three-dimensional in vitro model of colorectal cancer. J Tissue Eng [Internet]. 2014 Jan [cited 2014 Dec 1];5(X):2041731414544183.

12.5 Chapter 5

1. Pinney JH, Smith CJ, Taube JB, Lachmann HJ, Venner CP, Gibbs SDJ, et al. Systemic amyloidosis in England: an epidemiological study. Br J Haematol [Internet]. 2013 May [cited 2014 Feb 20];161(4):525–32.

2. Gillmore JD, Wechalekar A, Bird J, Cavenagh J, Hawkins S, Kazmi M, et al. Guidelines on the diagnosis and investigation of AL amyloidosis. Br J Haematol [Internet]. 2014 Oct 14 [cited 2014 Oct 15];1–12.

3. Gilmore I, Burroughs A, Murray-Lyon I. Indications, methods and outcomes of percutaneous liver biopsy in England and Wales: an audit by the British Society of Gastroenteriology and the Royal College of Physicians of London. Gut [Internet]. 1995 Mar [cited 2012 Jul 17];36(3):437–41.

4. Banypersad SM, Sado DM, Flett AS, Gibbs SDJ, Pinney JH, Maestrini V, et al. Quantification of myocardial extracellular volume fraction in systemic AL amyloidosis: an equilibrium contrast cardiovascular magnetic resonance study. Circ Cardiovasc Imaging [Internet]. 2013 Jan 1 [cited 2014 Mar 24];6(1):34–9.

5. Anderson KR, Sutton MG, Lie JT. Histopathological types of cardiac fibrosis in myocardial disease. J Pathol [Internet]. 1979 Jun [cited 2012 Jul 17];128(2):79–85.

6. Tanaka M, Fujiwara H, Onodera T, Wu DJ, Hamashima Y, Kawai C. Quantitative analysis of myocardial fibrosis in normals, hypertensive hearts, and hypertrophic cardiomyopathy. Br Heart J [Internet]. 1986 Jun;55(6):575–81.

7. Loustaud-Ratti VR, Cypierre A, Rousseau A, Yagoubi F, Abraham J, Fauchais A-L, et al. Non-invasive detection of hepatic amyloidosis: FibroScan, a new tool. Amyloid [Internet]. 2011 Mar [cited 2012 Feb 29];18(1):19–24.

8. 8 Flett AS, Hayward MP, Ashworth MT, Hansen MS, Taylor AM, Elliott PM, et al. Equilibrium contrast cardiovascular magnetic resonance for the measurement of diffuse myocardial fibrosis: preliminary validation in humans. Circulation [Internet]. 2010 Jul 13 [cited 2011 Jun 15];122(2):138–44.

9. Sado DM, Flett AS, Moon JC. Novel imaging techniques for diffuse myocardial fibrosis. Future Cardiol. 2011;7(5):643–50.

10. Hawkins PN, Myers MJ, Lavender JP, Pepys MB. Diagnostic radionuclide imaging of amyloid: Biological targeting by circulating human serum amyloid P component. Lancet. 1988;1(8600)(June):1413–8.

11. Hawkins PN, Richardson S, MacSweeney JE, King a D, Vigushin DM, Lavender JP, et al. Scintigraphic quantification and serial monitoring of human visceral amyloid deposits provide evidence for turnover and regression. Q J Med [Internet]. 1993 Jun;86(6):365–74.

12. Banypersad SM, Sado DM, Flett AS, Gibbs SDJ, Pinney JH, Maestrini V, et al. Quantification of myocardial extracellular volume fraction in systemic AL amyloidosis: an equilibrium contrast cardiovascular magnetic resonance study. Circ Cardiovasc Imaging [Internet]. 2013 Jan 1 [cited 2014 Mar 24];6(1):34–9.

13. Hawkins P, Lavender J, Pepys M. Evaluation of systemic amyloidosis by scintigraphy with 123I-labeled serum amyloid P component. N Engl J Med [Internet]. 1990 [cited 2012 Jul 17];323(8):508–13.

14. Rydh A, Suhr O, Hietala S. Serum amyloid P component scintigraphy in familial amyloid polyneuropathy: regression of visceral amyloid following liver transplantation. Eur J Nucl Med [Internet]. 1998 [cited 2012 Aug 17];25(7).

15. Orton MR, Miyazaki K, Koh D-M, Collins DJ, Hawkes DJ, Atkinson D, et al. Optimizing functional parameter accuracy for breath-hold DCE-MRI of liver tumours. Phys Med Biol [Internet]. 2009 Apr 7 [cited 2012 Apr 8];54(7):2197–215.

16. Calvaruso V, Burroughs AK, Standish R, Manousou P, Grillo F, Leandro G, et al. Computer-assisted image analysis of liver collagen: relationship to Ishak scoring and hepatic venous pressure gradient. Hepatology [Internet]. 2009 Apr [cited 2012 Nov 13];49(4):1236–44.

17. Standish RA, Cholongitas E, Dhillon a P, Burroughs a K. An appraisal of the histopathological assessment of liver fibrosis. Gut [Internet]. 2006 Apr [cited 2012 Jan 3];55(4):569–78. Available from:

18. Levitt DG. The pharmacokinetics of the interstitial space in humans. BMC Clin Pharmacol [Internet]. 2003 Jul 30;3:3.

19. Benjaminsen IC, Brurberg KG, Ruud E-BM, Rofstad EK. Assessment of extravascular extracellular space fraction in human melanoma xenografts by DCE-MRI and kinetic modeling. Magn Reson Imaging [Internet]. 2008 Feb [cited 2012 Jul 17];26(2):160–70.

20. Li SP, Padhani AR. Tumor response assessments with diffusion and perfusion MRI. J Magn Reson Imaging [Internet]. 2012 Apr [cited 2012 Jul 17];35(4):745–63.

21. Padhani A, Hayes C, Landau S, Leach MO. Reproducibility of quantitative dynamic MRI of normal human tissues. NMR Biomed [Internet]. 2002 [cited 2012 Jul 17];15:143–53.

22. Piechnik SK, Ferreira VM, Dall'Armellina E, Cochlin LE, Greiser A, Neubauer S, et al. Shortened Modified Look-Locker Inversion recovery (ShMOLLI) for clinical myocardial T1-mapping at 1.5 and 3 T within a 9 heartbeat breathhold. J Cardiovasc Magn Reson [Internet]. 2010 Jan [cited 2011 Aug 1];12:69.

12.6 Chapter 6

1. Flett AS, Hayward MP, Ashworth MT, Hansen MS, Taylor AM, Elliott PM, et al. Equilibrium contrast cardiovascular magnetic resonance for the measurement of diffuse myocardial fibrosis: preliminary validation in humans. Circulation. 2010 Jul 13;122(2):138–44.

2. Schelbert EB, Testa SM, Meier CG, Ceyrolles WJ, Levenson JE, Blair AJ, et al. Myocardial extravascular extracellular volume fraction measurement by gadolinium cardiovascular magnetic resonance in humans: slow infusion versus bolus. J Cardiovasc Magn Reson. BioMed Central Ltd; 2011 Jan;13(1):16.

3. Landis CS, Li X, Telang FW, Coderre J a, Micca PL, Rooney WD, et al. Determination of the MRI contrast agent concentration time course in vivo following bolus injection: effect of equilibrium transcytolemmal water exchange. Magnetic resonance in medicine : official journal of the Society of Magnetic Resonance in Medicine / Society of Magnetic Resonance in Medicine. 2000 Oct;44(4):563–74.

4. Coelho-Filho OR, Mongeon F-P, Mitchell R, Moreno H, Nadruz W, Kwong R, et al. The Role of Transcytolemmal Water Exchange in Magnetic Resonance Measurements of Diffuse Myocardial Fibrosis in

Hypertensive Heart Disease. Circulation. Cardiovascular imaging. 2012 Nov 15;(617).

5. Olsson B, Aulie A, Sveen K, Andrew E. Human Pharmacokinetics of Iohexol. Invest Radiol. 1982;18.

6. McChesney EW, Hoppe JO. Studies of the tissue distribution and excretion of sodium diatrizoate in laboratory animals. The American journal of roentgenology, radium therapy, and nuclear medicine. 1957 Jul;78(1):137–44.

7. Dean P, Kivisaari L, Kormano M. The Diagnostic Potential of Contrast Enhancement Pharmacokinetics. Investigative Radiology. 1978;

8. Oppenheimer D, Young S. Diatrizoate CT distribution Kinetics: A Study of Human Tissue Characterization. Journal of computer assisted tomography. 1983;7(2):274–7.

9. Nacif MS, Kawel N, Lee JJ, Zavodni A, Sibley CT, Lima JAC. Interstitial Myocardial Fibrosis Assessed as extracellular Volume Fraction with Low-Radiation-Dose Cardiac CT. Radiology. 2012;264(3).

10. Burgener F, Hamlin D. Contrast enhancement in abdominal CT: bolus vs. infusion. American Journal of Roentgenology. 1981;137:351–8.

11. Brändström E, Grzegorczyk A, Jacobsson L, Friberg P, Lindahl A, Aurell M. GFR measurement with iohexol and 51Cr-EDTA. A comparison of the two favoured GFR markers in Europe. Nephrol Dial Transplant. 1998;13(5):1176–82.

12. Shrimpton PC, Hillier MC, Lewis MA, Dunn M. National survey of doses from CT in the UK: 2003. Br J Radiol. . 2006 Dec;79(948):968–80.

13. Piechnik SK, Ferreira VM, Dall'Armellina E, Cochlin LE, Greiser A, Neubauer S, et al. Shortened Modified Look-Locker Inversion recovery (ShMOLLI) for clinical myocardial T1-mapping at 1.5 and 3 T within a 9 heartbeat breathhold. J Cardiovasc Magn Reson. 2010 Jan;12:69.

14. Bland JM, Altman DG. Statistical methods for assessing agreement between two methods of clinical measurement. The Lancet. 1986;307–10.

15. Ugander M, Oki AJ, Hsu L-Y, Kellman P, Greiser A, Aletras AH, et al. Extracellular volume imaging by magnetic resonance imaging provides insights into overt and sub-clinical myocardial pathology. Eur Heart J. 2012 Jan 24;im:1–11.

16. White S, Sado D, Fontana M, Banypersad S, Maestrini V, Hausenloy D, et al. T1 Mapping for Myocardial Extracellular Volume Measurement by Cardiovascular Magnetic Resonance: Bolus only vs Primed Infusion Technique. JACC Cardiovasc Imaging. 2012;

17. Balvay D, Kachenoura N. Signal-to-Noise Ratio Improvement in Dynamic Contrast-enhanced CT and MR Imaging with Automated Principal Component Analysis Filtering. Radiology. 2011;258(2):435–45.

18. Siebert E, Bohner G, Dewey M, Bauknecht C, Klingebiel R. Dose related, comparative evaluation of a novel bone-subtraction algorithm in 64-row cervico-cranial CT angiography. Eur J Radiol. 2010 Jan;73(1):168–74.

19. Venema H, Hulsmans F, Heeten G den. CT Angiography of the Circle of Willis and Intracranial Internal Carotid Arteries: Maximum Intensity Projection with Matched Mask Bone Elimination—Feasibility Study. Radiology. 2001;893–8.

20. Chen X, Nacif MS, Liu S, Sibley C, Summers RM, Bluemke D a, et al. A Framework of Whole Heart Extracellular Volume Fraction Estimation for Low Dose Cardiac CT Images. IEEE T. Inf. Technol. B. 2012 Jun 12;[Epub].

21. Milano AD, Faggian G, Dodonov M, Golia G, Tomezzoli A, Bortolotti U, et al. Prognostic value of myocardial fibrosis in patients with severe aortic valve stenosis. J Thorac Cardiovasc Surg. 2012 Jan 11;[Epub].

12.7 Chapter 7

1. Bosetti C, Levi F, Lucchini F, Zatonski W a, Negri E, La Vecchia C. Worldwide mortality from cirrhosis: an update to 2002. J Hepatol [Internet]. 2007 May [cited 2014 Jan 29];46(5):827–39.

2. Cowie BC, Carville KS, MacLachlan JH. Mortality due to viral hepatitis in the Global Burden of Disease Study 2010: new evidence of an urgent global public health priority demanding action. Antivir Ther [Internet]. 2013 Jan [cited 2014 Mar 21];18(8):953–4.

3. Ellis EL, Mann D a. Clinical evidence for the regression of liver fibrosis. J Hepatol [Internet]. European Association for the Study of the Liver; 2012 May [cited 2014 Feb 17];56(5):1171–80.

4. Gilmore I, Burroughs A, Murray-Lyon I. Indications, methods and outcomes of percutaneous liver biopsy in England and Wales: an audit by the British Society of Gastroenteriology and the Royal College of Physicians of London. Gut [Internet]. 1995 Mar [cited 2012 Jul 17];36(3):437–41.

5. Juergen Nord H. Biopsy diagnosis of cirrhosis: blind percutaneous versus guided direct vision techniques—a review. Gastrointest Endosc [Internet]. Elsevier; 1982 May [cited 2014 Mar 24];28(2):102–4.

6. Regev A, Berho M, Jeffers LJ, Milikowski C, Molina EG, Pyrsopoulos NT, et al. Sampling error and intraobserver variation in liver biopsy in patients with chronic HCV infection. Am J Gastroenterol [Internet]. 2002 Oct;97(10):2614–8.

7. Foucher J. Diagnosis of cirrhosis by transient elastography (FibroScan): a prospective study. Gut [Internet]. 2006 Mar 1 [cited 2014 Mar 21];55(3):403–8.

8. Castera L. Noninvasive methods to assess liver disease in patients with hepatitis B or C. Gastroenterology [Internet]. Elsevier Inc.; 2012 May [cited 2014 Mar 21];142(6):1293–302.e4.

9. Rosenberg WMC, Voelker M, Thiel R, Becka M, Burt A, Schuppan D, et al. Serum markers detect the presence of liver fibrosis: A cohort study. Gastroenterology [Internet]. 2004 Dec [cited 2012 Aug 27];127(6):1704–13.

10. Abignano G, Cuomo G, Buch MH, Rosenberg WM, Valentini G, Emery P, et al. The enhanced liver fibrosis test: a clinical grade, validated serum test, biomarker of overall fibrosis in systemic sclerosis. Ann Rheum Dis [Internet]. 2014 Feb 1 [cited 2014 Jan 14];73(2):420–7.

11. Wahl K, Rosenberg W, Vaske B, Manns MP, Schulze-Osthoff K, Bahr MJ, et al. Biopsy-controlled liver fibrosis staging using the enhanced liver fibrosis (ELF) score compared to transient elastography. PLoS One [Internet]. 2012 Jan [cited 2013 Aug 11];7(12):e51906.

12. Parkes J, Guha IN, Roderick P, Rosenberg W. Performance of serum marker panels for liver fibrosis in chronic hepatitis C. J Hepatol [Internet]. 2006 Mar [cited 2014 Jan 20];44(3):462–74.

13. Nacif MS, Kawel N, Lee JJ, Chen X, Yao J, Zavodni A, et al. Interstitial myocardial fibrosis assessed as extracellular volume fraction with low-radiation-dose cardiac CT. Radiology [Internet]. 2012 Sep [cited 2014 Mar 24];264(3):876–83.

14. Banypersad SM, Sado DM, Flett AS, Gibbs SDJ, Pinney JH, Maestrini V, et al. Quantification of myocardial extracellular volume fraction in systemic AL amyloidosis: an equilibrium contrast cardiovascular magnetic resonance study. Circ Cardiovasc Imaging [Internet]. 2013 Jan 1 [cited 2014 Mar 24];6(1):34–9.

15. Flett AS, Hayward MP, Ashworth MT, Hansen MS, Taylor AM, Elliott PM, et al. Equilibrium contrast cardiovascular magnetic resonance for the measurement of diffuse myocardial fibrosis: preliminary validation in humans. Circulation [Internet]. 2010 Jul 13 [cited 2011 Jun 15];122(2):138–44.

16. Bandula S, Banypersad S, Sado D. Measurement of Tissue Interstitial Volume in Healthy Patients and Those with Amyloidosis with Equilibrium Contrast-enhanced MR Imaging. Radiology [Internet]. 2013 [cited 2014 Feb 5];268(3).

17. Varenika V, Fu Y, Maher JJ, Gao D, Kakar S, Cabarrus MC, et al. Hepatic fibrosis: evaluation with semiquantitative contrast-enhanced CT. Radiology [Internet]. 2013 Jan [cited 2014 Mar 24];266(1):151–8.

18. Zissen MH, Wang ZJ, Yee J, Aslam R, Monto A, Yeh BM. Contrast-enhanced CT quantification of the hepatic fractional extracellular space: correlation with diffuse liver disease severity. AJR Am J Roentgenol [Internet]. 2013 Dec [cited 2014 Jan 28];201(6):1204–10.

19. Menghini G. One-second biopsy of the liver--problems of its clinical application. N Engl J Med [Internet]. 1970 Sep 10 [cited 2014 Mar 21];283(11):582–5.

20. Cholongitas E, Burroughs AK. Liver: Transjugular liver biopsy yields high-quality samples. Nat Rev Gastroenterol Hepatol [Internet]. Nature Publishing Group; 2012 Sep [cited 2014 Jan 20];9(9):491–2.

21. Hall AR, Tsochatzis E, Morris R, Burroughs AK, Dhillon AP. Sample size requirement for digital image analysis of collagen proportionate area in cirrhotic livers. Histopathology [Internet]. 2013 Feb [cited 2014 Jan 20];62(3):421–30.

22. Knodell RG, Ishak KG, Black WC, Chen TS, Craig R, Kaplowitz N, et al. Formulation and application of a numerical scoring system for assessing histological activity in asymptomatic chronic active hepatitis. Hepatology [Internet]. 1981;1(5):431–5.

23. Calvaruso V, Burroughs AK, Standish R, Manousou P, Grillo F, Leandro G, et al. Computer-assisted image analysis of liver collagen: relationship to Ishak scoring and hepatic venous pressure gradient. Hepatology [Internet]. 2009 Apr [cited 2012 Nov 13];49(4):1236–44.

24. Bandula S, White SK, Flett AS, Lawrence D, Pugliese F, Ashworth MT, et al. Measurement of myocardial extracellular volume fraction by using equilibrium contrast-enhanced CT: validation against histologic findings. Radiology [Internet]. 2013 Nov [cited 2014 Mar 24];269(2):396–403.

25. Christner J a, Braun NN, Jacobsen MC, Carter RE, Kofler JM, McCollough CH. Size-specific dose estimates for adult patients at CT of the torso. Radiology [Internet]. 2012 Dec;265(3):841–7.

26. Calvaruso V, Dhillon AP, Tsochatzis E, Manousou P, Grillo F, Germani G, et al. Liver collagen proportionate area predicts decompensation in patients with recurrent hepatitis C virus cirrhosis after liver transplantation. J Gastroenterol Hepatol [Internet]. 2012 Jul [cited 2013 Aug 17];27(7):1227–32.

27. Armonis A, Patch D, Burroughs A. Hepatic Venous Pressure Measurement : An Old Test As a New Prognostic Marker in Cirrhosis ? Hepatology [Internet]. 1997 [cited 2012 Sep 13];9–12.

28. Parkes J, Roderick P, Harris S, Day C, Mutimer D, Collier J, et al. Enhanced liver fibrosis test can predict clinical outcomes in patients with chronic liver disease. Gut [Internet]. 2010 Sep [cited 2012 Feb 29];59(9):1245–51.

29. Wong TC, Piehler K, Meier CG, Testa SM, Klock AM, Aneizi A a, et al. Association between extracellular matrix expansion quantified by cardiovascular magnetic resonance and short-term mortality. Circulation [Internet]. 2012 Sep 4 [cited 2014 Mar 24];126(10):1206–16.

30. Banypersad SM, Sado DM, Flett AS, Gibbs SDJ, Pinney JH, Maestrini V, et al. Quantification of Myocardial Extracellular Volume Fraction in Systemic AL Amyloidosis: An Equilibrium Contrast Cardiovascular Magnetic Resonance Study. Circ Cardiovasc Imaging [Internet]. 2012 Nov 28 [cited 2012 Dec 21];

31. Hopper KD, Weingast G, Rudikoff J, Thickman D. Vicarious Excretion of Water-Soluble Contrast Media into the Gallbladder in Patients with

Normal Serum Creatinine. Invest Radiol [Internet]. 1988 Aug [cited 2014 Aug 21];23(8):604–8.

32. Chen B, Marin D, Richard S, Husarik D, Nelson R, Samei E. Precision of iodine quantification in hepatic CT: effects of iterative reconstruction with various imaging parameters. AJR Am J Roentgenol [Internet]. 2013 May [cited 2014 Mar 21];200(5):W475–82.

33. Shuman WP, Green DE, Busey JM, Kolokythas O, Mitsumori LM, Koprowicz KM, et al. Model-based iterative reconstruction versus adaptive statistical iterative reconstruction and filtered back projection in liver 64-MDCT: focal lesion detection, lesion conspicuity, and image noise. AJR Am J Roentgenol [Internet]. 2013 May [cited 2014 Mar 21];200(5):1071–6.

34. Ionizing radiation exposure of the population of the United States - NCRP Report No. 160. 2009.

35. Hendee WR, O'Connor MK. Radiation risks of medical imaging: separating fact from fantasy. Radiology [Internet]. 2012 Aug;264(2):312–21.

36. White SK, Sado DM, Fontana M, Banypersad SM, Maestrini V, Flett AS, et al. T1 mapping for myocardial extracellular volume measurement by CMR: bolus only versus primed infusion technique. JACC Cardiovasc Imaging [Internet]. 2013 Sep [cited 2014 Mar 24];6(9):955–62.

37. Robic MA, Procopet B, Métivier S, Péron JM, Selves J, Vinel JP, et al. Liver stiffness accurately predicts portal hypertension related complications in patients with chronic liver disease: a prospective study. J Hepatol [Internet]. 2011 Nov [cited 2014 Feb 6];55(5):1017–24.

12.8 Chapter 8

1. Perugini, E., et al., Noninvasive etiologic diagnosis of cardiac amyloidosis using 99mTc-3,3-diphosphono-1,2-propanodicarboxylic acid scintigraphy. J Am Coll Cardiol, 2005. 46(6): p. 1076-84.

2. Gertz, M. A., Comenzo, R., Falk, R. H., Fermand, J. P., Hazenberg, B. P., Hawkins, P. N., … Grateau, G. (2005). Definition of organ involvement and treatment response in immunoglobulin light chain amyloidosis (AL): A consensus opinion from the 10th International Symposium on Amyloid and Amyloidosis. American Journal of Hematology, 79(4), 319–328. doi:10.1002/ajh.20381

3. Maceira, A.M., et al., Cardiovascular magnetic resonance and prognosis in cardiac amyloidosis. Journal of cardiovascular magnetic resonance : official journal of the Society for Cardiovascular Magnetic Resonance, 2008. 10: p. 54.

4. Banypersad, S.M., et al., Quantification of myocardial extracellular volume fraction in systemic AL amyloidosis: an equilibrium contrast

cardiovascular magnetic resonance study. Circulation. Cardiovascular imaging, 2013. 6(1): p. 34-9.

5. Bandula, S., et al., Measurement of myocardial extracellular volume fraction by using equilibrium contrast-enhanced CT: validation against histologic findings. Radiology, 2013. 269(2): p. 396-403.

6. Nacif, M.S., et al., Interstitial myocardial fibrosis assessed as extracellular volume fraction with low-radiation-dose cardiac CT. Radiology, 2012. 264(3): p. 876-83.

7. Nacif, M.S., et al., 3D left ventricular extracellular volume fraction by low-radiation dose cardiac CT: assessment of interstitial myocardial fibrosis. Journal of cardiovascular computed tomography, 2013. 7(1): p. 51-7.

8. Fontana, M., et al., Native T1 Mapping in Transthyretin Amyloidosis. JACC. Cardiovascular imaging, 2014.

9. Perugini, E., et al., Noninvasive etiologic diagnosis of cardiac amyloidosis using 99mTc-3,3-diphosphono-1,2-propanodicarboxylic acid scintigraphy. Journal of the American College of Cardiology, 2005. 46(6): p. 1076-84.

10. Comenzo, R.L., et al., Consensus guidelines for the conduct and reporting of clinical trials in systemic light-chain amyloidosis. Leukemia, 2012. 26(11): p. 2317-25.

11. Hausleiter, J., et al., Estimated radiation dose associated with cardiac CT angiography. JAMA : the journal of the American Medical Association, 2009. 301(5): p. 500-7.

12. Piechnik, S.K., et al., Shortened Modified Look-Locker Inversion recovery (ShMOLLI) for clinical myocardial T1-mapping at 1.5 and 3 T within a 9 heartbeat breathhold. Journal of cardiovascular magnetic resonance : official journal of the Society for Cardiovascular Magnetic Resonance, 2010. 12: p. 69.

13. Flett, A.S., et al., Equilibrium contrast cardiovascular magnetic resonance for the measurement of diffuse myocardial fibrosis: preliminary validation in humans. Circulation, 2010. 122(2): p. 138-44.

12.9 Chapter 9

1. Joseph P, Mandal AK, Singh SK, Mandal P, Sankhwar SN, Sharma SK. Computerized tomography attenuation value of renal calculus: can it predict successful fragmentation of the calculus by extracorporeal shock wave lithotripsy? A preliminary study. J Urol [Internet]. 2002 May;167(5):1968–71.

2. Schieda N, Alrashed A, Flood TA, Samji K, Shabana W, McInnes MDF. Comparison of Quantitative MRI and CT Washout Analysis for Differentiation of Adrenal Pheochromocytoma From Adrenal Adenoma. AJR Am J Roentgenol [Internet]. 2016 Jun;206(6):1141–8.

3. Ambrose J, Hounsfield G. Computerized transverse axial tomography. Br J Radiol [Internet]. 1973 Feb;46(542):148–9.

4. Bandula S, White SK, Flett AS, Lawrence D, Pugliese F, Ashworth MT, et al. Measurement of myocardial extracellular volume fraction by using equilibrium contrast-enhanced CT: validation against histologic findings. Radiology [Internet]. 2013 Nov [cited 2014 Mar 24];269(2):396–403.

5. Barrett JF, Keat N. Artifacts in CT: recognition and avoidance. Radiographics [Internet]. 2004 [cited 2014 May 2];24(6):1679–91.

6. Boas FE, Fleischmann D. CT artifacts: causes and reduction techniques. Imaging Med. 2012;4(2):229–40.

7. Boas FE, Fleischmann D. Evaluation of two iterative techniques for reducing metal artifacts in computed tomography. Radiology [Internet]. 2011 Jun;259(3):894–902.

12.10 Chapter 10

1. Blancas-Mejía LM, Ramirez-Alvarado M. Systemic amyloidoses. Annu Rev Biochem [Internet]. 2013 Jan [cited 2014 Nov 11];82:745–74.

2. Araoz P, Batts K, MacCarty R. Amyloidosis of the alimentary canal: radiologic–pathologic correlation of CT findings. Abdom Imaging [Internet]. 2000 [cited 2012 Jul 30];44:38–44.

3. Spuler S, Emslie-smith A, Engel AG. Amyloid Myopathy : An Underdiagnosed Entity. 1998;719–28.

4. Richards DB, Cookson LM, Berges AC, Barton S V, Lane T, Ritter JM, et al. Therapeutic Clearance of Amyloid by Antibodies to Serum Amyloid P Component. N Engl J Med [Internet]. 2015;373(12):1106–14.

5. Hutt DF, Quigley A-M, Page J, Hall ML, Burniston M, Gopaul D, et al. Utility and limitations of 3,3-diphosphono-1,2-propanodicarboxylic acid scintigraphy in systemic amyloidosis. Eur Heart J Cardiovasc Imaging [Internet]. 2014 Nov [cited 2015 Jan 18];15(11):1289–98.

6. Bandula S, Banypersad S, Sado D. Measurement of Tissue Interstitial Volume in Healthy Patients and Those with Amyloidosis with Equilibrium Contrast-enhanced MR Imaging. Radiology [Internet]. 2013 [cited 2014 Feb 5];268(3).

7. Banypersad SM, Sado DM, Flett AS, Gibbs SDJ, Pinney JH, Maestrini V, et al. Quantification of myocardial extracellular volume fraction in systemic AL amyloidosis: an equilibrium contrast cardiovascular magnetic resonance study. Circ Cardiovasc Imaging [Internet]. 2013 Jan 1 [cited 2014 Mar 24];6(1):34–9.

8. Fontana M, Banypersad SM, Treibel T a, Maestrini V, Sado DM, White SK, et al. Native T1 mapping in transthyretin amyloidosis. JACC

Cardiovasc Imaging [Internet]. 2014 Feb [cited 2014 Aug 6];7(2):157–65.

9. Flett AS, Hayward MP, Ashworth MT, Hansen MS, Taylor AM, Elliott PM, et al. Equilibrium contrast cardiovascular magnetic resonance for the measurement of diffuse myocardial fibrosis: preliminary validation in humans. Circulation [Internet]. 2010 Jul 13 [cited 2011 Jun 15];122(2):138–44.

12.11 Chapter 11

1. Nyga A, Neves J, Stamati K, Loizidou M, Emberton M, Cheema U. The next level of 3D tumour models: immunocompetence. Drug Discov Today [Internet]. 2016 Apr 22;

2. Richards DB, Cookson LM, Berges AC, Barton S V, Lane T, Ritter JM, et al. Therapeutic Clearance of Amyloid by Antibodies to Serum Amyloid P Component. N Engl J Med [Internet]. 2015;373(12):1106–14.

3. Flett AS, Hayward MP, Ashworth MT, Hansen MS, Taylor AM, Elliott PM, et al. Equilibrium contrast cardiovascular magnetic resonance for the measurement of diffuse myocardial fibrosis: preliminary validation in humans. Circulation [Internet]. 2010 Jul 13 [cited 2011 Jun 15];122(2):138–44.

4. Gomez-Dominguez, E., Mendoza, J., Rubio, S., Moreno-Monteagudo, J. A., Garcia-Buey, L., & Moreno-Otero, R. (2006). Transient elastography: a valid alternative to biopsy in patients with chronic liver disease. Alimentary Pharmacology & Therapeutics, 24(3), 513–518. doi:Doi 10.1111/J.1365-2036.2006.02999.X

13 APPENDICES

13.1 Appendix 1

13.1.1 Presentations and Abstracts

1. S Sivarajan, T Treibel, S Punwani, J Moon, P Hawkins, S Taylor, **S Bandula.** Measurement of interstitial volume to assess abdominal organ amyloid burden using Quantitative Equilibrium-CT. ECR 2016

2. S Sivarajan, T Treibel, S Punwani, J Moon, P Hawkins, S Taylor, **S Bandula**. Practical application of Computed Tomographic Quantitative Imaging. Medical Society of London Annual Conference Feb 2016

3. Treibel TA, **Bandula S**, Fontana M, White SK, Gilbertson JA, Gillmore JD, Punwani S, Hawkins PN, Taylor SA, Moon JC. Eur Heart J Cardiovasc Imaging. 2015 May

4. Treibel TA, **Bandula S**, Fontana M, White SK, Gilbertson JA, Gillmore JD, Punwani S, Hawkins PN, Taylor SA, Moon JC. Quantification cardiac amyloid by cardiac computed tomography. ICNC12 Madrid, 4th May 2015

5. **Bandula S**, Magdeldin T, Stevens N, Moon JC, Taylor SA, Cheema U, Punwani S. Initial validation of Equilibrium Contrast Imaging for extracellular volume quantification used a 3D engineered tissue model. UCL Division of Medicine Awayday, April 2015

6. **Bandula S**, Punwani S, Rosenberg WM, Jalan R, Hall AR, Dhillon A, Moon JC, Taylor SA. Equilibrium contrast computed tomography for the evaluation of hepatic fibrosis – preliminary validation against histopathology. UCL Division of Medicine Awayday, June 2015

7. **Bandula S**, Punwani S, Rosenberg WM, Jalan R, Hall AR, Dhillon A, Moon JC, Taylor SA. Biomarker and Imaging: Equilibrium Imaging for the quantification of hepatic fibrosis. British Society for the Study of the Liver. Annual Retreat. June 2014

8. **S Bandula**, S. Banypersad, D. Sado, AS. Flett; SA .Taylor; PN. Hawkins, S. Punwani, JC. Moon Measurement of tissue extracellular volume in health and amyloidosis using equilibrium contrast MRI. ISMRM 2013

9. Banypersad SM, **Bandula S**, Sado D, Pinney J, Gibbs S, Maestrini, Fontana M, White SK, Punwani S, Taylor SA, Hawkins PN, Moon JC. Multiorgan ECV as measured by EQ-MRI in systemic amyloidosis. SCMR 2013 Scientific sessions

10. **Bandula S**, Punwani S, Rosenberg WM, Jalan R, Hall AR, Dhillon A, Moon JC, Taylor SA. Equilibrium imaging for liver extracellular volume quantification. NIHR trainee faculty conference. Nov 2013

11. C. Morgan, **S. Bandula**, A. Bainbridge, S. Rice, D. Sado, J. Moon, S. Punwani. Towards Optimising Equilibrium Magnetic Resonance Imaging: Modelling and Validation of Bolus and Infusion Protocols. ISMRM 2012

12. **Bandula S**, Sado D, Yeung J, Morgan C, Punwani S, Taylor S, Piechnik S, Moon JC. Equilibrium contrast MRI measurement of tissue extracellular volume of distribution in normal volunteers using ShMOLLI T1 quantification. ISMRM 2012

13. **S. Bandula**, J. Yeung, D. Sado, S. Punwani, S.A. Taylor, J. Moon. Measurement of abdominal tissue extracellular volume of distribution (Vd) in normal volunteers using equilibrium contrast (EQ) MRI. ESGAR 2012

14. **S. Bandula**, J. Yeung, D. Sado, S. Punwani, J. Moon, S.A. Taylor. Measurement of abdominal tissue extracellular volume of distribution (Vd) in normal volunteers using equilibrium contrast (EQ) MRI. UKRC 2012

15. **S. Bandula**, J. Yeung, D. Sado, S. Punwani, S.A. Taylor, J. Moon. Measurement of abdominal tissue extracellular volume of distribution (Vd) in normal volunteers using equilibrium contrast (EQ). Joint RCR/Wellcome Trust Research Day 2012

13.1.2 Original Articles

1. **Bandula S**, Magdeldin T, Stevens N, Yeung J, Moon JC, Taylor SA, Cheema U, Punwani S. Initial validation of equilibrium contrast imaging for extracellular volume quantification using a three-dimensional engineered tissue model. J Magn Reson Imaging. 2016 May;43(5):1224-9. doi: 10.1002/jmri.25066. Epub 2015 Oct 19. PubMed PMID: 26477540.
2. Treibel TA, **Bandula S**, Fontana M, White SK, Gilbertson JA, Herrey AS, Gillmore JD, Punwani S, Hawkins PN, Taylor SA, Moon JC. Extracellular volume quantification by dynamic equilibrium cardiac computed tomography in cardiac amyloidosis. J Cardiovasc Comput Tomogr. 2015 Nov-Dec;9(6):585-92. doi: 10.1016/j.jcct.2015.07.001. Epub 2015 Jul 10. PubMed PMID: 26209459; PubMed Central PMCID: PMC4684159.
3. **Bandula S**, Punwani S, Rosenberg WM, Jalan R, Hall AR, Dhillon A, Moon JC, Taylor SA. Equilibrium contrast-enhanced CT imaging to evaluate hepatic fibrosis: initial validation by comparison with histopathologic sampling. Radiology. 2015 Apr;275(1):136-43. doi: 10.1148/radiol.14141435. Epub 2014 Dec 8. PubMed PMID:25490188.
4. **Bandula S**, White SK, Flett AS, Lawrence D, Pugliese F, Ashworth MT, Punwani S, Taylor SA, Moon JC. Measurement of myocardial

extracellular volume fraction by using equilibrium contrast-enhanced CT: validation against histologic findings. Radiology. 2013 Nov;269(2):396-403. doi: 10.1148/radiol.13130130. Epub 2013 Jul 22. PubMed PMID: 23878282.

5. **Bandula S**, Banypersad SM, Sado D, Flett AS, Punwani S, Taylor SA, Hawkins PN, Moon JC. Measurement of Tissue interstitial volume in healthy patients and those with amyloidosis with equilibrium contrast-enhanced MR imaging. Radiology. 2013 Sep;268(3):858-64. doi: 10.1148/radiol.13121889. Epub 2013 May 14. PubMed PMID: 23674785.

13.2 Appendix 2

13.2.1 Derivation of T1 recovery function

13.3 Appendix 3

13.3.1 Full Published Articles

Spin Lattice Relaxation (T_1)

23.03.2013

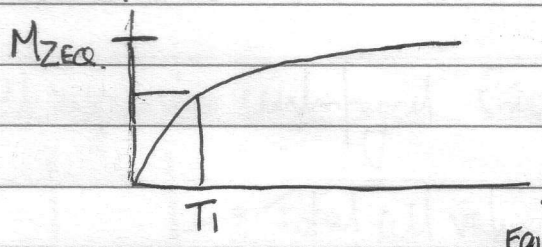

Relaxation towards thermodynamic equilibrium M_{ZEQ}.

Equilibrium. Start point

$$M_z(t) = M_{ZEQ} - \left[M_{ZEQ} - M_z(0) \right] e^{-t/T_1}.$$

where M tilted into xy plane
the start point z magnit. is 0.
$\therefore M_z(0) = 0.$

$$M_z(t) = M_{ZEQ} - \left[M_{ZEQ} - 0 \right] e^{-t/T_1}.$$

$$M_z(t) = M_{ZEQ} - M_{ZEQ} \times e^{-t/T_1}$$

$$= M_{ZEQ} \left(1 - e^{-t/T_1} \right)$$

IR experiment M is inverted $\therefore M_z(0) = -M_{ZEQ}$.

$$M_z(t) = M_{ZEQ} - \left[M_{ZEQ} + M_{ZEQ} \right] e^{-t/T_1}$$

$$M_z - 2M_{ZEQ} \cdot e^{-t/T_1}$$

$$= M_{ZEQ} \left(1 - 2e^{-t/T_1} \right)$$

$$M_z(t) = M(0) \left(1 - 2e^{-t/T_1} \right)$$

for IR experiment

$M_z(t)$ ↑ measured SI

$M(0)$ ↑ unknown constant

T_1 ↑ unknown constant.

13:3 Appendix 3